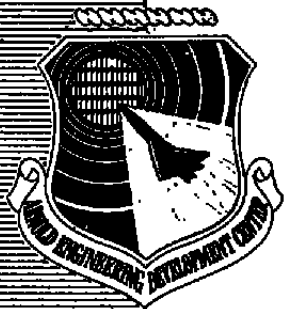


Dahlen  
Neumann  
Hillman  
Fine

AEDC-TR-81-5

## Test Section Turbulence in the AEDC/VKF Supersonic/Hypersonic Wind Tunnels



W. T. Strike, Jr., J. C. Donaldson, and D. K. Beale  
ARO, Inc.

July 1981

Final Report for Period October 1, 1979 – September 30, 1980

Approved for public release; distribution unlimited.

**ARNOLD ENGINEERING DEVELOPMENT CENTER  
ARNOLD AIR FORCE STATION, TENNESSEE  
AIR FORCE SYSTEMS COMMAND  
UNITED STATES AIR FORCE**

## NOTICES

When U. S. Government drawings, specifications, or other data are used for any purpose other than a definitely related Government procurement operation, the Government thereby incurs no responsibility nor any obligation whatsoever, and the fact that the Government may have formulated, furnished, or in any way supplied the said drawings, specifications, or other data, is not to be regarded by implication or otherwise, or in any manner licensing the holder or any other person or corporation, or conveying any rights or permission to manufacture, use, or sell any patented invention that may in any way be related thereto.

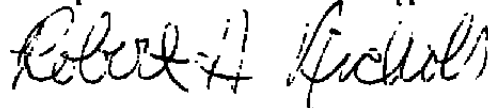
Qualified users may obtain copies of this report from the Defense Technical Information Center.

References to named commercial products in this report are not to be considered in any sense as an indorsement of the product by the United States Air Force or the Government.

This report has been reviewed by the Office of Public Affairs (PA) and is releasable to the National Technical Information Service (NTIS). At NTIS, it will be available to the general public, including foreign nations.

## APPROVAL STATEMENT

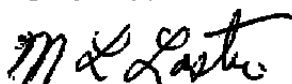
This report has been reviewed and approved.



ROBERT H. NICHOLS  
Directorate of Technology  
Deputy for Operations

Approved for publication:

FOR THE COMMANDER



MARION L. LASTER  
Director of Technology  
Deputy for Operations

**UNCLASSIFIED**

# **UNCLASSIFIED**

## **20. ABSTRACT, Concluded.**

results are presented and discussed, and the anemometer and dynamic pitot pressure measurements are compared.

## PREFACE

The work reported herein was conducted by the Arnold Engineering Development Center (AEDC), Air Force Systems Command (AFSC) at the request of the Directorate of Technology (DOT), AEDC. The test and analysis were performed by ARO, Inc., AEDC Group (a Sverdrup Corporation Company), operating contractor for the AEDC, AFSC, Arnold Air Force Station, Tennessee. The experimental phases of the program were conducted in the von Kármán Gas Dynamics Facility (VKF) under ARO Project Numbers 41A/B-W1 (FY 78) and V41A/B-52 (FY 79). The final analysis of the experimental results was accomplished under ARO Project Number V32C-01. The Air Force Project Manager was Mr. A. F. Money. The manuscript was submitted for publication on January 2, 1981.

The authors gratefully acknowledge the assistance of Mr. Charles G. Nelson, who supervised operation of the instrumentation used in the data acquisition and spectral analysis, Mr. Michael B. Krauth, who programmed the dynamic pressure computer routines, Mr. Tommy R. Pyle, who programmed the hot-wire anemometer data reduction computer routines, and Mr. Herman R. Farris, who fabricated the hot-wire anemometer probes.

Messrs. W. T. Strike and J. C. Donaldson are currently employed by Calspan Field Services, Inc., AEDC Division. Mr. D. K. Beale is an employee of Sverdrup Technology, Inc., AEDC Division.

## CONTENTS

	<u>Page</u>
<b>1.0 INTRODUCTION .....</b>	<b>7</b>
<b>2.0 BACKGROUND .....</b>	<b>7</b>
<b>3.0 TEST FACILITIES</b>	
<b>3.1 Tunnel A .....</b>	<b>11</b>
<b>3.1.1 Description .....</b>	<b>11</b>
<b>3.1.2 Test Installation .....</b>	<b>12</b>
<b>3.2 Tunnel B .....</b>	<b>13</b>
<b>3.2.1 Description .....</b>	<b>13</b>
<b>3.2.2 Test Installation .....</b>	<b>13</b>
<b>3.3 Plant .....</b>	<b>14</b>
<b>4.0 APPARATUS</b>	
<b>4.1 Models .....</b>	<b>14</b>
<b>4.1.1 Flat Plate Model .....</b>	<b>15</b>
<b>4.1.2 Sharp Cone Model .....</b>	<b>15</b>
<b>4.2 Probes .....</b>	<b>16</b>
<b>4.2.1 Anemometer Probes .....</b>	<b>16</b>
<b>4.2.2 Dynamic Pitot Pressure Probes .....</b>	<b>17</b>
<b>4.2.3 Pitot Pressure and Total Temperature Probes .....</b>	<b>17</b>
<b>4.2.4 Probe Holders .....</b>	<b>18</b>
<b>4.3 Instrumentation .....</b>	<b>18</b>
<b>4.3.1 Hot-Wire Anemometer .....</b>	<b>18</b>
<b>4.3.2 Dynamic Pressure Sensors .....</b>	<b>19</b>
<b>4.3.3 Signal Processing Equipment .....</b>	<b>19</b>
<b>5.0 DATA ANALYSIS</b>	
<b>5.1 Signal Processing and Normalization .....</b>	<b>20</b>
<b>5.1.1 Procedure .....</b>	<b>20</b>
<b>5.1.2 Statistical Uncertainties .....</b>	<b>21</b>
<b>5.1.3 Data Processing .....</b>	<b>21</b>
<b>5.1.4 Normalization .....</b>	<b>23</b>
<b>5.2 Anemometer Signal Analysis .....</b>	<b>23</b>
<b>5.2.1 Spectral Analysis .....</b>	<b>23</b>
<b>5.2.2 Signal Enhancement .....</b>	<b>24</b>
<b>5.2.3 Modal Analysis .....</b>	<b>26</b>
<b>5.3 Dynamic Pressure Analysis .....</b>	<b>31</b>
<b>6.0 RESULTS</b>	
<b>6.1 Tunnel A Stilling Chamber .....</b>	<b>35</b>
<b>6.2 Tunnel A and B Test Section Turbulence .....</b>	<b>36</b>

6.2.1 Test Section Pressure Fluctuations .....	36
6.2.2 Tunnel A Side Wall Static Pressure Fluctuations .....	40
6.3 Cone Surface Static Pressure Fluctuations .....	41
6.4 Summary of Tunnel A and B Pressure Fluctuation Results .....	43
<b>7.0 CONCLUDING REMARKS .....</b>	<b>44</b>
<b>REFERENCES .....</b>	<b>46</b>

## ILLUSTRATIONS

<u>Figure</u>	<u>Page</u>
1. Tunnel A .....	53
2. Typical Installation of the Tunnel Wall Flush-Mounted Dynamic Pressure Sensors .....	58
3. Tunnel A Flat Plate Installation (FY78) .....	59
4. Tunnel A Installation with Nominal Locations of the Dynamic Pressure Sensors (Transducers) .....	60
5. Tunnel A Flow-Field Survey Mechanism (FY 79) .....	61
6. Test Installation in Tunnel A (FY 79) .....	62
7. Tunnel B .....	63
8. Test Installation in Tunnel B .....	64
9. Flat Plate Model for Dynamic Pressure Sensor Measurement .....	66
10. Flat Plate Installation in Tunnel B, Typical Shadowgram at Mach Number 8 and Reynolds Number $2 \times 10^6$ per foot .....	67
11. Model Details, 6-deg Sharp Nose Cone .....	68
12. Hot-Wire Anemometer Probe .....	70
13. Dynamic Pitot Pressure Probes .....	72
14. Mean Flow-Field Survey Probes .....	73
15. Tunnel A Stilling Chamber Pressure Fluctuations .....	74
16. Summary of Stilling Chamber Turbulence Measurements in Tunnel A .....	75
17. Typical Tunnel A Stilling Chamber Pressure Fluctuation Spectra .....	76
18. Tunnel A Test Section Pressure Fluctuations .....	82
19. Tunnel B Test Section Pressure Fluctuations .....	84
20. Spectrum of Pressure Fluctuations Inferred from Hot-Wire Measurements, $M_\infty = 6$ , $RE_\infty = 3 \times 10^6$ per foot .....	85
21. Spectrum of Pressure Fluctuations Inferred from Hot-Wire Measurements, $M_\infty = 4$ , $RE_\infty = 3 \times 10^6$ per foot .....	86
22. Normalized Distributions of Fluctuations Inferred from Hot-Wire Measurements, $M_\infty = 4$ , $RE_\infty = 3 \times 10^6$ per foot .....	87

<u>Figure</u>	<u>Page</u>
23. Normalized Distributions of Fluctuations Inferred from Hot-Wire Measurements, $M_\infty = 6$ , $RE_\infty = 3 \times 10^6$ per foot .....	89
24. Normalized Distributions of Fluctuations Inferred from Hot-Wire Measurements, $M_\infty = 8$ , $RE_\infty = 3 \times 10^6$ per foot .....	91
25. Pitot Pressure Fluctuation Spectral Content in AEDC Tunnels A and B (Based on FY79 Pitot Probe), $\Delta f = 200$ Hz .....	94
26. Typical Tunnel A Pitot-Acoustic Pressure Spectra .....	95
27. Comparison of Acoustical Pitot Probe Results, Mach Number 6.0 at $RE_\infty = 1 \times 10^6$ per foot .....	99
28. Tunnel A Tare for the Dynamic Pressure Sensor of the Pitot Acoustic Probe (FY78) .....	100
29. Tunnel B Tare for the Dynamic Pressure Sensor of the Pitot Acoustic Probe (FY78) .....	101
30. Typical Spectral Distribution in the Wall Static Pressure at Tunnel Station 125 in. (Mach Number 4.0, $RE_\infty = 4 \times 10^6$ per foot) .....	102
31. Tunnel A Nonoperating Side Wall Static Pressure Fluctuation Spectra at $RE_\infty = 4 \times 10^6$ per foot .....	104
32. 6-deg Sharp Cone Surface Pressure Fluctuation Coefficients .....	105
33. Pressure Fluctuation Spectra on a 6-deg Sharp Nose Cone at Mach Number 6.0 (Zero Angle of Attack) .....	108
34. Normalized Power Spectral Density of the Surface Pressure Fluctuations on a 6-deg Sharp Nose Cone .....	112
35. Typical Pressure Fluctuation Levels in the AEDC Wind Tunnels A and B .....	113
36. Summary of Pressure Fluctuation Levels in AEDC Tunnels A, B, and C at Nominal $RE_\infty = 2 \times 10^6$ to $4 \times 10^6$ per foot .....	114

## APPENDIXES

A. HOT-WIRE ANEMOMETER CALIBRATION .....	115
B. DYNAMIC PRESSURE SENSOR CALIBRATION .....	119
C. WIND TUNNEL TEST PARAMETERS .....	147
D. SIX-DEGREE SHARP NOSE CONE SURFACE AND FLOW-FIELD PROPERTIES .....	160
NOMENCLATURE .....	163

## 1.0 INTRODUCTION

To enhance the understanding of flow quality in the AEDC Supersonic Wind Tunnel (A) and Hypersonic Wind Tunnel (B) and to provide documentation of the wind tunnel test section turbulence, a comprehensive experimental and analytical program was conducted during the period October 1977 to September 1980. This report presents a comprehensive compilation of fluctuating measurements from these wind tunnels.

The objectives of this program were as follows: (1) to experimentally evaluate and document the test section turbulence levels in Tunnels A and B; (2) to assess any differences found between dynamic pressure measurements and hot-wire anemometer results; and (3) to formulate and implement test procedures, data reduction techniques, and software needed for obtaining hot-wire and dynamic pressure data.

The scope of this report includes the identification of some of the general operational and physical features of the facility which may directly or indirectly affect the tunnel turbulence measurements or the interpretations of dynamic measurements in the wind tunnel. The experimental phase covers the Mach number and Reynolds number range in Tunnel A ( $M_\infty = 1.5$  to 5.0 and  $RE = 0.5$  to  $6 \times 10^6$  per foot) and in Tunnel B ( $M_\infty = 6.0$  and 8.0, and  $RE = 0.5$  to  $5.0 \times 10^6$  per foot). The measurements include dynamic pressure data obtained from surface-mounted instrumentation on a flat plate and a sharp-nosed 6-deg cone, pitot acoustic probe data, and hot-wire anemometry results. The report also identifies the calibration procedures with some typical calibration results, the normalizing parameters usually applied to tunnel wall turbulence measurements, and a synopsis of the FFT (Fast Fourier Transform) signal processing used in this study.

## 2.0 BACKGROUND

Wind tunnel test section turbulence, its intensity, spatial distribution, and spectral content, has become increasingly important in the analysis of test data. The sector-supported model in the test section and the model instrumentation, particularly the dynamic pressure sensors (transducers) and the hot-wire survey probes, are directly affected by the test section turbulence. Aerodynamically, test section turbulence can affect the character of the flow over the model, particularly the turbulence or instability within the model boundary layer and the location of boundary-layer transition on the model. Therefore, it is important that these turbulence and noise factors be measured, identified, and documented so that a proper interpretation and correlation can be made of flow fluctuation measurements obtained in the wind tunnel.

In a high-speed wind tunnel ( $M_\infty > 1$ ), particularly in an unheated test unit, a major source of fluctuating disturbances in the free-stream flow is the turbulent tunnel wall

boundary layer in the form of pressure fluctuations (a sound source), as noted in Refs. 1 through 14. Briefly, this tunnel flow disturbance mechanism is viewed as a moving sound source which has been modeled by examining the characteristics of wavelets produced by a turbulent boundary layer in a supersonic stream (Refs. 11 and 12). The wavelets produced by the shear layer are rationalized by assuming that a moving, fluid-dynamic type of wavy wall is submerged within the shear layer. This wavy wall disturbance moves downstream at a velocity greater than the local speed of sound. The wavy wall concept supposedly can be attributed to the velocity or vorticity fluctuations within the boundary layer which in turn are viewed as internal shear layer disturbances produced by moving "finite-shaped bodies" or "randomly spaced pulses" (Ref. 1). These moving fluid-dynamic bodies represent finite-sized cells of vorticity or circulation moving within the turbulent shear layer which transmit pressure pulses (wavelets) into the external stream producing the test section pressure fluctuations.

This concept of a moving sound source generated by the turbulent tunnel wall boundary layer has been used to model analytically certain tunnel flow fluctuating properties. With a number of simplifying assumptions such as small (relative to mean flow properties) localized fluctuations in a two-dimensional flow regime, the surface pressure fluctuation is approximately proportional to the local surface shear (Refs. 15, 16), that is,  $\tilde{P}$  is proportional to  $\tau_w$ . Therefore, as aptly shown in Ref. 15, the rms (root-mean-square) level of the pressure fluctuations can be described in terms of the following semi-empirical relationship:

$$\tilde{P}/\bar{q}_\infty = A \cdot c_f = \frac{[2A(0.0296)/RE_x^{0.2}]}{[0.5[1 + (TW/\bar{T})] - 0.22\eta[(y - 1)/2]M_\infty^2]^{0.64}} \quad (1)$$

Also, the power spectral distribution,  $F(f)$ , of the stream pressure fluctuation can be shown analytically (Refs. 1 and 15) and by well defined experimental measurements (Refs. 1, 9, 10 and 11) to be approximated by the following function:

$$F_p(f)/\tilde{P}^2 = F\{1.0/[1 + (2\pi f\delta^*/u_c)^2]\} \quad (2)$$

This simply suggests the procedure for normalizing tunnel turbulence spectral distributions; it further suggests that the spectral distribution approaches asymptotically some finite upper limit as the frequency ( $f$ ) decreases toward the d-c level.

Some of the significant wind tunnel and, in some cases, model parameters which will aid in the correlation of tunnel turbulence measurements are identified and discussed in the literature (for example see Refs. 1, 3, 8, 10, and 15). These normalizing parameters include the following:

1. For a length, the boundary-layer displacement or momentum thickness.
2. For time, the ratio of the boundary-layer thickness parameter to the free-stream or local sound source convective velocity.
3. For a force per unit area, the local wall shear value or local dynamic pressure.
4. For the velocity, the convective velocity of the sound source or the free-stream velocity.

These are the major parameters that will be considered in the present document.

Previous attempts to measure flow-field fluctuations in Tunnels A and B were not always successful. As noted or implied in Refs. 3, 5, 6, and 7, there exists a fundamental disagreement between the hot-wire and dynamic pressure (microphone) results. Donaldson (Ref. 7) and Laderman (Ref. 3) indicated that although the hot-wire results were reasonable (that is, consistent with measurements made in similar facilities), the dynamic pressure measurements obtained from microphones appear to be unrealistically high.

Several factors are known to affect the performance or response of a dynamic pressure transducer. In the case of a microphone, the response of the transducer is influenced by the natural resonance of the gage, increasing the rms of the gage output. Also, the scale factor or response level of the transducer changes with the local temperature and pressure level of the transducer environment. In the present study, an effort was made to calibrate the transducers statically and dynamically in a subatmospheric environment closely approaching those conditions existing in the Tunnel A and B environments. In general, the resonant frequency of most of the transducers used in this study were well above the maximum frequency of the fluctuation levels sensed in the tunnel flow.

Another factor which affects the dynamic pressure measurement is associated with the transducer installation (Refs. 17 and 18). Hanly's investigation (Ref. 17) conducted on a tunnel wall with supersonic flow (Mach numbers 1.68 and 2.5) revealed that the most consistent and reliable results were obtained when the transducer was flush mounted or slightly recessed (less than  $0.0005\delta$ ) in the tunnel (or model) wall. Dynamic pressure gages protruding as little as 0.05 percent of the total boundary-layer thickness ( $\delta$ ) produced significant changes in the gage output and in the outputs of gages located immediately downstream of the protruding gage. Increasing the local stream velocity tended to increase the gage sensitivity to effects produced by a slightly protruding gage. These studies (Refs. 17 and 18) demonstrate that the transducer protuberance affects the mid-range of the spectrum of recorded transducer response. In the present study every effort was made to insure that

wall or surface-mounted transducers were either flush with the model surface or slightly recessed (about 0.005 in.).

As found in subsonic tunnels (Refs. 18 and 19) and in the supersonic and hypersonic wind tunnels (Refs. 5 and 7), the pressure transducer outputs are sensitive to acceleration effects, electronic noise, and sound sources transmitted through the structural members supporting the probe model containing the dynamic pressure sensors (DPS). One way to monitor these extraneous effects is to compare the output of an active gage (one exposed to the tunnel flow) with the output from a dummy or inactive gage (one isolated from the tunnel flow but installed immediately adjacent to an active gage). In general, these external disturbances tend to distort (increase) the amplitude of the pressure signal at the lower frequencies. The pressure spectra obtained from the hot-wire analyses, the more reliable pressure measurements (see Refs. 9, 10, 18, 19, and 20), and theoretical models (see for example Refs. 1 and 15) all support the contention that the pressure fluctuation spectrum should decrease abruptly as the frequency approaches zero (the d-c level). However, most of the pressure spectra obtained from wind tunnel measurements where the lower frequency components of the spectra were retained tend to increase abruptly at the lower frequencies, thus supporting the idea that "spurious" pressure fluctuations (discussed in Ref. 19) are being sensed by the transducer. Therefore, the true rms level of a pressure signal associated with the turbulence in the flow must be evaluated with these spurious components of the signal spectrum identified and removed or reduced to a realistic level.

The hot-wire measurements in Tunnel A were used to identify pressure fluctuations in the tunnel test section. As mentioned previously this disturbance is introduced primarily by the turbulent boundary layer along the tunnel wall. At the lower Mach numbers (Mach number < 2.0), velocity (vorticity) fluctuations may be introduced by the stilling chamber screens. At the higher free-stream Mach numbers, these screen disturbances are usually damped out by the isentropic compression and expansion through the supersonic nozzle. Temperature (or entropy) fluctuations are generally negligible since Tunnel A operates at moderate temperatures (on the order of 100 to 200°F). In Tunnel B, which operates at higher stagnation temperatures, particularly at Mach number 8, where the normal operating stagnation temperature is 890°F, the temperature fluctuations or spottiness becomes measureable and must be taken into consideration in the hot-wire analysis. As indicated in Ref. 2, until pressure fluctuation measurements obtained from dynamic pressure sensors become more reliable, hot-wire anemometry appears to be the most reliable means for identifying the turbulence in a supersonic/hypersonic test regime (Tunnels A, B, and C).

In general, the measurements made in Tunnel A were obtained with 50- $\mu$ in.-diam hot-wire probes and in Tunnel B, at Mach numbers 6 and 8, with 20- $\mu$ in.-diam probes. Although

the acquisition of hot-wire measurements at hypersonic speeds in Tunnel B is a fairly standard operational procedure, the results obtained in Tunnel A at lower supersonic speeds are unique for a facility of this size (40-by 40-in. test section). In comparison to Tunnel B, the Tunnel A environment is much more severe in that the hot wires are exposed to greater dynamic loads, greater flow-field particle contamination, and higher free-stream humidity levels. This study shows that in spite of these severe environmental effects and the slightly higher loss of hot wires, it is still possible to obtain useful hot-wire measurements in Tunnel A.

## 3.0 TEST FACILITIES

### 3.1 TUNNEL A

#### 3.1.1 Description

Tunnel A (Fig. 1) is a continuous, closed-circuit, variable density wind tunnel with an automatically driven flexible-plate-type nozzle and a 40- by 40-in. test section. The tunnel can be operated at Mach numbers from 1.5 to 6 at maximum stagnation pressures from 29 to 200 psia, respectively, and at stagnation temperatures up to 750°R at Mach number 6. Minimum operating pressures range from about 1/10 to 1/20 of the maximum at each Mach number. The tunnel is equipped with a model injection system which allows removal of the model from the test section while the tunnel remains in operation. A description of the tunnel and airflow calibration information may be found in the *Test Facilities Handbook* (Ref. 21).

In addition to the turbulent boundary layer on the nozzle walls, there are other potential sources of disturbance generated in the Tunnel A circuit, and some of these will be identified and discussed. Figure 1c is an illustration of the valves, ducting, screens, and stilling chamber located immediately upstream of the Tunnel A nozzle. The pressure level in the tunnel circuit is controlled in part by the addition of high-pressure air through valve 337 or 237. Each valve operates by opening and closing at regular intervals to maintain the tunnel pressure. At low Mach numbers, this operation generates strong pressure pulses which can interfere with the recording of dynamic data. Also, the addition of the air through the valve creates a sound source which can propagate through the tunnel structure and through the flow in the circuit. For testing involving dynamic measurements, a manually operated valve (017) located downstream of the diffuser provides a more favorable, alternate method of adding air to the Tunnel A circuit.

The stilling chamber shown in Fig. 1d contains up to 12 screens of various mesh sizes. The purpose of the screens is to filter the air flow and minimize flow gradients entering the

nozzle region, but at the lower nozzle Mach numbers these screens may be a small source of velocity fluctuations which may reach the test section region (see Ref. 7).

Downstream of the tunnel nozzle region, the model injection tank and the diffuser section are two additional sources of disturbance which may affect the recording of dynamic measurements. The flow over the slot in the doors over the model injection tank is a source of acoustical disturbances or vibration. The turbulent boundary-layer interaction with the shock wave structure in the diffuser is another potential source of disturbance.

### 3.1.2 Test Installation

Dynamic pressure sensors (DPS) were installed at various stations between the stilling chamber and test section of Tunnel A. A flush-mounted DPS unit was located in the stilling chamber as shown in Figs. 1c, d, and e. As noted in Fig. 1e, the 0.2 in.-diam transducer was located in the center of the 3.5-in.-diam surface with nominally a 0.25-in. gap between the cylindrical segment (or disk-shaped surface) and the stilling chamber wall. Four additional DPS units were implanted at three other stations in the wind tunnel nozzle; two DPS units were located on opposite sides of the tunnel at station 125 (see Fig. 1f), one at station 30.7, and one in the model injection tank. The fixture containing the DPS units inserted into the nozzle side walls is shown in Fig. 2. A pressure tap was provided so that the local nozzle wall static pressure could be measured.

The first test installation (1978) for the study consisted of a mechanism supporting the flow-field probes which could be traversed relative to a flat plate model (Figs. 3 and 4). The retractable shielding mechanism shown in Fig. 3 for the hot-wire probes rotated about a fixed point. This particular design was subsequently found to be unsatisfactory because of the strong shock system produced when the shield was retracted. The dynamic pitot probe was mounted on top of the retractable probe-shielding mechanism.

In the 1979 entry, the retractable shielding mechanism was modified so that the shield moved almost vertically with respect to the probes (see Fig. 5). Also, a new pitot acoustic probe was mounted on the retractable shield fixture. As in the case of the FY78 installation, the probing system was mounted on the translating mechanism above a conical body which was also instrumented with DPS units as shown in Fig. 6. Both the FY78 and FY79 installations could be retracted into the model injection tank for additional model work and replacement of hot-wire probes.

## 3.2 TUNNEL B

### 3.2.1 Description

Tunnel B (Fig. 7) is a closed-circuit hypersonic wind tunnel with a 50-in.-diam test section. Two axisymmetric contoured nozzles are available to provide Mach numbers of 6 and 8, and the tunnel may be operated continuously at pressure level ranges from 20 to 300 psia at Mach number 6, and from 50 to 900 psia at Mach number 8, with air supplied by the VKF main compressor plant. Stagnation temperatures sufficient to avoid air liquefaction in the test section (up to 850°R at Mach No. 6 and up to 1,350°R at Mach No. 8) are obtained through the use of a natural gas-fired combustion heater located 250 ft from the Tunnel B nozzle. The entire tunnel (throat, nozzle, test section, and diffuser) is cooled by integral, external water jackets. The tunnel is equipped with a model injection system, which allows removal of the model from the test section while the tunnel remains in operation. A description of the tunnel may be found in the *Test Facilities Handbook* (Ref. 21).

Except for the thermal disturbances, the disturbances produced in the stilling chamber of Tunnel B are attenuated by the isentropic compression through the nozzle. As in the case of Tunnel A, the flow over the Tunnel B model injection tank and the unstable flow in the diffuser section aft of the tunnel test section are additional sources for disturbances that may be sensed by dynamic pressure probes.

### 3.2.2 Test Installation

For the 1978 testing the flat plate used in the Tunnel A studies was mounted on the Tunnel B sector. The probes were supported on the x-z probe mechanism shown schematically in Fig. 8.

In 1979 the tests used the x-z probing mechanism and the sector-mounted 6-deg sharp cone as shown in Fig. 8a. A pitot acoustic probe was strut mounted to the sting of the sharp cone model. The pitot-acoustic probe was removed from the installation while flow-field surveys were made with the x-z probe mechanisms. The pitot acoustic probe could not be exposed to the high thermal environment of Tunnel B for the longer periods of time required to obtain flow-field surveys with the x-z probe mechanism.

### 3.3 PLANT

The VKF main compressor plant operates over an extremely wide range of pressures, pressure ratios, and mass flow rates to meet the requirements for closed circuit operation of the continuous flow Tunnels A, B, and C. A detailed description of this plant is given in Ref. 21. The plant machinery (the drive motors and compressors — see Figs. 2.1 and 2.2 of Ref. 21) generates vibrations close to the rotational speeds and harmonics of these speeds of the various stages of plant operation. These vibrations are transmitted through the structures to the Tunnel A, B, and C tunnel areas. A summary of the rotational speeds is presented below.

Stages of Operation	Plant Operation	
	Nominal Rotational Speeds (Hz)	Tunnel Mach Number
1	60	1.5 to 2.0 (Tunnel A)
2	60	1.5 to 3.0
3	47	3.0 to 4.0
4	68	4.0 to 5.5
5	99	5.5 to 6.0
6	162	5.5 to 6.0
7	201	6.0, 8.0 (Tunnel B)
8	203	10.0 (Open Circuit)
9	200	10.0

For example, on the shaft of compressor 81 (which is included in the eighth stage) a significant vibration at 60 Hz with secondary frequencies of 20, 40, 124, and 220 Hz was recorded. Significant vibrations at 108 and 208 Hz were recorded on the shaft of compressor 71 when it was operating in an unusual manner. Of course, several stages of the plant were operating when the aforementioned vibrations were detected and were simply transmitted to, for example, compressors 81 and 71. These vibrations have been identified to explain potential acceleration modes which might be transmitted and detected or superimposed on dynamic signals recorded in the tunnel test section area.

### 4.0 APPARATUS

#### 4.1 MODELS

A flat plate model (in 1978) and a sharp cone model (in 1979) were used to measure wall static pressure fluctuations on representative model surfaces in the test sections of Tunnels A and B. These model measurements were used in a comparison with the static pressure fluctuations inferred from the hot-wire anemometer measurements and the dynamic pitot pressure measurements made during the present investigation.

#### 4.1.1 Flat Plate Model

The flat plate model (Fig. 9) had a length of 10 in. and a span of 8 in. and was fabricated of stainless steel. The plate was instrumented with two flush-mounted piezoelectric dynamic pressure transducers, two static pressure taps, two thermocouples, and three flush-mounted thermopile heat-transfer gages. The dynamic pressure transducers had circular sensing areas with nominal diameters of 0.2 and 0.4 in. that were centered at stations 5 in. from the leading edge of the flat plate and 0.5 in. on either side of the axial centerline of the plate. The transducers were mounted in nylon inserts in the flat surface of the model and were installed as indicated in Fig. 9. The use of this method of mounting the transducers was subsequently judged to be unsatisfactory, as discussed in Section 4.2.2. The pressure orifices, which had an inside diameter of 0.064 in., were spaced 2 in. apart, in the axial direction. The static pressures were used to confirm alignment of the flat surface with the free-stream flow. The thermocouples were Chromel® -Alumel® junctions finished flush with the flat surface and were used primarily to monitor the temperature of the model to safeguard the dynamic pressure sensors. The heat-transfer gages were included with the instrumentation in anticipation of the use of the model with roughness elements applied to the surface to promote boundary-layer transition over the dynamic pressure sensors. However, time did not permit this extension of the study. The model was equipped with sideplates to contain the higher-pressure air on the underside of the model. A shadowgram of the flat plate model in the Mach number 8 flow in Tunnel B is presented in Fig. 10.

#### 4.1.2 Sharp Cone Model

The sharp cone model (Fig. 11) was a 6-deg (half-angle) right-angle cone with a length of approximately 43 in. and a base diameter of 9 in. and was fabricated of stainless steel. The cone was instrumented with dynamic pressure transducers, static pressure taps, and thermocouples. Surface pressure fluctuations were measured using nine dynamic pressure transducers located at three axial stations along the model. The sensor mounting stations were chosen so that the transducers at the forward and aft positions would be located under laminar and turbulent boundary-layer flows, respectively. The cone boundary layer over the transducers mounted at the central station was laminar, transitional, or turbulent depending upon tunnel test conditions. In addition one dynamic pressure transducer was used as a "blind" transducer in the cone to assess the acceleration effects imposed upon the surface-mounted sensors by model vibration. The dynamic pressure transducers installed in the cone surface were mounted in molded silicone rubber inserts of RTV® -60 (red) as illustrated in Fig. 11b. The insert partially isolated the sensor from model vibrations and thereby reduced associated acceleration effects. For the measurements in Tunnel B a 0.005-in.-thick cap of RTV-732 (white) was added to cover the transducer sensing surface and provide protection

from the high-temperature environment. (The white compound has better adhesive characteristics than the red compound, according to manufacturer's specifications.) Each cap was contoured with the cone surface; however, the small diameters of the sensing areas of the PCB® -105 transducers resulted in only a small indentation in the model contour when caps were not used in Tunnel A. The blind transducer was threaded into a metal insert implanted in the inner surface of the model wall (Fig. 11) and operated in the environment, particularly the pressure, of the interior cavity of the cone model.

Eight static pressure measurements were obtained using surface pressure taps located circumferentially at 90-deg intervals around the model at two stations near the forward and central transducer mounting stations. The static pressure measurements provided a direct indication of the cone alignment with the free-stream flow direction and were used in reducing boundary-layer survey data.

In addition to the rubber caps discussed earlier, the following provisions were made to protect the dynamic pressure transducers in the high-temperature environment of Tunnel B: the nose of the model was integrally water-cooled when the model was exposed to the tunnel flow for long periods of time, and six thermocouples were used to monitor model wall temperature. Three Chromel-Alumel thermocouples were attached to the inside wall of the cone, and three Chromel-constantan coaxial thermocouples were mounted flush with the exterior surface of the model. Sensor locations are indicated in Fig. 11.

## 4.2 Probes

The principal measurements in the free-stream flow in the test section of each tunnel were made using hot-wire anemometer and dynamic pitot-pressure probes. These measurements were supplemented using conventional pitot pressure and total temperature probes. All probes were fabricated by personnel at AEDC.

### 4.2.1 Anemometer Probes

The hot-wire anemometer probes were made using platinum - 10 percent rhodium wires, drawn by the Wollaston process, of 20- and 50- $\mu$ in. nominal diameter and approximately 150 diameters length. The sensor wire was attached to sharpened 3-mil nickel wire supports using a gold-bonding technique developed by Philco-Ford Corporation (Ref. 22). The probe body (Fig. 12) was composed of an alumina cylinder of 0.031-in. diam and 0.40-in. length bonded to a second alumina cylinder of 0.093-in. diam and 3.0-in. length using ceramic cement. The cylinders (thermocouple insulators) were manufactured with two holes along their length that were used for the leads of the sensor. The nickel wire supports that passed

through the smaller cylinder were silver-soldered to copper leads that were inserted into the larger cylinder. Ceramic cement was used at each end of the probe body to secure the supports and leads. The physical and heat-transfer characteristics of each hot-wire anemometer probe used for measurements were determined by calibration procedures discussed in Appendix A. The probes, which were designed to meet the structural and high-frequency requirements for measurements in hypersonic flow, performed well at Mach numbers as low as 3. Only a very limited amount of anemometer data was acquired at Mach numbers 1.5 and 2. It is believed that the principal causes of wire loss at the lower Mach numbers were particulate matter in the flow and the high aerodynamic loads on the wire.

#### **4.2.2 Dynamic Pitot Pressure Probes**

Dynamic pitot pressure probes of two designs (Fig. 13) were used in this investigation. In the initial design a single dynamic pressure transducer was mounted in a frustum-shaped stainless steel tip threaded to hold the transducer with no provision for isolation from the probe body vibration (Fig. 13a). The mounting included a thin (of the order of 0.015 in. thick) silicone rubber (RTV-732) cap to protect the transducer sensing surface from particles in the flow in the tunnels and the more intense Tunnel B thermal environment.

The second probe design (Fig. 13b) was developed to furnish some degree of isolation of the transducer from probe body vibration effects and included provision for mounting an identical transducer to serve as a blind sensor to assess the remaining vibration effects. The two transducers were mounted in molded silicone rubber inserts which were separated by a nylon sleeve. The assembly was held in the probe body by a threaded plug at the base of the probe and was separated from the rubber insert holding the blind transducer by a second nylon sleeve. The measurements made using the second probe design were found to be characterized by a higher signal-to-noise ratio than those measurements made with the probe of the initial design. The sensing surface of the primary transducer was protected by a thin silicone rubber (RTV-732) cap, as in the first probe design. It should be noted that the dynamic pressure transducers used in these probes may be unstable when the temperature of the transducer exceeds 250°F. As a consequence, the length of time that the probe was continuously exposed to the free-stream flow in Tunnel B was quite short (less than one minute).

#### **4.2.3 Pitot Pressure and Total Temperature Probes**

The pitot pressure probe (Fig. 14) was designed for boundary-layer surveys on the models in the vicinity of selected surface-mounted dynamic pressure transducers. The probe was made by flattening a 0.032-in. O.D. (0.022-in. I.D.) tube to an inside vertical height of

0.005 in. for the probe orifice. The tube was bent to align it parallel to the model surface over a length of 0.38 in. from the probe orifice. The probe was also used to determine local Mach number in the vicinity of the anemometer probe tip.

The total temperature probe (Fig. 14) was fashioned from a length of sheathed thermocouple leads (Chromel-Alumel) with wires of 1.5-mil diam. The wires were bared for a length of 15 mils, and a thermocouple junction of 5-mil diam was formed at the end of the wires. The thermocouple was used without shielding to reduce the probe dimensions and make it more comparable to those of the pitot pressure probe. The probe was used in Tunnel B for free-stream and boundary-layer measurements.

#### 4.2.4 Probe Holders

Holders for mounting the anemometer, pitot pressure, and total temperature probes as required were fabricated with 0.125-in.-diam (O.D.) tubes in which the position of each probe could be individually adjusted so that the sensing tips or orifice would be located at the same model axial station for surveys of the model boundary layer. Centerlines of the tubes of the probe holders were laterally spaced approximately 0.13 in. apart in a common plane. Each probe was held in place by a set screw, facilitating efficient replacement of probes. The holder used in Tunnel A measurements accommodated two probes, and the holder of the three probes used in Tunnel B could accommodate as many as four probes.

### 4.3 INSTRUMENTATION

#### 4.3.1 Hot-Wire Anemometer

Constant-current hot-wire anemometer instrumentation was used for the present investigation. The anemometer current control (Philco-Ford Model ADP-13), which supplies the heating current to the sensor wire, is capable of maintaining the current at any one of 15 preset (adjustable) levels individually selected using pushbutton switches. The anemometer amplifier (Philco-Ford Model ADP-12), which amplifies the wire response (a-c voltage) signal, contains the circuits required to electronically compensate the signal for the thermal lag that is a result of the finite heat capacity of the wire. A square-wave generator (Shapiro/Edwards Model G-50) was used to determine the time constant of the sensor wire whenever required. The wire heating current and mean voltage were fed to autoranging digital voltmeters for a visual display and to a magnetic tape machine for recording (see Section 4.3.3). The sensor response (a-c voltage) was fed to an oscilloscope for visual display of the real-time signal and to a wave analyzer (Hewlett-Packard Model 8553B/8552B) for visual display of the spectrum of the fluctuating signal in real time; the

sensor response was recorded on magnetic tape for subsequent analysis. A detailed description of the VKF hot-wire anemometer instrumentation is given in Ref. 23. In addition to the analog data records, a digital record of the wire heating current, mean voltage, and rms voltage of the sensor response is acquired (as of 1979) through the appropriate VKF tunnel data system.

#### **4.3.2 Dynamic Pressure Sensors**

Two types of transducers were used to record the sound spectra existing in the wind tunnel. The primary measuring instruments were piezoelectric sensors with diameters of 0.099-, 0.218-, and 0.405 in. These are, basically, quartz transducers in which the quartz element produces a change in response to an abrupt change in the applied pressure. Special calibration procedures were used in determining the dynamic response of these transducers (Appendix B). Depending on the size of the transducer, the sensitivity generally varied from 25 to 100 mv per psi, the resonant frequency varied from 250 to 500 kHz, and the rise time of the transducers was nominally 1 to 2  $\mu$ sec.

The remaining transducers used in this experiment were resistance-type sensors which had sensitivity factors of nominally 12 to 16 mv per psi and a frequency range from 1/5 to 1/10 of the range of the piezoelectric sensors. The uncertainty in the dynamic pressure measurements is based on significantly fewer calibration points (degrees of freedom); therefore, a higher Student's "t" value must be applied to the calibration standard deviation, and this indicates a higher measurement uncertainty. This is not an "end-to-end" calibration in that the input to the installed sensing gage could not be compared directly to the final displayed output. The same recording and signal processing instrumentation used in the calibrations was used in the wind tunnel tests.

#### **4.3.3 Signal-Processing Equipment**

Conditioned analog response signals from the hot-wire anemometer and dynamic pressure transducers were recorded on the VKF Bell and Howell model VR3700B magnetic tape machine in the FM mode. Each channel was calibrated and adjusted to have a signal-to-noise ratio of 35 db for a 1.00-v rms output. The tape machine frequency response was +1 to -3 db over a frequency range from dc to 500 kHz. In the present calibration, a sine wave generator was used to check each channel at several discrete frequencies, using an rms voltmeter which was periodically checked on 1-, 10-, and 100-v ranges and found to have an uncertainty of less than  $\pm$  1.0 percent of the reading within the frequency band from 25 Hz to 100 kHz. All magnetic tape recordings were made at a tape speed of 120 in./sec.

Sensor response signals recorded on magnetic tape during hot-wire anemometer and dynamic pressure transducer measurements were subsequently processed using the VKF spectrum analyzer, a Spectral Dynamics Corporation Model SD360 digital signal processor. This processor contains a dedicated computer programmed with a Fast Fourier Transform (FFT) algorithm to obtain single channel 1,024-point (or dual channel 512-point/channel) forward or inverse Fourier transforms. Other operations often required in signal analysis (for example, calculations of auto-correlation and cross-correlation functions and their respective Fourier transforms, the spectral density and cross-spectral density) can be performed by the processor. The frequency range for an analysis can be chosen from among 57 available ranges, full scale from 10 Hz to 150 kHz, and each range has a pair of anti-aliasing filters with 120 db/octave rolloff. The processor uses block floating-point arithmetic in the FFT computations to avoid loss of data by overflow. Rectangular and Kaiser-Bessel weighting functions are available for use in the data processing. Linear ensemble averaging and exponential averaging are available to obtain signal-to-noise enhancement or to improve the statistical confidence in the results.

The SD360 analyzer is interfaced with a VKF Digital Equipment Corporation PDP 11/40 minicomputer for disk storage of analysis results and subsequent transmission of the results to the VKF Digital Equipment Corporation DEC System 10 computer for further processing.

## 5.0 DATA ANALYSIS

### 5.1 SIGNAL PROCESSING AND NORMALIZATION

#### 5.1.1 Procedure

As noted previously (Section 4.3), the hot-wire anemometry and dynamic pressure signals were initially recorded on magnetic tape for further analysis. The Spectral Dynamics SD360 digital signal processor (see Section 4.3.3) was used to convert the recorded real time analog signal into a digitized spectrum in the frequency domain for further analysis and normalization. The SD360 samples an input signal at a rate equal to the reciprocal of the product of 2.048 times the selected bandwidth of the analysis.

Since the playback speed of the analog tape can be varied relative to the tape speed of the signal recording, the true bandwidth of the signal analysis using the SD360 can be changed significantly. For example, in the present analysis, the Tunnel B hot-wire results were effectively analyzed over a total signal bandwidth (spectrum) of 600 kHz. (The playback speed of the tape machine was one-fourth the recording speed, and the analyzer bandwidth was set at 150 kHz). In Tunnel A the total bandwidth of the hot wire results was 160 kHz because the tape speed ratio was one-half and the analyzer bandwidth was 80 kHz.

The DPS results were processed at selected total signal bandwidths of 50 kHz, 100 kHz, and 150 kHz. In this instance the playback and recording speeds were identical; that is, the tape speed ratio was one.

The SD360 was also used to digitize real time analog signals such as the real time response of the DPS units located in the transient flow of a shock-tube calibrator. In these situations, the bandwidth of the sampling rate was set at 150 kHz, and analog tape playback speed was one-fourth the recording speed (see Appendix B for further discussion). The actual real time signal was digitized at a rate of 0.8138  $\mu$ sec per point. The total length of the signal sample was 0.833 msec.

### 5.1.2 Statistical Uncertainties

The normalized statistically defined error (uncertainty) associated with the narrow-band spectral analysis follows (Ref. 24).

The random error in the mean square value of the signal is  $\epsilon(\overline{rms}^2)/\overline{rms}^2 \approx (BW \cdot T)^{-0.5}$ , or simply  $(N/2)^{-0.5}$ , since the sample length, T, equals  $N/(2.048 BW)$ . The term "N" is the total number of points in the interval T used to define  $\overline{rms}^2$ , the mean squared value of the signal. For the SD360, the value of N is either 1,024 or 2,048; therefore, the corresponding random error is either  $\pm 4.4$  percent or  $\pm 3.1$  percent.

The random error associated with the amplitude of the power spectral density (PSD) distribution is defined, according to Ref. 24, as  $\epsilon(F)/F \approx [\Delta f(n_d \cdot T)]^{-0.5}$ . Since  $\Delta f = 1/T$ , then  $\epsilon(F)/F = n_d^{-0.5}$ . The SD360 can take up to  $2^{15}$  signal samples ( $n_d$ ) and average the results. A summary of the random error analyses associated with the use of the SD360 analyzer is given in the following table.

ESTIMATED RANDOM ERRORS

Item	BW, kHz	<u>N</u>	$\epsilon(\overline{rms}^2)/\overline{rms}^2$ , percent	<u><math>n_d</math></u>	$\epsilon(F)/F$ , percent
Hot Wire (Tunnel A)	160	1,024	$\pm 4.4$	$2^6$	$\pm 12.5$
Hot Wire (Tunnel B)	600				
DPS (Tunnel A)	100				
DPS (Tunnel B)	150			$2^5$	$\pm 17.7$
DPS (Tunnel A/B)	50				

### 5.1.3 Data Processing

The Fourier transform provides a convenient vehicle for transforming real time signals into the frequency domain. These hot-wire and DPS signals are analyzed as if they were the

result of an essentially stationary (ergodic) random process. The continuous form of the transform (Ref. 25) is

$$H(f) = \int_{-\infty}^{\infty} h(t) e^{-j2\pi ft} dt \quad , \quad \text{units} = \text{sec} \quad (3)$$

and the inverse transform is

$$h(t) = \int_{-\infty}^{\infty} H(f) e^{j2\pi ft} df \quad , \quad \text{units} \quad (4)$$

Since the SD360 is an analog-to-digital analyzer with an FFT processor, the character of the discrete transform takes the following form:

$$H_D\left(\frac{n}{NT}\right) = \frac{1}{N} \sum_{k=0}^{N-1} h(kT) e^{-j2\pi n(k/N)} \quad , \quad \text{units} \quad (5)$$

The scaling between the discrete transform and the corresponding amplitude of the transform is as follows (see Ref. 26, p. 102):

$$H\left(\frac{n}{NT}\right) = (N \cdot T) H_D\left(\frac{n}{NT}\right) \quad , \quad \text{units} = \text{sec} \quad (6)$$

Where "NT," the total length of time of the sampled signal, equals  $N/(2.048 \cdot \text{BW})$  and the incremental bandwidth of the digital spectral analysis,

$$\Delta f = (N \cdot T)^{-1} \quad , \quad \text{sec}^{-1} \quad (7)$$

The power spectral density is normally defined as

$$F(f) = \lim_{\Delta t \rightarrow 0} \frac{1}{\Delta t \cdot T} \int_0^T h^2(t; \Delta f, f) dt \quad , \quad \text{units}^2 = \text{sec} \quad (8)$$

whereas the digital form is

$$F_D\left(\frac{n}{NT}\right) = F_D(n \cdot \Delta f) = \frac{1}{NT} [H_D(n, \Delta f) \cdot H_D^*(n, \Delta f)] \quad , \quad \text{units}^2/\text{sec} \quad (9)$$

where  $H_D^*(n, \Delta f)$  is the conjugate of  $H_D(n, \Delta f)$ . The corresponding amplitudes of PSD for the continuous function are

$$F(n \cdot \Delta f) = NT |H_D(n \cdot \Delta f)|^2 \quad , \quad \text{units}^2 = \text{sec} \quad (10)$$

Since the root-mean-square (rms<sup>2</sup>) of the signal is normally

$$\overline{\text{rms}}^2 = \int_0^{BW} F(f) df , \quad \text{units}^2 \quad (11)$$

then the digital form becomes

$$\overline{\text{rms}}^2 = \sum_{n=1}^{n/2} |H(n \cdot \Delta f)|^2 , \quad \text{units}^2 \quad (12)$$

This summarizes the definitions of parameters used to process the hot-wire and dynamic pressure signals where the "unit," the amplitude of the signal, is usually in millivolts (mv).

### 5.1.4 Normalization

The stilling chamber and test section properties and probe measurements included in this study are listed in Appendix C, Table 1. This listing contains most of the test conditions covered in this flow fluctuation study. Some of the tunnel circuit parameters such as PT, P, P<sub>p</sub>, and q were used in the normalization of the fluctuating parameters and also in the other aspects of the hot-wire analyses. A description of the normalization procedure and determination of normalization parameters is given in Appendixes C and D.

## 5.2 ANEMOMETER SIGNAL ANALYSIS

Hot-wire anemometry techniques were used to determine the levels of fluctuations in the free-stream flow along the centerline of the test sections of Tunnels A and B. The measurements included the hot-wire heating current, the d-c voltage drop across the wire, and the wire a-c voltage response to fluctuations in the flow. The a-c voltage component was recorded in analog form on magnetic tape for subsequent spectral analysis, and the rms level of the a-c voltage, unfiltered and including the electronic noise, was determined simultaneously using a true-rms meter. The procedure used to process the data and to interpret the results are discussed below.

### 5.2.1 Spectral Analysis

The anemometer a-c voltage response signals recorded on magnetic tape were used as input to the VKF SD-360 spectrum analyzer (Section 4.3) to obtain the digitized power density spectrum of the signals. The digital output of the SD-360 processor consisted of

1,024 points equally spaced over the selected frequency range of the analyzer. (See the listing in Section 5.1.2). Approximately 830 spectra were obtained from the free-stream measurements made in the investigation. Each spectrum corresponded to one wire heating current at one unit Reynolds number at one Mach number. Repeat measurements were made in many cases generally because of wire failure during a series of measurements. Although all of the spectra were examined, only approximately 30 percent of the data were used. In general, data were rejected for the present investigation under the following conditions: (1) if they were part of an incomplete set of measurements; (2) if the power density spectrum of the wire response signal was not clearly above that of the electronic noise over a "reasonable" bandwidth; (3) if spurious signals such as those caused by wire strain-gage effects were present in the spectrum; (4) if the general "shape" of the spectrum was inconsistent with that of the other data of the same set of measurements; and (5) if the hot-wire probe experienced a shift in unheated-wire resistance which was unrelated to a change in tunnel operating conditions.

### 5.2.2 Signal Enhancement

In the acquisition of data, the electronic noise of the assembled instruments of the anemometer system was recorded at each test condition for which flow fluctuation measurements were made. The noise (unheated wire) recordings were processed in the same manner as the response signals of the heated wire. The value of the power density spectrum of the noise was subtracted, at each discrete frequency, from that of the corresponding response signals of the heated wire to obtain the power density spectrum of the "noise-free" wire response signal.

The response of each of the principal instruments used to process the a-c voltage component of the hot-wire anemometer output prior to spectral analysis was characterized by a rolloff with frequency within the bandwidth of interest for the measurements. The method used by Laderman and Demetriades (Ref. 26) to enhance the output signals mathematically, to compensate for response degradation, has been used in processing the data acquired in the present investigation. For this purpose, the rolloff of the response of the wire sensor, without electronic compensation, was defined mathematically as a function of frequency. The frequency characteristics of the amplifier thermal lag compensation circuits, as a function of time-constant setting, and those of the amplifier high-cutoff filters were determined by calibration by the VKF, and the results were expressed mathematically for each instrument as a function of frequency. The inverse of each of the mathematical expressions for (1) the response of the wire, (2) the compensation circuit, and (3) the filtering

circuit was applied as a transfer function in the discrete-point data reduction procedures. The resulting "restored" form of the wire response spectrum was used in subsequent data processing.

Electronic compensation of the constant-current anemometer for thermal lag in the sensing wire, using the dedicated stage of the amplifier (Section 4.3.1), requires that the amplifier be adjusted manually to the appropriate thermal time constant of the wire, a factor that is altered by a change of the heating current of the wire or a change of the unit Reynolds number of the flow around the wire. (The appropriate value of the wire time constant is determined using the square-wave technique, Ref. 27.) However, appropriate compensation for sensor wire thermal lag can also be achieved mathematically, through the use of the transfer function. This is done after the fact and in lieu of manual adjustments of the amplifier time constant, for each heating current, before data acquisition. This option is available provided that the time constant of the given wire has been determined (by the square-wave method) for one heating current at one test condition. This optional procedure was used in the present investigation to improve the efficiency of the measurements and to minimize the exposure time of the wire to the hazards of the flow field.

At this point in the signal processing, the power density spectrum of the hot-wire a-c voltage response would be noise free, enhanced to restore signal content lost because of instrumentation deficiencies, and compensated for wire thermal lag. The discrete point spectrum can at this point be summed over the frequency range to yield the wide-band mean-square voltage fluctuation of the wire. It was found in the present investigation that the wide-band fluctuations of signals produced by low-level turbulence are well behaved when processed in the manner and sequence discussed above. This finding is in contrast with results obtained using the measured wide-band signal levels: when the mean-square of the measured wide-band noise signal (unheated wire) is subtracted from the mean-square of the measured wide-band response signal of the heated wire, the results are subject to uncertainties which can become unacceptable as the level of the response signal approaches that of the noise.

From this point in the signal processing, the data reduction can proceed in two ways: (1) the wide-band (summed spectrum) voltage fluctuation data can be reduced to the form of wide-band flow fluctuations, and (2) the discrete point spectra of the voltage fluctuation data can be reduced frequency by frequency to the form of discrete point spectra of the flow fluctuations. The modal analysis processes discussed in the next section are applicable to both the wide-band and the spectral data reduction, unless noted otherwise.

### 5.2.3 Modal Analysis

Procedures used in the interpretation of hot-wire anemometer measurements in a flow field for the purpose of inferring (1) which flow fluctuations are present and (2) the magnitudes of the fluctuations are generally referred to as "modal analysis" procedures. In supersonic flow the hot wire responds to fluctuations of mass flux and total temperature (the sensing variables) whereas the fluctuations which characterize an unsteady flow field are those of vorticity, entropy, and sound (the independent mode variables). Fluctuations in the sensing variables and the mode variables are inferred from hot-wire a-c voltage response (rms) measurements using the "mode" concept and associated techniques of "fluctuation diagrams" introduced by Kovasznay (Ref. 28) and expanded by Morkovin (Ref. 29). The comprehensive discussion by Morkovin (Ref. 29) of the derivation of the basic relations for the response of the hot wire has been outlined by various authors including Donaldson and Wallace (Ref. 7) and has not been repeated in the present report. The application of modal analysis procedures to hot-wire measurements made in high-speed flow has been discussed in detail by Laderman and Demetriades (Ref. 26) with special emphasis on flow fields characterized by the presence (significance) of more than one fluctuation mode variable and the possibility of cross-correlation between modes. Application in the case of a pure sound field, where only the sound-wave mode is present and can be attributed to a single sound source, has been discussed by Vrebalovich (Ref. 30). The methods of Refs. 26 and 30 have been used, as applicable, in the present investigation to accomplish the modal analysis and the subsequent determination of the fluctuations of the flow variables, namely velocity, static temperature, pressure, and density.

#### 5.2.3.1 Wire Response

The mean-square a-c voltage fluctuation ( $\bar{e}$ )<sup>2</sup> of the hot-wire output may be expressed in terms of the three nondimensional mode "amplitudes," vorticity ( $\bar{\tau}$ ), entropy ( $\bar{\sigma}$ ), and sound ( $\bar{\pi}$ ), and the three cross-correlations between the modes by the relation (Refs. 29 and 7)

$$\begin{aligned}
 (\bar{e})^2 = & \Delta e_r^2 (\bar{\tau})^2 + \Delta e_\sigma^2 (\bar{\sigma})^2 + \Delta e_\pi^2 (\bar{\pi})^2 - 2 \Delta e_r \Delta e_\sigma (\bar{\tau})(\bar{\sigma}) R_{r\sigma} \\
 & - 2 \Delta e_\sigma \Delta e_\pi (\bar{\sigma})(\bar{\pi}) R_{\sigma\pi} + 2 \Delta e_\pi \Delta e_r (\bar{\pi})(\bar{\tau}) R_{\pi\tau}
 \end{aligned} \tag{13}$$

where  $\Delta e_r$ ,  $\Delta e_\sigma$ , and  $\Delta e_\pi$  are the vorticity, entropy, and sound sensitivity coefficients, respectively, of the wire, where (~) denotes the rms value of the fluctuation, and where each

$R$  is a correlation coefficient identified by its two subscripts; for example  $R_{\sigma\sigma} = (\sigma\sigma)/(\bar{\sigma}\bar{\sigma})$  is the correlation coefficient between fluctuations of vorticity and entropy. In this presentation factors affecting the rms a-c voltage, such as the d-c gain, the signal enhancement, and the wire time constant have been accounted for in the term  $\tilde{e}$ ; moreover, the "finite-circuit" parameter (which accounts for the finite impedance of the "constant" current control) has been accounted for in each of the sensitivity coefficients.

The sensitivity coefficients ( $\Delta e_i$ ) of a given wire are functions of its physical and heat-transfer characteristics (see Table 1 in Ref. 7), which are determined from the results of the oven and flow calibrations of the wire (Appendix A). Changes of the wire heating current or local unit Reynolds number of the flow around the wire produce changes in the sensitivities, so that the values of the coefficients must be determined at each operating condition. It should be noted that in supersonic flow the wire Nusselt number and temperature recovery factor are essentially independent of Mach number.

In principle, six equations in six unknowns (the three mode "amplitudes" and the three correlation coefficients) could be obtained for a simultaneous solution if measurements were made at six distinct wire heating currents. In reality, the sensitivity coefficients and the rms voltage  $\tilde{e}$  have uncertainties which rule out this method of solution. It must be noted that the presence of sound-wave fluctuations involves amplitude and direction of propagation (that is, two possible variables, rather than one). For simplicity in the present discussion it has been assumed that there is a preferred direction of propagation of the sound waves and that the direction is independently known, unless otherwise indicated.

### 5.2.3.2 Fluctuation Diagram Technique

The fluctuation diagram technique makes use of the fact that the relative sensitivity of the hot wire to the various flow parameters varies with the temperature of the heated wire relative to that of the unheated wire (that is, with wire "overheat"). By making measurements at different wire overheat temperatures one obtains a diagram of the wire response which has a characteristic shape for each mode variable. More generally, when modes coexist and are cross-correlated, the diagram technique can be used — but only under certain restrictive conditions.

For supersonic flow the relation Eq. (13) can be rewritten as follows:

$$Y^2 = \tilde{\sigma}^2 - \tilde{\tau}^2 X^2 + \tilde{\pi}^2 (g_1 + g_2 X)^2 + 2 \tilde{\tau} \tilde{\sigma} R_{\tau\sigma} X + 2(g_1 - g_2 X)(\tilde{\sigma} \tilde{\pi} R_{\sigma\pi} + \tilde{\pi} \tilde{\tau} R_{\pi\tau} X) \quad (14)$$

where

$$X = \Delta e_r / \Delta e_\sigma \quad (15)$$

$$Y = \tilde{e} / \Delta e_\sigma \quad (16)$$

and

$$\Delta e_\pi / \Delta e_\sigma = g_1 + g_2 X \quad (17)$$

with

$$g_1 = \frac{-(\gamma - 1)(M^2 - 1)}{1 + (\gamma - 1)M^2} \quad (18)$$

and

$$g_2 = \frac{\gamma(1 + n_x M) - (M^2 - 1)(n_x/M)}{1 + (\gamma - 1)M^2} \quad (19)$$

where  $n_x$  is the direction cosine of the normal to the sound plane wave front relative to the local mean flow direction. (The hot wire aligned normal to the mean flow direction is sensitive to velocity variations in that direction, only.)

Equation (14) can be expanded in terms of X to yield

$$Y^2 = (\tilde{\sigma}^2 + g_1^2 \tilde{\pi}^2 + 2g_1 \tilde{\sigma} \tilde{\pi} R_{\sigma\pi}) + 2(\tilde{\sigma} \tilde{\pi} R_{\sigma\pi} - g_2 \tilde{\sigma} \tilde{\pi} R_{\sigma\pi}) X + (g_1^2 \tilde{\pi}^2 + 2g_2 \tilde{\sigma} \tilde{\pi} R_{\sigma\pi}) X^2 \quad (20)$$

which is of the form

$$Y^2 = D_1 + D_2 X + D_3 X^2 \quad (21)$$

where the coefficients  $D_i$  represent various combinations of the three mode amplitudes and their cross-correlations. If one mode variable predominates in the expressions for the coefficients so that the remaining terms are negligible, then the form of Eq. (20) degenerates to a pair of straight lines, as follows:

$$Y = \pm (D_4 + D_5 X) \quad (22)$$

Operation of the hot wire at a fixed location in the flow field for several wire heating currents (up to 11 in the present work) will yield corresponding values of the sensitivity coefficients and of the  $\overline{rms}$  voltage,  $\tilde{e}$ . For each heating current one point in the X-Y plane can be determined using Eqs. (15) and (16). The set of points (X, Y) for the several heating currents, plotted in rectangular coordinates, will indicate whether the fairing is of the form

of Eq. (21) or Eq. (22). Values of the coefficients of the appropriate fairing, obtained using the method of least-squares, are matched with the corresponding expressions of the coefficients.

### 5.2.3.3 Single Mode

The following discussion will illustrate the case of one-mode predominance:

(1) If vorticity (turbulent velocity) fluctuations predominate so that  $\tilde{\sigma} \approx \tilde{\pi} \approx 0$ , Eq. (20) becomes

$$Y = \pm \tilde{\tau} X \quad (23)$$

(2) If entropy (temperature spottiness) fluctuations predominate so that  $\tilde{\tau} \approx \tilde{\pi} \approx 0$ , Eq. (20) becomes

$$Y = \pm \tilde{\sigma} \quad (24)$$

(3) If sound (sound wave) fluctuations predominate so that  $\tilde{\tau} \approx \tilde{\sigma} \approx 0$ , Eq. (20) becomes

$$Y = \pm (g_1 + g_2 X) \tilde{\pi} \quad (25)$$

If the "best" fairing among a set of points (X, Y) is a straight line with nonzero intercept and nonzero slope, the fluctuation diagram technique would indicate the wire was located in a pure sound field. The principal variable in this case is pressure, and the relations among the thermodynamic variables are isentropic. If the least-squares fairing is given by

$$Y = D_4 + D_5 X$$

and the coefficients are matched with those of Eq. (25), the amplitude of the sound mode is found by

$$\tilde{\pi} = (D_4 / g_1) \quad (26)$$

From Morkovin (Ref. 29) with  $\tilde{\sigma} \approx 0$ , fluctuation variables can be determined using the relations

$$\tilde{\pi} = \frac{\tilde{\rho}}{\tilde{P}} = \frac{\tilde{P}}{\gamma \tilde{P}} = \frac{1}{\gamma - 1} \frac{\tilde{T}}{\tilde{T}} \quad (27)$$

A matching of the slope coefficients yields

$$g_2 \tilde{\pi} = D_5 \quad (28)$$

If Eq. (19) is solved for the direction cosine  $n_x$ , one obtains in the test section flow

$$n_x = g_2 M_\infty - \frac{\gamma M_\infty}{(\gamma - 1) M_\infty^2 + 1} \quad (29)$$

If  $g_2$  is obtained from Eq. (28) and substituted into Eq. (29), a preferred orientation of the sound waves intercepted by the hot wire can be determined. Laufer (Ref. 31) has adapted the theory of Phillips (Ref. 32) for the radiation of sound by a free shear layer to the case of boundary-layer sound radiation. In essence, a frozen eddy pattern acting as a wavy wall moves downstream within the boundary layer at a supersonic speed relative to the free-stream flow and radiates energy in the form of Mach waves. If the mean propagation velocity (streamwise) of the sound source is designated by  $\bar{u}_s$ , the mean velocity of the free stream relative to the virtual wavy wall is  $\bar{u}_r = \bar{u}_\infty - \bar{u}_s$ , and the corresponding Mach number is  $M_r$ :

$$M_r = \frac{\bar{u}_r}{a} = \frac{\bar{u}_\infty - \bar{u}_s}{a} = - \frac{1}{n_x} \quad (30)$$

#### 5.2.3.4 Coexisting Modes

If the "best" fairing among a set of points  $(X, Y)$  is a hyperbola, of the form of Eq. (21), a matching of the coefficients with those of Eq. (20) will give a set of three equations in the seven unknowns (including direction of sound wave propagation). Resolution of the fluctuations of coexisting modes from this underdetermined set of equations requires more information from independent sources, for example: (1) an acceptable fluid dynamics model of the flow field around the wire which would supply the required number of additional independent relations in some (or all) of the unknowns and/or (2) measurements of any of the fluctuations by independent methods which would serve to relax the *a priori* constraints inherent in use of the fluid dynamics model. In the present discussion three models suggested by Laderman and Demetriades (Ref. 26) have been considered:

Model 1: No sound; that is,  $\tilde{\pi} = 0$

with this constraint, Eq. (20) reduces to

$$Y^2 = \tilde{\sigma}^2 + 2\tilde{\tau}\tilde{\sigma}R_{\tau\sigma}\lambda - \tilde{\tau}^2\lambda^2 \quad (31)$$

and matching coefficients with the fitted hyperbola will yield values for vorticity and entropy fluctuations and for their correlation coefficient. This model is often used in reducing hot-wire anemometer measurements obtained in supersonic turbulent boundary-layer flow where sound fluctuations are considered negligible compared to those of vorticity and entropy.

**Model 2: Uncorrelated modes; that is,**

$$R_{\tau\sigma} = R_{\sigma\pi} = R_{\pi\tau} = 0$$

With these constraints, Eq. (20) reduces to

$$Y^2 = (\tilde{\sigma}^2 + g_1^2 \tilde{\pi}^2) + 2g_1 g_2 \tilde{\pi}^2 X + (\tilde{\tau}^2 + g_2^2 \tilde{\pi}^2) X^2 \quad (32)$$

A matching of coefficients with the fitted hyperbola can be made to yield a completely determined set of equations, if a preferred orientation of the sound waves [which enter through the direction cosine  $n_x$  in the term  $g_2$ , as shown in Eq. (19)] can be determined independently (or assumed). Kovásznay (Ref. 28) and Morkovin (Ref. 29) suggest that this model may be applicable in the free stream of supersonic wind tunnels.

**Model 3: Uncorrelated sound and anticorrelated vorticity and entropy; that is,**

$$R_{\sigma\pi} = R_{\pi\tau} = 0 \quad \text{and} \quad R_{\tau\sigma} = -1.0$$

With these constraints, Eq. (20) reduces to

$$Y^2 = (\tilde{\sigma}^2 + g_1^2 \tilde{\pi}^2) - 2(-\tilde{\sigma} + g_1 g_2 \tilde{\pi}^2) X + (\tilde{\tau}^2 + g_2^2 \tilde{\pi}^2) X^2 \quad (33)$$

A matching of coefficients with the fitted hyperbola can be made to yield a completely determined set of equations if the direction cosine  $n_x$  is supplied.

### 5.3 DYNAMIC PRESSURE ANALYSIS

In general, the PSD values presented herein are in engineering units, namely  $(\text{psi})^2/\text{Hz}$  or  $(\text{mv})^2\text{Hz}$ , or are normalized as follows:

$$C_{\zeta}^2 u_{\infty} / \delta^* = [(\zeta)^2 / \bar{q}_{\infty}^2] u_{\infty} / \delta^* \quad (34)$$

Note that  $C_{\zeta}$  is simply a pressure coefficient formed as a ratio of the fluctuating pressure parameter relative to the mean pressure level divided by the free-stream dynamic pressure.

A Strouhal number is formed for the frequency coordinate of the spectral distributions, as follows:

$$\text{Strouhal Number} = f \cdot \delta^* / u_{\infty}$$

If the convective velocity  $u_c$  of the sound source associated with the tunnel wall turbulent boundary layer had been well established, it would have been a more acceptable parameter

to use with the aforementioned parameters than the free-stream velocity component (see Section 2.0).

The remaining major normalizing parameters concern the ratio of the accumulated energy in the spectrum up to a given frequency to the total energy in the spectrum. This normalized energy distribution (NED) is defined as follows:

$$\text{NED}(k + \Delta k) = \sum_{n=1}^k E(n + \Delta k) \left/ \sum_{n=1}^{N/2} E(n + \Delta k) \right. \quad (35)$$

Note that  $BW = (N/2) \cdot \Delta f$ .

The frequency at which this ratio reaches (for example, 0.95) simply identifies the signal bandwidth of the spectrum which contains 95 percent of the energy of the fluctuation parameter.

Two fundamental relationships are used in this analysis in an attempt to correlate the results of the hot-wire anemometry to the dynamic pressure measurements. As noted in Ref. 14, for a plane wave, the free-stream pressure and velocity fluctuations are related as follows:

$$\tilde{P}/P = \gamma M_\infty^2 (\tilde{u}/\bar{u}) \quad (36)$$

or

$$C_{\tilde{P}} = 2(\tilde{u}/\bar{u})$$

The pressure measurements obtained from a pitot probe instrumented with dynamic pressure transducers is related to the static pressure fluctuations deduced from the hot-wire probe (Ref. 33). A good approximation to the relationship of the pitot probe pressure and the free-stream properties is as follows:

$$P_p = A \cdot \rho u^2 \quad (37)$$

where the constant "A" is primarily a function of  $\gamma$ , the ratio of the specific heats of the gas, and a very weak function of the free-stream Mach number. Actually, the value "A" varies from 0.953 at Mach number 1.5 to 1.085 at Mach number 8 ( $\gamma = 1.4$ ) and hereafter is arbitrarily set equal to one.

Equation (37) can be expanded in terms of the instantaneous fluctuations relative to the mean value, neglecting higher order terms, as follows:

$$\Delta P_p / P_p = (\Delta \rho / \rho) + 2(\Delta u / u) \quad (38)$$

Forming the mean square of this relationship of the instantaneous values yields the following result:

$$\overline{(\Delta P_p / P_p)^2} = \overline{(\Delta \rho / \rho)^2} + 4(\overline{\Delta u / u})^2 + \overline{4(\Delta \rho / \rho)(\Delta u / u)} \quad (39)$$

Typically,

$$(\tilde{P}_p / \overline{P}_p)^2 = \frac{1}{T} \int_0^T \overline{(\Delta P_p / P_p)^2} dt$$

where  $(\tilde{P}_p / \overline{P}_p)^2$  is the ratio of the mean square value of the fluctuation relative to the mean value,  $P_p$ . But the last term on the right in Eq. (39) is the cross correlation between the free stream density and velocity fluctuations and may be positive or negative. In general the averaged (mean) value of this term is defined as follows:

$$\overline{(\Delta \rho / \rho)(\Delta u / u)} = - \frac{\left( \frac{\Delta \rho}{\rho} \right) \left( \frac{\Delta u}{u} \right)}{\sqrt{\left( \frac{\Delta \rho}{\rho} \right)^2} \sqrt{\left( \frac{\Delta u}{u} \right)^2}} \cdot \sqrt{\left( \frac{\Delta \rho}{\rho} \right)^2} \sqrt{\left( \frac{\Delta u}{u} \right)^2} = R_{\rho u} \cdot \sqrt{\left( \frac{\Delta \rho}{\rho} \right)^2} \sqrt{\left( \frac{\Delta u}{u} \right)^2} \quad (40)$$

As noted in Ref. 14 the correlation factor was identified as being negative since the fluctuating properties are assumed to behave isentropically and the disturbance is primarily the result of a pure sound field emanating from the tunnel wall boundary layer. In addition, the fluctuations can be viewed as a plane wave with the following characteristics:

$$\frac{\Delta u}{u} = \left( \frac{n_x}{M_\infty} \right) \left( \frac{\Delta P}{P} \right)$$

That is,

$$\sqrt{(\tilde{u} / u)^2} = \sqrt{\frac{1}{T} \int_0^T \left( \frac{n_x}{M_\infty} \right)^2 \left( \frac{\Delta P}{P} \right)^2 dt} \quad (41)$$

and, as noted in Ref. 14,

$$n_x = \{[(u_s / u) - 1] M_\infty\}^{-1} \quad (42)$$

Therefore,

$$\sqrt{(\tilde{P}_p / \overline{P}_p)^2} = \sqrt{[\tilde{P}'(yP)]^2} [1 - 2n_x / M_\infty] \quad (43)$$

Based on the present hot-wire analyses and previous experimental work (Ref. 14), the ratio of the source velocity to the free-stream velocity was set equal to a nominal value of 0.40. Therefore, Eq. (43) was simplified as follows:

$$\sqrt{(\tilde{P}_p / \overline{P}_p)^2} = C_p (1 + 0.3M_\infty^2) / 0.3 \quad (44)$$

As noted in Ref. 34 and included in the previous expression, the measured fluctuating pitot probe pressure is twice the actual value in order to account for the reflection of the impinging fluctuating pressure wave on the probe face.

The terms  $\Delta P_p/P_p^2$ ,  $\Delta \rho/\rho^2$ , and  $\Delta u/u^2$  in Eq. (39) can be evaluated as the mean square value of the deviations from the mean value of the parameter, but the term  $(\Delta \rho/\rho)(\Delta u/u)$  is a cross-correlation term which may be either positive or negative. As noted in Ref. 14 and as exhibited in the modal analysis of the test data, this term is negative if the disturbance is assumed to be isentropic and the result of a pure sound field. In addition, the fluctuations can be viewed as a plane wave with the following characteristics:

$$\frac{\Delta u}{u} = \frac{n_x}{M_\infty} \frac{\Delta P}{\gamma P} \quad (45)$$

Basically, this analysis assumed that the rms value defined in Eq. (41) can be redefined simply as

$$\sqrt{\left(\frac{\tilde{u}}{u}\right)^2} = \left(\frac{n_x}{\gamma M_\infty}\right) \left\{ \frac{1}{T} \int_0^T \left( \frac{\Delta P}{P} \right)^2 dt \right\}^{1/2} \quad (46)$$

In this form the magnitude and the sign of the direction cosine ( $n_x$ ) between  $(\tilde{u}/u)$  and  $(\tilde{p}/p)$  are preserved and unaffected by the rms procedure. If, on the other hand, the absolute value of  $n_x$  must prevail, the agreement between the hot-wire and the pitot acoustic results becomes extremely poor at the lower free-stream Mach numbers since Eq. (44) must be defined as follows:

$$\sqrt{\left(\frac{\tilde{p}}{p}\right)^2} = \sqrt{\left(\frac{\tilde{P}}{\gamma P}\right)^2} \left\{ 1 - \frac{2n_x}{M_\infty} \right\} \quad (47)$$

Correspondingly, Eq. (43) becomes

$$\sqrt{\left(\frac{\tilde{P}}{P_p}\right)^2} = C_p \left\{ (0.3M_\infty^2 - 1)/0.3 \right\} \quad (48)$$

## 6.0 RESULTS

### 6.1 TUNNEL A STILLING CHAMBER

The stilling chamber measurements in Tunnel A were made downstream of the screens near the maximum diameter of the stilling chamber (see Fig. 1d). The pressure fluctuation levels, as expected, are essentially independent of the nozzle throat contour but appear to be directly related to the mean value of the total pressure in the stilling chamber, as shown in Fig. 15. The addition of high-pressure makeup air upstream of the screens (using valve 337 or 237) momentarily perturbs this level to a higher value by more than an order of magnitude (an increase of nominally 24 db for the case shown in Fig. 15). Except for the effects produced by the make-up air, the stilling chamber pressure fluctuation levels appear to vary with the measured stilling chamber pressure (PT) as follows:

$$\tilde{P}_T/PT(\text{percent}) = 0.235(PT)^{-0.90} \quad (49)$$

for  $4 \text{ psia} > PT > 130 \text{ psia}$  in Tunnel A.

A comparison of some previously unpublished hot-wire results obtained in November 1965 with the present dynamic pressure measurements obtained in Tunnel A stilling chamber is shown in Fig. 16. The temperature fluctuation levels based on the hot wire anemometer measurements were negligible, less than 0.1 percent of the stilling chamber mean value. In Ref. 4, the relation between the velocity fluctuations obtained from the hot-wire measurements and those deduced from a stilling chamber surface-mounted dynamic pressure gage is as follows:

$$\sqrt{\left(\frac{\tilde{u}}{u}\right)^2} = \sqrt{\left(\frac{\tilde{P}_T}{PT}\right)^2} / (y M_{ST}) \quad (50)$$

Using this relationship and converting the measured stilling chamber pressure fluctuation to the corresponding velocity values shows (Fig. 16b) that the hot-wire results obtained in November 1965 (open symbols) are in fair agreement with the present pressure fluctuation measurement (solid symbols). The flagged values correspond to fluctuation levels occurring at the maximum tunnel stagnation pressure. In general, the velocity fluctuations were found to be less than 1 percent, and the measured level of the pressure fluctuations was nominally less than 0.1 percent.

Samples of the spectra of the pressure fluctuation signal obtained in the stilling chamber are given in Fig. 17 for various stilling chamber pressure levels and plant staging configurations. Also, the frequencies where more significant energy levels occur are identified. Most of the energy occurs below 5 kHz. A comparison of Figures 17e and f clearly shows that the addition of makeup air to maintain the tunnel stilling chamber pressure level (flow rate or test section free-stream Reynolds number) produces a significant disturbance which in previous acoustical test programs has compromised the dynamic pressure signals recorded in the tunnel test section.

## 6.2 TUNNEL A AND B TEST SECTION TURBULENCE

The evaluation of the test section turbulence levels in Tunnels A and B is based on free-stream hot-wire anemometry measurements, free-stream dynamic pitot pressure probe data (pitot-acoustic probe), and surface static pressure fluctuation measurements. The surface pressure fluctuation measurements were obtained from a flat plate and the Tunnel A side wall surfaces in 1978 and from a 6-deg sharp cone in 1979.

The 1978 flat plate surface measurements were subsequently found to be unsatisfactory (signal-to-noise ratio was too low) for defining the test section turbulence. The nylon insert containing the dynamic transducers (see Fig. 9) was too flexible and, when pressure was applied to the nylon surface, tended to preload or alter the signal level from the piezoelectric dynamic pressure sensor. The signal from the smaller transducer was extremely noisy and indicated that the gage was not flush with the nylon insert (i. e., the mid-frequency range of the signal was attenuated). Also, the Corcos gage size correction factor (see Ref. 35) for the two transducers, nominally 0.2 and 0.4 in. in diameter, was extremely large. It seemed to be unrealistic to apply these gage size corrections to such poor signal responses.

In all subsequent installations, the dynamic pressure transducers were mounted in a thin cylindrical RTV sleeve to insulate the gages from vibrational (or acceleration) disturbances and to isolate potential acoustical noise sources to prevent their being transmitted through the model to the gage. Although the present flat plate results are highly questionable and are not included in this document, this flat plate acoustics model is available for future investigations.

### 6.2.1 Test Section Pressure Fluctuations

A comparison of the free-stream static pressure fluctuations inferred from the hot-wire anemometry and pitot-acoustic probe data as a function of free-stream Reynolds number based on the effective test section diameter (DE) is given in Figs. 18 and 19. In general,

considering the data scatter, the results from the two measuring techniques are in agreement in Tunnel A (Fig. 18) and in Tunnel B at the maximum Reynolds number (Fig. 19). The difference in the results between the two measurement techniques at Mach number 6 at the low Reynolds numbers is, at this time, unresolved.

In general, the results obtained at Mach numbers 2.0, 4.0 and 5.0 in Tunnel A and the pitot acoustic data in Tunnel B indicate that the static pressure fluctuations vary as  $(RE_{DE})^{-1/4}$ , which is in reasonable agreement with the data trends shown in Ref. 5. The hot wire results in Tunnel B do not follow this Reynolds number trend (that is,  $C_p^- = f(RE_{DE})^{-1/4}$ ). Although the actual reason for this anomaly is presently unknown, it is possible that the difference in the hot-wire and pitot acoustic probe location or orientation with respect to the tunnel flow or tunnel walls affected these results.

### 6.2.1.1 Hot-Wire Anemometer Spectral Results

Selected spectra of the fluctuations determined from the hot-wire measurements are presented in Figs. 20 through 24. These spectra were obtained with a free-stream unit Reynolds number of  $RE_\infty = 3$  million per foot for  $M_\infty = 4, 6$ , and  $8$ .

At  $M_\infty = 4$  and  $6$  the fluctuations in the free-stream flow are dominated by the sound mode (Section 5.2.3.4), wherein the principal variable is pressure. Velocity and static temperature fluctuations in this case are induced by the pressure fluctuations and are inferred from them using isentropic relations, which are simply multiplication factors. (The sound waves are assumed to have a single or "preferred" direction.) As a consequence, the pressure fluctuation spectrum serves to illustrate the spectra of the other fluctuating parameters. The spectrum of the pressure fluctuations for  $RE_\infty = 3$  million per foot at  $M_\infty = 6$  is shown plotted in a semilog format in Fig. 20, and the spectrum for the same unit Reynolds number at  $M_\infty = 4$  is shown in a log-log format in Fig. 21.

The power density spectrum of the pressure fluctuations for  $M_\infty = 4$  is presented in Fig. 22 with the amplitude normalized using the value of  $\tilde{P}/\bar{P} = 0.000669$  (for  $f = 150$  Hz), which is the value of  $\tilde{P}/\bar{P}$  at 150 Hz. The frequency has been nondimensionalized using the free-stream velocity and the longitudinal integral scale given by

$$A_p = \frac{\bar{u}_\infty}{4} \frac{\tilde{P}(f = 150 \text{ Hz})}{\tilde{P}(\text{wide band})}$$

The velocity fluctuation power density spectrum normalized using  $\tilde{u}/\bar{u} = 0.0000445$  (for  $f = 150$  Hz) is also shown in Fig. 22, where the integral scale

$$A_u = \frac{\bar{u}_\infty}{4} \frac{\tilde{u}(f = 150 \text{ Hz})}{\tilde{u}(\text{wide band})}$$

has been used in nondimensionalizing the frequency.

The corresponding spectra obtained from the  $M_\infty = 6$  measurements are presented in Fig. 23. In this case the values  $\tilde{P}/\bar{P} = 0.00306$  and  $\tilde{u}/\bar{u} = 0.00159$  (for  $f = 600$  Hz, in both cases) were used to normalize the respective amplitudes, and the integral scales

$$\Lambda_p = \frac{\bar{u}_\infty}{4} \frac{\tilde{P}(f=600 \text{ Hz})}{\tilde{P}(\text{wide band})}$$

and

$$\Lambda_u = \frac{\bar{u}_\infty}{4} \frac{\tilde{u}(f=600 \text{ Hz})}{\tilde{u}(\text{wide band})}$$

were used in nondimensionalizing the frequency in the respective abscissas.

At  $M_\infty = 8$  the free-stream fluctuations are not dominated by the sound mode (Section 5.2.3.4). Presented in Fig. 24 are the power density spectra of the pressure, velocity, and static temperature fluctuations obtained after it was specified that 1) the sound is uncorrelated with either vorticity or entropy, and that the latter two modes are perfectly anticorrelated (that is,  $R_{\tau\theta} = -1.0$ ,  $R_{\sigma\pi} = R_{\pi\tau} = 0$ ), and 2) the sound-wave source velocity is the same at both  $M_\infty = 6$  and 8. The fluctuations have been normalized using the following values:  $\tilde{P}/\bar{P} = 0.00452$ ,  $\tilde{u}/\bar{u} = 0.000164$ , and  $\tilde{T}/\bar{T} = 0.00388$  (all for  $f = 600$  Hz). The frequency has been made nondimensional using the free-stream velocity and the respective integral scales

$$\Lambda_p = \frac{\bar{u}_\infty}{4} \frac{\tilde{P}(f=600 \text{ Hz})}{\tilde{P}(\text{wide band})}$$

$$\Lambda_u = \frac{\bar{u}_\infty}{4} \frac{\tilde{u}(f=600 \text{ Hz})}{\tilde{u}(\text{wide band})}$$

$$\Lambda_T = \frac{\bar{u}_\infty}{4} \frac{\tilde{T}(f=600 \text{ Hz})}{\tilde{T}(\text{wide band})}$$

### 6.2.1.2 Pitot-Acoustic Probe Spectral Results

Typical power spectral density (PSD) of the pitot pressure fluctuations in Tunnels A and B are shown in Fig. 25. The local free-stream velocity and dynamic pressure and the tunnel wall boundary-layer displacement thickness (defined in Appendix C) were used to normalize these spectra. The free-stream Reynolds number for the spectra shown for Mach number 1.5

(Tunnel A) to 6.0 (Tunnel B) vary nominally from  $3 \times 10^6$  to  $4 \times 10^6$  per foot. The Mach number 8 data of Tunnel B were obtained at a Reynolds number of  $1 \times 10^6$  per foot (the analysis for the higher Reynolds number results was questionable). Except for the Mach number 8 results, the other spectra fall nominally within an amplitude bandwidth of  $\pm 6.5$  db.

The results in Fig. 26a include a repeat of the signal analysis obtained for the 1979 probe. The difference between these two spectra is nominally 3 db or slightly more than 2 standard deviations of the random error cited in Section 5.1.2. The effect of small changes in free-stream Reynolds number on the spectra are shown in Figs. 26b and c for Mach numbers 2 and 3, respectively. In general, the Reynolds number effects are not clearly evident because of the statistical uncertainty in the spectral analysis. The Mach number 5 spectral comparisons of the two probes were deleted from this set because the 1978 results were questionable. Figure 27 contains a spectrum obtained for the 1979 pitot acoustic probe in Tunnel B at Mach number 6.

A comparison of the pitot pressure spectra obtained with two different pitot acoustic probes (the 1978 and 1979 probes shown in Fig. 13) is also shown in Fig. 26. In general, the output from the 1978 probe was highly susceptible to various high-frequency vibrations of the probe support system as indicated in Figs. 28 and 29.

Although the true  $\overline{rms}$  (TRMS) of the signal shown in Fig. 28 from the FY78 probe in Tunnel A was only 0.1 percent of the atmospheric pressure, there is a pronounced peak or resonance in the spectra at 320 to 400 Hz obtained with the probe in the model injection tank and with no flow through the tunnel circuit. This result was unaffected by whether or not the tunnel was operating. Venting the tank to the tunnel static conditions or reducing the model injection tank pressure doubled the signal level and revealed additional vibrational modes which were picked up by the pitot acoustic transducer. Theoretically, the harmonics for these vibrational bending modes vary as follows:  $6.26 f_o$ ,  $17.55 f_o$ ,  $34.39 f_o$ , etc. (see Ref. 36, pp. 71-73). In general, the fundamental mode ( $f_o$ ) is proportional to the radius of gyration of the beam or probe section and inversely proportional to the square of the beam (probe) length.

The results in Fig. 28 were used as a tare run to identify those signal frequency modes which are not considered to be a part of the signal when the probe is exposed to the tunnel flow. As shown in Fig. 26, the spectra were faired through at these frequencies which were attributed to transducer vibration. The signals were then reintegrated to define the true  $\overline{rms}$  (TRMS) of the pressure fluctuations sensed by the probe when exposed to the tunnel flow.

The pitot acoustic probe installation in Tunnel B differed from that in Tunnel A, and this resulted in different probe vibrational bending modes, as shown in Fig. 29. The probe consists of two cylindrical sections pinned together. Apparently one clearly identifiable vibration was produced by the entire probe support "L2" and another was produced by the section closest to the probe support, "L1." The longer beam length was responsible for the lower frequencies.

As indicated in Fig. 29, with no flow in the circuit and the model injection tank at atmosphere, the two fundamental vibrational modes appear to be present even though the overall true rms energy level signal is negligible (TRMS < 0.05 percent). With flow in the tunnel, the energy level (TRMS) increases to 0.6 percent. Venting the model injection tank to the tunnel (reducing the tank pressure) significantly increases the signal level so that the higher vibrational frequencies appear in the signal spectrum. As in the case of the Tunnel A results, these vibrational frequencies were then used to fair through or filter the spectra obtained when the probe was exposed to the tunnel flow.

### 6.2.2 Tunnel A Side Wall Static Pressure Fluctuations

In Tunnel A, two side wall static taps were instrumented with dynamic pressure sensors. The results shown in Fig. 30 identify the total amount of energy existing (NED) in the profile up to a given frequency. For example, of the energy detected by the nonoperating side wall (the side opposite the tunnel control room) gage, 80 percent is contained in the frequency envelope up to 22.5 kHz. For the operating side, 80 percent of the energy detected is in the frequency envelope up to 12.5 kHz.

Although the two gages are supposedly identical, the operating side gage must be protruding slightly from the tunnel wall, causing a reduction in the mid range frequency response of the gage as shown in Fig. 30b (see Ref. 17). Unfortunately, the gage installation was removed before this problem with the operating side wall gage could be visually confirmed. Obviously, the capability of performing some online spectral analysis would aid in the validation of dynamic measurements.

The wall static spectra obtained on the nonoperating tunnel side wall, shown in Fig. 31, provide a reasonable description of the effect of Mach number on the tunnel wall static pressure fluctuations in Tunnel A. The levels of these spectra are higher than those associated with the free-stream test section pressure fluctuation levels deduced from the hot-wire or pitot acoustic probes. These results in Fig. 31 are simply a fairing of the spectra obtained at various Tunnel A Mach number nozzle settings at a nominal Reynolds number of  $4 \times 10^6$  per foot.

### 6.3 CONE SURFACE STATIC PRESSURE FLUCTUATIONS

The 6-deg sharp cone was instrumented with dynamic pressure gages at nominally three stations along the model. The  $\overline{rms}$  level is shown in Fig. 32 in coefficient form as a function of free-stream Reynolds number based on the axial distance from the nose to the instrumented station (Sta). These results can be used to identify the nominal level of the surface pressure fluctuation sensed on a model in Tunnels A and B under a laminar, transitional, and in some cases, a fully turbulent boundary layer.

In general, as shown in Fig. 32, the larger size gages (square symbols) produce an attenuated response relative to the smaller gages (circular symbols). This reduction in the response of the larger gage is expected and simply reflects that a correction like the one formulated by Corcos (Ref. 35) and discussed in Appendix B must be applied before the true pressure fluctuation level is experimentally established. The applicability of the Corcos type of correction to results obtained in the environment of a large supersonic/hypersonic test unit would have to be thoroughly evaluated before it could be applied as a standard procedure. Presently, the minimum size transducers used in Tunnels A and B are 0.10 in. in diameter, which means that the maximum ratio of  $(\omega \cdot r/u_c)$  varies from 1.5 to 1.8 (for  $f = 100$  kHz) depending on the free-stream Mach number (and the corresponding convective velocity). Large values of  $\omega \cdot r/u_c$  result in significant gage attenuation effects.

Except for the results at Mach number 2, these results indicate that the nominal transitional Reynolds number (where  $C_p$  reaches a maximum value) is nominally  $4 \times 10^6$  and is essentially independent of the free-stream Mach number. In general, the transition location based on past observations of a sharp cone (half-angles less than 9 deg) can be empirically correlated as follows for Tunnels A, B and C with the model wall temperature nominally at 540 to 600°R:

$$X_t(\text{end}) = 7.5(\text{RE/in.} \cdot 10^{-6})^{-5/4} \quad (51a)$$

$$X_t(\text{beginning}) = 4.6(\text{RE/in.} \cdot 10^{-6})^{-5/4} \quad (51b)$$

This correlation can be rearranged and solved to show that the transition locations indicated in Fig. 32 are bracketed by the correlation.

In general, the gages of the same size located diametrically opposite each other at model station 11.0 produced the same result. Small differences between the two measurements can be attributed to slight deviations in the pitch angle from the desired zero angle of attack attitude, which has an effect on the state of the boundary layer. Also, uncertainties associated with the gage calibration and flushness of the gage installation can affect the transducer response and contribute to the differences shown.

Figure 33 illustrates the effects of free-stream Reynolds number (boundary-layer transition) and gage location on the power spectral density distribution of the pressure fluctuation measurements [(psi)<sup>2</sup>/Hz versus frequency] made on the 6-deg sharp nose cone at Mach number 6. An interesting phenomenon appeared in the spectra of the dynamic pressure signals obtained on the cone at Mach number 6. At the model base station (Sta 40), at the minimum free-stream Reynolds number where transition was in close proximity to the model base, two distinguishable nodes (like the two humps on a Bactrian camel) appeared in the pressure fluctuation spectrum. Increasing the Reynolds number from  $0.5 \times 10^6$  to  $1.0 \times 10^6$  produced an abrupt increase in the magnitude of the spectra, and the nodes reduced from two to one (like the hump on a dromedary camel). A further increase in the free-stream Reynolds number caused the nodes to disappear, and the overall level of the signal diminished slightly. A similar phenomenon was observed in some recent results obtained on an 8-deg cone in Tunnel B at Mach number 8 and is reported in Ref. 37.

The variation in the level of the spectra as transition moves over the gage is quite normal; that is, the maximum level occurs with transition over the gage, the minimum value occurs when the flow is laminar, and the turbulent condition produces a signal level which is slightly less than the level existing when the boundary layer was transitional.

No unusually prominent nodes appear in the spectra of the small gage (0.10-in. diam) at the mid-body station of 25 in. at the zero roll location, but the larger gage (0.20-in. diam) at the same station (25.0 in.) at the 180-deg roll location has a single hump (peak at 110 kHz) in the spectra at the minimum free-stream Reynolds number (0.5 million per foot).

Also, both transducers at station 25 contain a discrete step in the spectra at a frequency of 33 to 35 kHz. This type of disturbance was observed in the surface pressure fluctuation spectra of a sharp nose cone at free-stream Mach numbers of 6 and 8 and is reported in Ref. 5. The source of the disturbances reported in Ref. 5 occurred at a frequency of 45 to 48 kHz and was not identified. A similar disturbance was noted at 56 kHz in the spectra shown in Fig. 33d for pressure fluctuations obtained at Sta 11.0 in.

The results obtained in the presence of a laminar boundary layer (the data from Fig. 33d) are presented in terms of the normalized parameters  $(\bar{P}^2/q_\infty^2)u_\infty/\delta^*$  and wave number  $f\delta^*/u_\infty$  in Fig. 34. This figure contains a listing of the overall bandwidth of the fluctuation which includes 95 percent of the energy of the fluctuation, designated as NED (0.95). This tabulation simply shows that as the free-stream Reynolds number decreases, the bandwidth of the fluctuation increases.

## 6.4 SUMMARY OF TUNNEL A AND B PRESSURE FLUCTUATION RESULTS

A summary of the pressure fluctuation levels inferred or measured in Tunnels A and B is given in Fig. 35. The band associated with results inferred from the dynamic pitot probe reflect primarily the variations produced by the free-stream Reynolds number variations. In general, the FY79 probe results are smaller than those obtained in FY78. The nozzle wall static pressure fluctuations measured about 125 in. upstream of the test section are consistently higher than the inferred free-stream values. All the results suggest that the minimum pressure fluctuation level occurs around Mach number 4 in Tunnel A. The equivalent sound pressure level (SPL) in the test section can be computed as follows:

$$SPL = 20 \log_{10} C_p + 20 \log_{10} q_\infty + 170.75 \quad (52)$$

where  $q_\infty$  is given in lbf/in.<sup>2</sup>.

The curve, based on analysis from Ref. 15 and included in the figure for reference purposes only, is the predicted variation in the pressure fluctuation as a function of free-stream Mach number as formulated by Lawson (see Ref. 15). This curve provides a rough estimate of the Mach number trend in the pressure fluctuation levels in Tunnel A. Actually, the hot-wire results in most cases (Fig. 19) suggest that the static pressure fluctuations in Tunnel B are less than the values inferred from the pitot acoustic probe and also less than the values based on the Lawson curve.

The results in Fig. 35b describe the typical pressure fluctuation levels detected on a body of revolution. As expected, the free-stream Reynolds number and the nature of the boundary layer on the body have a direct effect on the response of a surface flush-mounted dynamic pressure transducer. The maximum fluctuations sensed by the dynamic pressure sensor on the cone occur when transition is at the gage location. Also as noted previously, the gage size can have a pronounced effect on the gage response: the larger the gage, the weaker the response.

Figure 36 summarizes the attempts to identify the test section static pressure fluctuation levels in Tunnels A and B. In general, in the Reynolds number range from 2 to 4 million per foot, the static pressure fluctuation levels deduced from the hot-wire and pitot acoustic probes are in reasonably good agreement. The cone surface static pressure fluctuations increase with the free-stream Mach number and deviate significantly from the hot-wire and pitot probe results. Apparently, there is some amplification of the free-stream disturbance as it propagates through the laminar boundary-layer flow to the transducer on the cone.

surface, and this amplification increases with the free-stream Mach number. These results also suggest that the magnitude of the pressure fluctuations decreases as the cone half-angle increases.

The correlation term used to curve fit the free-stream static pressure fluctuation variation with Mach number was suggested in Ref. 15. The term in the denominator is simply the Eckert reference temperature ratio with  $T_w$  being the nominal tunnel wall temperature and the recovery factor ( $\eta$ ) equal to 0.891. This curve fit was used to estimate the pressure fluctuation level in Tunnel C at Mach number 10.

## 7.0 CONCLUDING REMARKS

The free-stream fluctuation or turbulence levels which have been determined in Tunnels A and B are based on free-stream hot-wire anemometer, pitot-acoustic probe, and cone surface pressure fluctuation measurements. The accomplishments and significant results of this investigation are as follows:

1. Reasonable correlations based on the analysis from Ref. 34 were established between the pitot-acoustic probe data and hot-wire data. In addition it was noted that as the free-stream Mach number increased, the surface static pressure fluctuations measured on a cone underneath a laminar boundary layer deviated from the free-stream pressure fluctuation levels based on the hot-wire and pitot-acoustic probes. These results should resolve most of the discrepancies that had previously existed between the AEDC dynamic pressure measurements and the free-stream hot-wire results noted previously in Refs. 3, 5, 6, and 7.
2. Pressure fluctuations measured on the surface of a cone model in the presence of a laminar boundary layer may not be a true measure of the absolute level of the free-stream pressure fluctuations which characterize the free-stream flow. This fact should be taken into account for wind tunnel tests in which the influence of free-stream flow fluctuations is significant, as in the case of naturally occurring boundary-layer transition.
3. In general, at nominal free-stream Reynolds numbers of 2 to 4 million per foot, the free-stream pressure fluctuations as a function of nozzle Mach number, tunnel wall temperature, test section static temperature, and dynamic pressure vary as follows:

$$\sqrt{\langle \hat{p} \rangle^2} = 0.0029 \eta_{\infty} / (T^* / T_{\infty})$$

where

$$(\Gamma^*/\Gamma_\infty) = \{0.5[(\Gamma_w/\Gamma_\infty) + 1] + 0.22\eta[(\gamma - 1)/2]M_\infty^2\}$$

4. The results at Mach numbers 2, 4, and 5 in Tunnel A and the pitot-acoustic data in Tunnel B at Mach number 6 suggest that the free-stream fluctuation ratio ( $\bar{p}/\bar{p}$ ) decreases with increasing free-stream Reynolds number; that is, ( $\bar{p}/\bar{p}$ ) is proportional to  $(RE_{DE})^{-0.25}$ .
5. An evaluation of the pressure fluctuations sensed by the pitot-acoustic probe could not be established until the spectral content of the probe transducer response signal was analyzed. The probe mounting or support system, the transducer mounting, and the dynamic calibration of the transducers could and in some cases did affect the evaluation of the pitot probe pressure fluctuations. Basically, the spectral distribution provides the method for identifying those dynamic disturbances sensed by the probe which are not a part of the test section sound source (turbulence).
6. A by-product of this study was the development of the software and analysis used to interface the SD360 signal processor with the facility computer. The signal processor was used to convert the analog signals into a digital spectral format (transform, power spectral, or cross-spectral density), and the facility computer was used to normalize and plot the spectra, digitally filter and recompute the root-mean-square of the signals, and provide additional digital signal processing for further analysis of the signal results.
7. The stilling chamber pressure fluctuations were found to correlate simply as a function of the mean value of the stilling chamber pressure. As expected, the addition of high-pressure makeup air to maintain the flow rate in the tunnel circuit was found to significantly increase the stilling chamber turbulence. The hot-wire measurements obtained in 1965 and the present surface static pressure fluctuation measurements were in good agreement.

In addition to these accomplishments, this present effort revealed the following problems:

1. Additional test results and analysis are needed at Mach numbers 6 and 8 to understand the trend in which the pressure fluctuation ratio based on the hot-wire measurements increases with the free-stream Reynolds number.

2. In the present studies, the fluctuation measurements were made at one point in the test section. The question remains concerning the spatial variation in the fluctuations throughout the test section. In particular, the presence of a small region of nonuniform flow along the axis of the axisymmetric nozzles of Tunnel B suggests that some effort is warranted to define the radial variation in the tunnel test section turbulence. Since the sound disturbances emanate from the tunnel wall turbulent boundary layer, there is a need to map the variation in the turbulence level near the tunnel wall.
3. The possibility exists for gleaning additional information from the present flow quality turbulence data by examining the correlations that may exist between the various types of measurements. This additional analysis would require some additional programming and evaluation of the existing data source. Possibly, the convective velocity of the sound source associated with the flow over a typical conical body could be identified for various wind tunnel conditions.
4. The turbulence levels sensed by the instrumentation in a planar surface aligned with the flow need to be established. This would require reinstrumenting the flat plate and testing it in Tunnels A and B.
5. The results presented in this report should be supplemented by an investigation of the flow fluctuations which characterize the interior of the boundary layer above the surface-mounted transducers. Such an effort would address the need for an improved understanding of the differences between free-stream and surface pressure fluctuations. A limited inquiry for this purpose could be made using existing hot-wire anemometer measurements acquired during the present test and earlier tests using slender cone models in Tunnel B. However, the reduction and analysis of these data for this purpose were beyond the scope and resources of the earlier tests and of the present effort.

## REFERENCES

1. Schopper, M. R. "A Model for the Noise Radiated by Turbulent Boundary Layers and Its Interaction with Laminar Layers in Supersonic Flow." AIAA Paper 79-1523, AIAA 12th Fluid and Plasma Dynamics Conference, Williamsburg, Virginia, July 23-25, 1979.
2. Anders, J. B, Stainback, P. C., and Beckwith, I. E. "A New Technique for Reducing Test Section Noise in Supersonic Wind Tunnels." AIAA Paper 78-817, 10th Aerodynamic Testing Conference, San Diego, California, April 19-21, 1978.

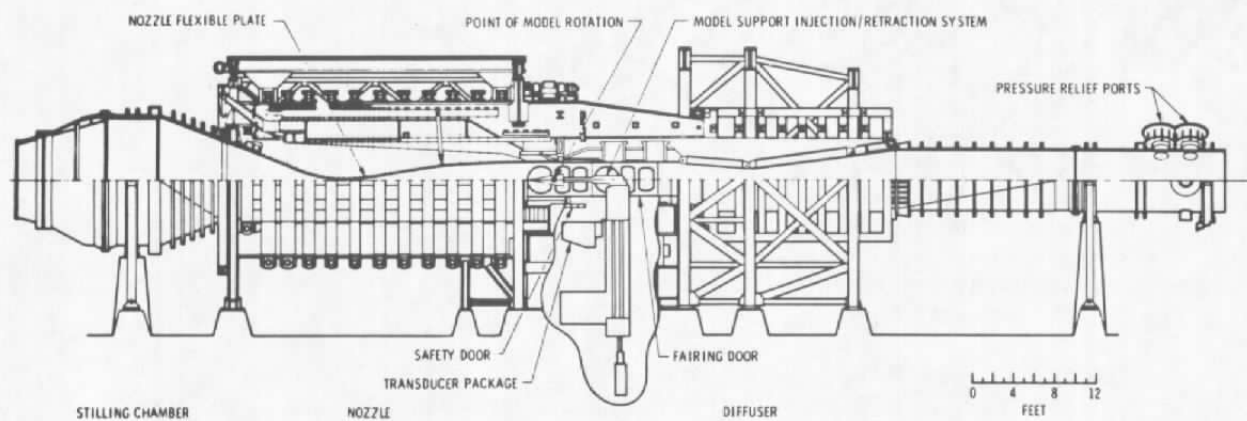
3. Ladberman, A. J. "Review of Wind-Tunnel Freestream Pressure Fluctuations." *AIAA Journal*, Vol. 15, No. 4, April 1977, pp. 605-608.
4. Anders, J. B., Stainback, P. C., Keefe, L. R., and Beckwith, I. E. "Sound and Fluctuating Disturbance Measurements in the Stilling Chamber and Test Section of a Small, Mach 5 Wind Tunnel." *ICIASF '75 RECORD* (1975), pp. 329-340.
5. Stainback, P. C., Fisher, M. C., and Wagner, R. D. "Effects of Wind-Tunnel Disturbances on Hypersonic Boundary-Layer Transition." *AIAA Paper 72-181*, AIAA 10th Aerospace Sciences Meeting, San Diego, California, January 17-19, 1972.
6. Bergstrom, E. R. and Raghunathan, S. "Aerodynamic Noise and Boundary-Layer Transition Measurements in Supersonic Test Facilities." *AIAA Journal*, Vol. 10, No. 11, November 1972, pp. 1531-32.
7. Donaldson, J. C. and Wallace, J. P. "Flow Fluctuation Measurements at Mach Number 4 in the Test Section of the 12-Inch Supersonic Tunnel (D)." *AEDC-TR-71-143 (AD728630)*, August 1971.
8. Pate, S. R. and Schueler, C. J. "Radiated Aerodynamic Noise Effects on Boundary-Layer Transition in Supersonic and Hypersonic Wind Tunnels." *AIAA Journal*, Vol. 7, No. 3, March 1969, pp. 450-457.
9. Blake, W. K. "Turbulent Boundary-Layer Wall-Pressure Fluctuations on Smooth and Rough Walls." *Journal of Fluid Mechanics*, Vol. 44, Part 4, 16 December 1970, pp. 637-660.
10. Bull, M. K. "Wall-Pressure Fluctuations Associated with Subsonic Turbulent Boundary Layer Flow." *Journal of Fluid Mechanics*, Vol. 28, Part 4, 1967, pp. 719-754.
11. Laufer, J. "Some Statistical Properties of the Pressure Field Radiated by a Turbulent Boundary Layer." *Physics of Fluids*, Vol. 7, No. 8, August 1964, pp. 1191-1197.
12. Ffowcs Williams, J. E. "The Noise from Turbulence Convected at High Speeds." *Philosophical Transactions of the Royal Society of London*, A255, April 1963, pp. 469-503.

13. Laufer, J. "Sound Radiation from a Turbulent Boundary Layer." *Mechanics of Turbulence* (National Research Center, International Symposium, Marseilles, France, August 28-September 2, 1961), published by Gordon and Breach Science Publisher, New York, 1964, pp. 381-393.
14. Laufer, J. "Aerodynamic Noise in Supersonic Wind Tunnels." *Journal of the Aerospace Sciences*, Vol. 28, No. 9, September 1961, pp. 685-692.
15. Laganelli, A. L. and Howe, J. R. "Prediction of Pressure Fluctuations Associated with Manuvering Re-Entry Weapons." AFFDL-TR-77-59, July 1977.
16. Willmarth, W. W. and Wooldridge, C. E. "Measurements of the Correlation Between the Fluctuating Velocities and the Fluctuating Wall Pressure in a Thick Turbulent Boundary Layer." North Atlantic Treaty Organization, AGARD Report No. 456, April 1963.
17. Hanly, R. D. "Effects of Transducer Flushness on Fluctuating Surface Pressure Measurements. "AIAA Paper 75-534, AIAA 2nd Aero-Acoustics Conference, Hampton, Virginia, March 24-26, 1975.
18. Gaudet, L. "The Influence of Transducer Misalignment on the Measurement of Fluctuating Surface Pressure at Low Speeds." Royal Aircraft Establishment (RAE) TM AERO 1752, February 1978.
19. Willis, J. A. B. "Spurious Pressure Fluctuations in Wind Tunnels." *The Journal of the Acoustical Society of America*, Vol. 43, No. 5, 1968, pp. 1049-1054.
20. Bies, D. A. "A Review of Flight and Wind Tunnel Measurements of Boundary Layer Pressure Fluctuations and Induced Structural Response." NASA CR-626, October 1966.
21. *Test Facilities Handbook* (Eleventh Edition). "von Karman Gas Dynamics Facility, Vol. 3." Arnold Engineering Development Center, June 1979.
22. Doughman, E. L. "Development of a Hot-Wire Anemometer for Hypersonic Turbulent Flows." Philco-Ford Corporation Publication No. U-4944, December 1971; and *The Review of Scientific Instruments*, Vol. 43, No. 8, August 1972, pp. 1200-1202.

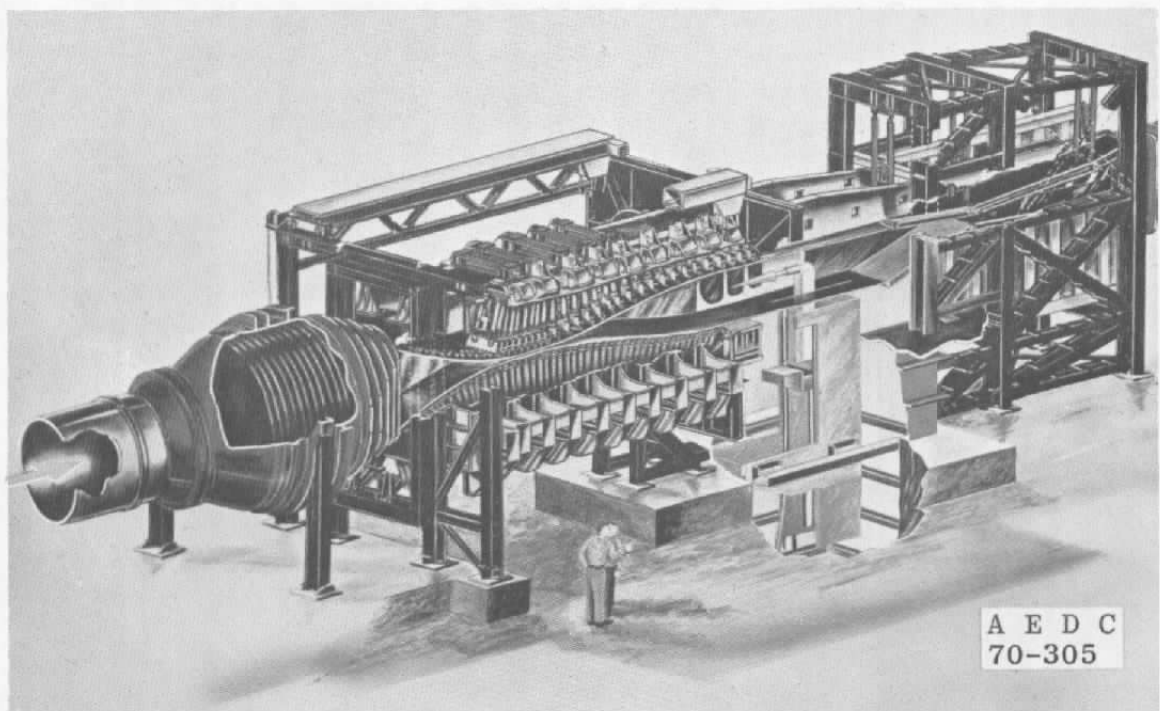
23. Donaldson, J. C., Nelson, C. G., and O'Hare, J. E. "The Development of Hot-Wire Anemometer Test Capabilities for  $M_\infty = 6$  and  $M_\infty = 8$  Applications." AEDC-TR-76-88 (AD-A029570), September 1976.
24. Bendat, J. S. and Piersol, A. G. *Random Data: Analysis and Measurement Procedures*. John Wiley & Sons, Inc., New York, 1971.
25. Brigham, E. O. *The Fast Fourier Transform*. Princeton-Hall, Inc., Englewood Cliffs, New Jersey, 1974.
26. Laderman, A. J. and Demetriades, A. "Turbulence Measurements in the Hypersonic Boundary Layer over a Cooled Wall." Philco-Ford Corporation Publication No. U-5079, September 1972.
27. Kovasznay, Leslie S. G. "Turbulence Measurements." *High Speed Aerodynamics and Jet Propulsion*, R. W. Ladenburg, ed. Princeton University Press, 1954, Vol. 9, Section F, pp. 213-285.
28. Kovasznay, Leslie S. G. "Turbulence in Supersonic Flow." *Journal of the Aeronautical Sciences*, Vol. 20, No. 10, October 1953, pp. 657-674, 682.
29. Morkovin, Mark V. "Fluctuations and Hot-Wire Anemometry in Compressible Flows." AGARDograph 24, November 1956.
30. Vrebalovich, Thomas. "Application of Hot-Wire Techniques in Unsteady Compressible Flows." Jet Propulsion Laboratory Technical Report No. 32-229, May 1962.
31. Laufer, John. "Sound Radiation from a Turbulent Boundary Layer." Jet Propulsion Laboratory Technical Report No. 32-119, November 1961.
32. Phillips, O. M. "On the Generation of Sound by Supersonic Turbulent Shear Layers." *Journal of Fluid Mechanics*, Vol. 9, Part 1, September 1960, pp. 1-28.
33. Harvey, W. D., Bushnell, D. M., and Beckwith, I. E. "Fluctuating Properties of Turbulent Boundary Layers for Mach Numbers up to 9." NASA-TN D-5496, October 1969.

34. Stainback, P. C. and Wagner, R. D. "A Comparison of Disturbance Levels Measured in Hypersonic Tunnels Using a Hot-Wire Anemometer and a Pitot Pressure Probe." AIAA Paper No. 72-1003, AIAA 7th Aerodynamic Testing Conference, Palo Alto, California, September 13-15, 1972.
35. Corcos, G. M. "Resolution of Pressure in Turbulence." *The Journal of the Acoustical Society of America*, Vol. 35, No. 2, February 1961, pp. 192-199.
36. Kinsler, L. E. and Frey, A. R. *Fundamentals of Acoustics*. John Wiley and Sons, Inc., New York, 1962 (Second Edition).
37. Demetriades, A. "Extended Analysis of the Boundary-Layer Transition Signals from the ATM Test Sensors," Kaman Science Corporation, May 1980.
38. Strike, W. T. and Donaldson, J. C. "Acoustical Loading and Heat-Transfer-Rate Distributions on a 7.2-Degree Cone at Mach Numbers 4, 8, and 10." AEDC-TR-72-129 (AD903643), September 1972.
39. Spangenberg, W. G. "Heat-Loss Characteristics of Hot-Wire Anemometers at Various Densities in Transonic and Supersonic Flow." NACA TN 3381, May 1955.
40. Jones, J. H. "An Investigation of the Boundary-Layer Characteristics in the Test Section of a 40 by 40-Inch Supersonic Tunnel." AEDC-TN-60-189 (AD245362), October 1960.
41. Matthews, R. K. and Trimmer, L. L. "Nozzle Turbulent Boundary Layer Measurements in the VKF 50-in. Hypersonic Tunnels." AEDC-TR-69-118, (AD854309), June 1969.
42. Van Driest, E. R. "The Problem of Aerodynamic Heating." Aeronautical Engineering Review, Vol. 15, No. 10, October 1956, pp. 26-41.
43. Winter, K. G. and Gaudet, L. "Turbulent Boundary-Layer Studies at High Reynolds Numbers at Mach Numbers Between 0.2 and 2.8." Aeronautical Research Council, London, R & M No. 3712, December 1970.
44. Whitfield, D. L. "Analytical, Numerical, and Experimental Results on Turbulent Boundary Layers." AEDC-TR-76-62 (AD-A027588), July 1976.

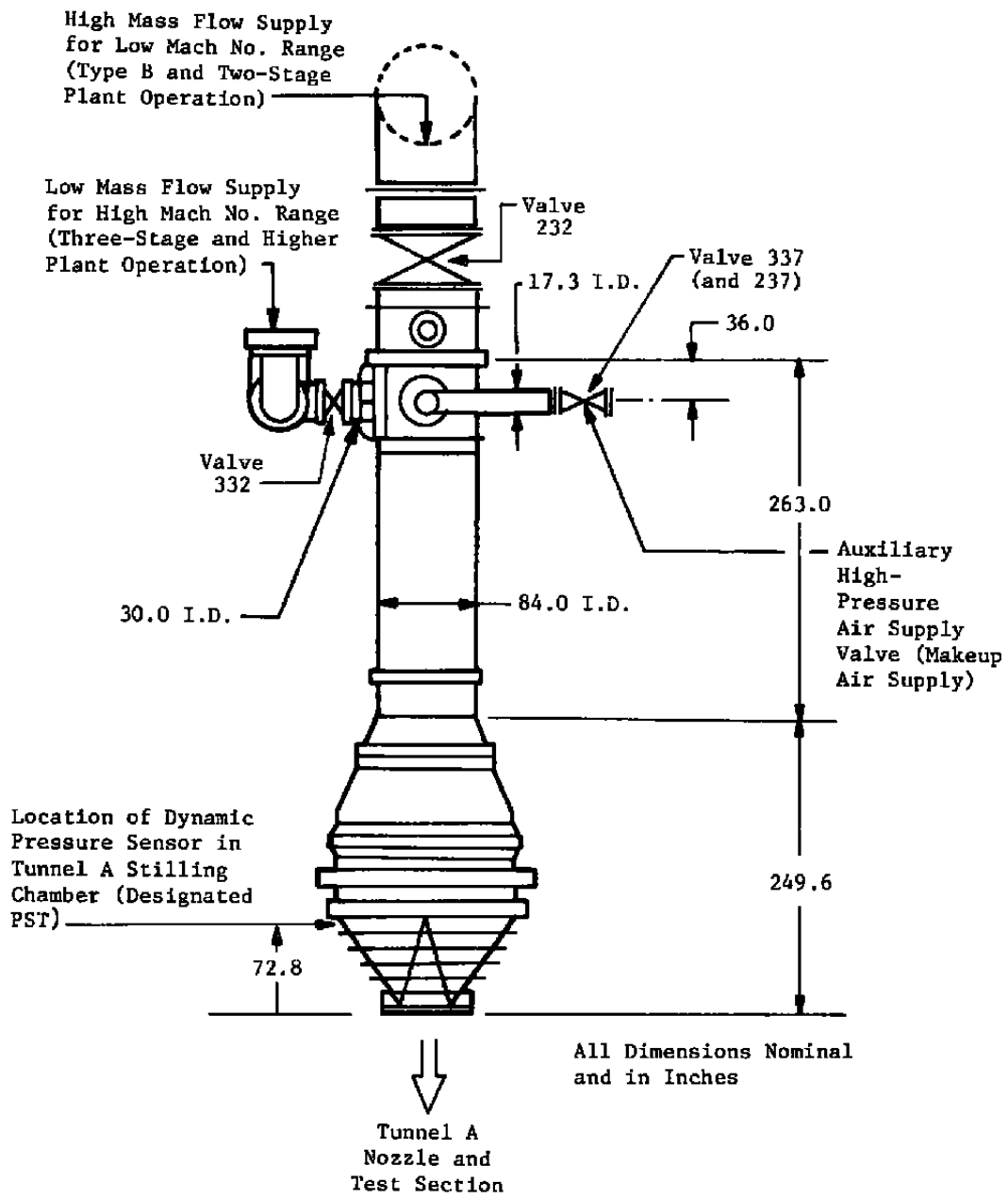
45. Taylor, G. I. and MacColl, J. W. "The Air on a Cone Moving at High Speeds." *Proceedings of the Royal Society of London, Series A*, Vol. 139, February 1, 1933, pp. 278-311.
46. Mayne, A. W., Jr. "Analysis of Laminar Boundary Layers on Right Circular Cones at Angle of Attack, Including Streamline-Swallowing Effects." AEDC-TR-72-134 (AD750130), October 1972.
47. Adams, J.C., Jr. "Implicit Finite-Difference Analysis of Compressible Laminar, Transitional, and Turbulent Boundary Layers Along the Windward Streamline of a Sharp Cone at Incidence." AEDC-TR-71-235 (AD734535), December 1971.



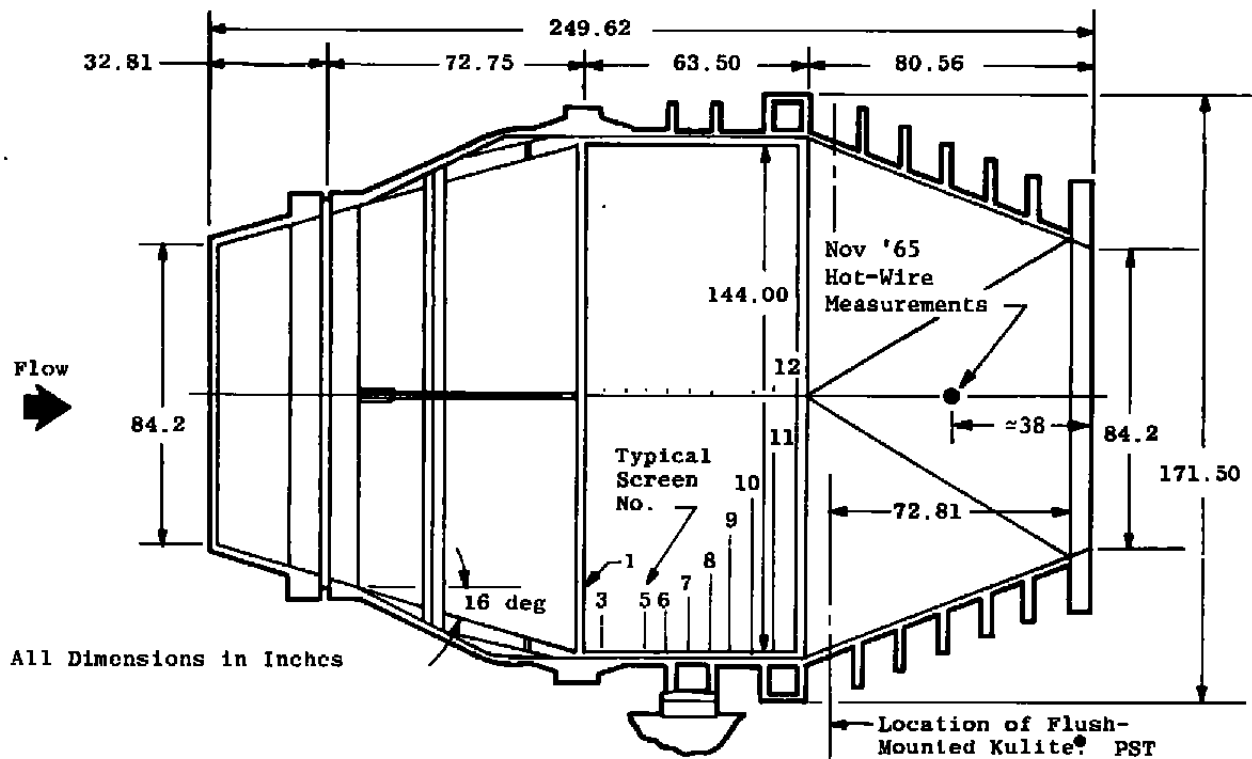
a. Tunnel assembly



b. Tunnel test section  
Fig. 1 Tunnel A



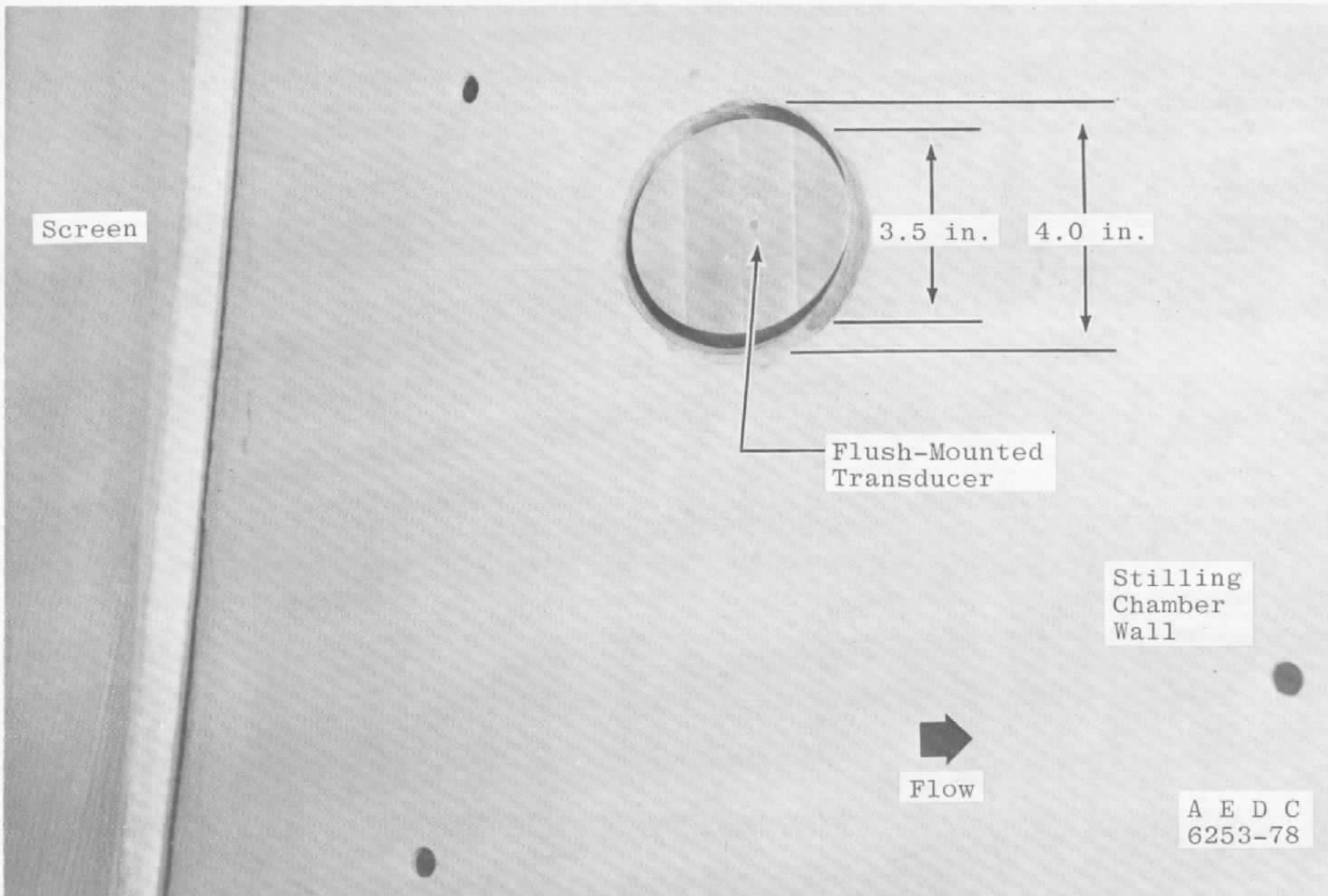
c. Upstream of Tunnel A nozzle  
Figure 1. Continued.



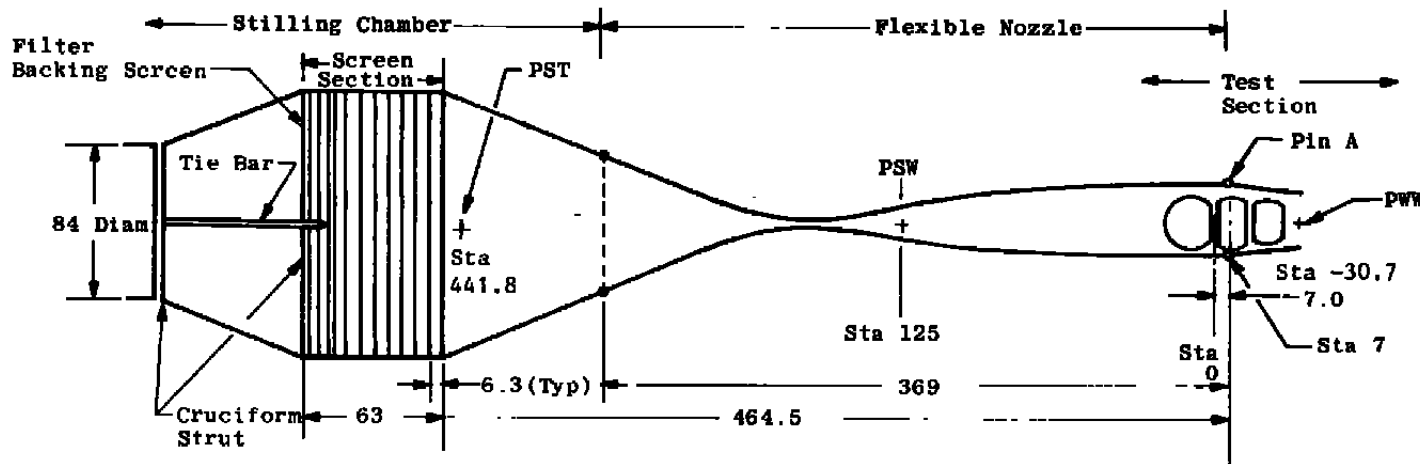
Screen No.	Diam	Wire Diam	Percent Open Area	Mesh
1	148	0.041	57	6
2		Out		
3 - 7		0.0075	62	28
8 - 10		0.0080	58	30

All Dimensions Shown in Inches  
Except as Noted

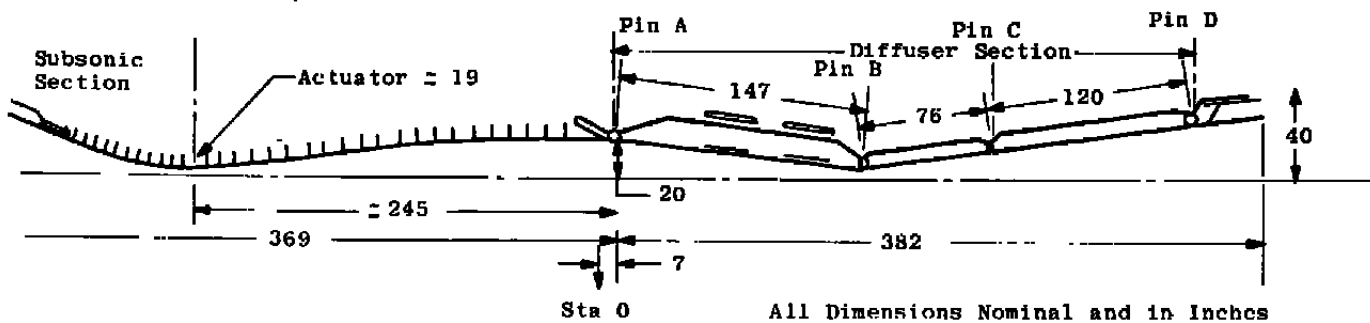
d. Stilling Chamber (as of FY78)  
Figure 1. Continued.



e. Transducer installation in the stilling chamber  
Figure 1. Continued.



f. Stilling Chamber — nozzle section



g. Nozzle — diffuser section  
Figure 1. Concluded.

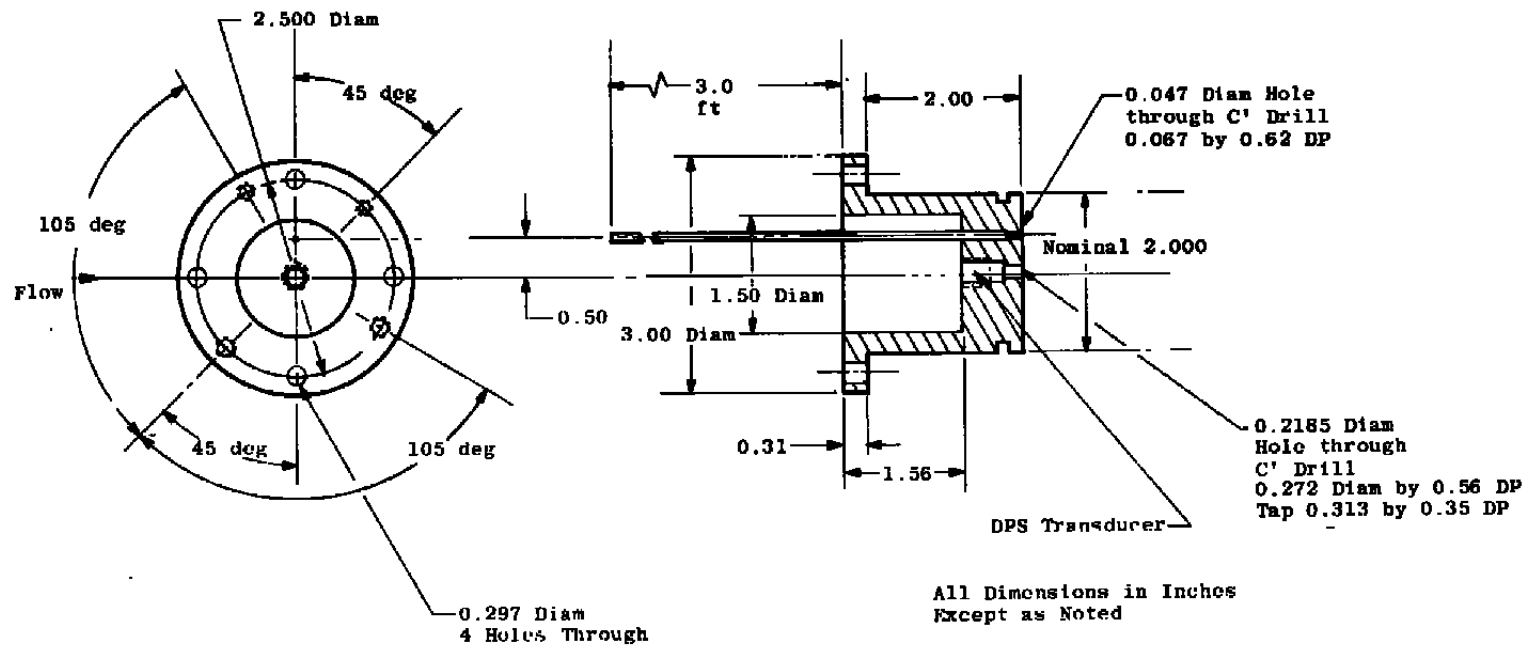


Figure 2. Typical installation of the tunnel wall flush-mounted dynamic pressure sensors.

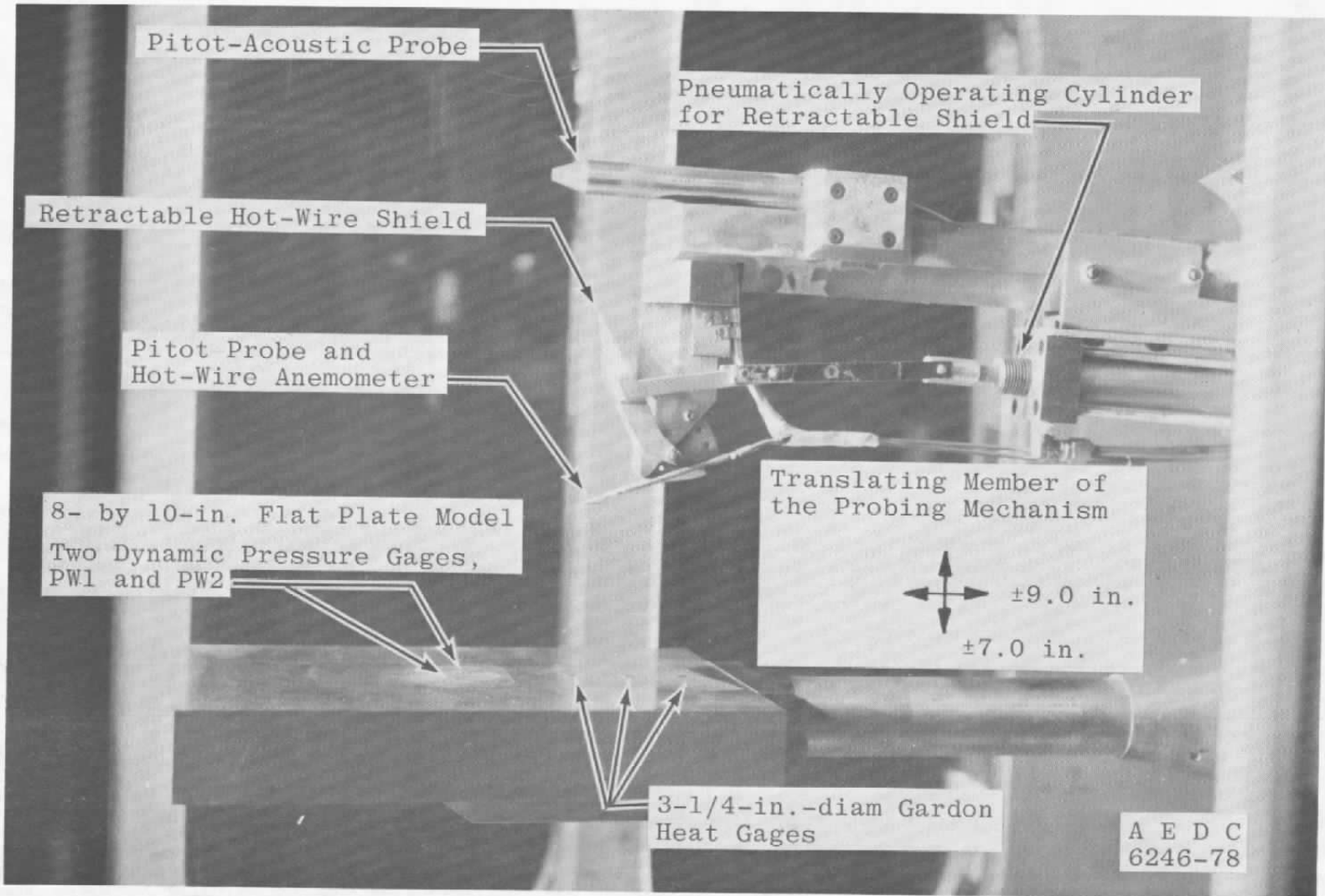


Figure 3. Tunnel A flat plate installation (FY78).

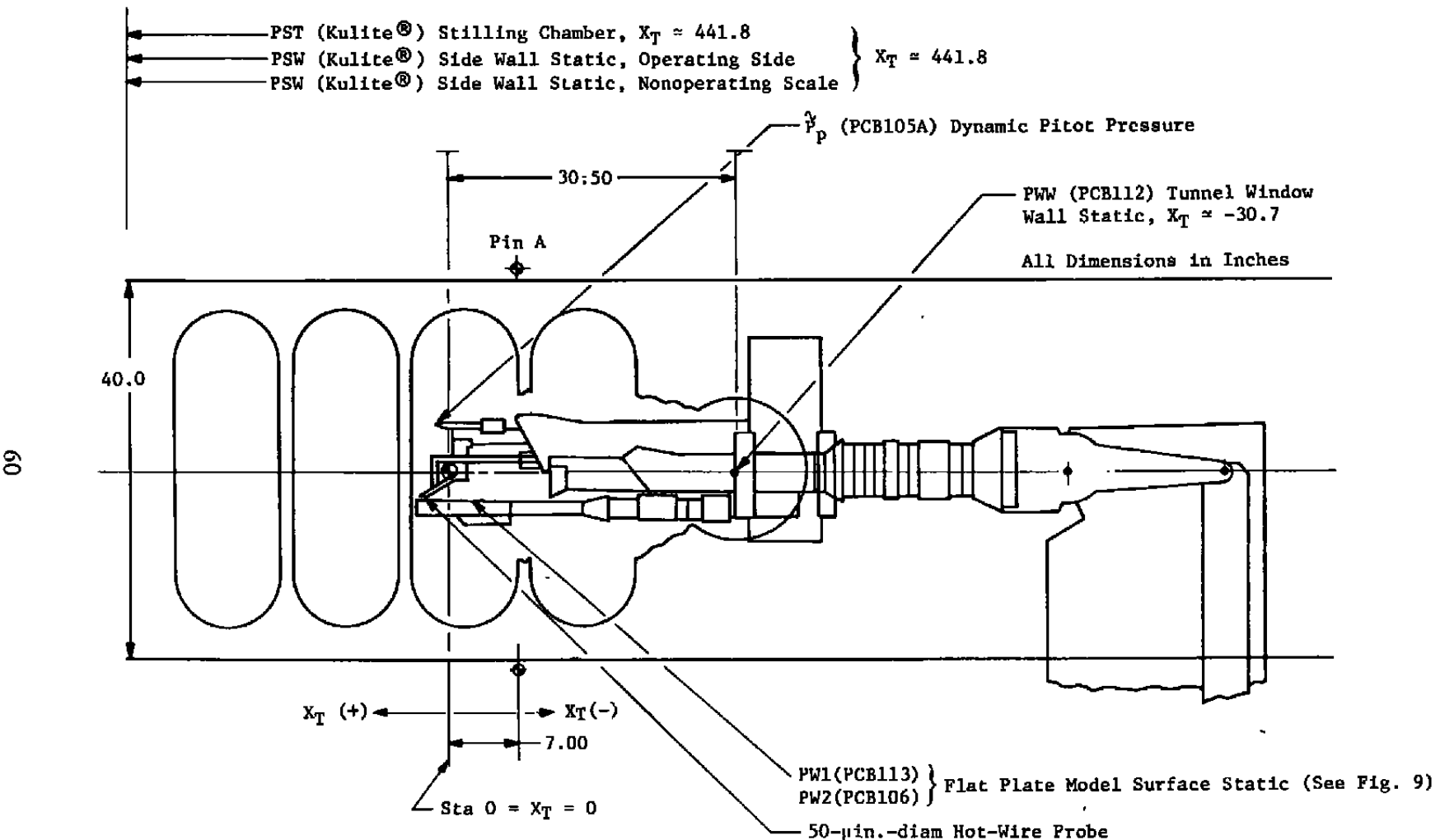


Figure 4. Tunnel A installation with nominal locations of the dynamic pressure sensors (transducers).

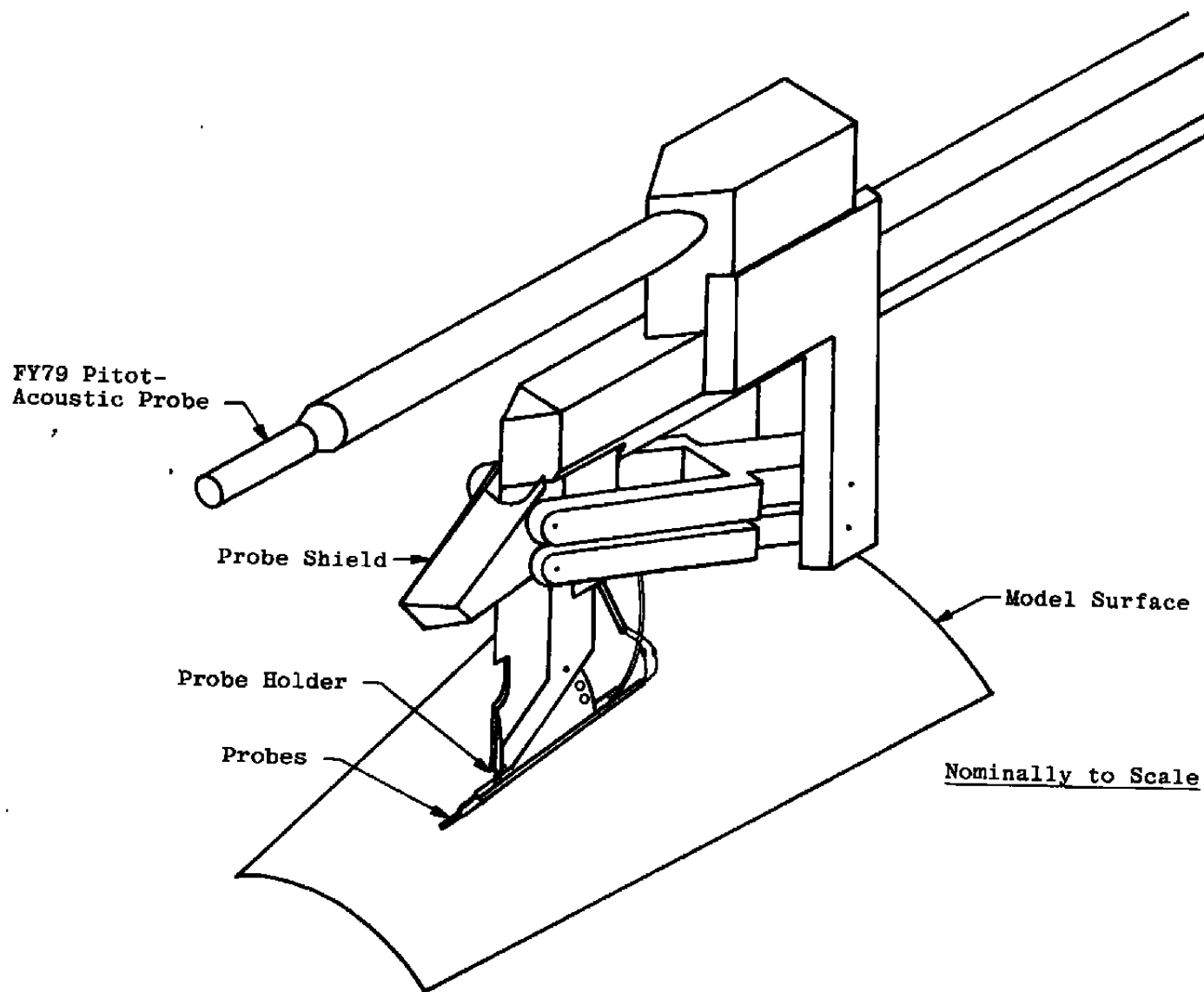


Figure 5. Tunnel A flow-field survey mechanism (FY79).

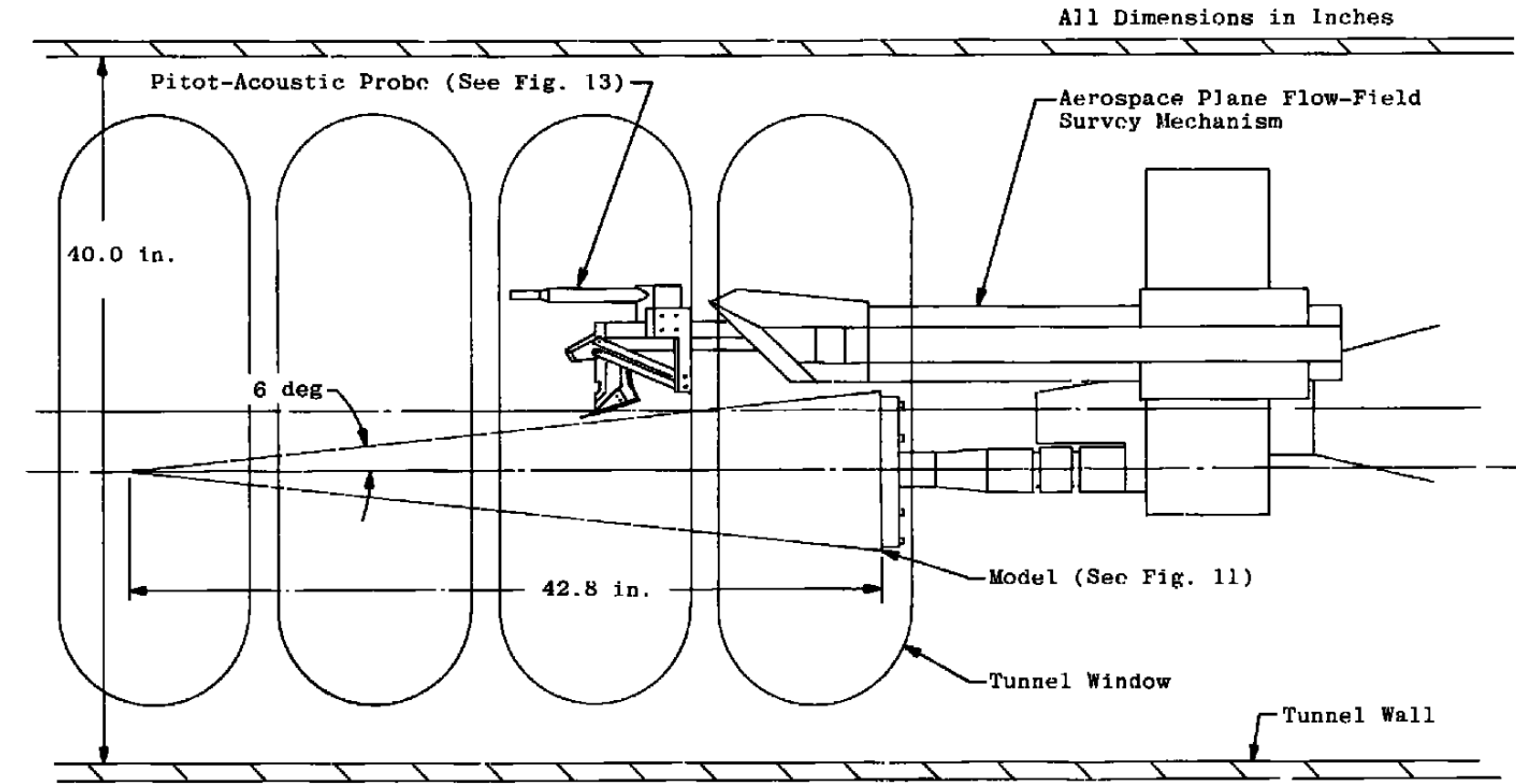
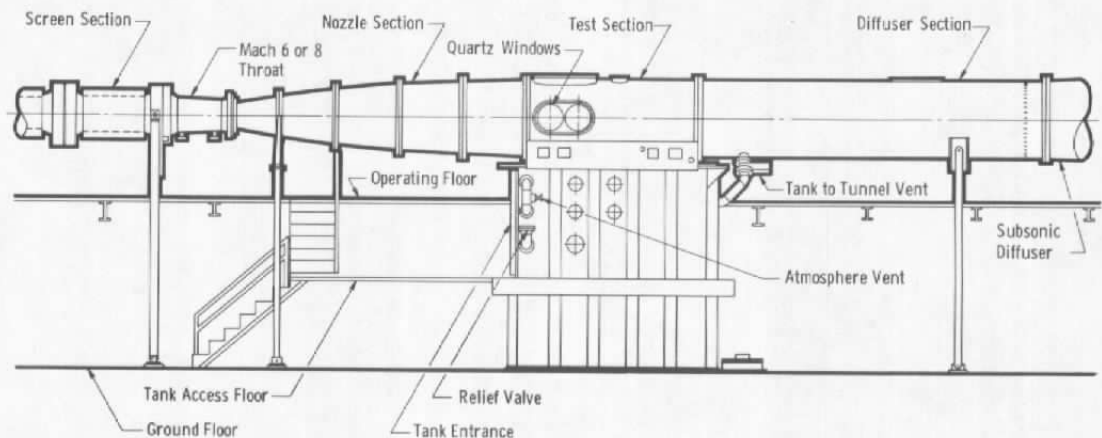
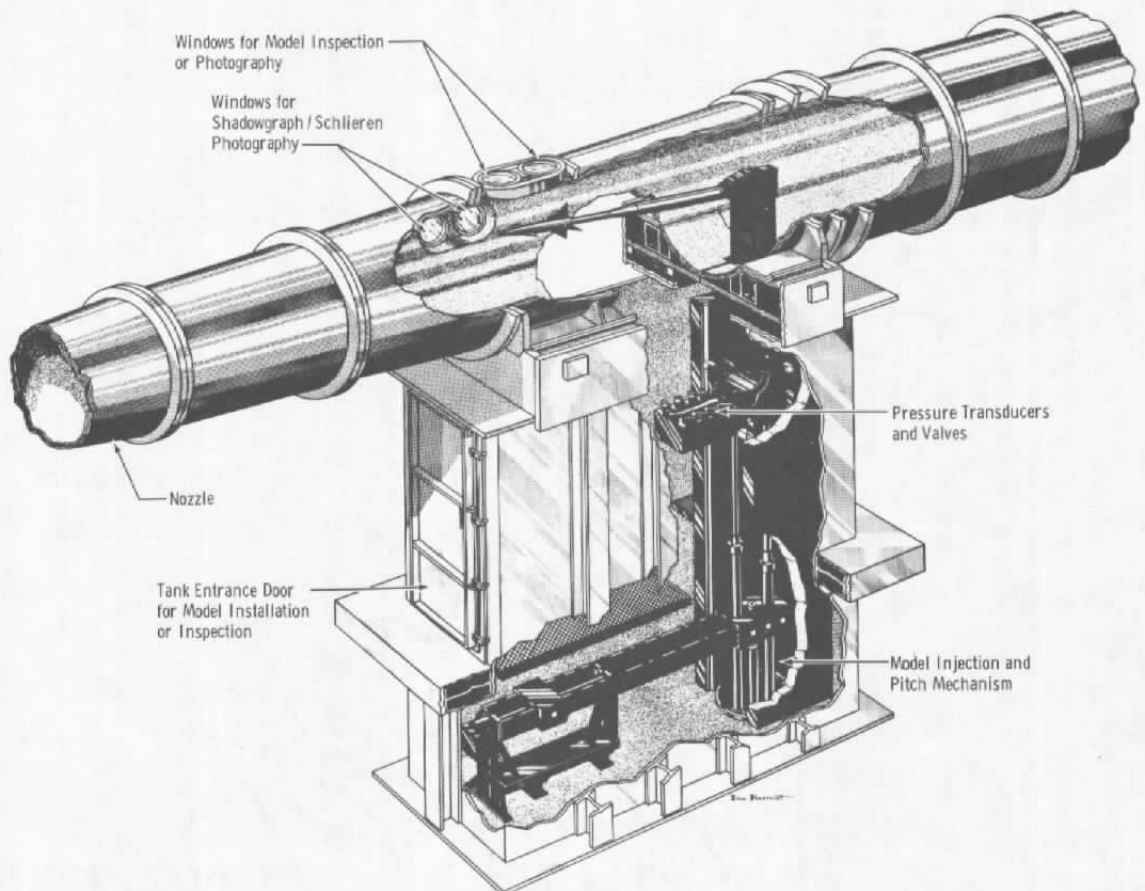


Figure 6. Test installation in Tunnel A (FY79).

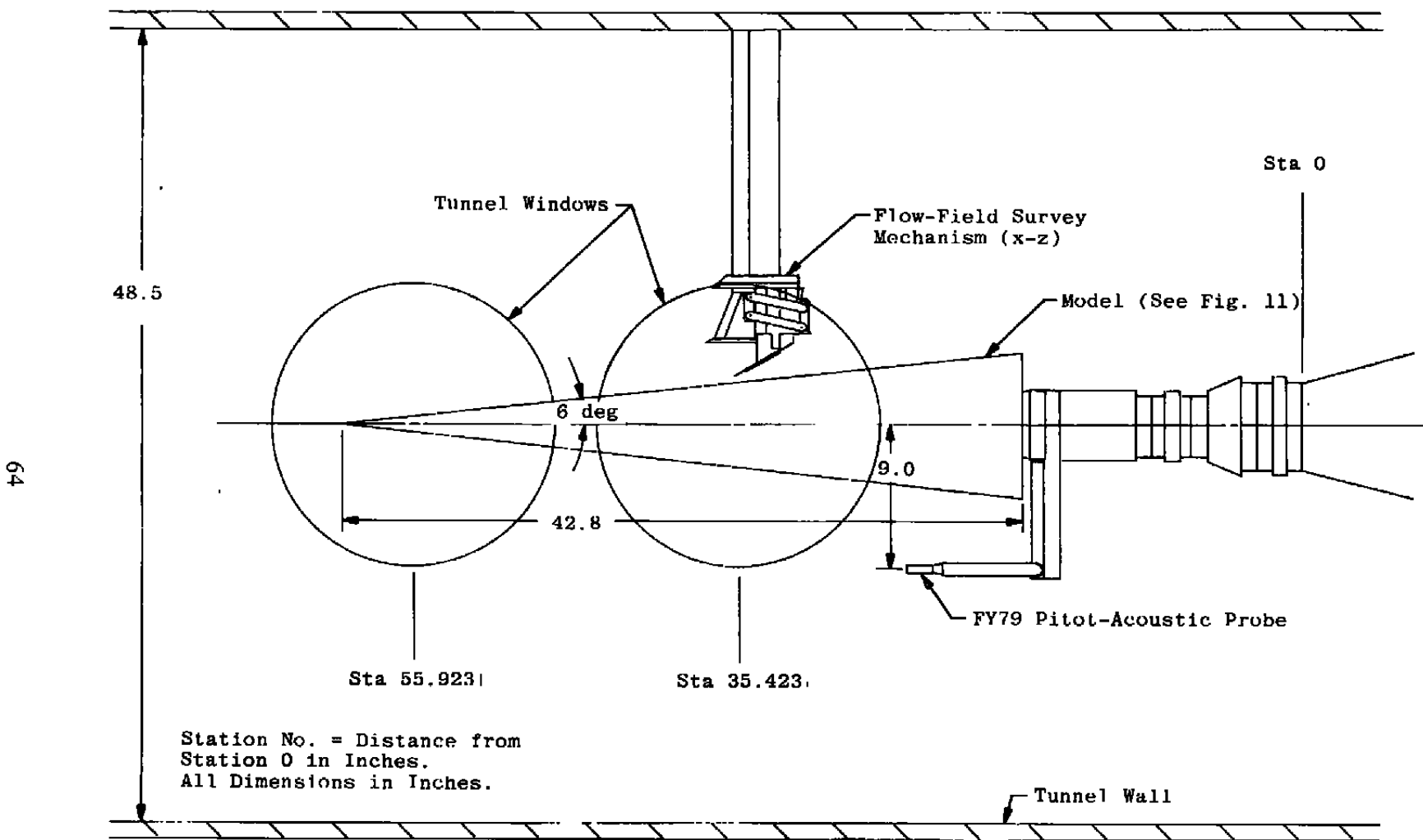


a. Tunnel assembly

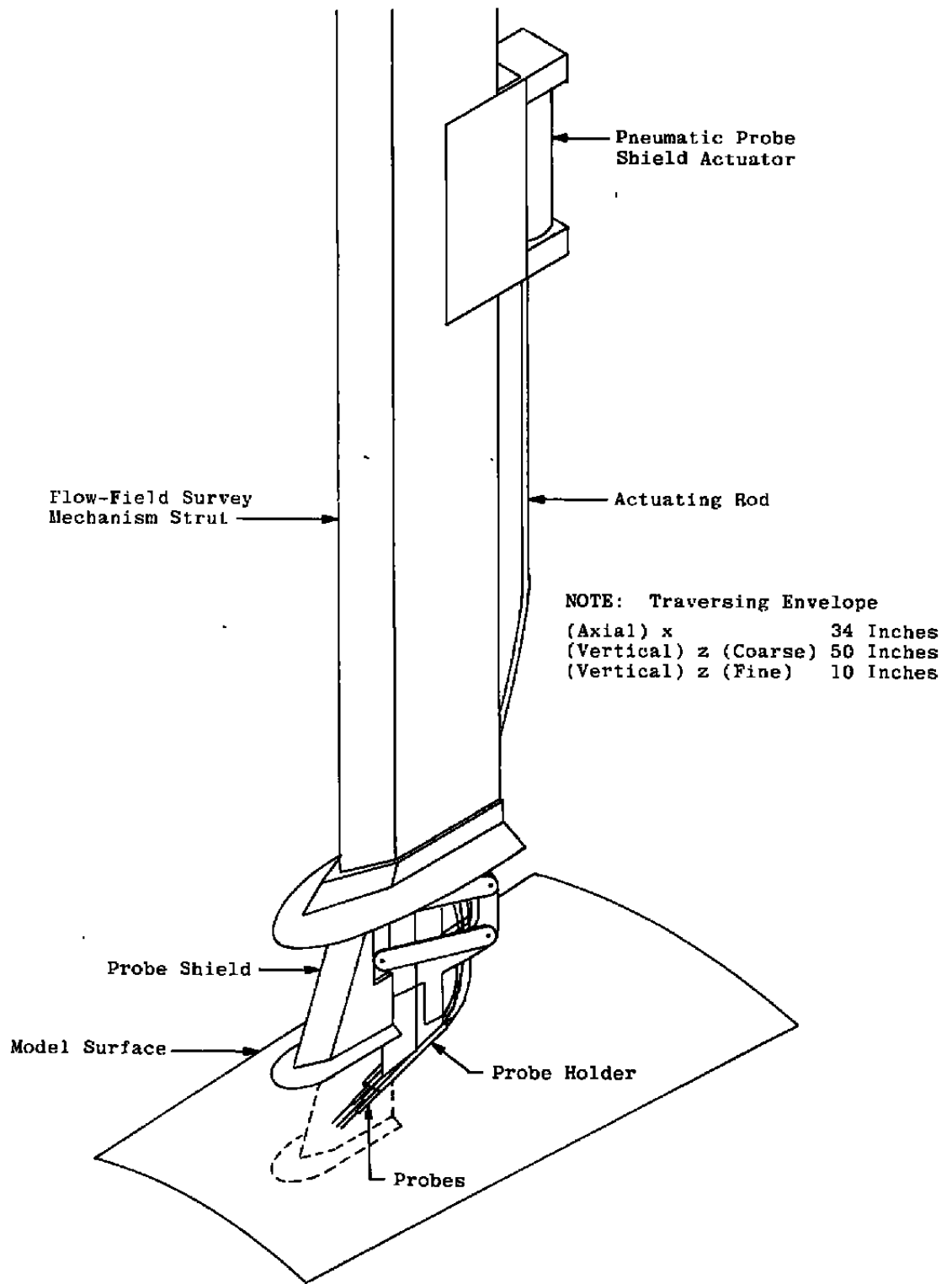


b. Tunnel test section

Figure 7. Tunnel B.



a. Installation sketch  
**Figure 8.** Test installation in Tunnel B.



b. Details of the x-z flow-field survey mechanism  
Figure 8. Concluded.

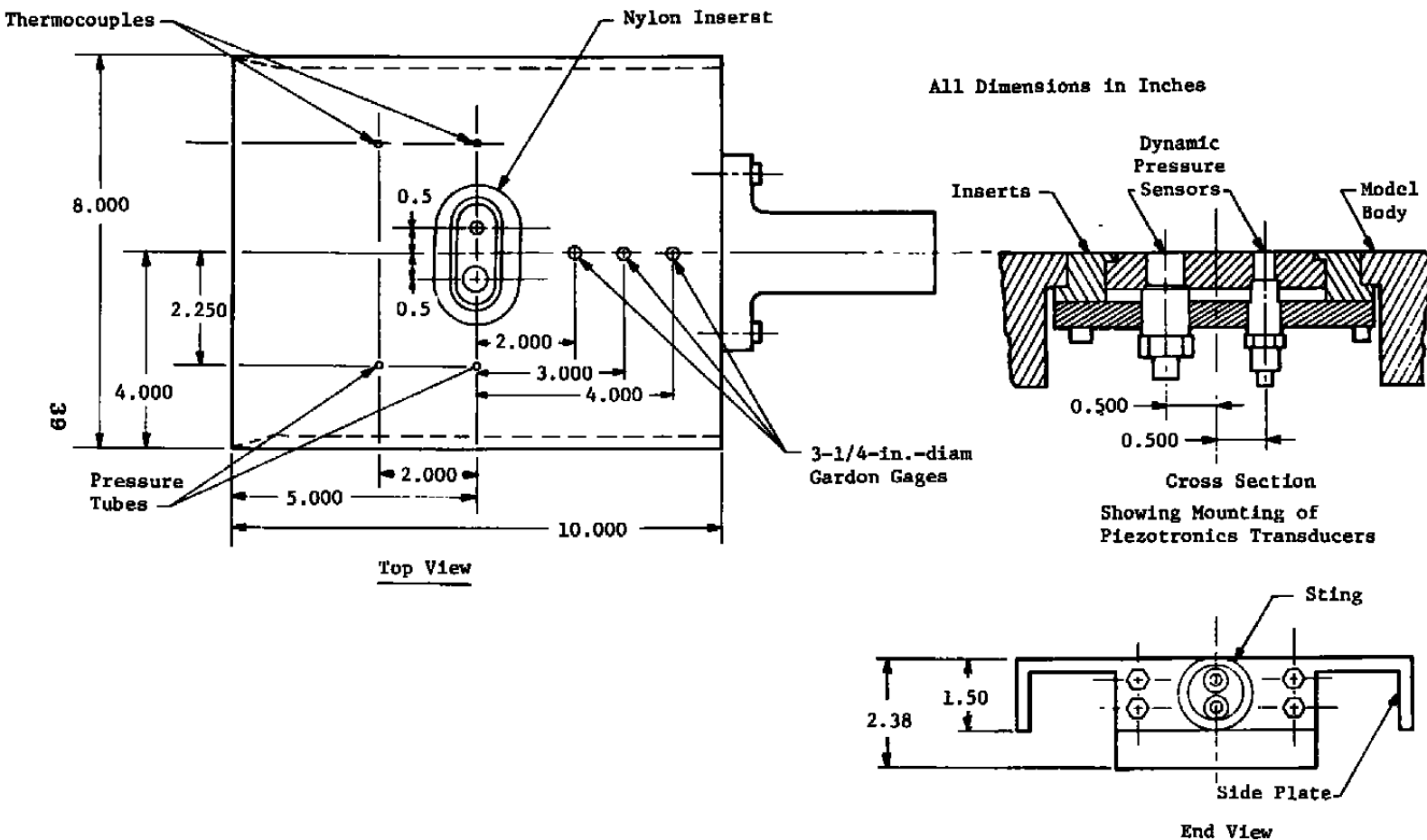


Figure 9. Flat plate model for dynamic pressure sensor measurement.

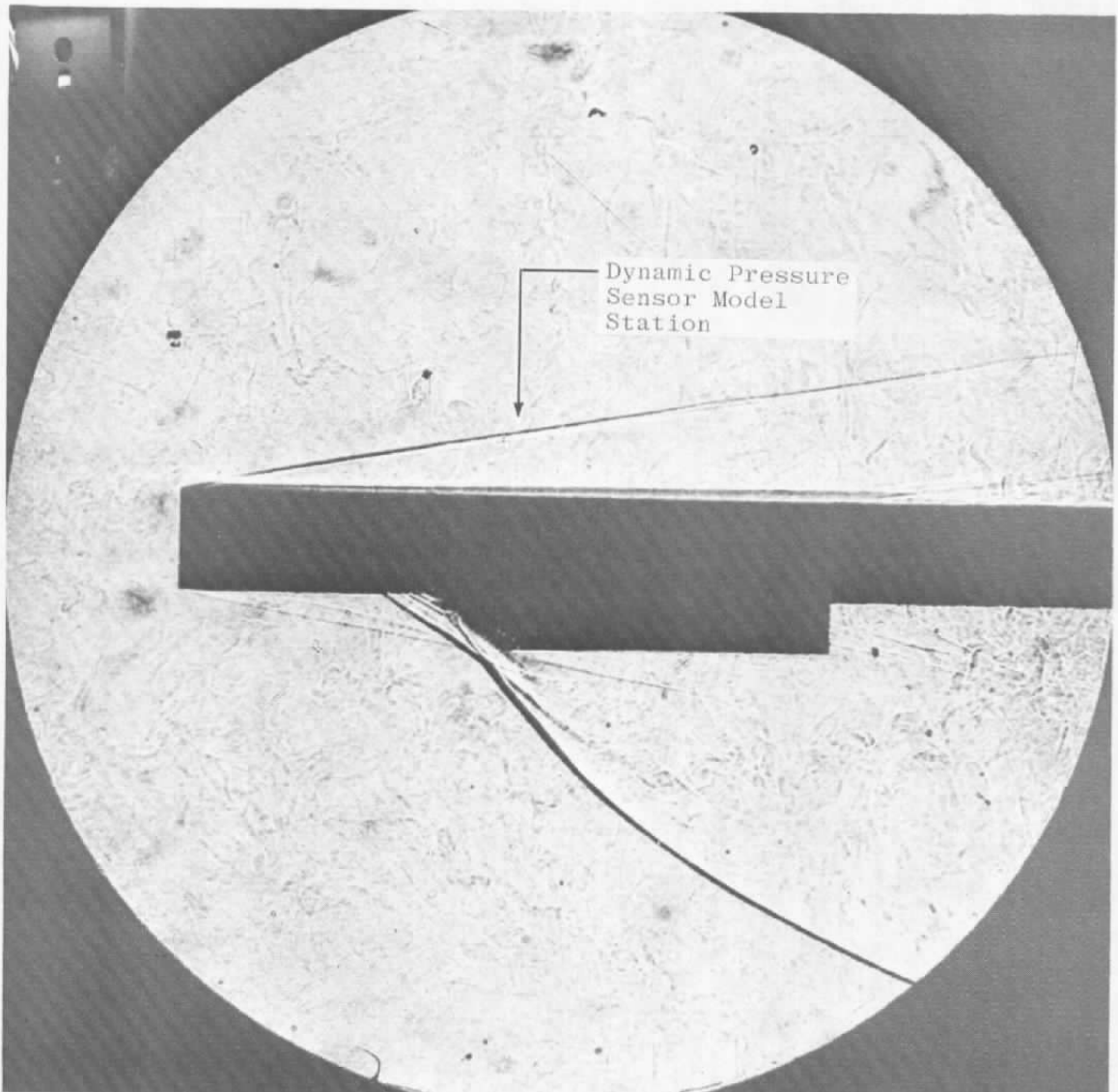
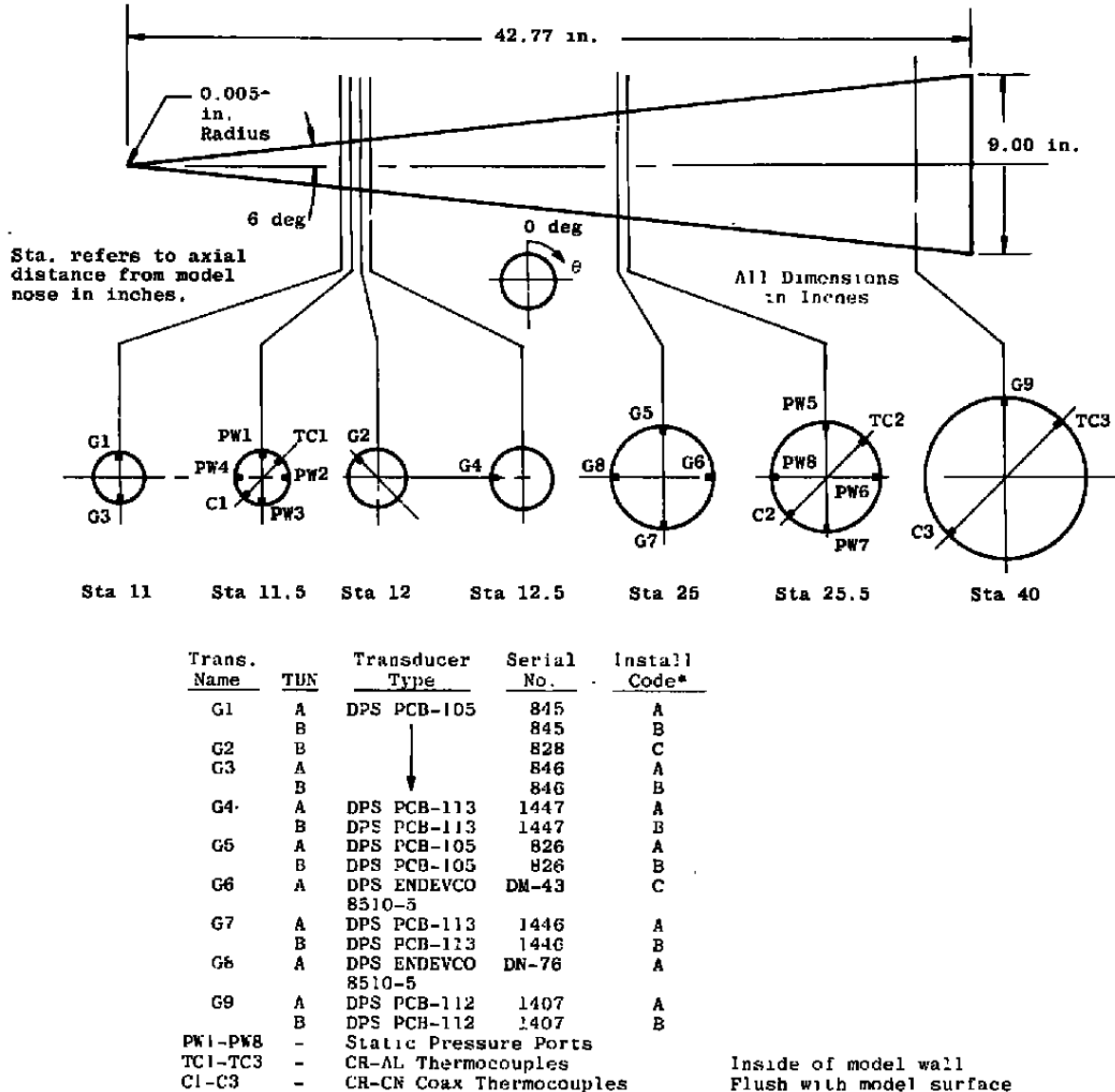


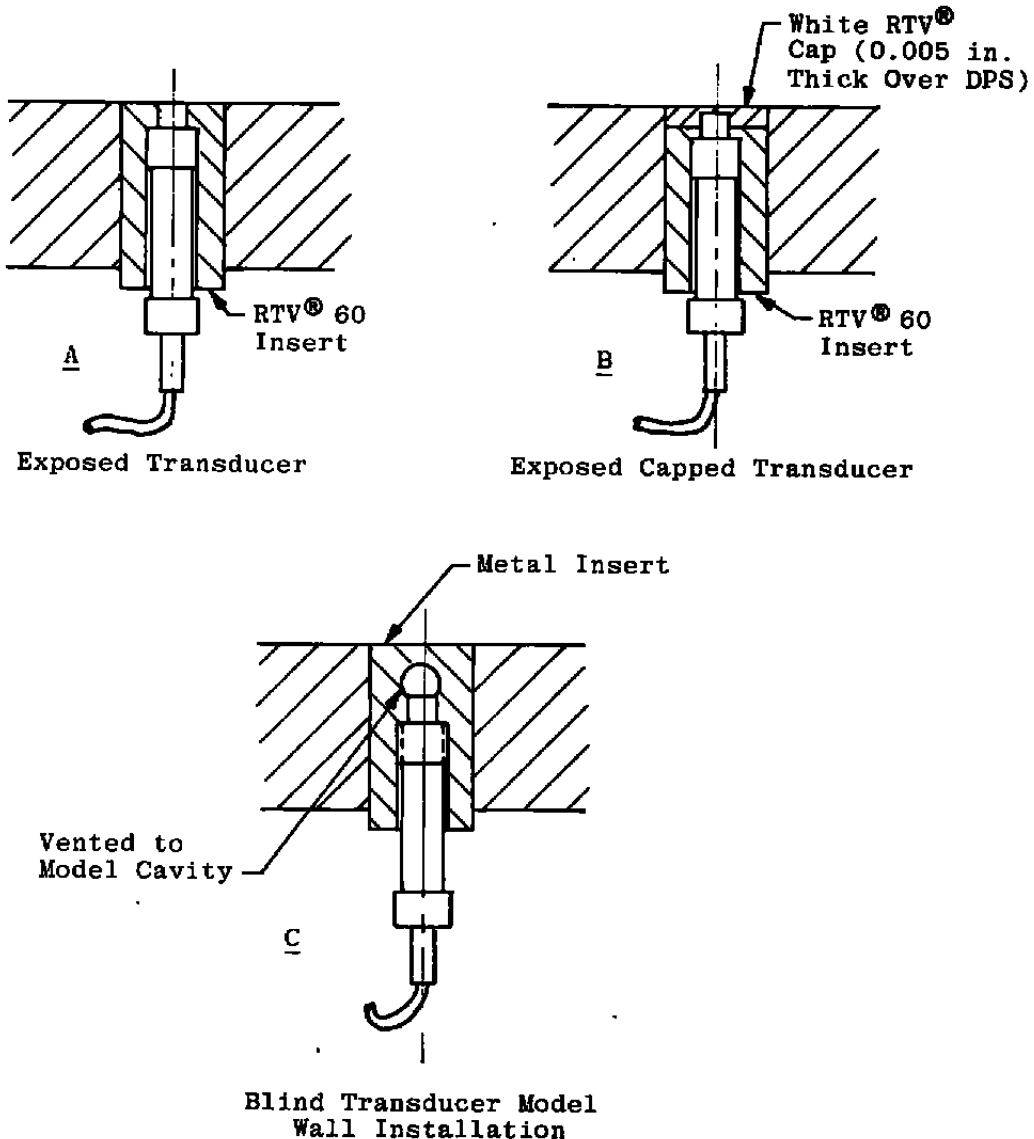
Figure 10. Flat plate installation in Tunnel B, typical shadowgram at Mach number 8 and Reynolds number  $2 \times 10^6$  per feet.



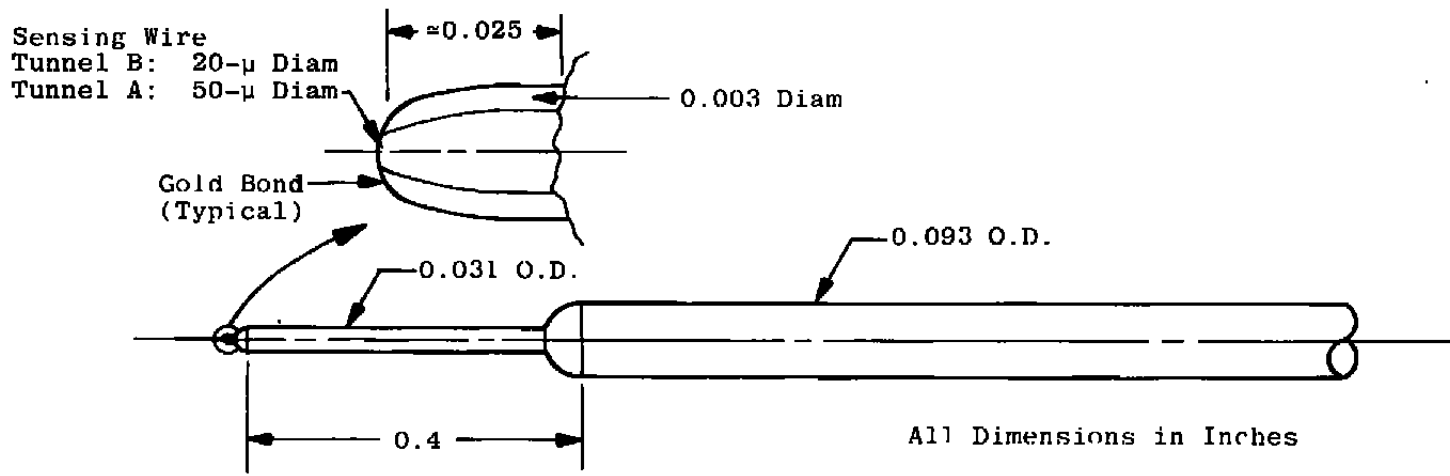
\*Next page.

## a. Instrumentation locations

Figure 11. Model details, 6-deg sharp nose cone.

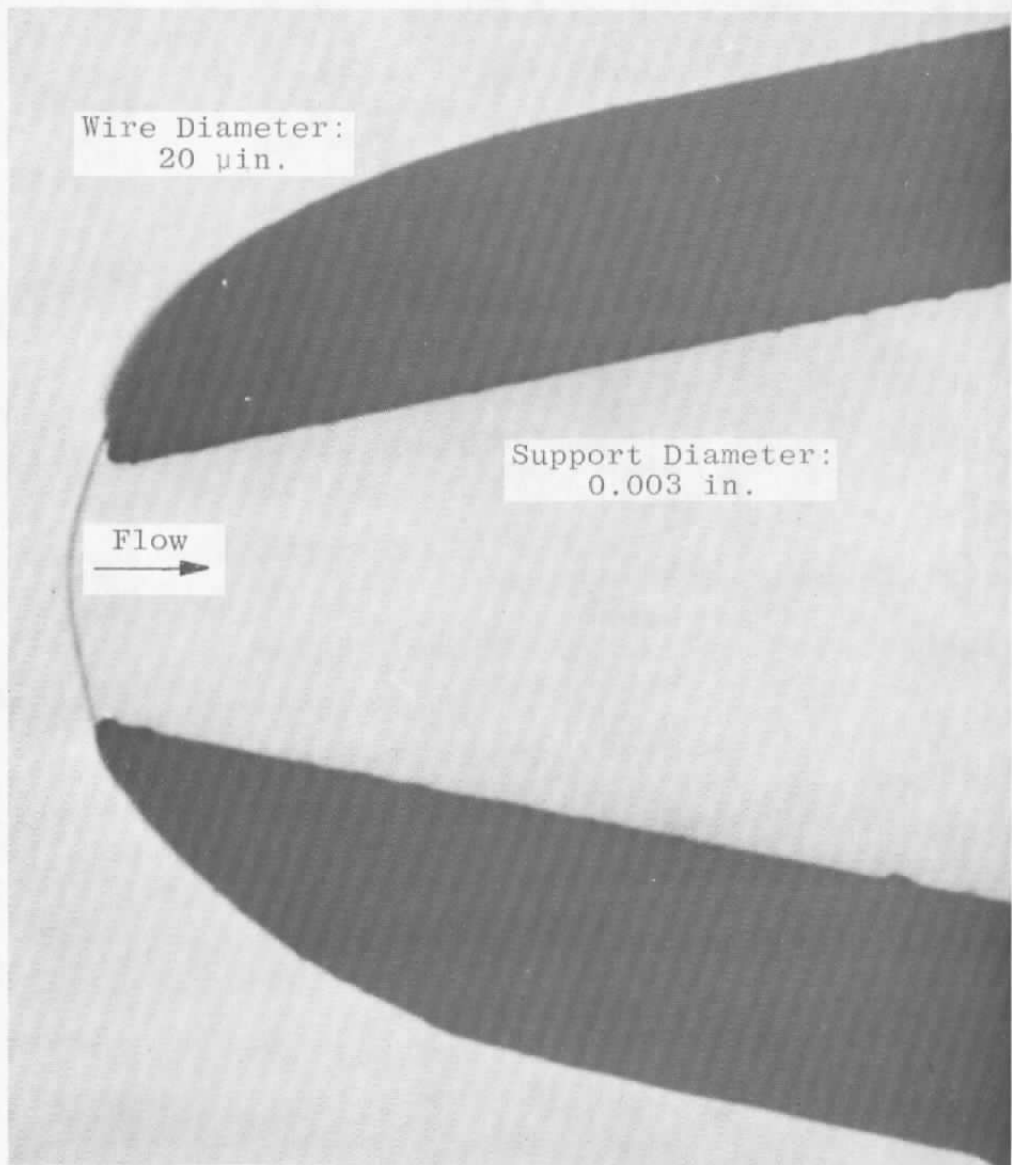


**b. Installation codes**  
**Figure 11. Concluded.**

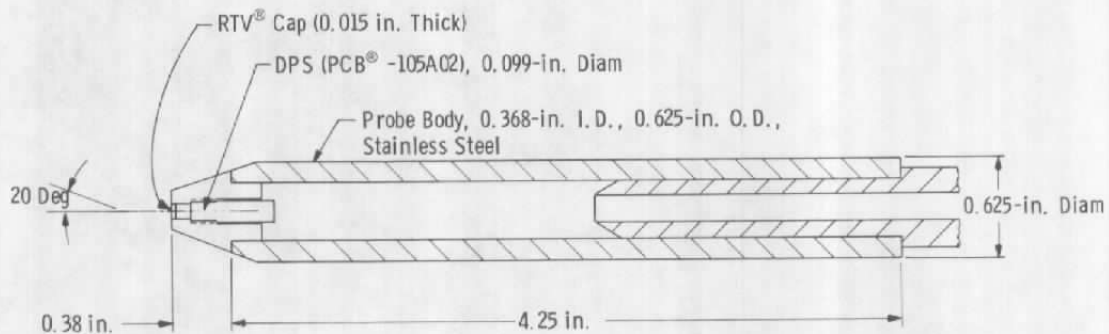


a. Details

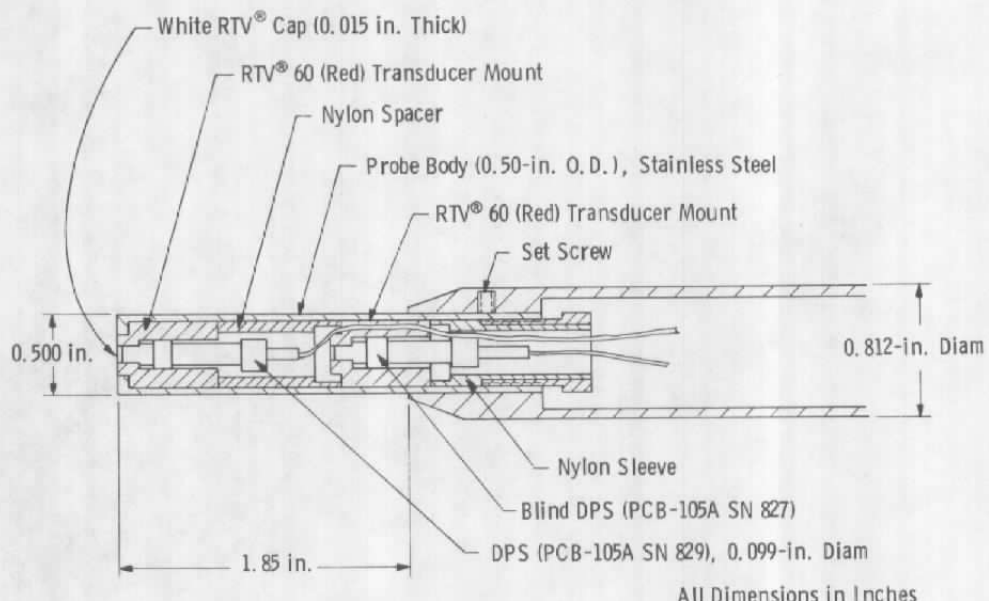
Figure 12. Hot-wire anemometer probe.



b. Silhouette photograph  
Figure 12. Concluded.

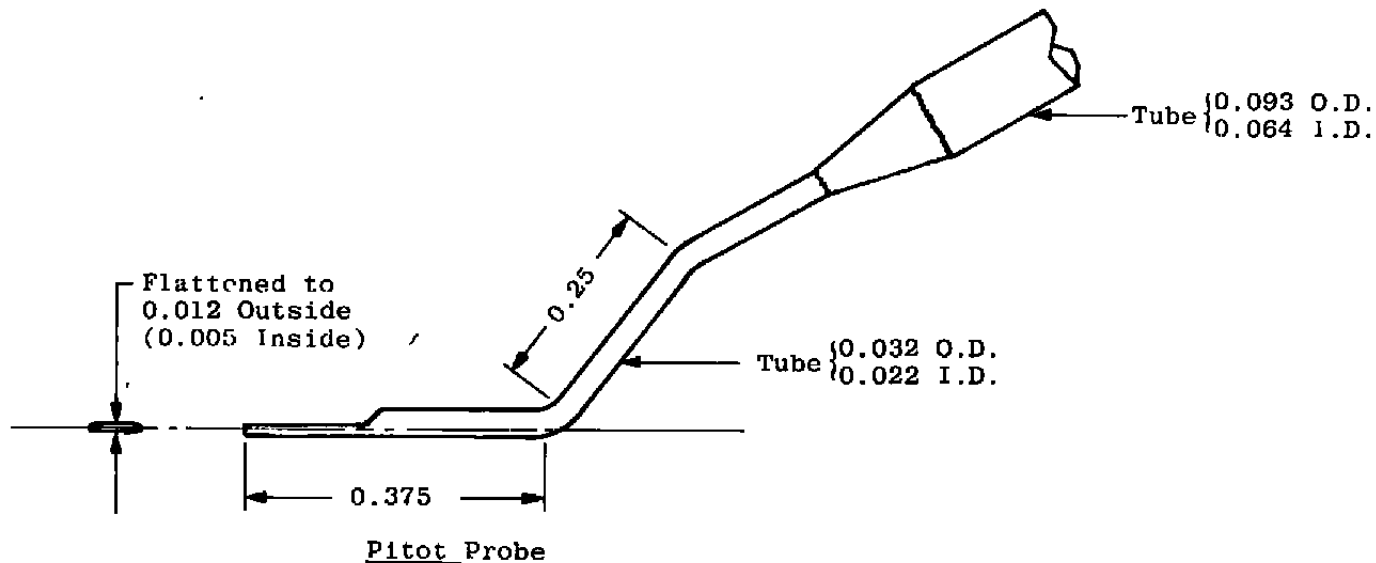


a. FY78 probe



b. FY79 probe

Figure 13. Dynamic pitot pressure probes.



All Dimensions in Inches

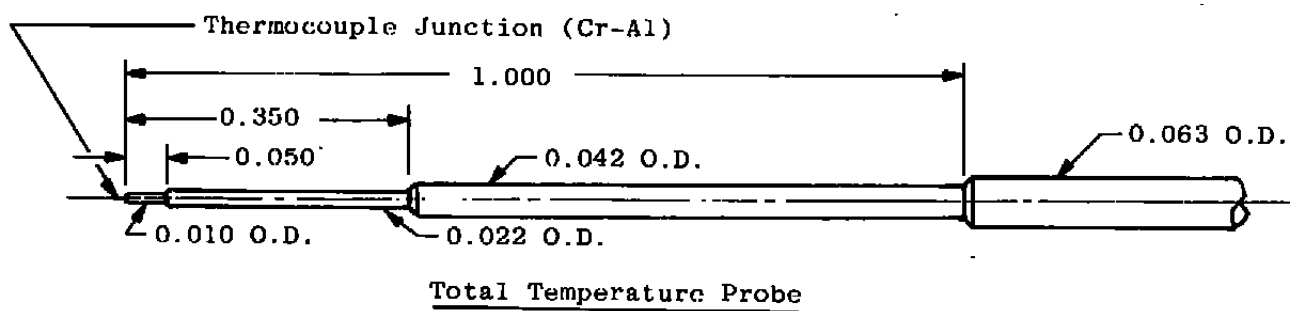


Figure 14. Mean flow-field survey probes.

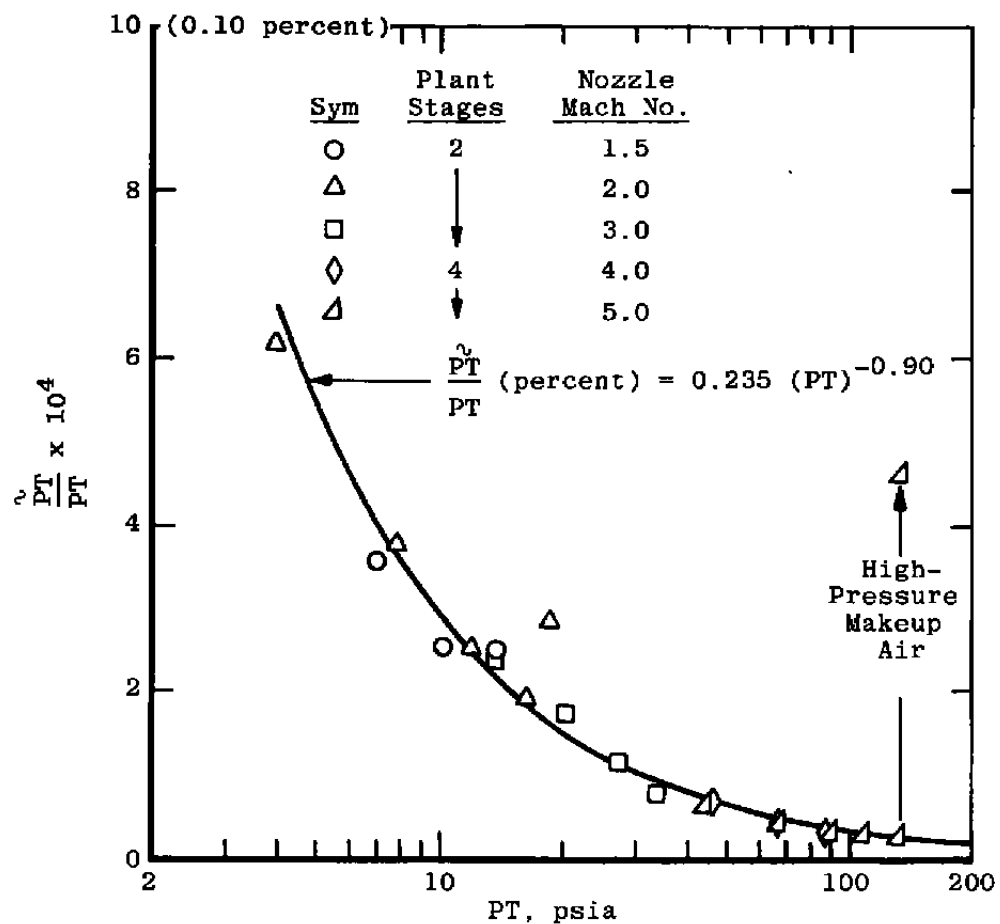
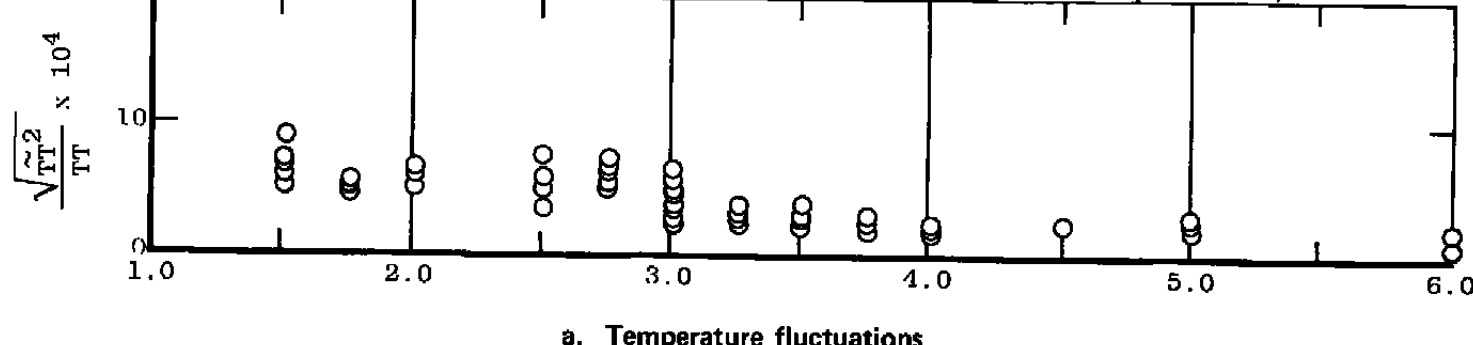


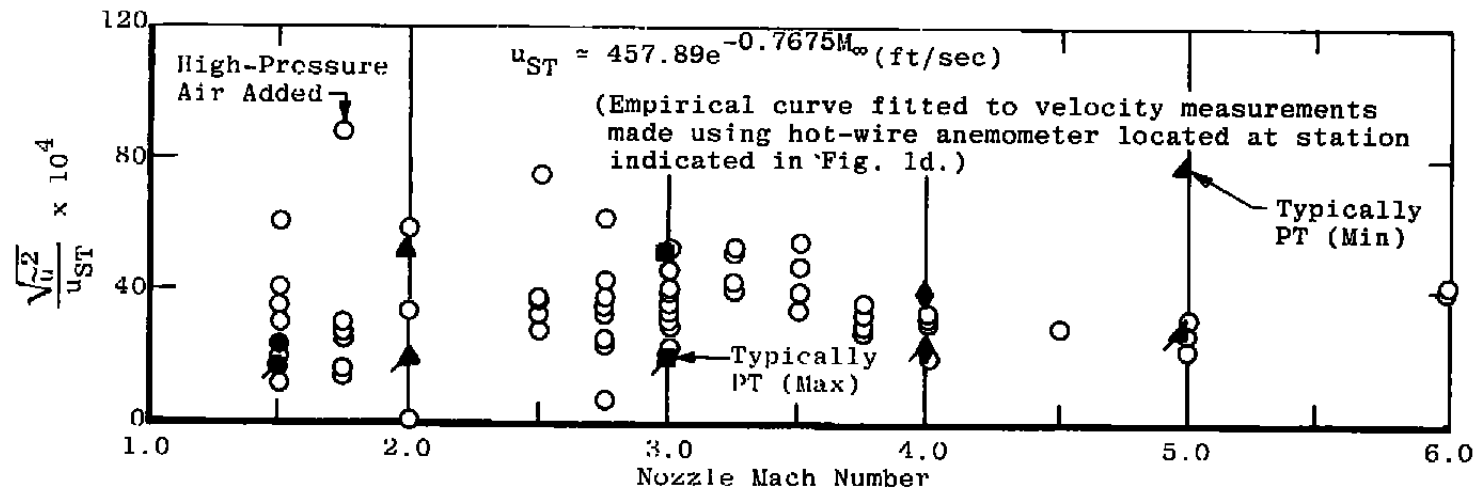
Figure 15. Tunnel A stilling chamber pressure fluctuations.

NOTE: Open Symbols ~ Nov. 1965 Hot Wire Data Analysis  
 Solid Symbols ~ FY 1978 Wall Static Pressure

$$\text{Fluctuation Analysis, } \sqrt{\frac{\langle \tilde{u}^2 \rangle}{u_{ST}^2}} = \sqrt{\frac{\langle \tilde{P}_T^2 \rangle}{P_T^2}} / \sqrt{\gamma M_{ST}}$$

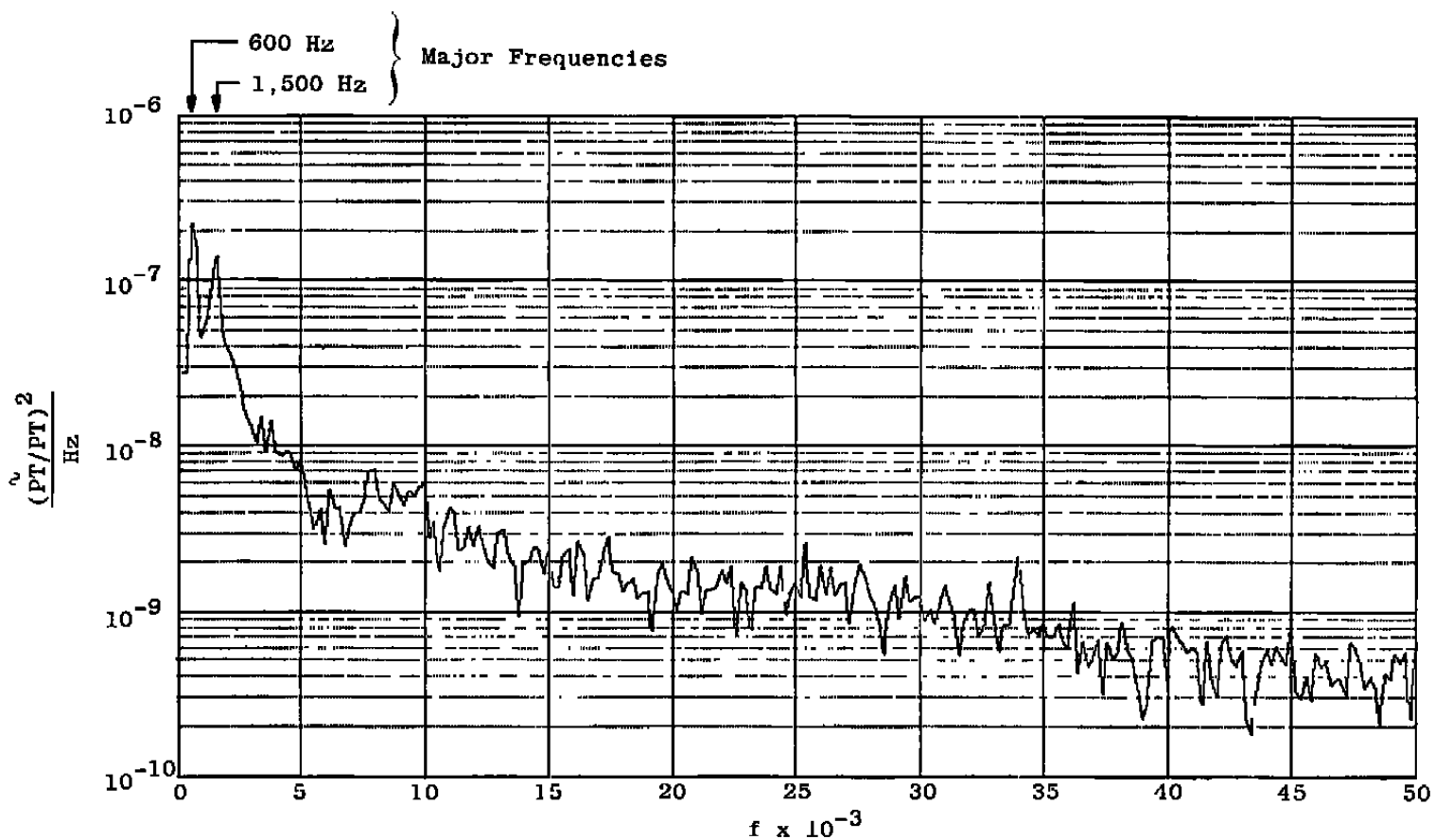


a. Temperature fluctuations

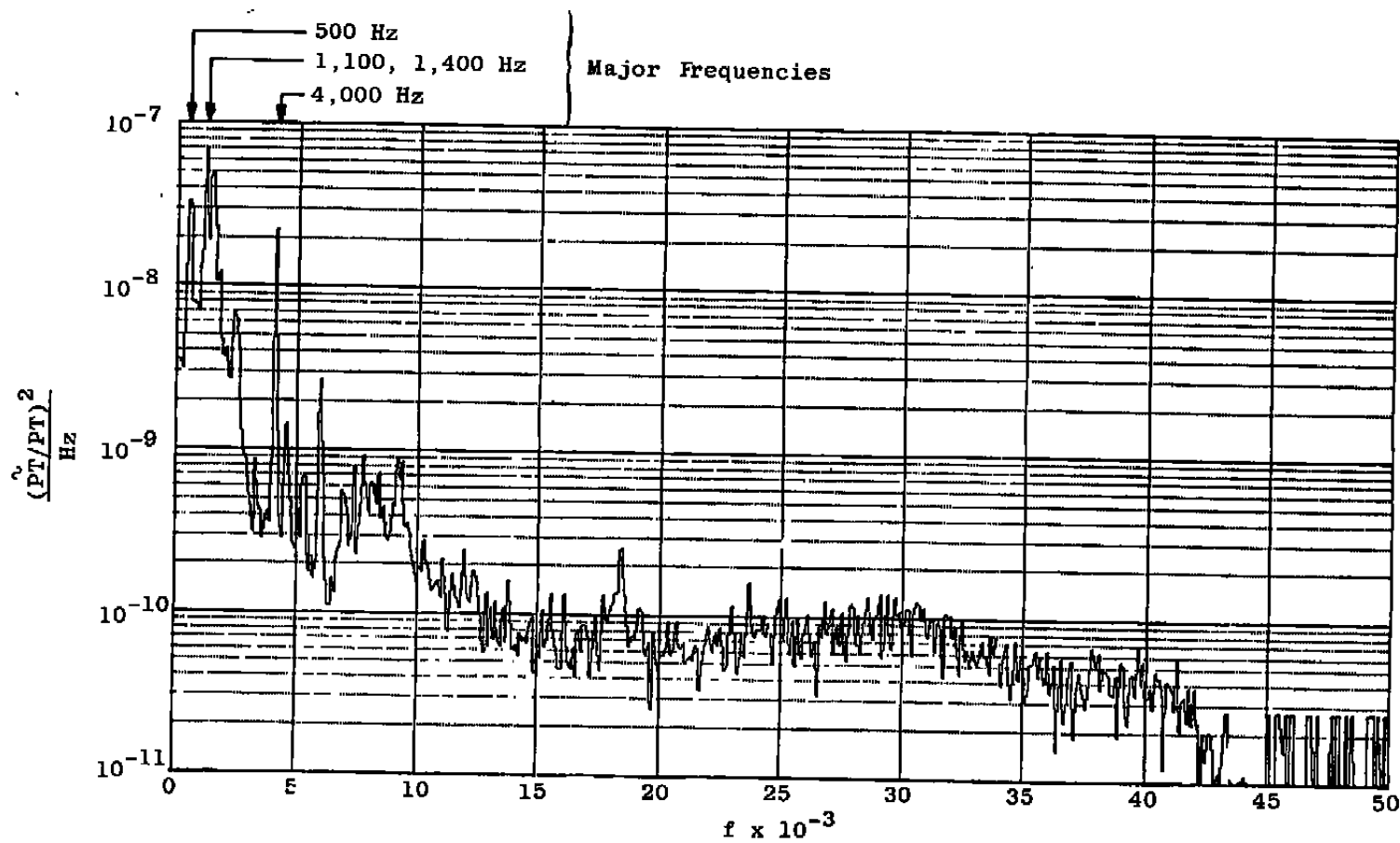


b. Velocity fluctuations

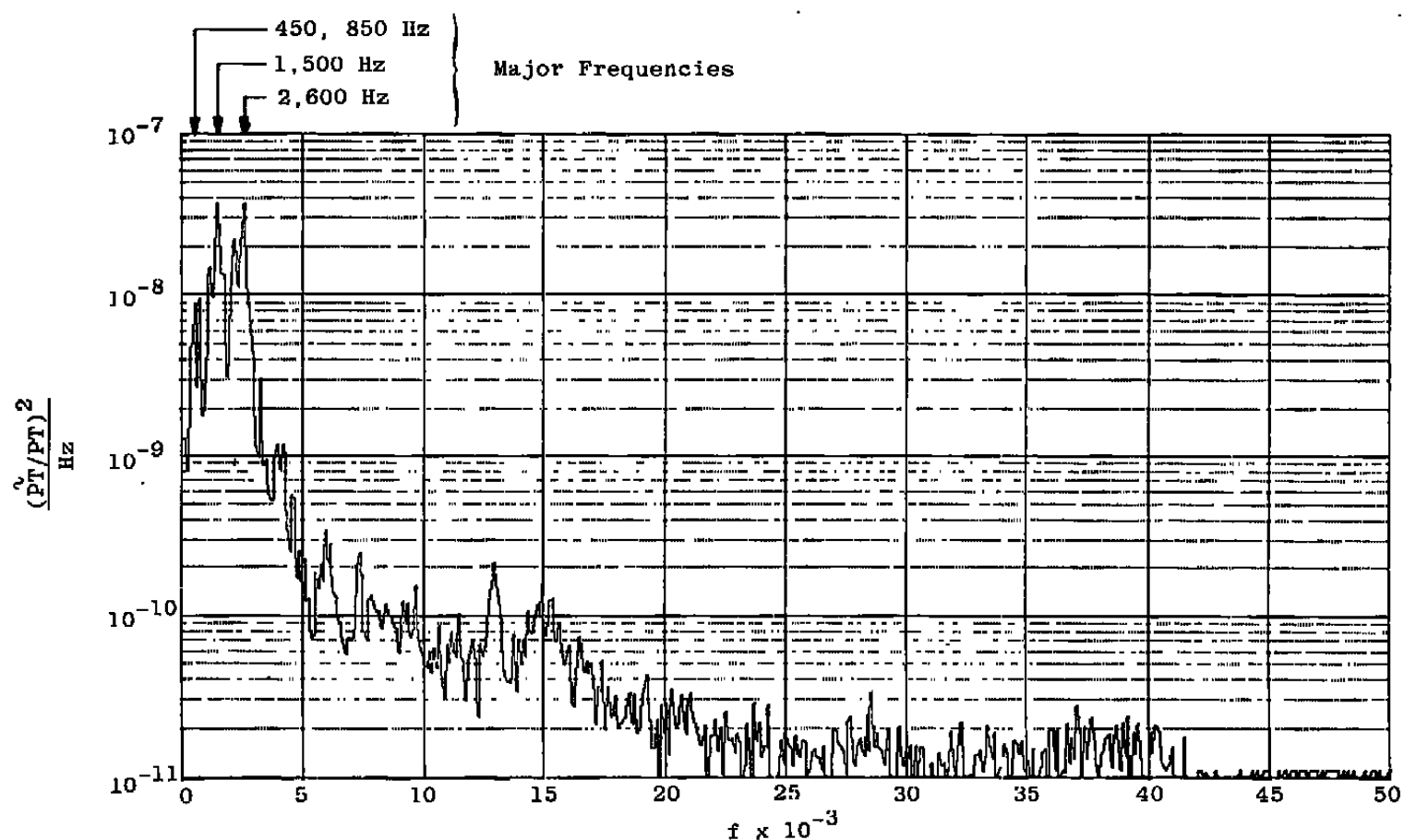
Figure 16. Summary of stilling chamber turbulence measurements in Tunnel A.



a.  $PT = 3.98 \text{ psia}$ ,  $\tilde{PT}/PT = 0.0617 \text{ percent}$ ,  $\Delta f = 200 \text{ Hz}$ , two-stage plant configuration  
Figure 17. Typical Tunnel A stilling chamber pressure fluctuation spectra.

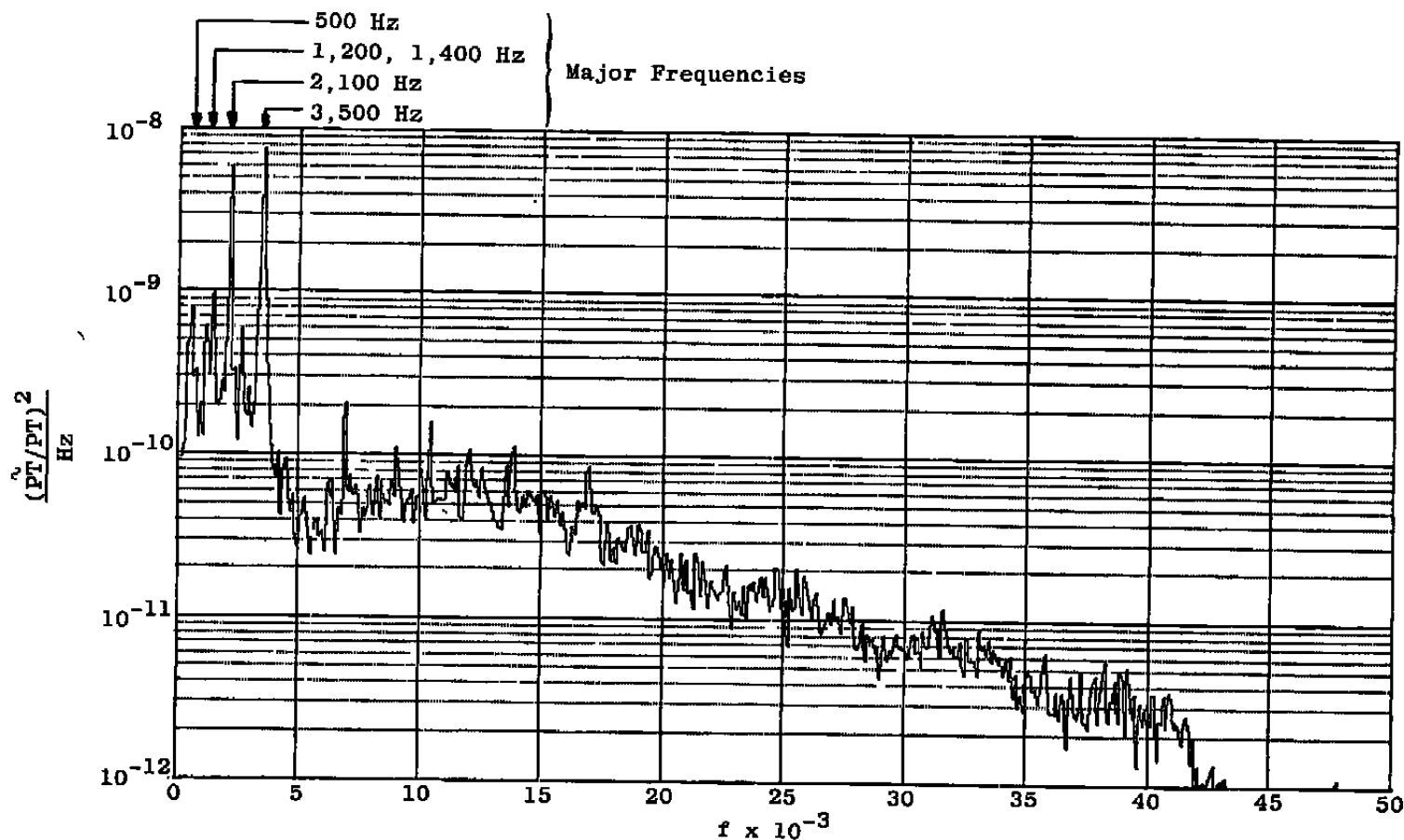


b.  $PT = 16.1$  psia,  $\tilde{PT}/PT = 0.014$  percent,  $\Delta f = 100$  Hz, two-stage plant configuration  
 Figure 17. Continued.



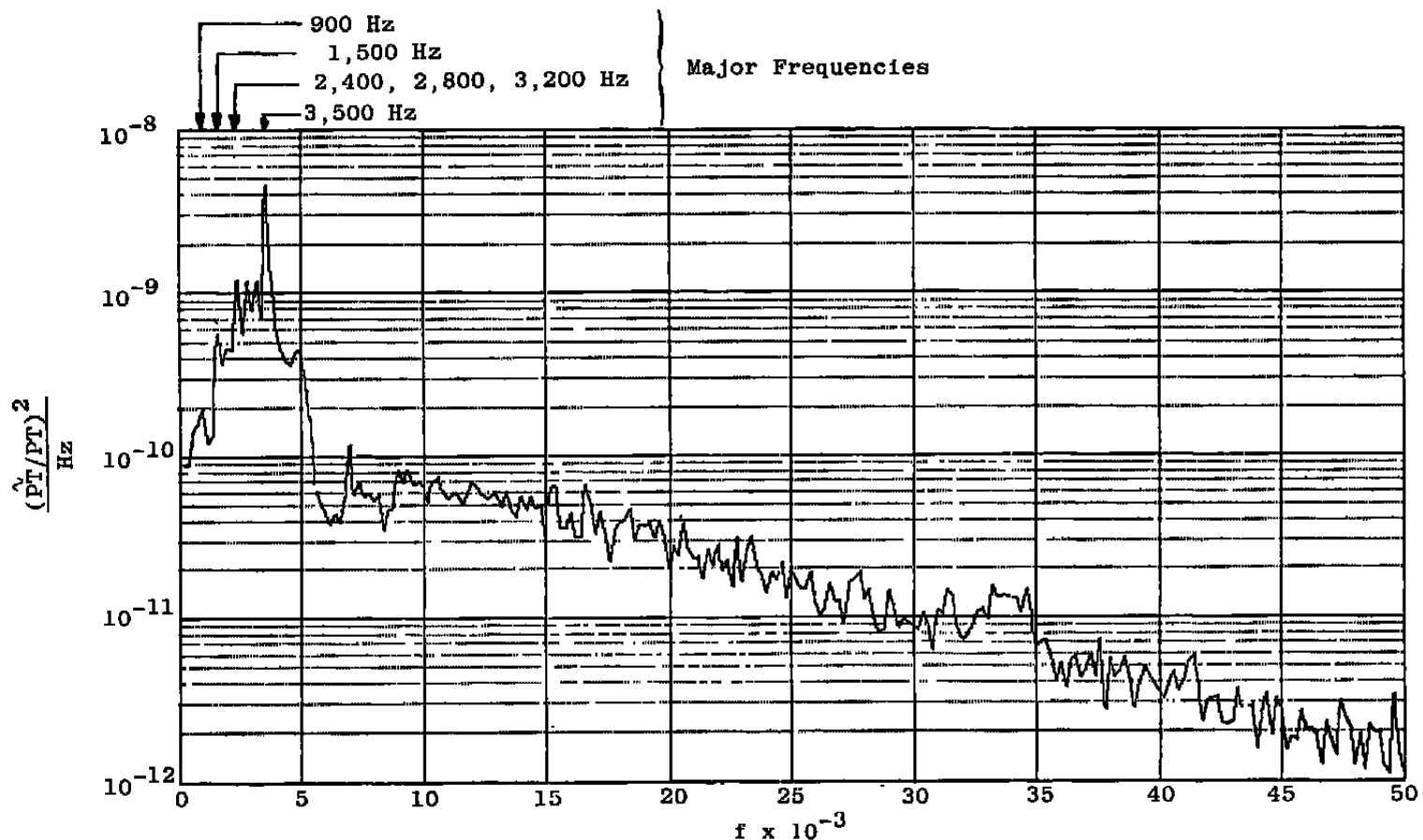
c.  $PT = 27.0$  psia,  $\tilde{P}_T/PT = 0.011$  percent,  $\Delta f = 100$  Hz, three-stage plant configuration.

Figure 17. Continued.

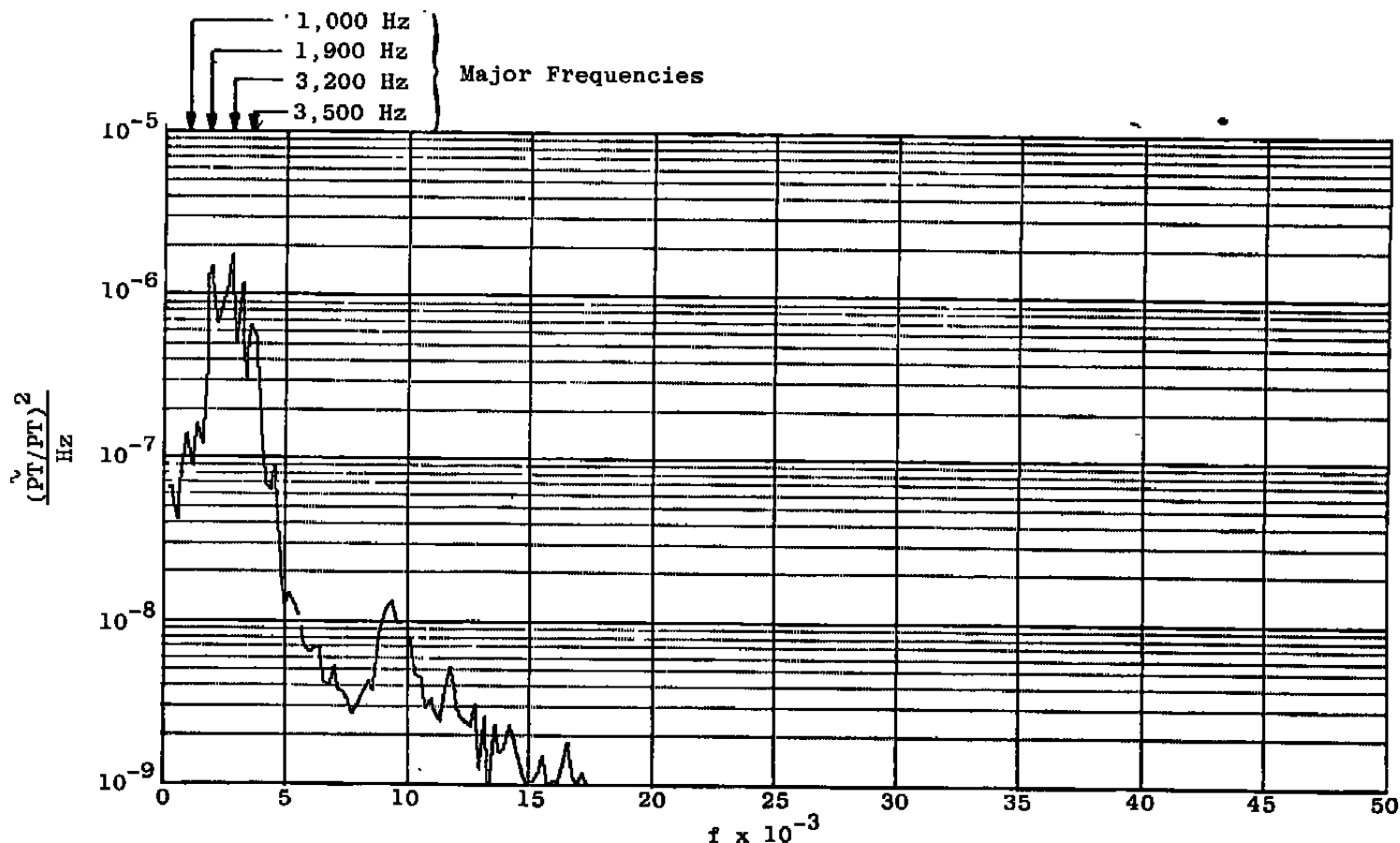


d.  $PT = 91.3 \text{ psia}$ ,  $\tilde{PT}/PT = 0.0020 \text{ percent}$ ,  $\Delta f = 100 \text{ Hz}$ , four-stage plant configuration.

Figure 17. Continued.



e.  $PT = 137.2$  psia,  $\tilde{PT}/PT = 0.0028$  percent,  $\Delta f = 200$  Hz, four-stage plant configuration.  
Figure 17. Continued.



f.  $PT = 137.2$  psia (high-pressure makeup air added),  $\tilde{PT}/PT = 0.0462$  percent,  
 $\Delta f = 200$ , four-stage plant configuration.

Figure 17. Concluded.

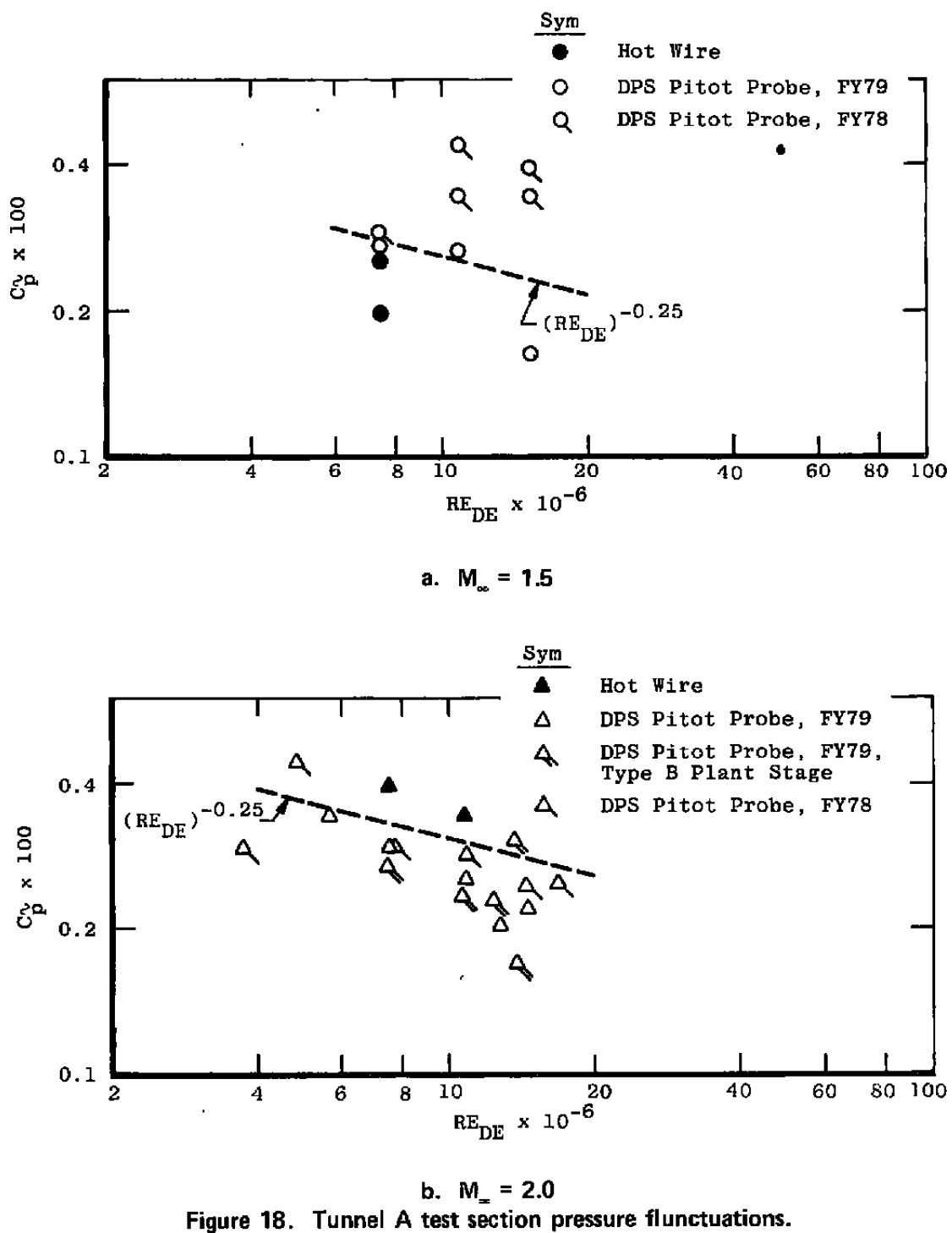


Figure 18. Tunnel A test section pressure fluctuations.

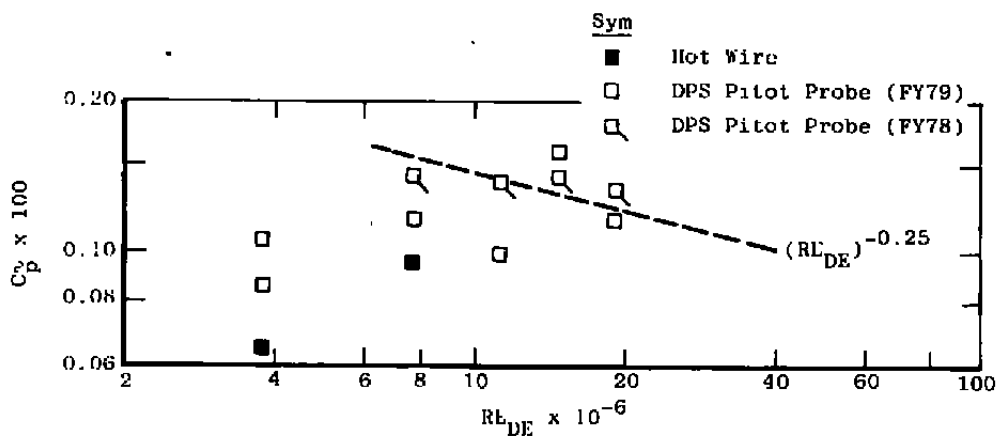
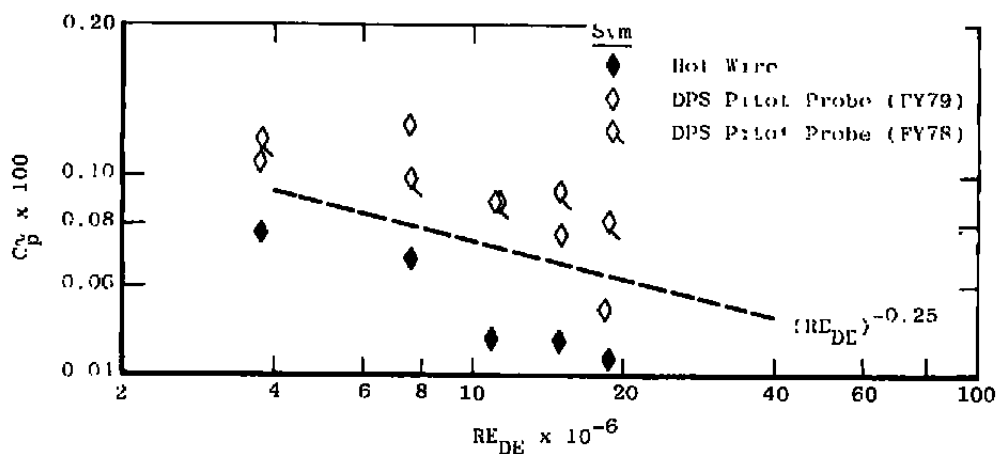
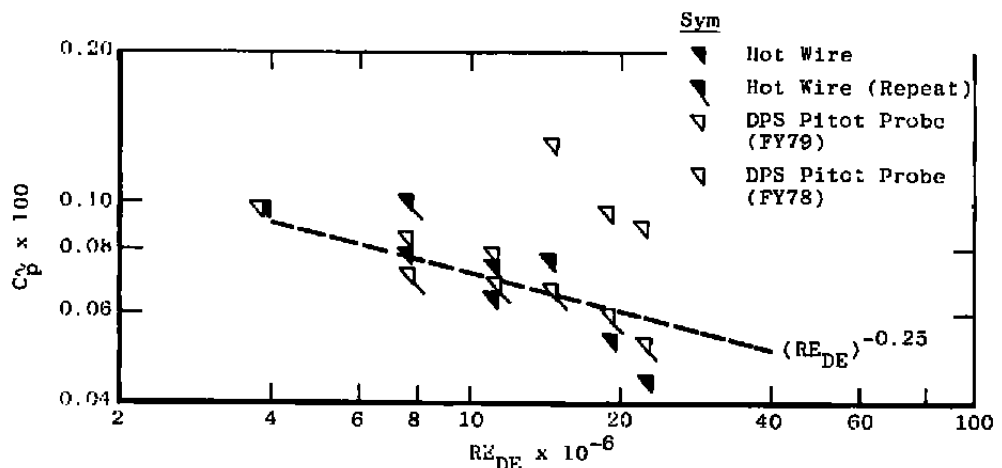
c.  $M_\infty = 3.0$ d.  $M_\infty = 4.0$ e.  $M_\infty = 5.0$ 

Figure 18. Concluded.

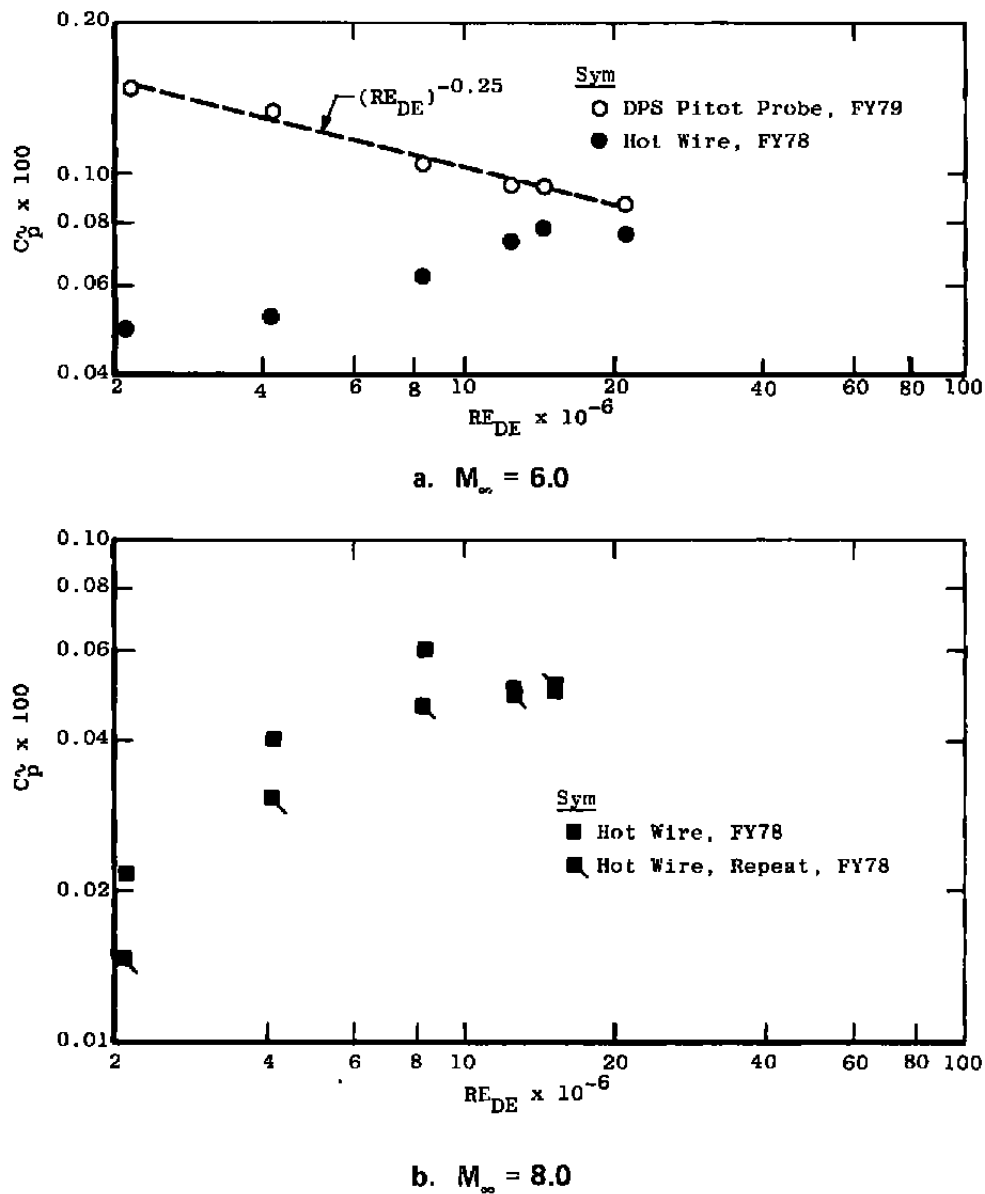


Figure 19. Tunnel B test section pressure fluctuations.

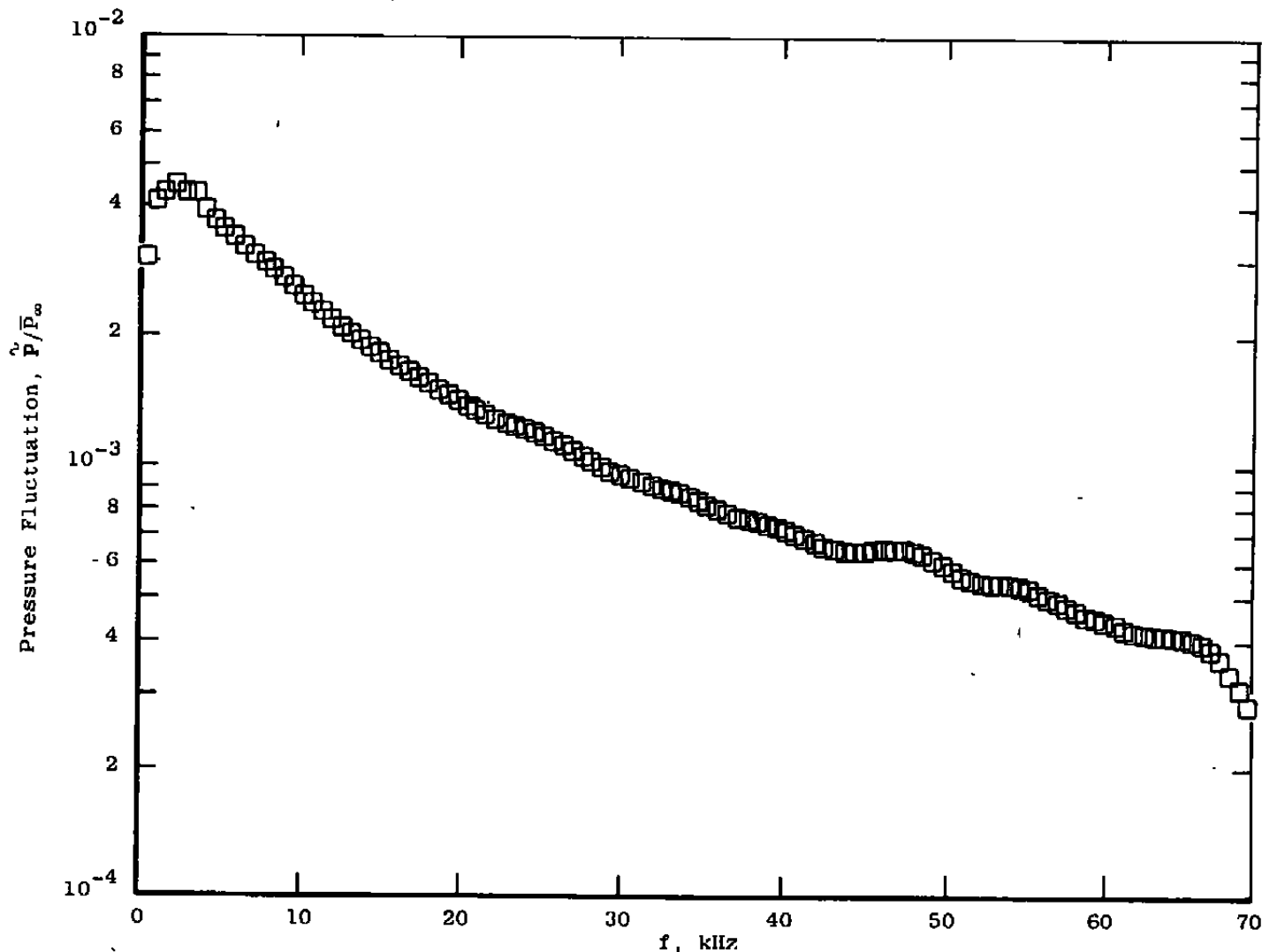


Figure 20. Spectrum of pressure fluctuations inferred from hot-wire measurements,  
 $M_\infty = 6$ ,  $RE_\infty = 3 \times 10^6$  per foot.

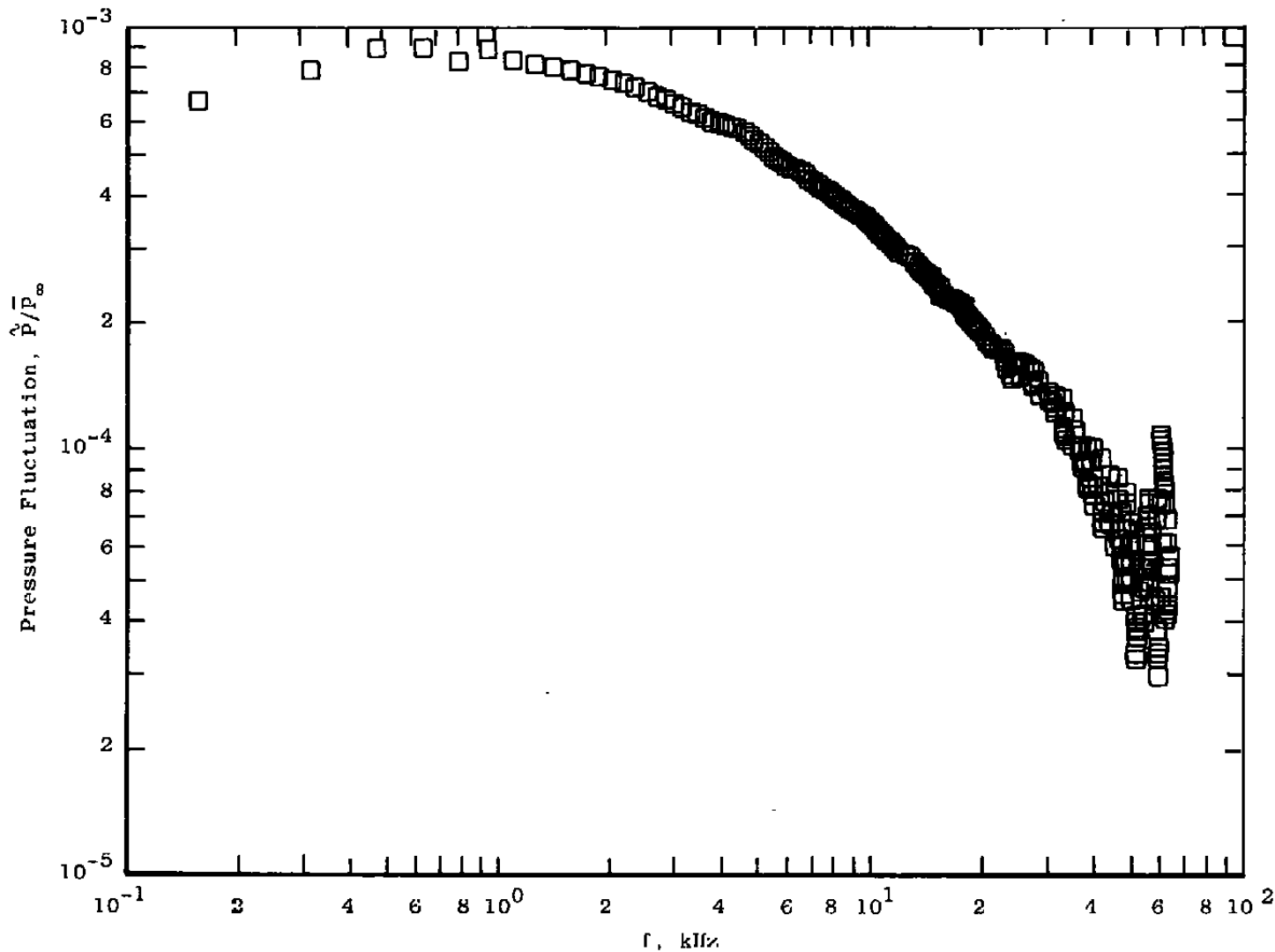
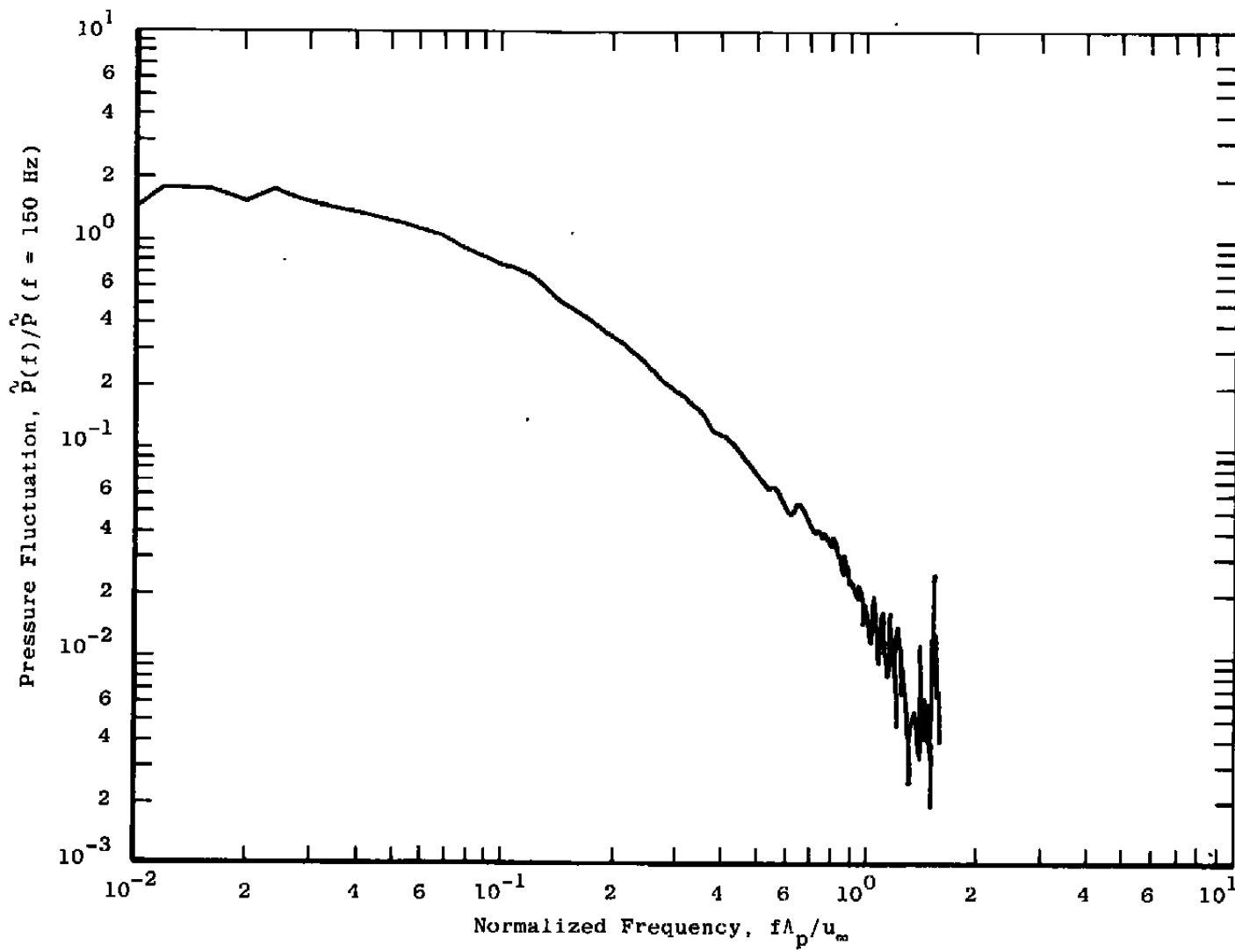
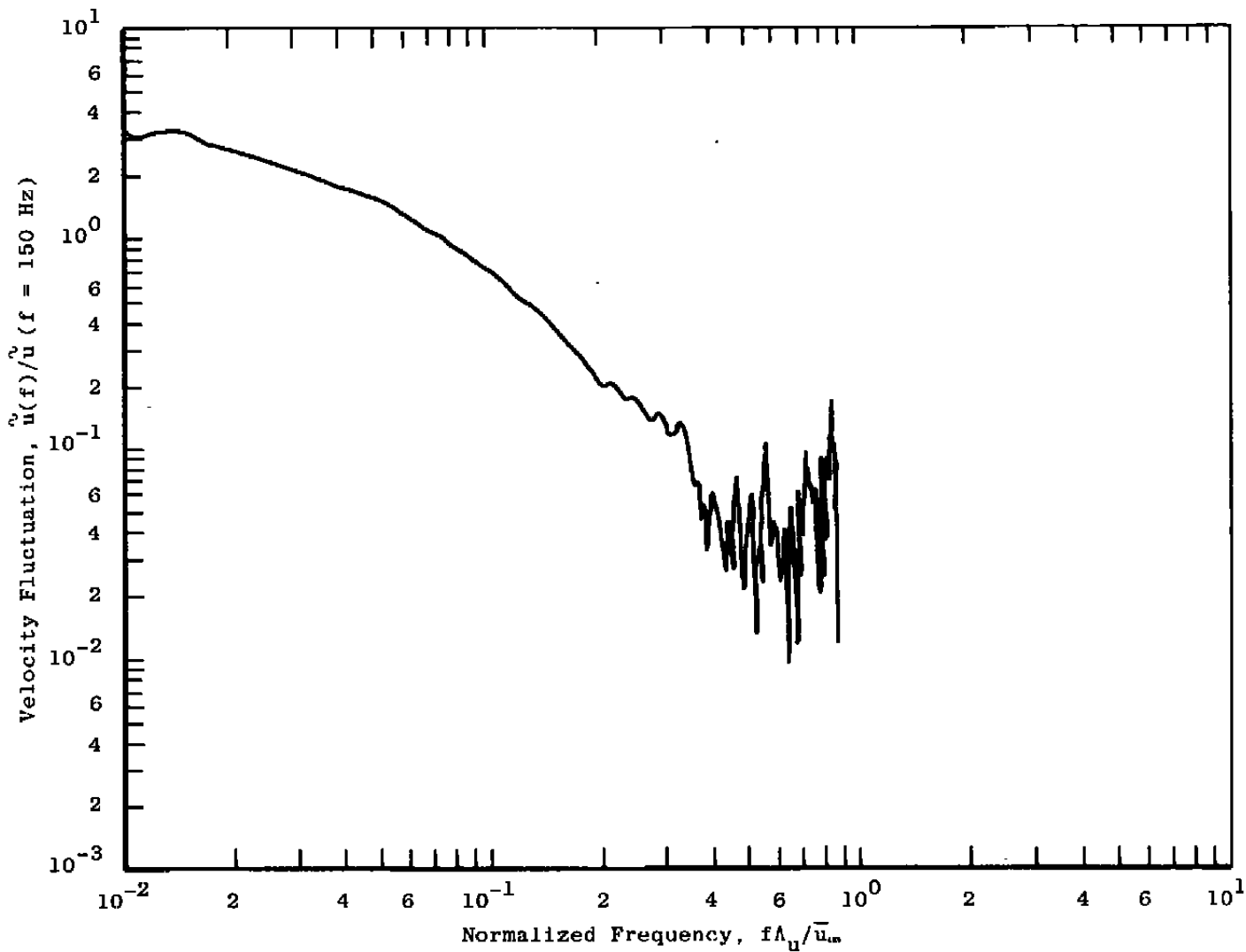


Figure 21. Spectrum of pressure fluctuations inferred from hot-wire measurements,  
 $M_\infty = 4$ ,  $RE_\infty = 3 \times 10^6$  per foot.

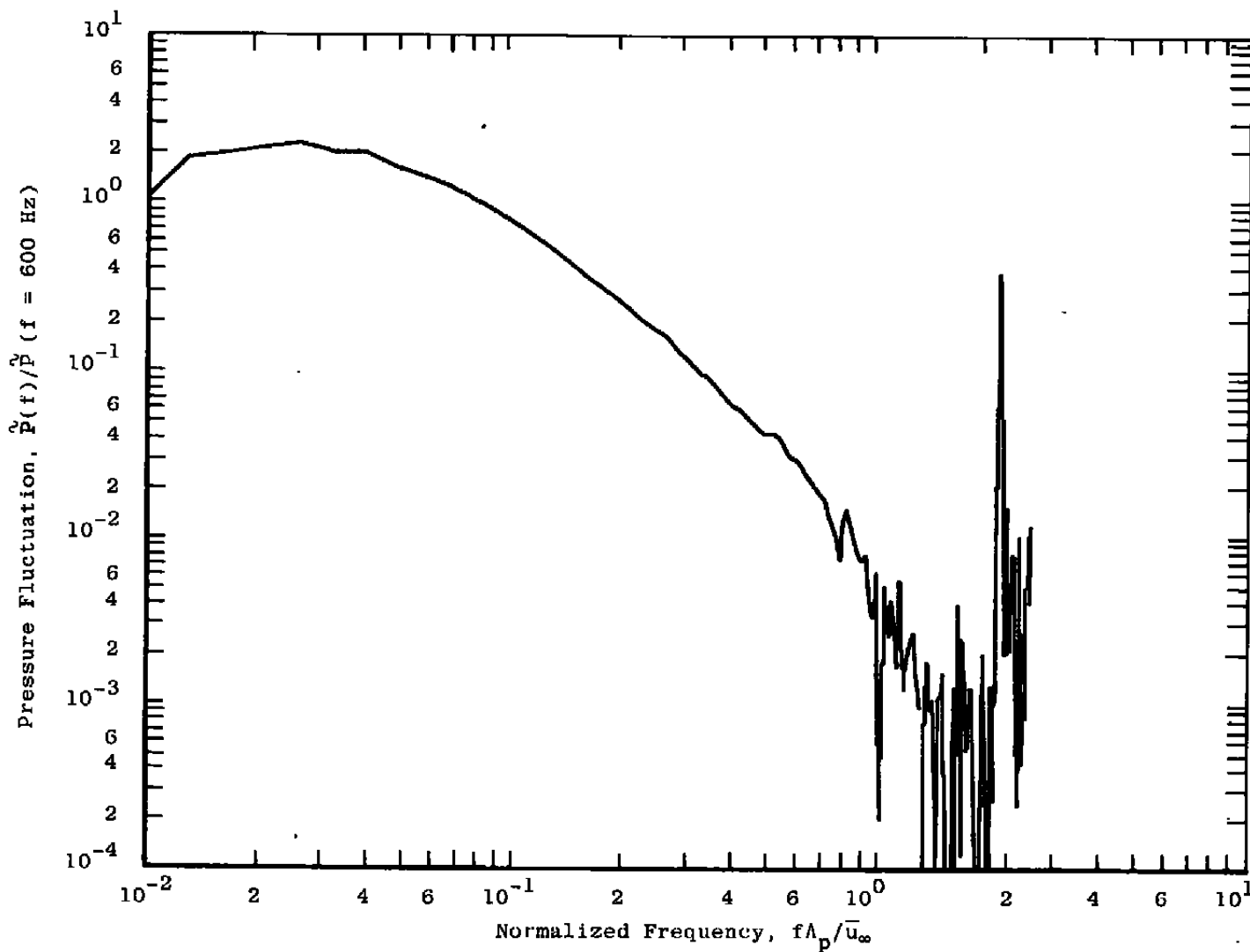


a. Normalized pressure fluctuations

Figure 22. Normalized distributions of fluctuations inferred from hot-wire measurements,  
 $M_\infty = 4$ ,  $RE_\infty = 3 \times 10^6$  per foot.

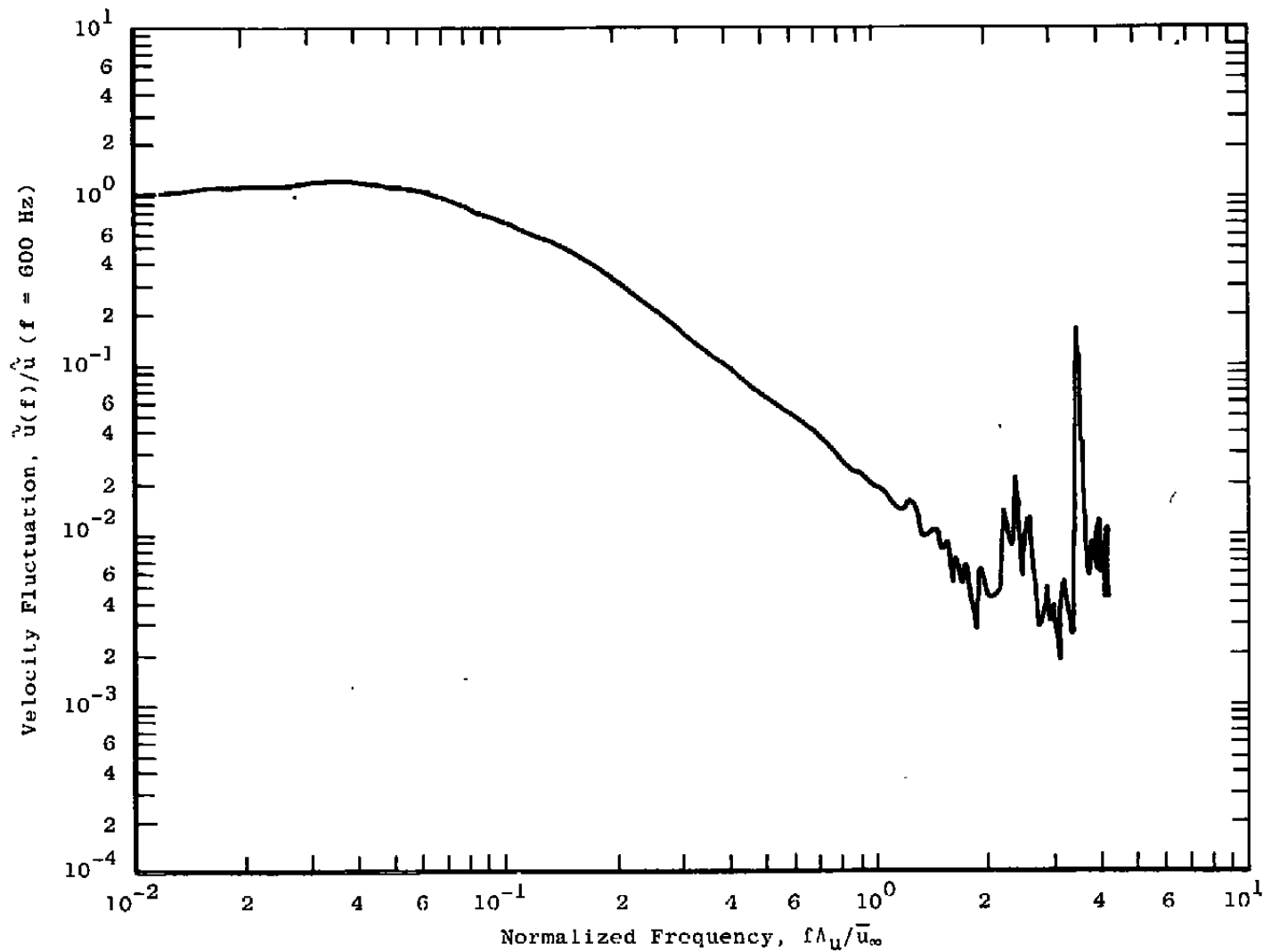


b. Normalized velocity fluctuations  
Figure 22. Concluded.

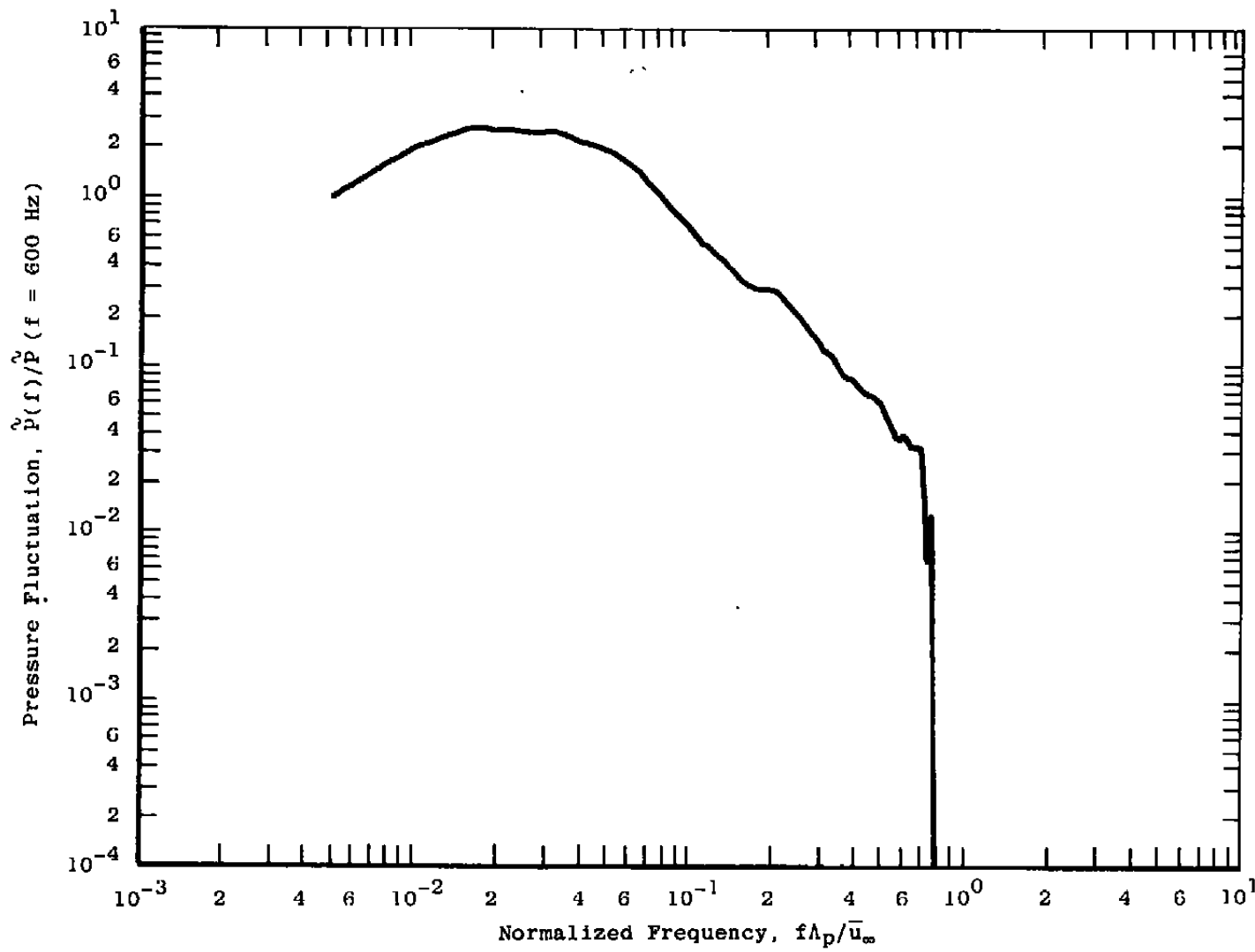


a. Normalized pressure fluctuations

Figure 23. Normalized distributions of fluctuations inferred from hot-wire measurements,  
 $M_\infty = 6$ ,  $RE_\infty = 3 \times 10^6$  per foot.

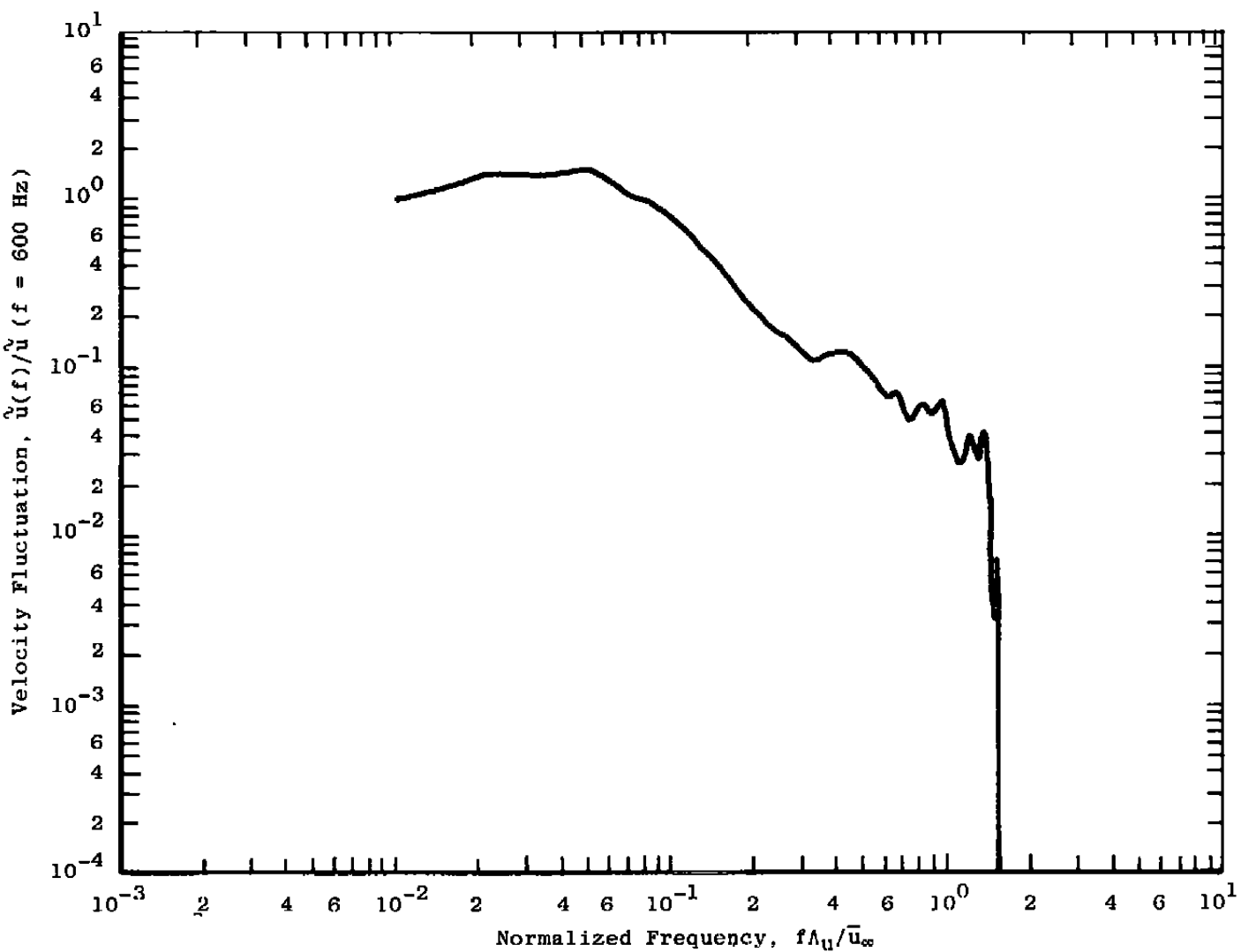


b. Normalized velocity fluctuations  
Figure 23. Concluded.

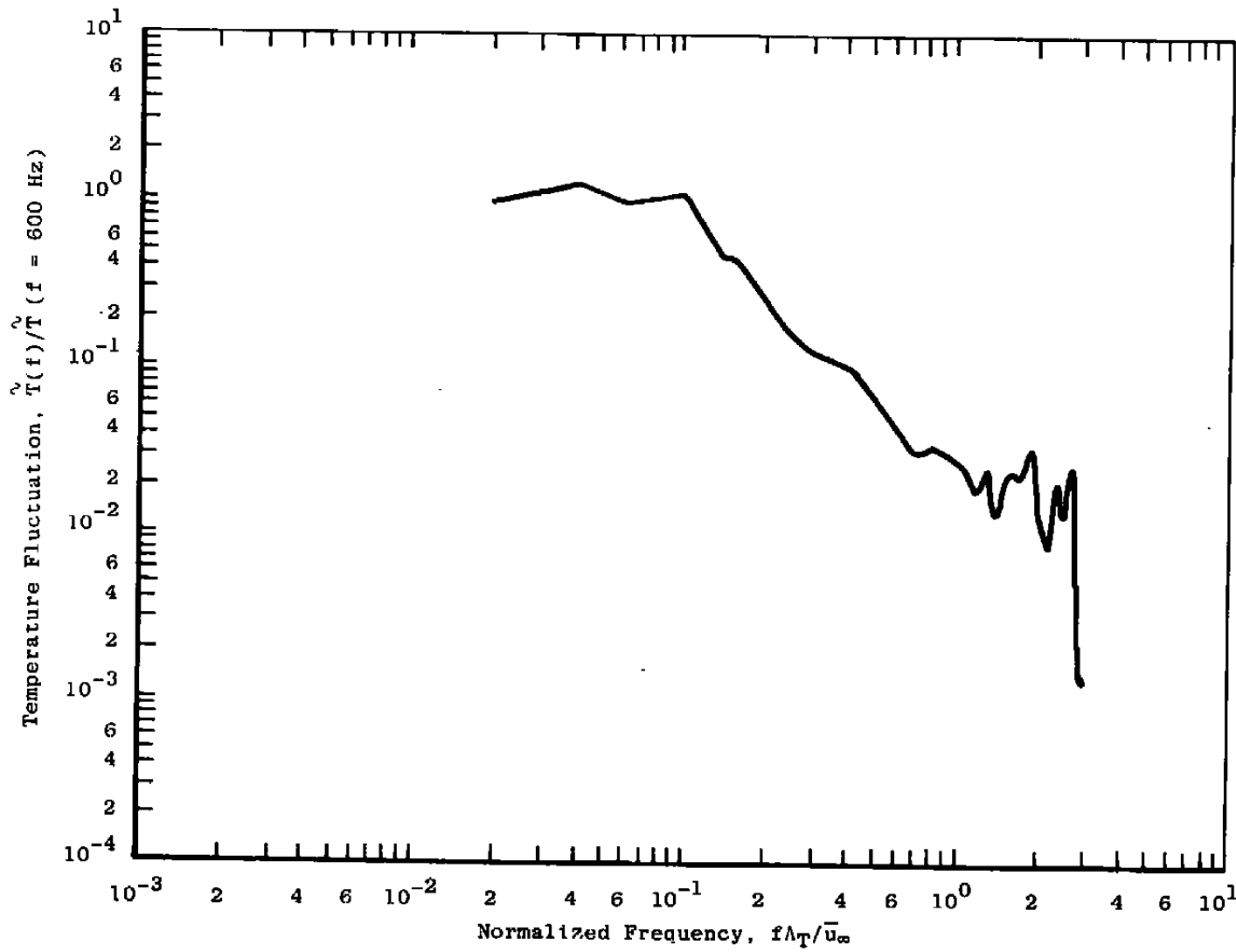


a. Normalized pressure fluctuations

Figure 24. Normalized distributions of fluctuations inferred from hot-wire measurements,  
 $M_\infty = 8$ ,  $RE_\infty = 3 \times 10^6$  per foot.



b. Normalized velocity fluctuations  
Figure 24. Continued.



c. Normalized temperature fluctuations  
Figure 24. Concluded.

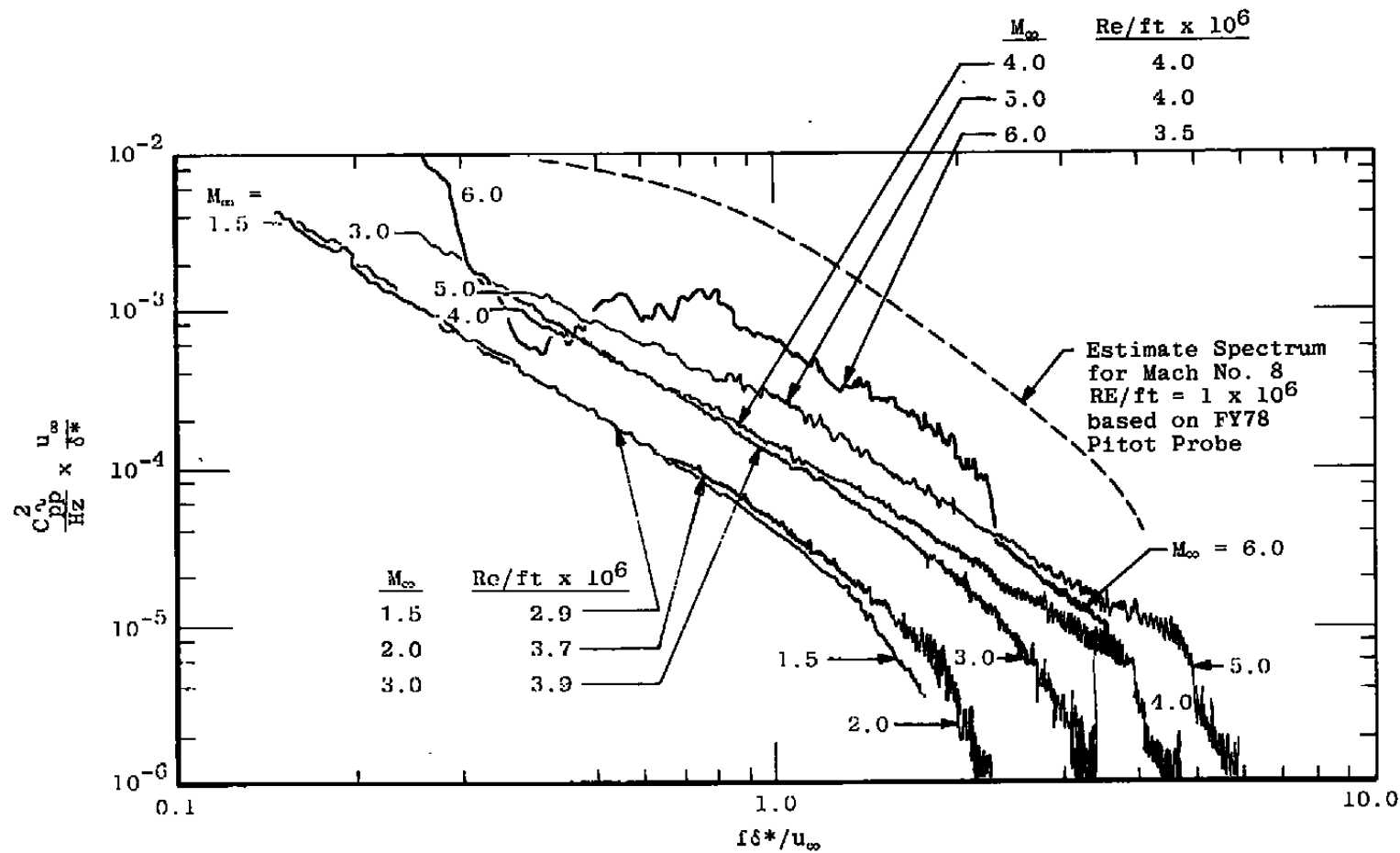
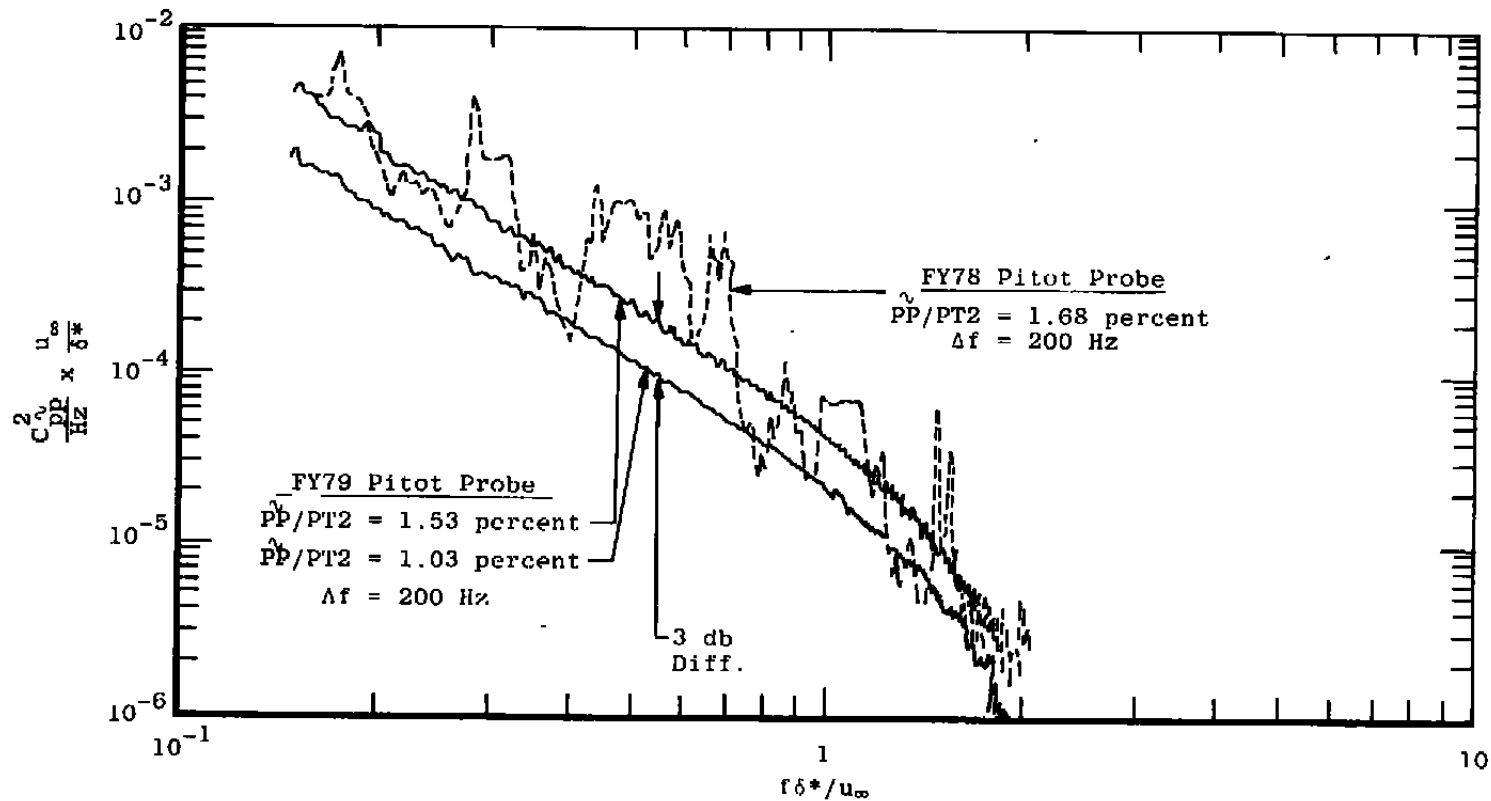
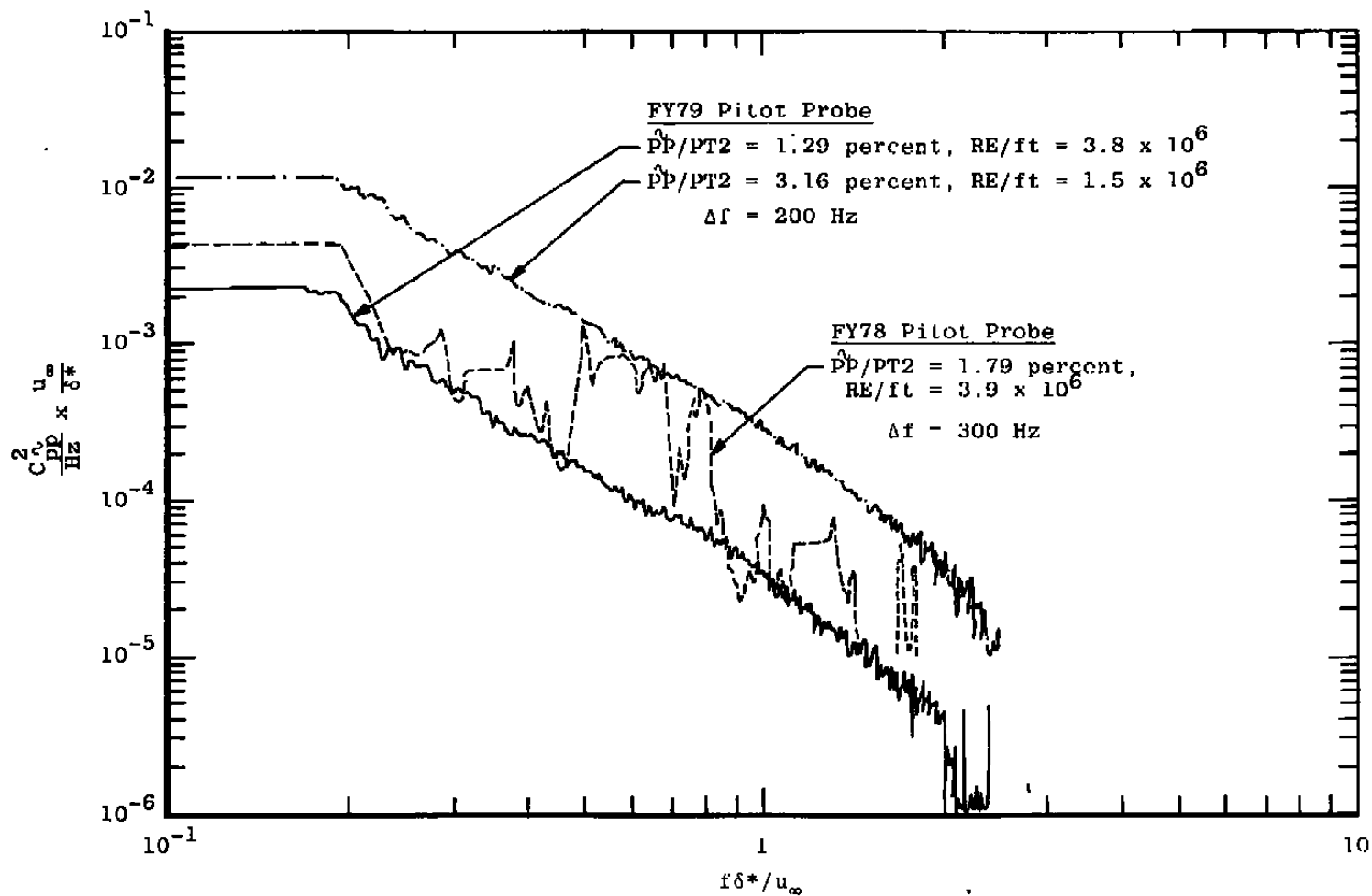


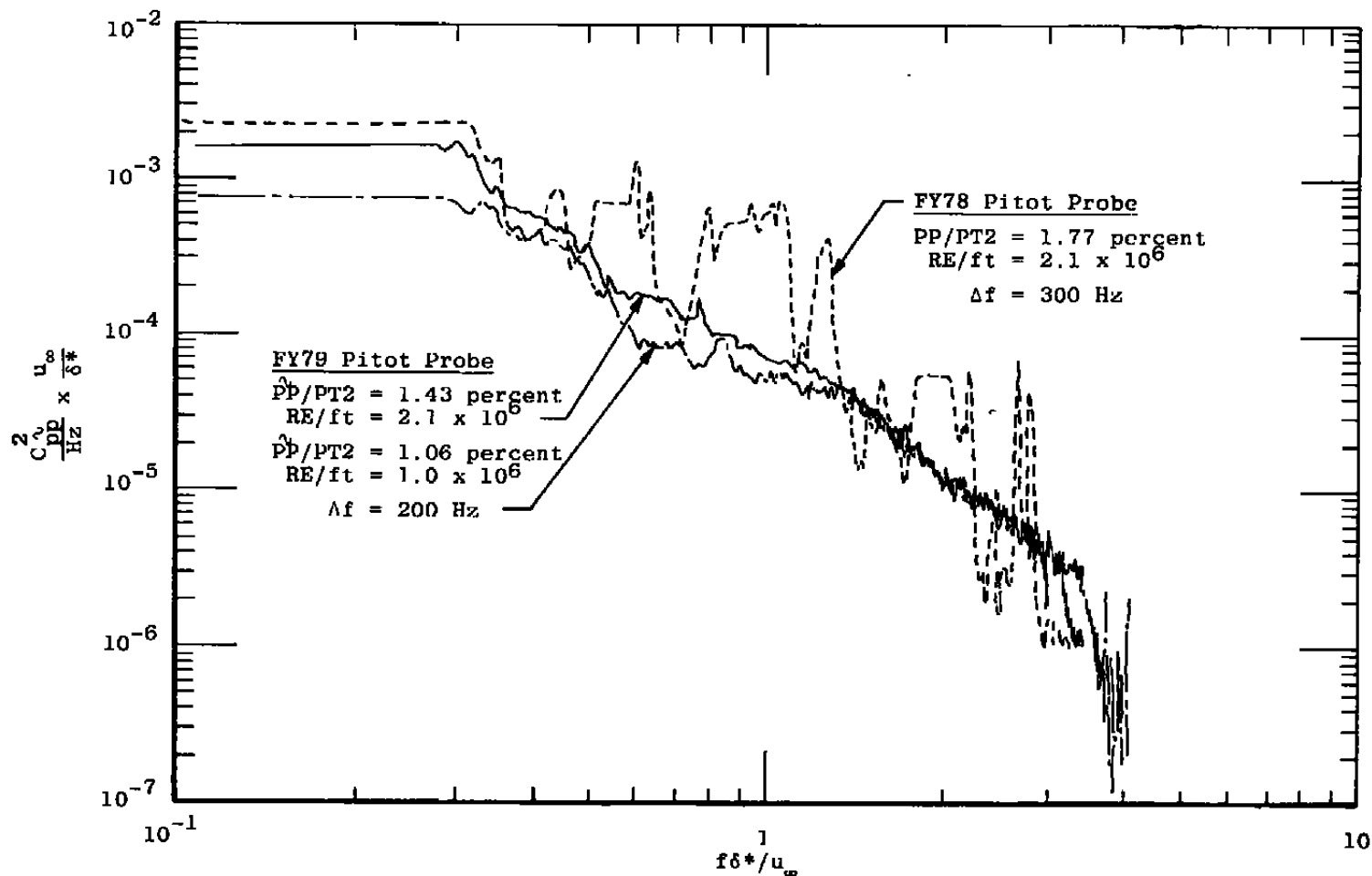
Figure 25. Pitot pressure fluctuation spectral content in AEDC Tunnels A and B (based on FY79 pitot probe),  $\Delta f = 200$  Hz.



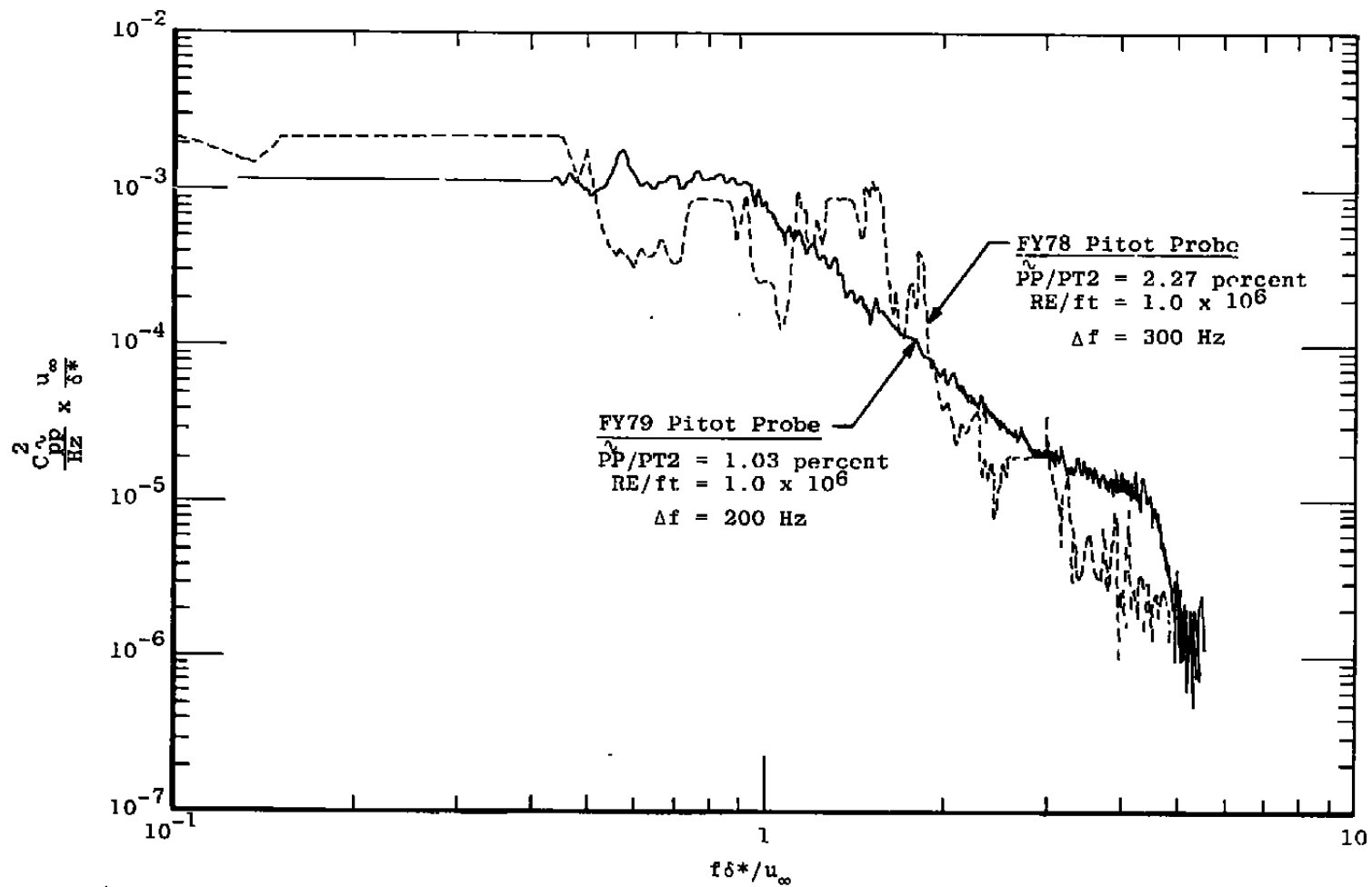
a.  $M_\infty = 1.51$  and  $RE_\infty = 2 \times 10^6$  per foot  
Figure 26. Typical Tunnel A pitot-acoustic pressure spectra.



b.  $M_\infty = 2.0$ , RE varies  
Figure 26. Continued.



c.  $M_\infty = 2.0$ ,  $RE$  varies  
 Figure 26. Continued.



d.  $M_\infty = 4.0$ ,  $RE = 1.0 \times 10^6$  per foot  
Figure 26. Concluded.

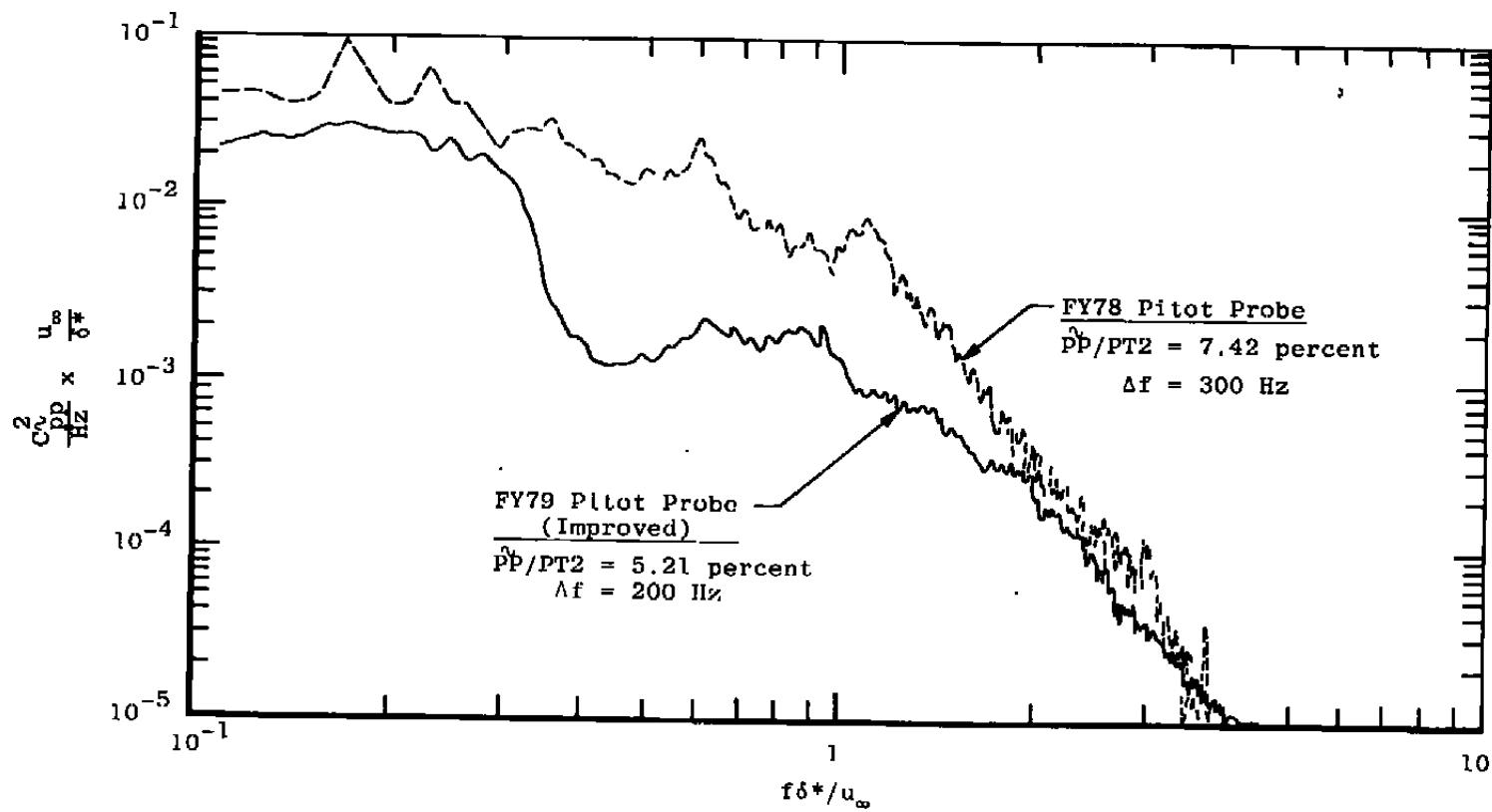


Figure 27. Comparison of acoustical pitot probe results, Mach number 6.0 at  $RE_\infty = 1 \times 10^6$  per foot.

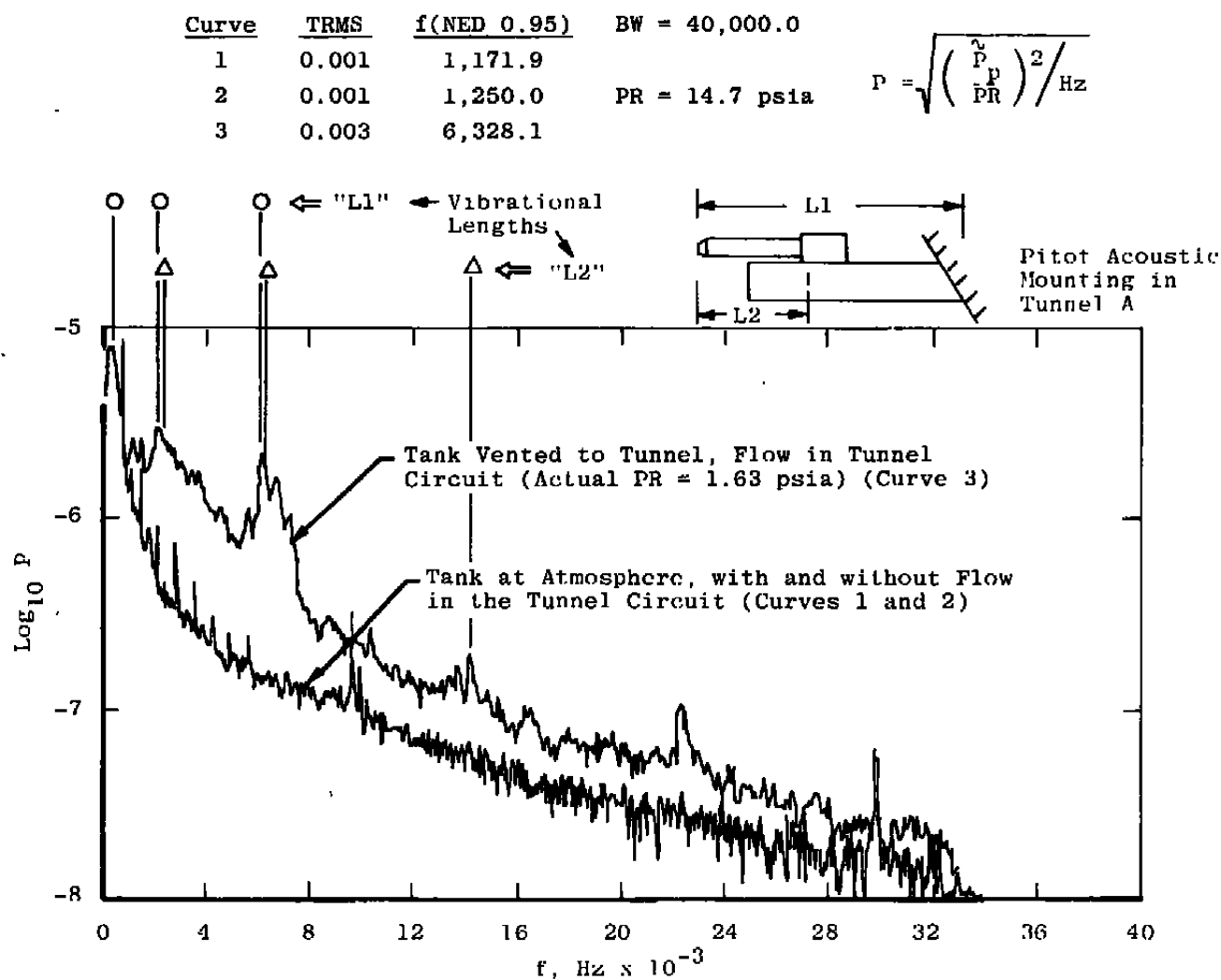


Figure 28. Tunnel A tare for the dynamic pressure sensor of the pitot acoustic probe (FY78).

Curve	TRMS	f(NED 0.95)	BW = 40,000.0
1	0.000	37,968.8	
2	0.006	1,406.3	PR = 14.7 psia
3	0.007	5,468.8	$P = \sqrt{\left(\frac{P_p}{P_R}\right)^2 / \text{Hz}}$

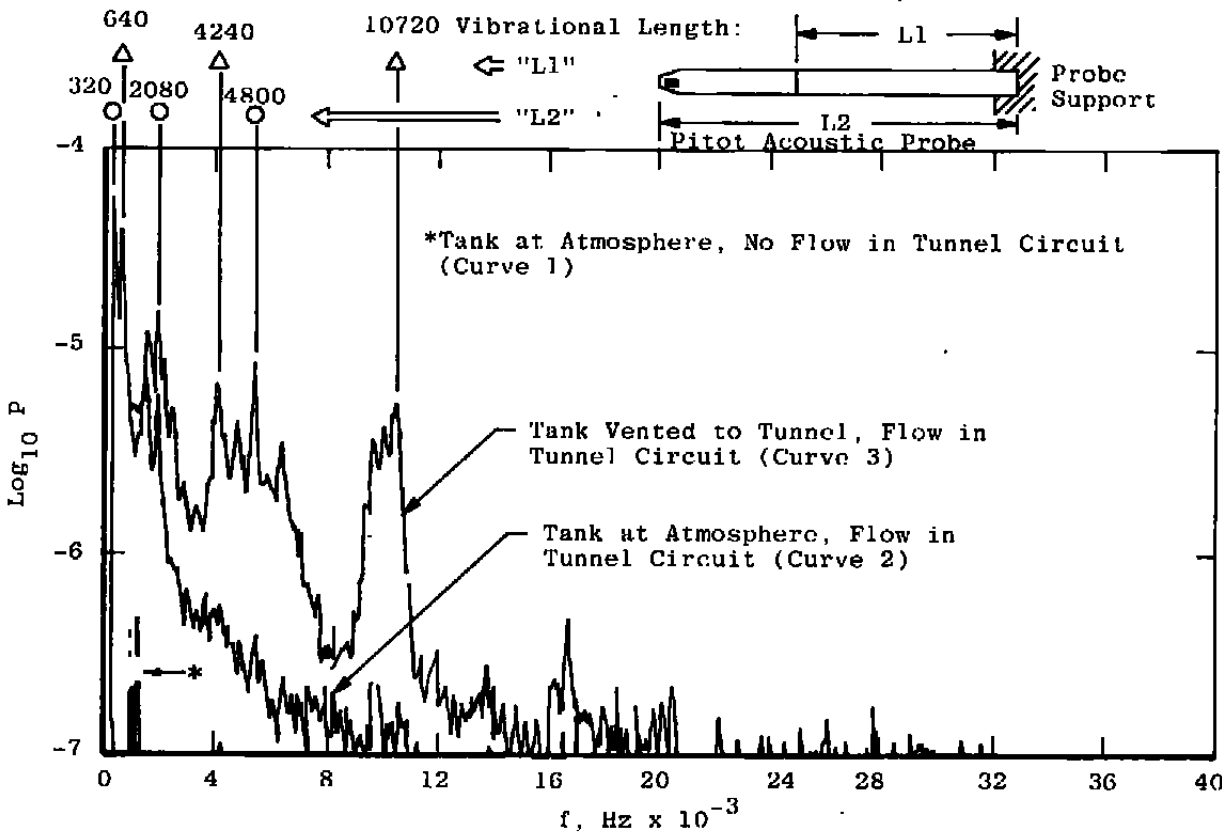
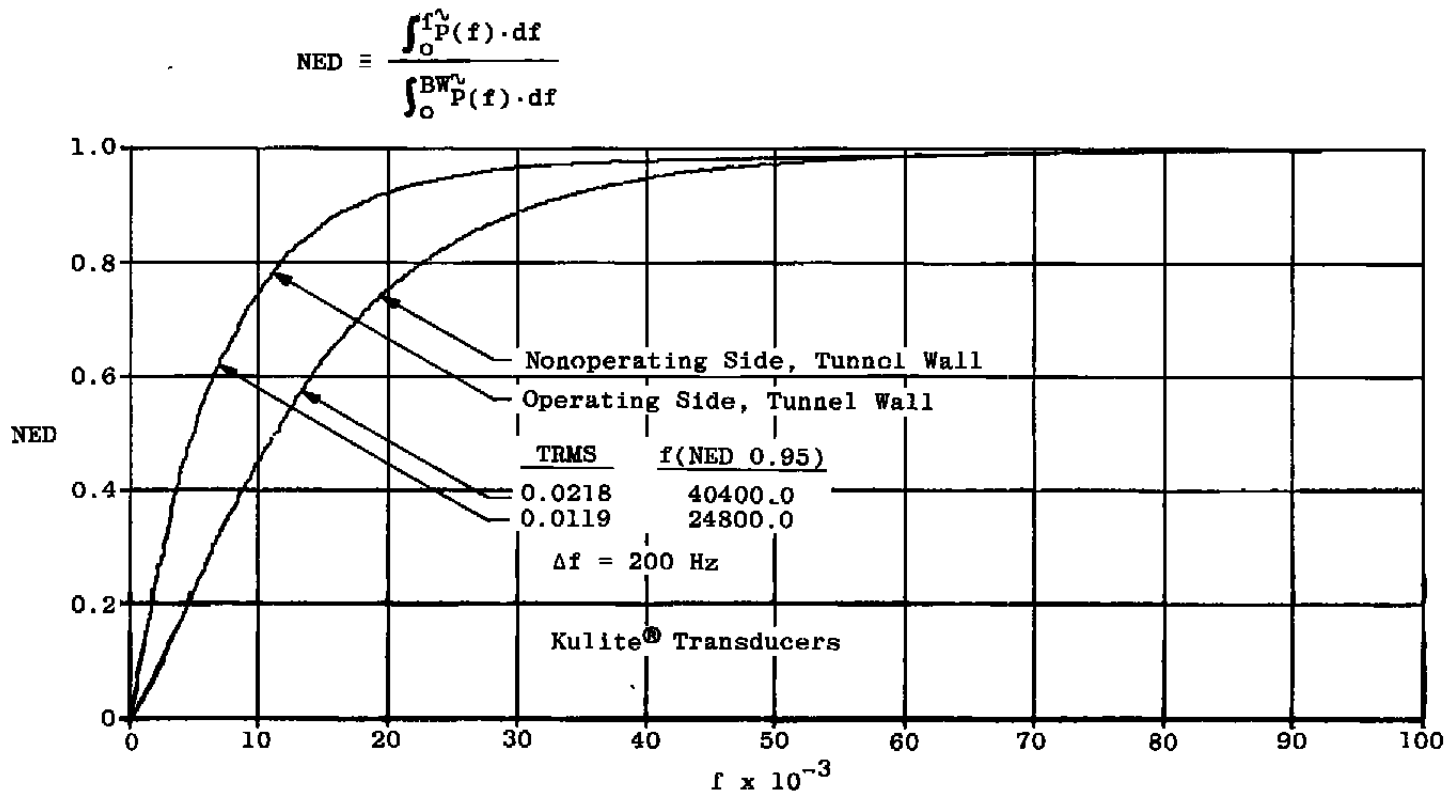
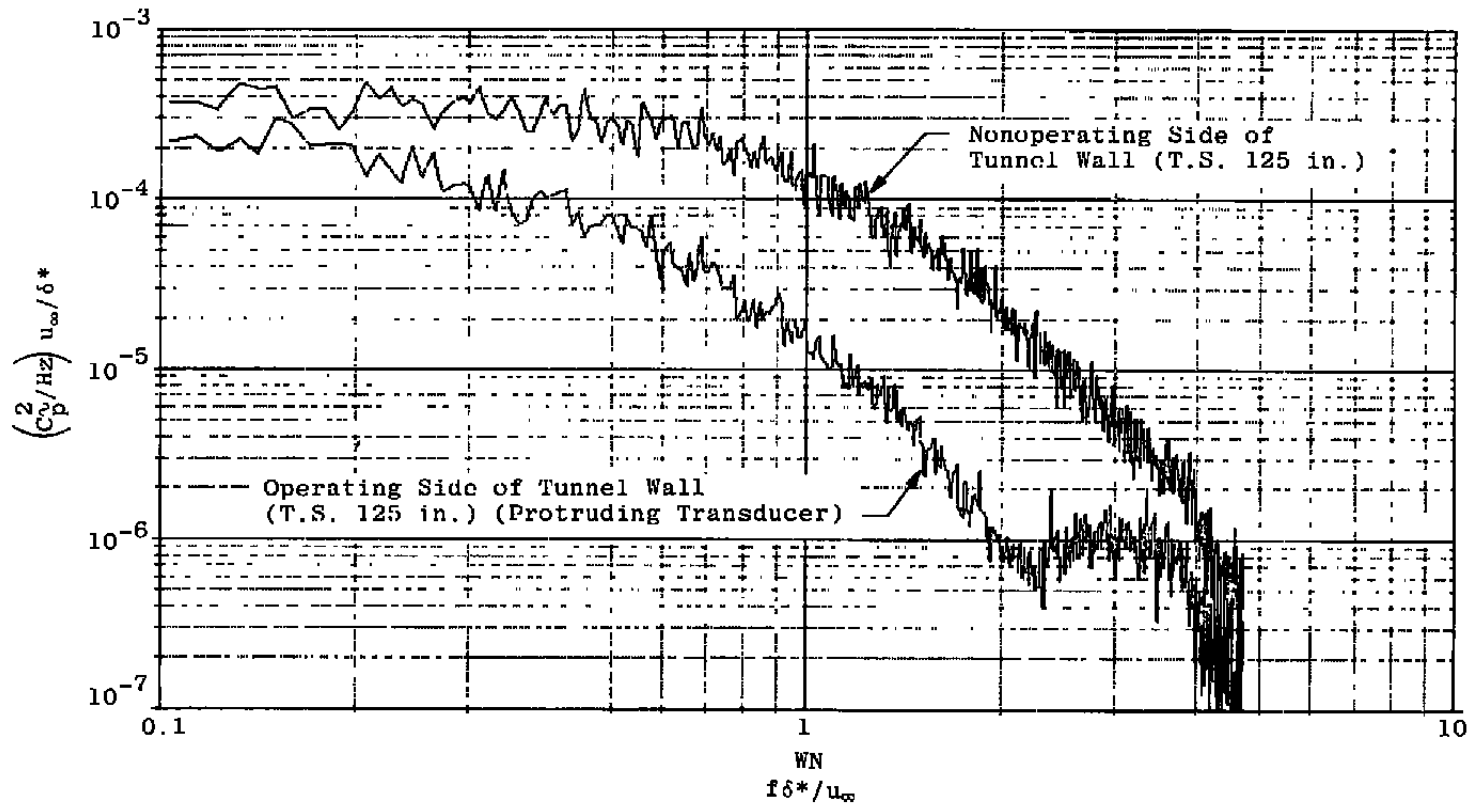


Figure 29. Tunnel B tare for the dynamic pressure sensor of the pitot acoustic probe (FY78).



a. Normalized energy distribution

Figure 30. Typical spectral distribution in the wall static pressure at tunnel Station 125 in.  
(Mach number 4.0,  $RE_{\infty} = 4 \times 10^6$  per foot).



b. Typical power spectral density distribution  
Figure 30. Concluded.

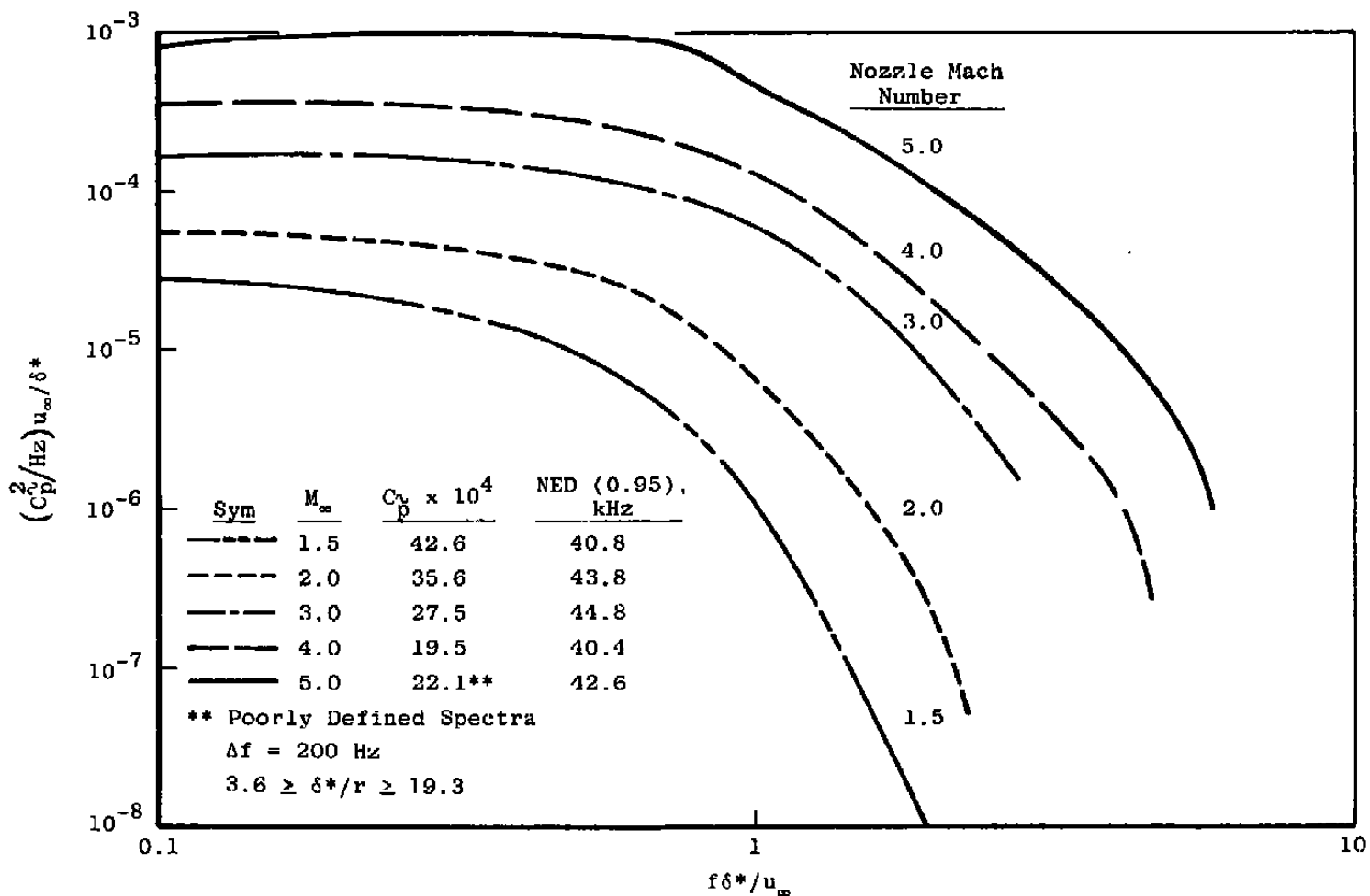


Figure 31. Tunnel A nonoperating sidewall static pressure fluctuation spectra at  $RE_\infty = 4 \times 10^6/\text{ft.}$

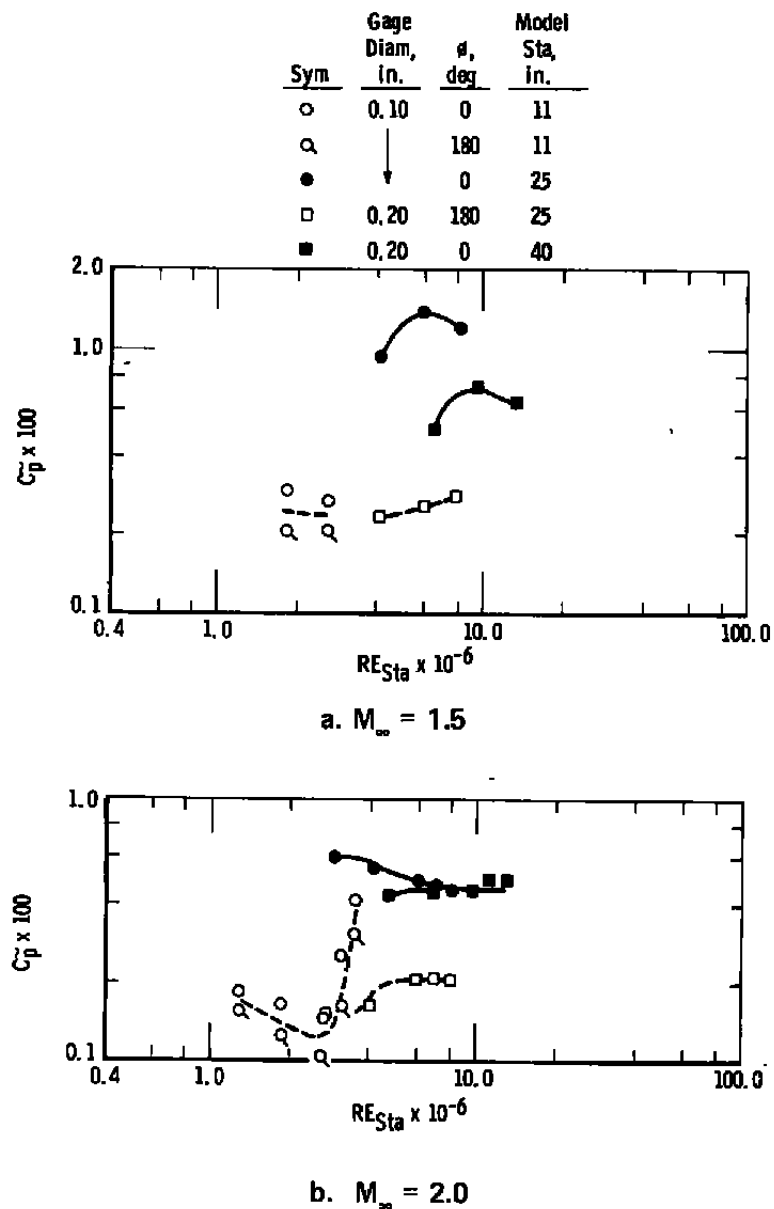
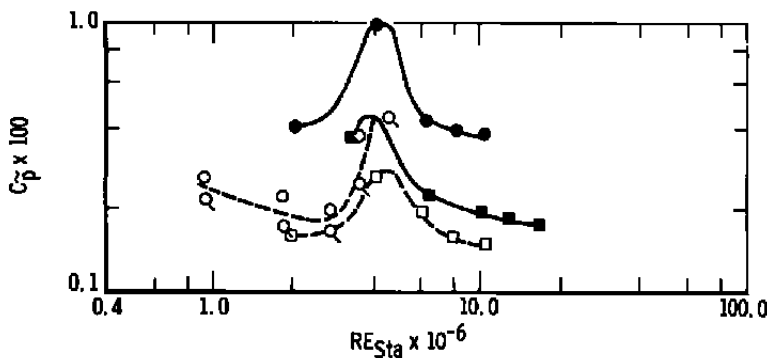
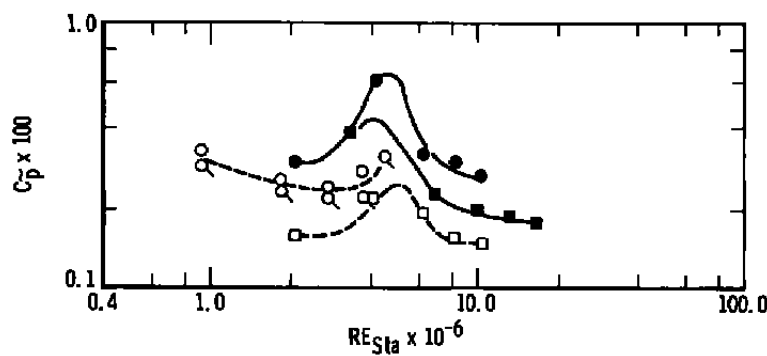
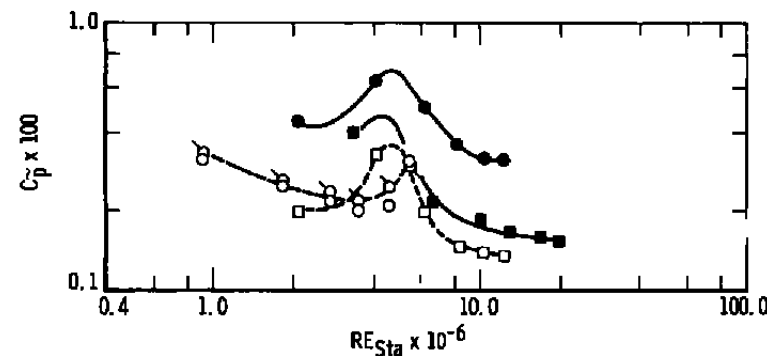


Figure 32. 6-deg sharp cone surface pressure fluctuation coefficients.

Sym	Gage Diam, in.	$\phi$ , deg	Model Sta, in.
○	0.10	0	11
○		180	11
●		0	25
□	0.20	180	25
■	0.20	0	40

c.  $M_{\infty} = 3.0$ d.  $M_{\infty} = 4.0$ e.  $M_{\infty} = 5.0$   
Figure 32. Continued.

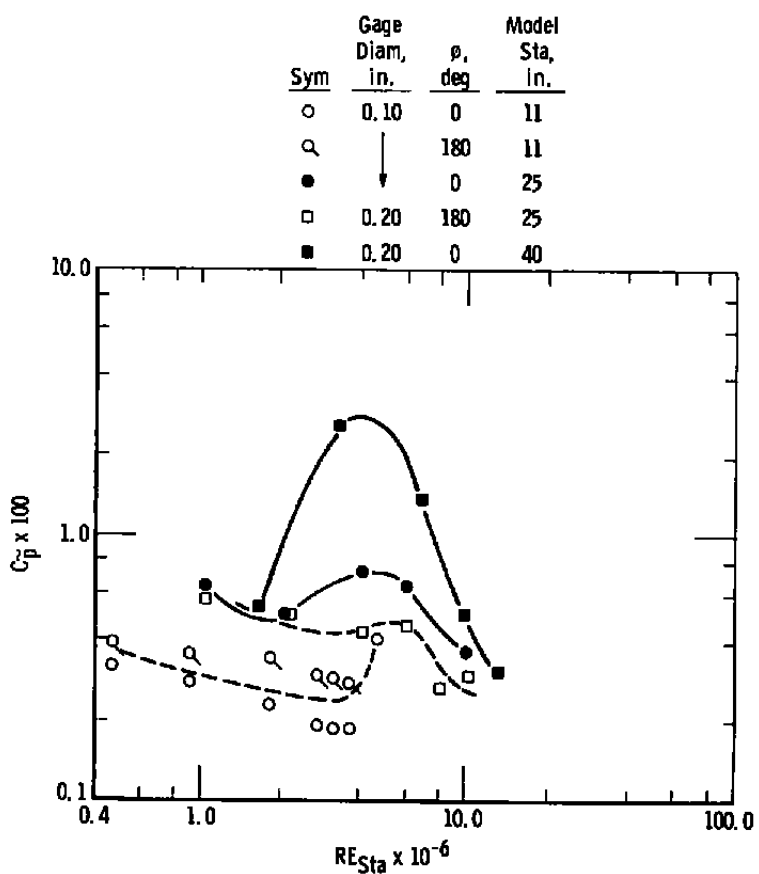
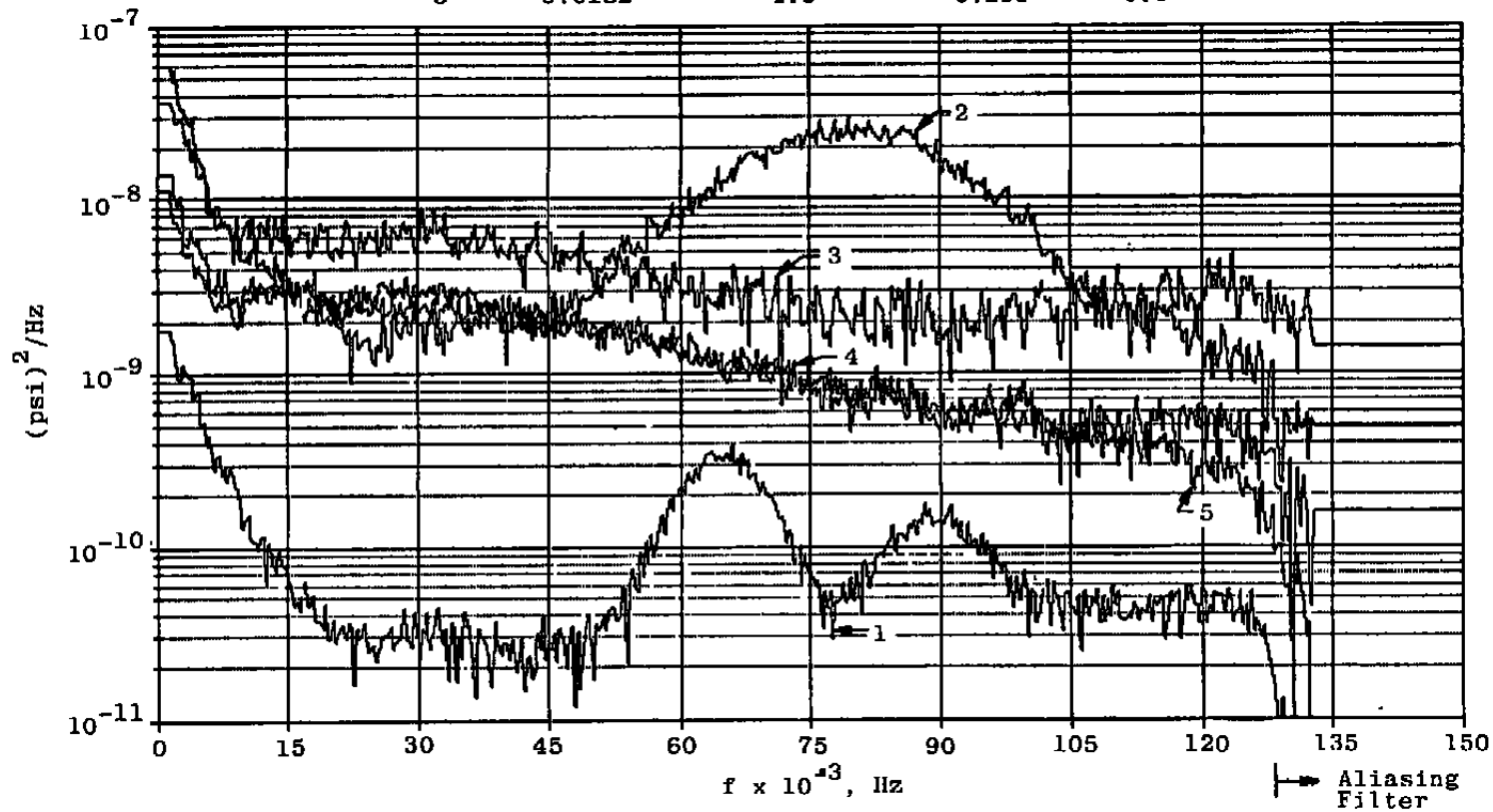
f.  $M_\infty = 6.0$  (Tunnel B)

Figure 32. Concluded.

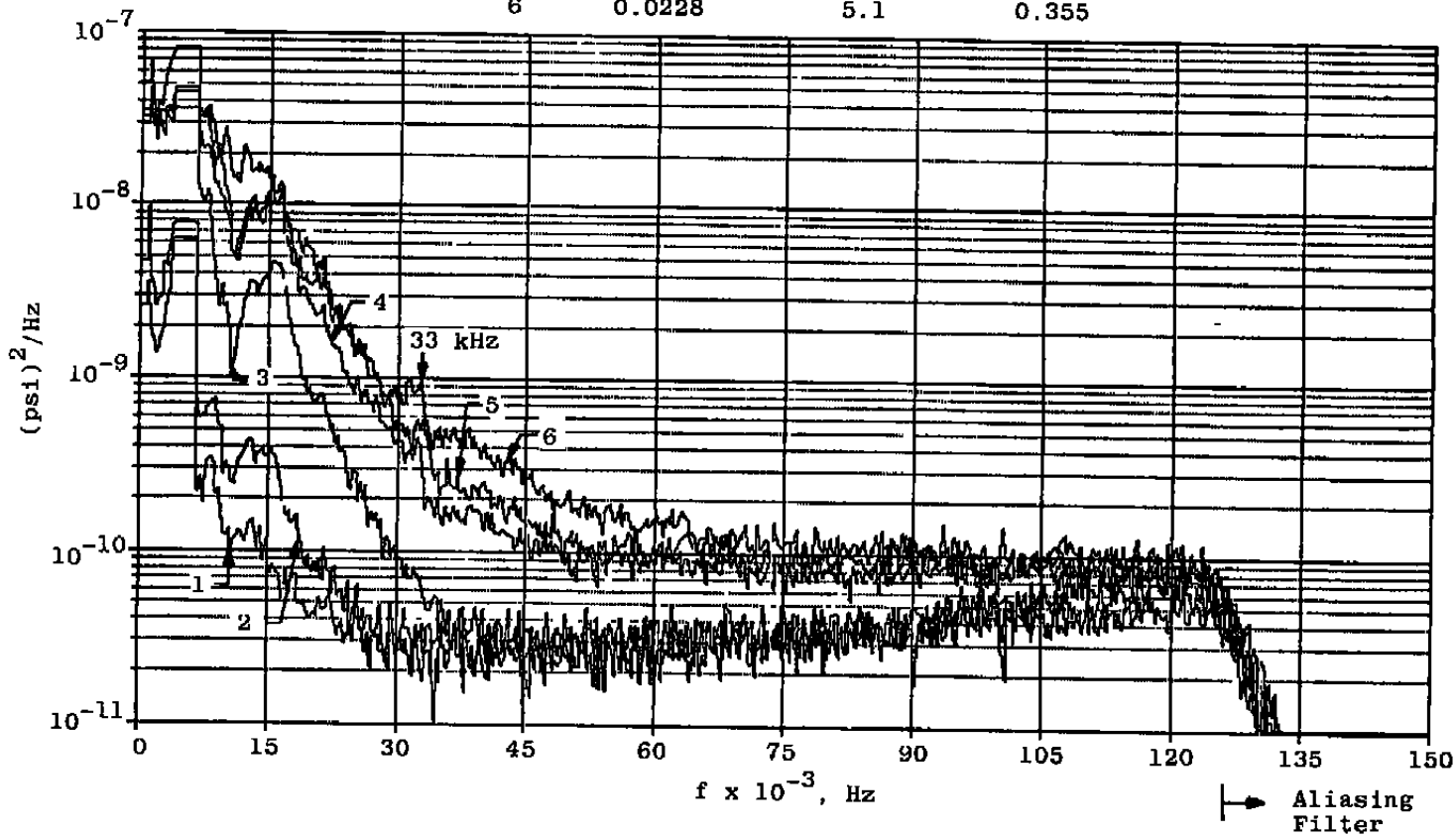
Sym	TRMS, psi	$RE_\infty/ft \times 10^{-6}$	$100 \hat{C}_p$	$X_t$ (Est.)
1	0.0050	0.5	0.520	3.7
2	0.0383	1.0	2.548	2.3
3	0.0350	2.0	1.341	1.4
4	0.0191	3.0	0.492	1.0
5	0.0152	4.0	0.299	0.8



a. PCB®113 at Station 40.0 (3.33 ft)

Figure 33. Pressure fluctuation spectra on a 6-deg sharp nose cone at Mach number 6.0 (zero angle of attack).

Sym	TRMS, psi	$RE_\infty/ft \times 10^{-6}$	$100 \text{ Cg}$
1	0.0062	0.5	0.646
2	0.0075	1.0	0.499
3	0.0183	2.0	0.701
4	0.0244	3.0	0.628
5	0.0203	4.0	0.400
6	0.0228	5.1	0.355



b. PCB®105 at Station 25.0 (2.08 ft)

Figure 33. Continued.

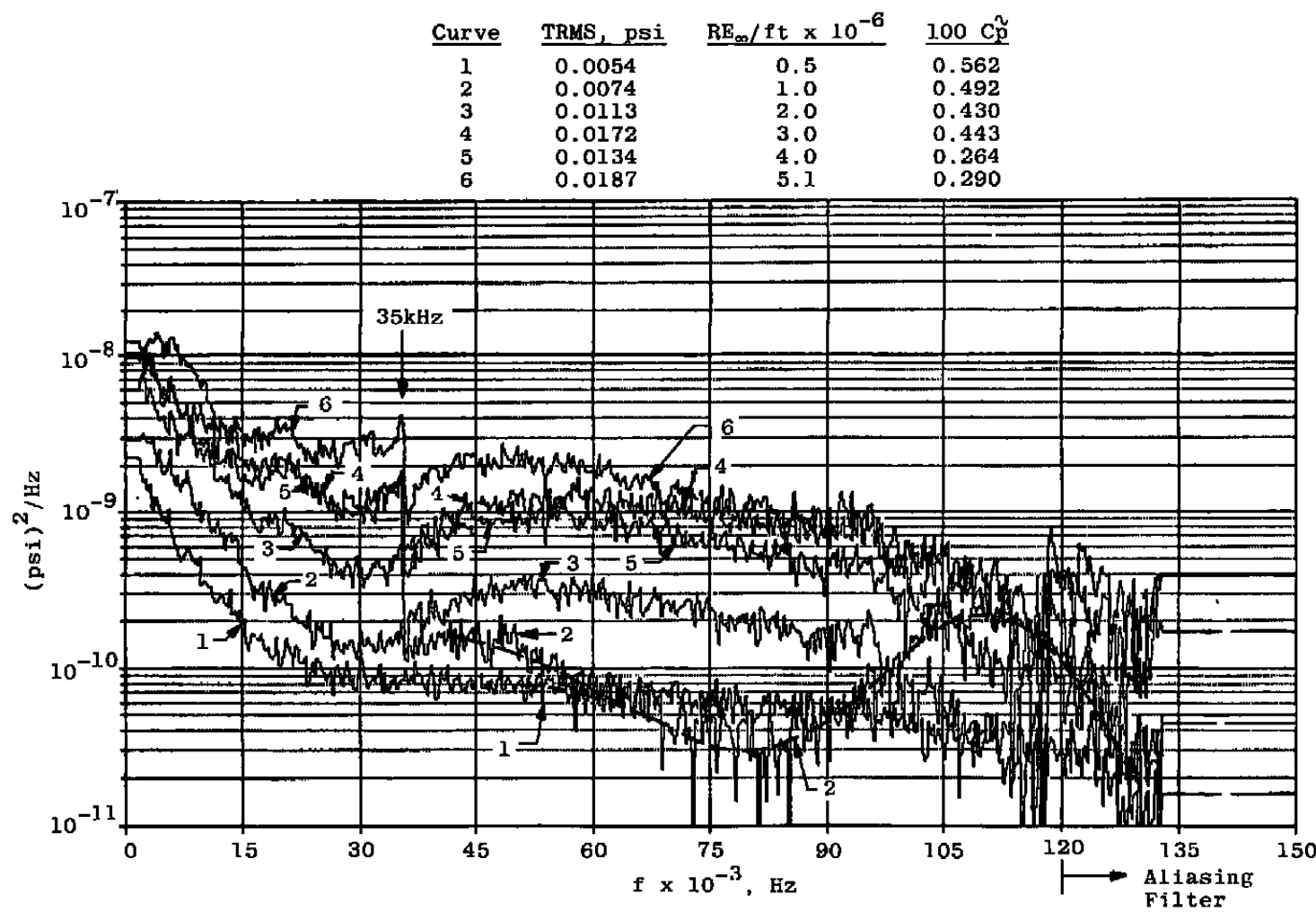
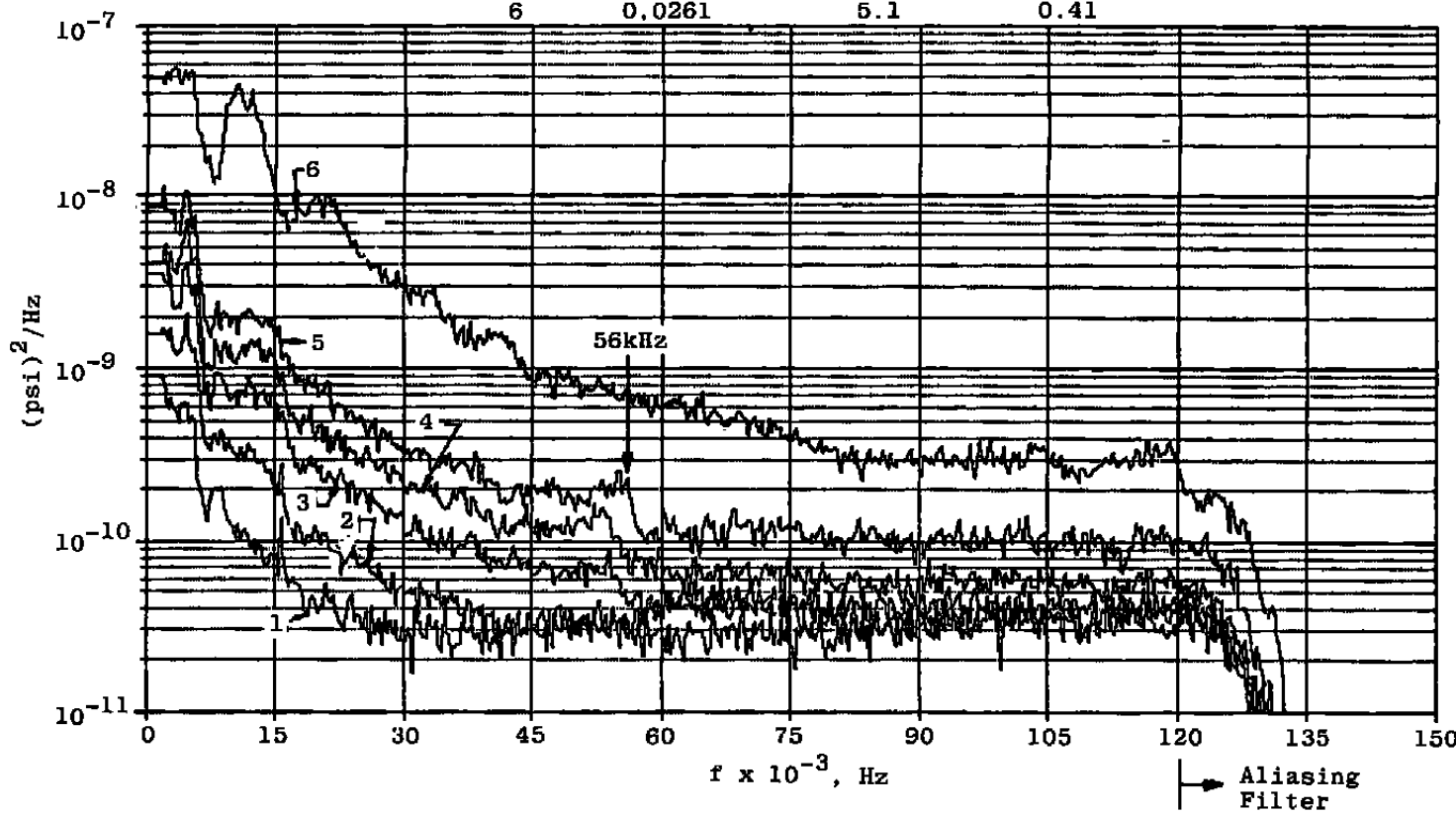
c. PCB®113 at Station 25.0 (2.08 ft),  $\phi = 180$  deg

Figure 33. Continued.

Curve	TRMS, psi	$RE_\infty/ft \times 10^{-6}$	$100 Cp^2$
1	0.0036	0.5	0.38
2	0.0044	1.0	0.29
3	0.0061	2.0	0.23
4	0.0075	3.0	0.19
5	0.0097	4.0	0.19
6	0.0261	5.1	0.41



d. PCB® 1.5 at Station 11.0 (0.92 ft)  
Figure 33. Concluded.

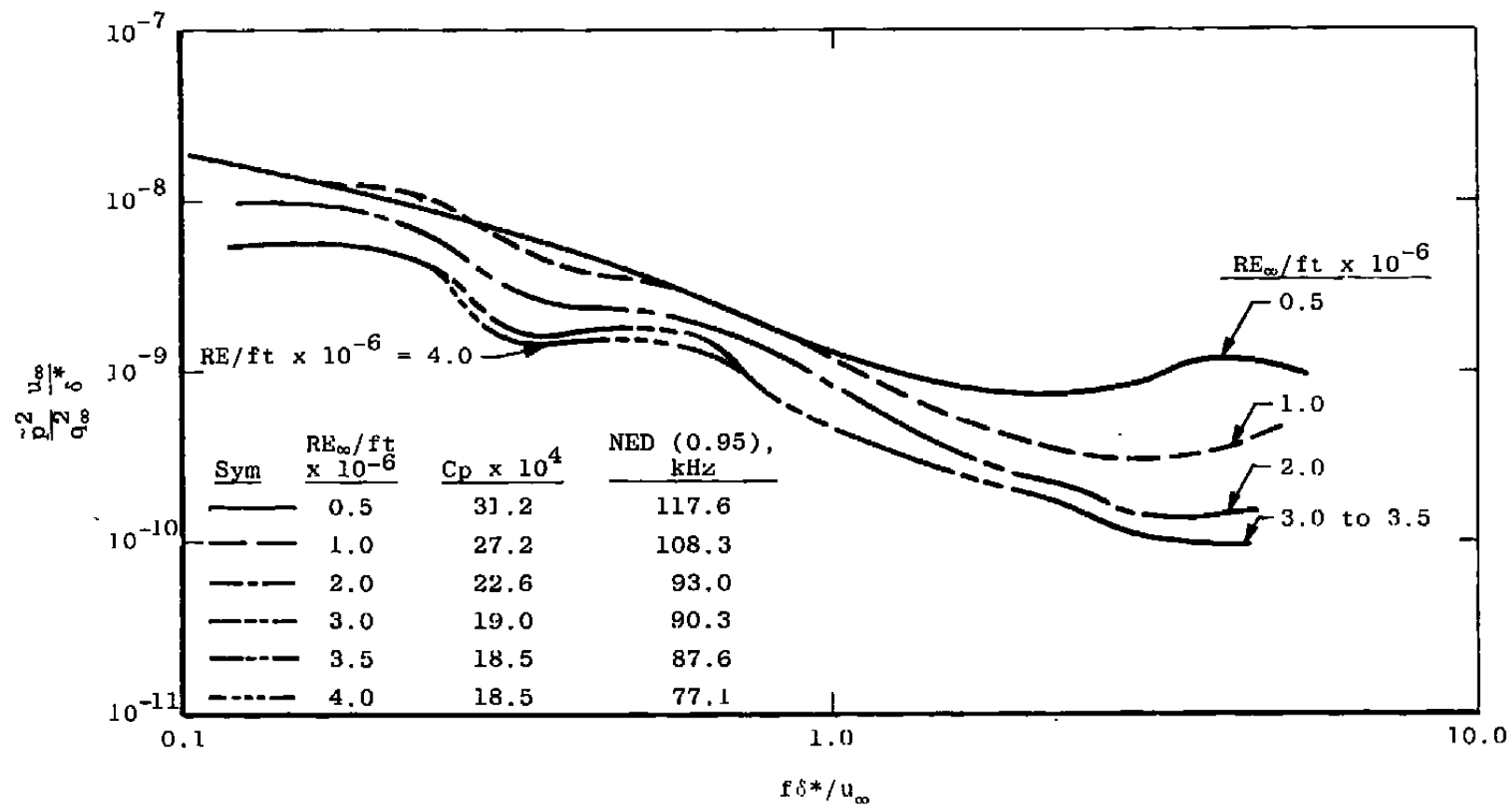


Figure 34. Normalized power spectral density of the surface pressure fluctuations on a 6-deg sharp nose cone.

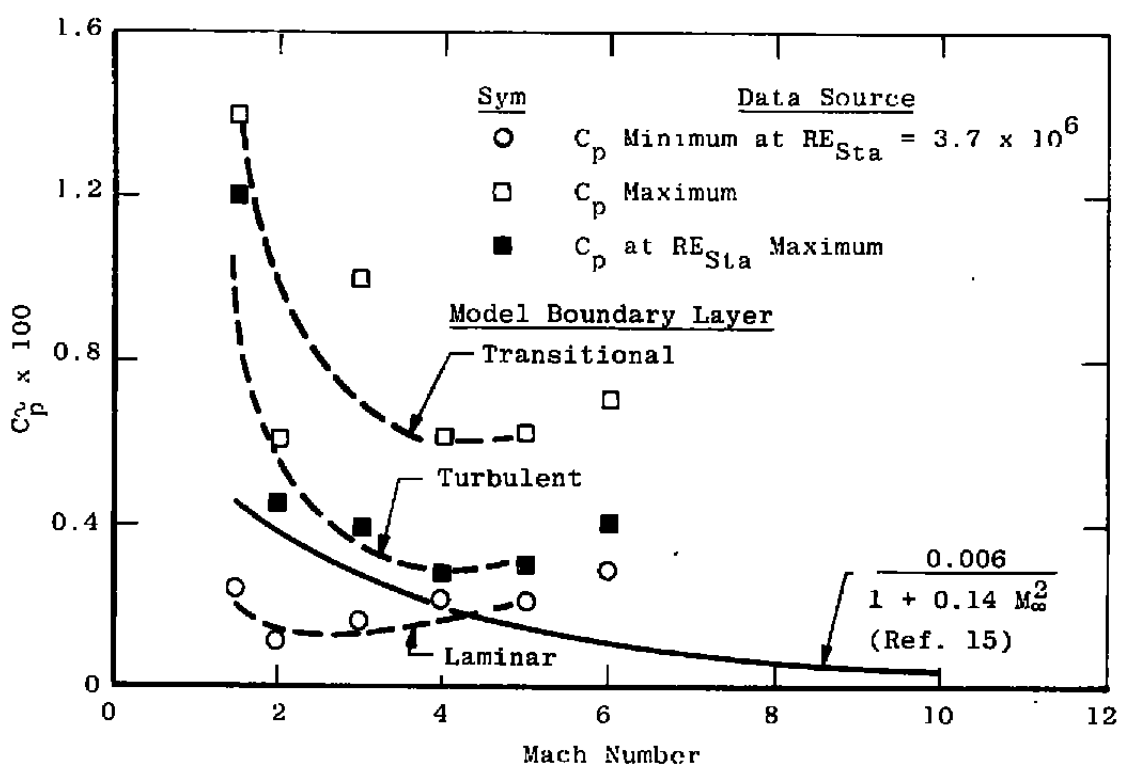
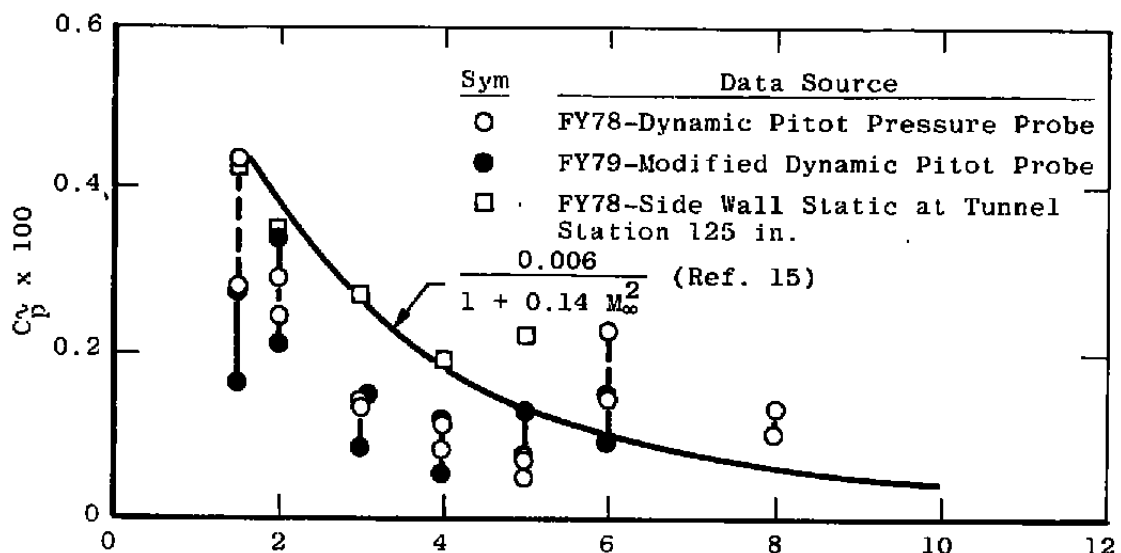


Figure 35. Typical pressure fluctuation levels in the AEDC Wind Tunnels A and B.

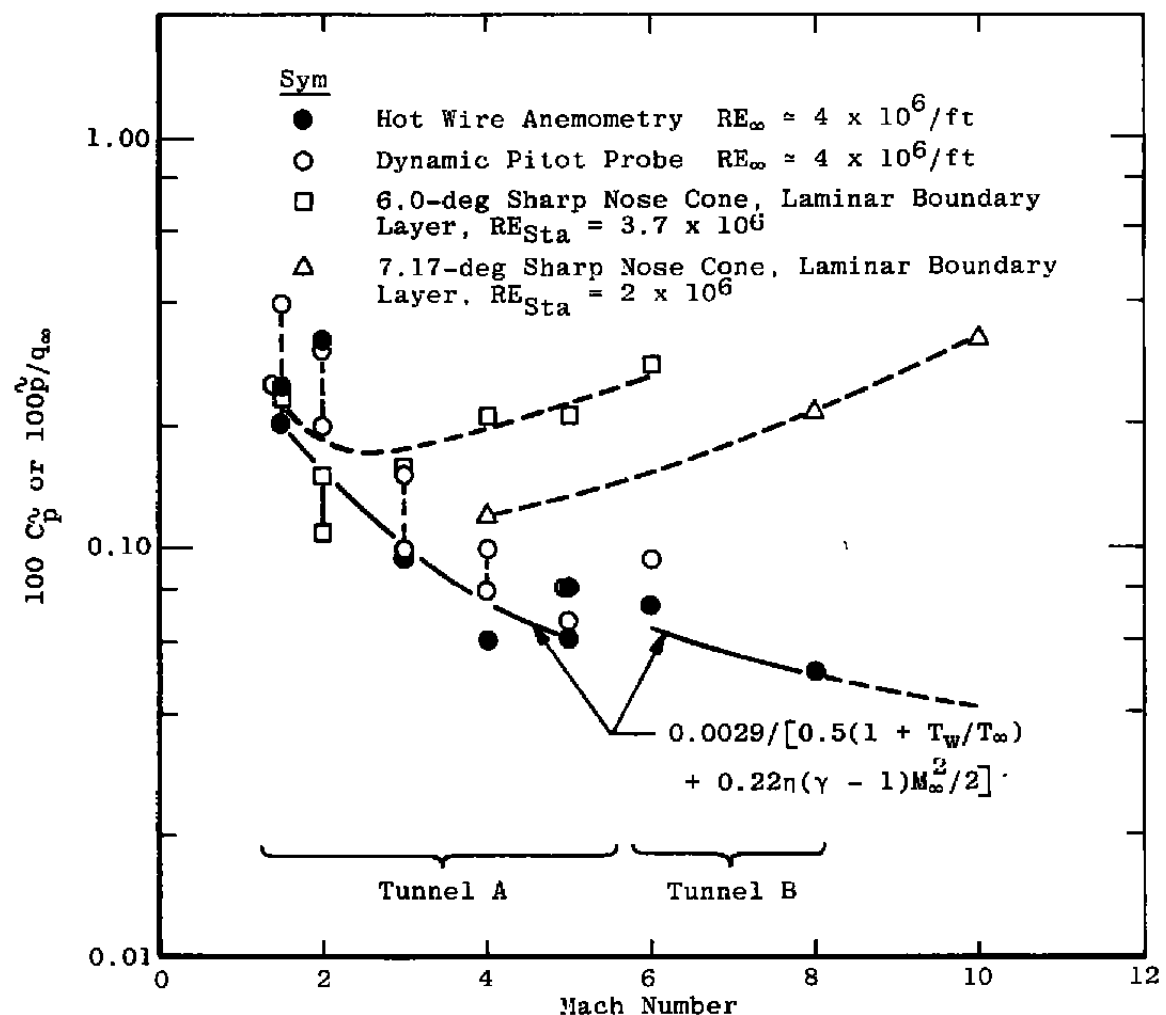


Figure 36. Summary of pressure fluctuation levels in AEDC Tunnels A, B and C at nominal  $RE_{\infty} = 2 \times 10^6$  to  $4 \times 10^6$  per foot.

## APPENDIX A

### HOT-WIRE ANEMOMETER CALIBRATION

Two types of calibration are required for the hot-wire probes if quantitative data are to be extracted from flow-field measurements made using hot-wire anemometry techniques.

The first calibration is made to determine certain physical characteristics of the sensor: wire resistance at zero current at a reference temperature  $\bar{T}_r = 32^\circ\text{F}$ , the first-order temperature resistivity coefficients at the reference temperature, and the wire effective length. This calibration is done in the VKF instrumentation laboratory prior to the wind tunnel measurements, and a posttest calibration is performed on those wires which survive wind tunnel use. Probes are placed in a laboratory heat-treating furnace, and the sensor resistance is measured at a series of six temperature levels from room temperature up to  $500^\circ\text{F}$  for wires used in Tunnel A and seven temperature levels up to  $900^\circ\text{F}$  for wires used in Tunnel B. At each oven temperature level the sensor resistance is measured at each of six wire heating currents up to 1.2 ma for  $50\text{-}\mu\text{in.}-\text{diam}$  wires and up to 0.6 ma for  $20\text{-}\mu\text{in.}-\text{diam}$  wires. At each temperature level the results, in the form of measured resistance *versus* heating current-squared (for example, see Fig. A-1), are extrapolated to zero current using a first order, least squares curve fit. Data from the various temperature levels are combined in the form of zero-current resistance *versus* temperature (Fig. A-2) according to the formula  $R = R_r[1 + \alpha_r(T - T_r)]$ . A first-order, least squares fit of the data yields the sensor reference resistance,  $R_r$ , at  $\bar{T} = \bar{T}_r$  and the linear coefficient of resistivity. Wires of platinum-10 percent rhodium alloy of  $10\text{-}\mu\text{in. diam}$  were found to have a zero second-order temperature coefficient of resistivity by Philco-Ford (Ref. 22) and earlier, for  $50\text{-}\mu\text{in.}-\text{diam}$  wires, by Spangenberg (Ref. 39). This finding was assumed to be valid for the 20- and  $50\text{-}\mu\text{in.}-\text{diam}$  wires used for the tunnel free-stream measurements of the present report.

The second calibration of the probes is made in the wind tunnel to determine the relationship of wire heat-loss coefficient (Nusselt number) and wire temperature recovery factor as functions of the wire Reynolds number. (For example, see Fig. A-3.) This Reynolds number (Ref. 29) is calculated using local density and velocity and the dynamic viscosity based on local total temperature. The wire diameter is used as the characteristic length. The Reynolds number variations are obtained by varying the tunnel total pressure,  $PT$ , while holding the tunnel total temperature,  $TT$ , nominally constant. Each wire was calibrated at the free-stream Mach number(s) for which it was used. The Nusselt number and recovery factor can be considered independent of Mach number for  $M_\infty \geq 1.5$  (Ref. 29).

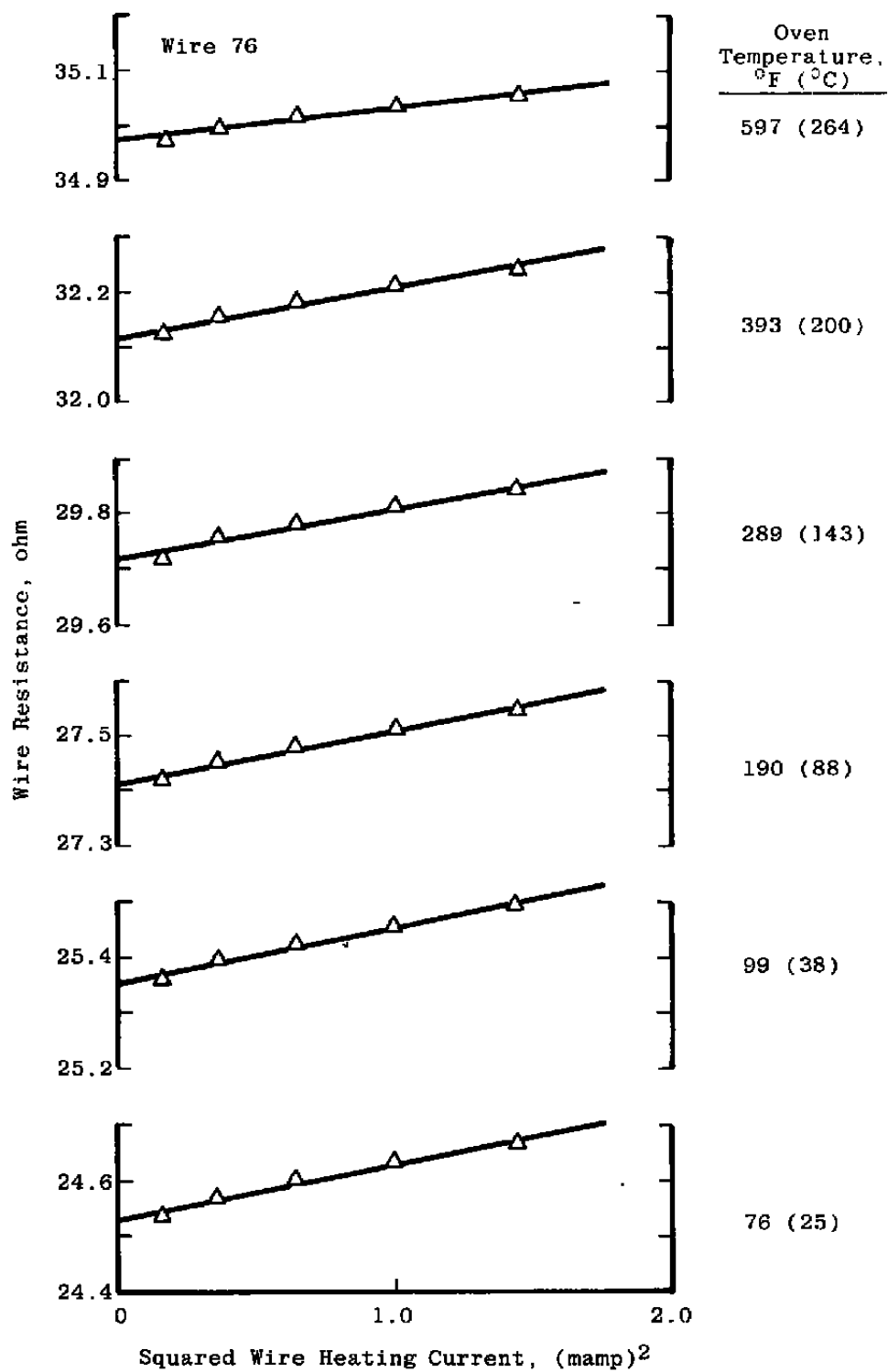


Figure A-1. Typical oven calibration measurements.

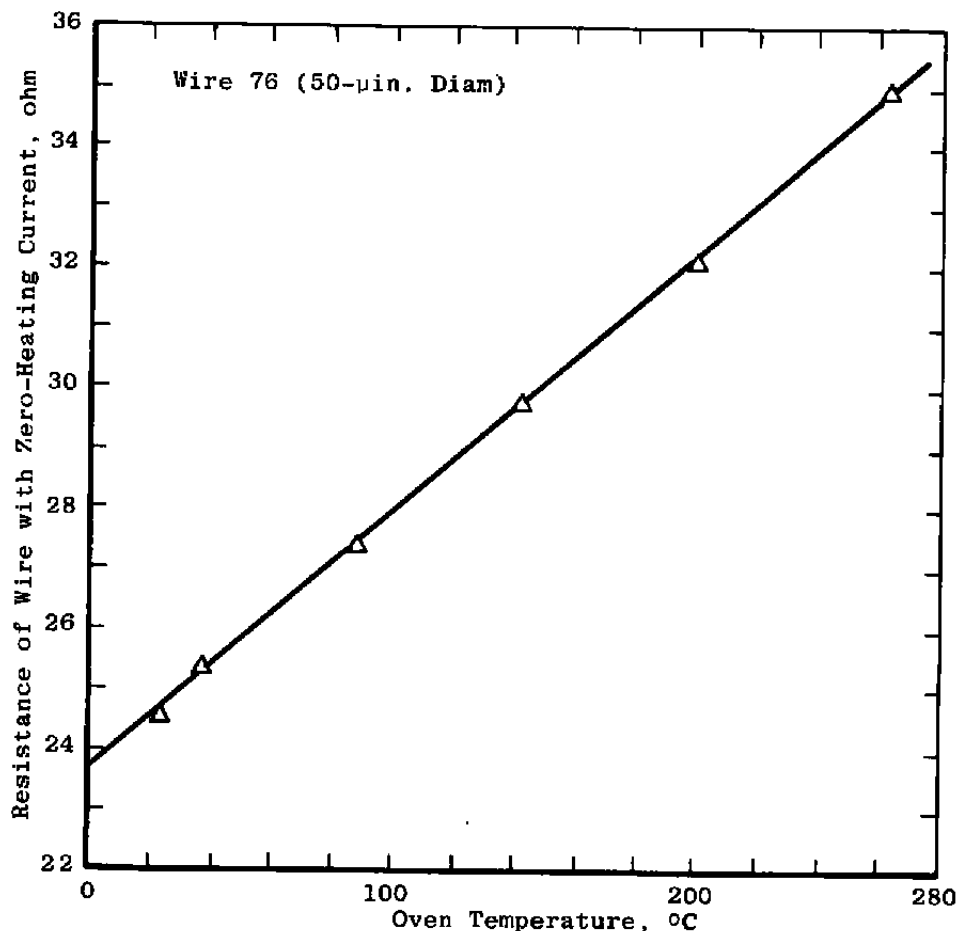


Figure A-2. Typical oven calibration results.

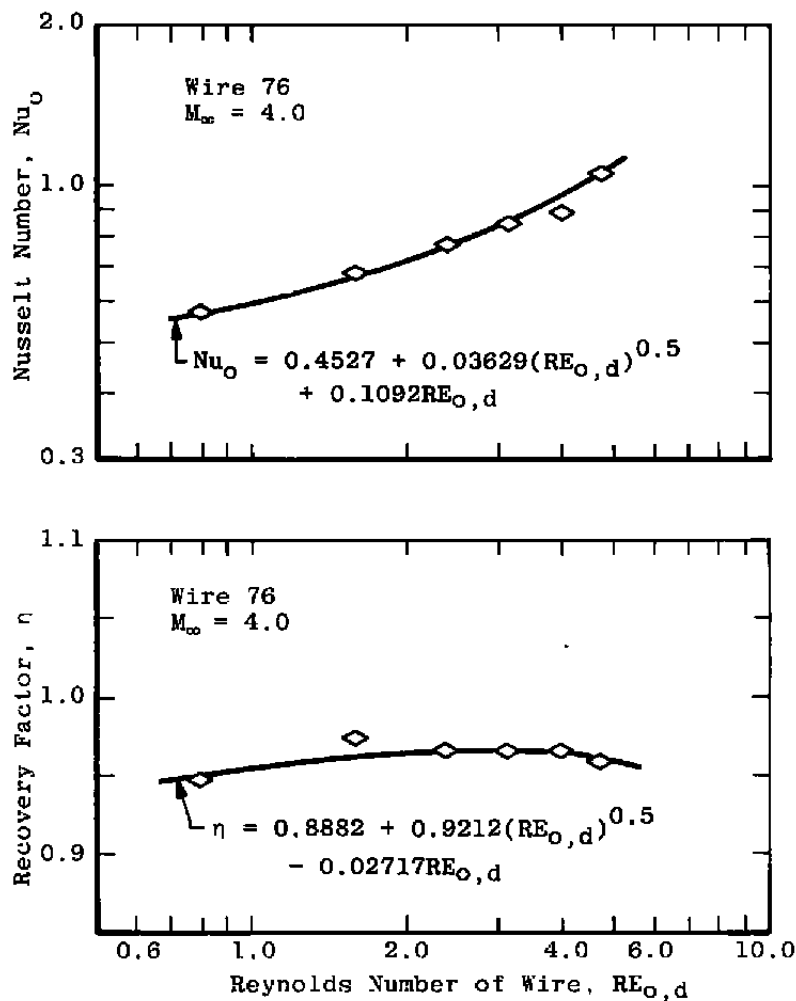


Figure A-3. Typical flow calibration results.

## APPENDIX B

### DYNAMIC PRESSURE SENSOR CALIBRATION

#### B.1.0 INTRODUCTION

In some cases, dynamic calibrations of the DPS transducers were obtained using the VKF shock tube. In each calibration, the shock tube subjected the transducer to a known transient pressure input closely resembling a step. Analysis of the transducer response generated a useful calibration in the form of a transfer function. A description of the apparatus and general procedure, with results, follows.

Tables B-1 and B-2 summarize the d-c calibration results of the transducers used in this study. In some cases the effects of subatmospheric environmental pressure level on the gage calibrations are included.

#### B.2.0 APPARATUS

##### B.2.1 SHOCK TUBE

The VKF shock tube, shown in Fig. B-1, is approximately 10 ft long with an inside diameter of 2.5 in. A Mylar® diaphragm separates the high-pressure "driving" section from the low-pressure "driven" section, the latter being approximately 8 ft in length. When a sufficient pressure differential is developed across the diaphragm, it ruptures, producing a shock wave. The wave travels down the tube past a strut-supported hemisphere-cylinder pressure probe. The transducer, mounted flush at the probe tip, experiences a sudden rise in pressure and temperature corresponding to the establishment of supersonic flow behind the shock. Following 400 to 850  $\mu$ sec of steady flow the reflected waves return and result in flow breakdown.

The shock wave strength and velocity determine the magnitude of the pressure rise imposed on the probe. These factors are, in turn, determined by the pressure ratio across the diaphragm. As the shock tube lacks a mechanical diaphragm puncture mechanism, the primary controls are the driven section charge pressure and diaphragm thickness. To fire the tube, the driver section pressure is gradually increased until the diaphragm ruptures. However, as will be shown in Section B.4.0, the shock tube conditions are highly repeatable. The measured parameters include the driven section temperature, the driven section initial pressure, and the shock velocity. The shock velocity, ( $V_s$ ), is determined by measuring the time required for the shock to travel a known distance along the tube. Two highly responsive thin film resistance thermometers, located 1.001 ft apart along the tube, are used to detect

the passing of the shock. An electronic counter measures the time between the responses of the temperature probes (see Fig. B-2).

### B.2.2 DATA SYSTEM

The data acquisition hardware is illustrated schematically in Fig. B-1. During a calibration run the transducer output signal is conditioned, amplified, and recorded on analog tape at maximum tape speed, 120 in./sec. Following the run, the spectral analyzer is used to digitize the analog data. To maximize the number of digital data points characterizing the short event, the tape is run at a lower speed, 30 in./sec, during playback while the analyzer samples at a maximum frequency of 307.2 kHz. Compensating for the factor of four reduction in tape speed produces an effective sample frequency of 1228.8 kHz. The analyzer utilizes 1,024 points to define the transducer output. It is capable of filtering the output to prevent aliasing, transforming the output into the frequency domain, and obtaining transfer functions with the assumption of a pure step input. The minicomputer records the analyzer results on disk. The data are then available for plotting on a graphics terminal. The minicomputer also serves as an interface with the facility computer. The calibrations can be transferred to the facility computer for use in more detailed calibration analysis and in wind tunnel test data reduction.

### B.3.0 DATA REDUCTION

A transfer function is generated by analyzing the transducer response to a known transient pressure input. The pressure input produced in the shock tube can be characterized as a perfect step or a modified step, technically representing all frequencies in the spectrum. The modified step, the overshoot, accounts for the transient establishment of the probe bow shock, requiring a finite time following the passage of the tube shock. Modified inputs can be generated analytically or by using extremely responsive transducers, such as the PCB-113, to define the shape for less responsive transducers. Pure step inputs are utilized in this Appendix for illustration purposes. Figure B-2 presents the analytical expressions used to calculate the step input from shock tube measurements.

The analysis of the dynamic pressure data is performed in the frequency domain. The time domain and frequency domain representations of analog data are related by the continuous Fourier transform pair:

$$H(f) = \int_{-\infty}^{\infty} h(t) e^{-j2\pi ft} dt \quad (\text{Forward Transform})$$

$$h(t) = \int_{-\infty}^{\infty} H(f) e^{j2\pi ft} df \quad (\text{Inverse Transform})$$

Digital (sampled) data are transformed using the discrete Fourier transform:

$$H\left(\frac{n}{NT}\right) = \sum_{k=0}^{N-1} h(kt) e^{-j2\pi nk/N} \quad (\text{Forward Transform})$$

$$h(kt) = \frac{1}{N} \sum_{n=0}^{N-1} H\left(\frac{n}{NT}\right) e^{j2\pi nk/N} \quad (\text{Inverse Transform})$$

The spectral analyzer and facility computer calculate the discrete transform using an algorithm called the fast Fourier transform, or FFT. The FFT greatly reduces the number of numerical operations required to define the transform, and therefore the FFT is a practical tool for dynamic data analysis.

A data point in the frequency domain can be represented by a complex number or an amplitude and phase angle. The representations are related as follows;

$$|H(f)| = \sqrt{R^2(f) + I^2(f)}$$

$$\phi(f) = \text{Tan}^{-1}[I(f)/R(f)]$$

where

$|H(f)|$  = Amplitude of the transform

$\phi(f)$  = Phase angle

$R(f)$  = Real part of the complex representation

$I(f)$  = Imaginary part

The amplitude/phase angle representation was used as the dynamic pressure transducer calibration.

Filtering is required when the data are digitized to prevent frequency foldover, or aliasing, in the frequency domain. The sample rate must be at least twice the maximum frequency present in the analog signal. The spectral analyzer applies the appropriate low-pass filter when the data are digitized. The filter cutoff frequency of the analyzer, corresponding to the 307.2-kHz maximum sample rate, is 120 kHz. When one compensates for the tape speed reduction (a factor of 4) during digitization, the effective cutoff frequency becomes 480 kHz.

Leakage in the frequency domain is reduced by applying one of several types of windows. The spectral analyzer windows the data using either a weighted rectangular window or a Kaiser-Bessel weighting function. The calibration program, on the facility computer, uses a subtraction scheme to window the data. A point near the center of the data, point 570 for example, is selected as the start point of the window. The remaining points are then redefined by subtracting consecutive points in the first half of the data from the window start point. The result is that the data contain the transient characteristics of the original signal with equal-valued end points. Other window techniques, such as the Kaiser-Bessel weighting, can easily be added to the calibration program. The effects of the window cancel during the calculation of the transfer function.

The procedure for generating pressure transducer transfer functions on the facility computer is illustrated in Fig. B-3. The transducer output signal and the input curve are compared to determine the d-c scale factor. The transducer output signal is multiplied by the d-c scale factor to convert from mv to psi. The input curve and output signal, in psi, are windowed and plotted together to check for time alignment. A misalignment is corrected by time shifting (signal rotation). The input curve and output signal are then transformed into the frequency domain. The transfer function is formed by calculating the quotient of the amplitudes and the difference between the phase angles as follows:

$$|H(f)|_{\text{Transfer}} = H(f)_{\text{Input}} / H(f)_{\text{Output}}$$

$$\phi(f)_{\text{Transfer}} = \phi(f)_{\text{Input}} - \phi(f)_{\text{Output}}$$

The transfer function, applied to wind tunnel test data, removes transducer response effects and thus reveals the true pressure input. The procedure is presented in Fig. B-4. The transducer output is converted to psi through multiplication with the d-c scale factor and is transformed into the frequency domain. The transfer function is applied to obtain the true input to the transducer:

$$|H(f)|_{\text{Test}} = |H(f)|_{\text{Transfer}} \cdot |H(f)|_{\text{Test}}$$

$$\text{Input} \qquad \qquad \qquad \text{Output}$$

$$\phi(f)_{\text{Test}} = \phi(f)_{\text{Transfer}} + \phi(f)_{\text{Test}}$$

$$\text{Input} \qquad \qquad \qquad \text{Output}$$

The true input, representing the pressure fluctuations experienced by the transducer, is then ready for analysis.

#### B.4.0 RESULTS AND DISCUSSION

The following dynamic pressure transducers were calibrated in support of the present research effort:

<u>Transducer</u>	<u>Serial No.</u>
PCB-113A21	1446
PCB-113A21	1447
PCB-112A21	1407
PCB-105A	568
PCB-106A	248
Kulite CQ-080-5	J1-36
Kulite CQ-080-5	J1-37
Endevco 8510-5	DM-43
Endevco 8510-5	DN-76

Three optimum shot conditions were used:

<u>Diaphragm</u>	<u>T1, °R</u>	<u>P1, psi</u>	<u>Δt, usec</u>	<u>PD1-P1, psi</u>
2 Layers, 0.002-in. Mylar	533	0.327	321	7.40
1 Layer, 0.002-in. Mylar	↓	0.135	312	3.36
1 Layer, 0.002-in. Mylar	↓	0.0234	262	1.02

The repeatability in the shot conditions is illustrated in Fig. B-5.

Sample calibrations are presented in Figs. B-6 through B-9 for the PCB-112 A21 (1407), PCB-113A21 (1447), PCB-105A (568), and the ENDEVCO B510-5 (DN-43), respectively. Each figure presents the example, step by step, in accordance with Fig. B-3. It should be noted that the signal noise was not averaged out in the examples.

The PCB-112A21 and PCB-105A have manufacturer's quoted resonant frequencies of 250 kHz which are clearly visible in the transfer functions. The response is relatively flat at the frequencies below resonance. The PCB-113A21 has a manufacturer's quoted resonant frequency of 500 kHz, which is beyond the useful frequency range of the transfer function. The decay in the PCB-105A transducer output is due to the temperature sensitivity of the transducer, which affects only low-frequency response of the transducer. This temperature effect has a negligible influence on the overall dynamic characteristics of the transducer. An RTV cap, nominally 0.015 in. thick, placed over the transducer attenuates the overall level of the response about 6 db. Although not shown, the variation of the transfer function across the frequency spectrum is not significantly affected.

The remaining factor which can alter the output of the transducer is its physical size and the local convective velocity of the pressure disturbance over the transducer surface. The diameters of the present transducer varied in size from 0.099 to 0.40 in. Most of the results presented in this report were obtained with a 0.099-in.-diam transducer.

G. M. Corcos (Ref.35) formulated a theoretical correction factor to account for the attenuation in the output of a finite size transducer. For convience purposes and future reference, these correction factors were curve fitted as follows.

1. Range:  $0.050 \geq \omega r/u_c \geq 1.00$

$$F_m/F = \sum_{n=0}^5 A_n (\omega r/u_c)^n$$

$$A_0 = 3.01394$$

$$A_1 = -4.33121$$

$$A_2 = 3.63664$$

$$A_3 = -1.68194$$

$$A_4 = 0.39941$$

$$A_5 = -0.03814$$

2. Range:  $1.00 \geq \omega r/u_c \geq 2.40$

$$A_0 = 1.25246$$

$$A_1 = -0.48254$$

$$A_2 = 0.098501$$

$$A_3 = -0.011444$$

$$A_4 = 0.00070593$$

$$A_5 = -0.000017893$$

3. Range:  $2.40 \geq \omega r/u_c \geq 3.5$

$$F_m/F = 3.29364 \exp [-1.50675 (\omega r/u_c)]$$

4. Range:  $3.5 \geq \omega r/u_c$

$$F_m/F = B_o (\omega r/u_c)^{-B_1}$$

Range	$B_0$	$B_1$
$3.5 > \omega r/u_c \geq 5.0$	0.090844	1.3184
$5.0 > \omega r/u_c$	0.50127	2.3835

Figure B-10 illustrates the type of correction that would have to be applied to, for example, a power spectrum for each of the three sizes of transducers used in the present study assuming the local convective velocity is 1,140 ft/sec. Since a major portion of the present data was obtained with a 0.099 in.-diam PCB, a smaller transducer, and in a flow field with higher convective velocities; the Corcos attenuation factor was not applied to the present results. Note that the Corcos factor is at a maximum at the higher frequencies where the signal content in the measured pressure spectra is usually smallest (i.e., negligible).

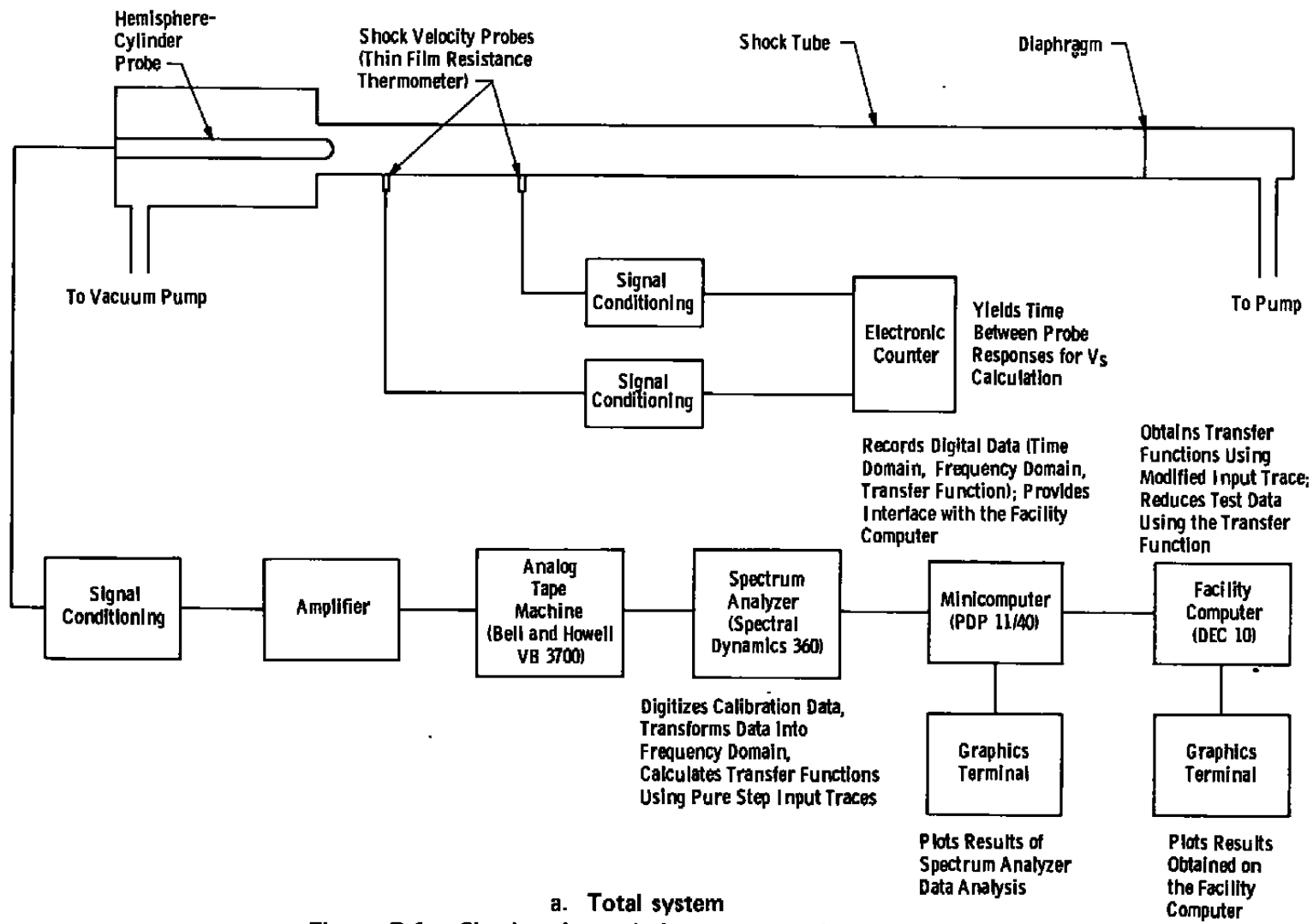
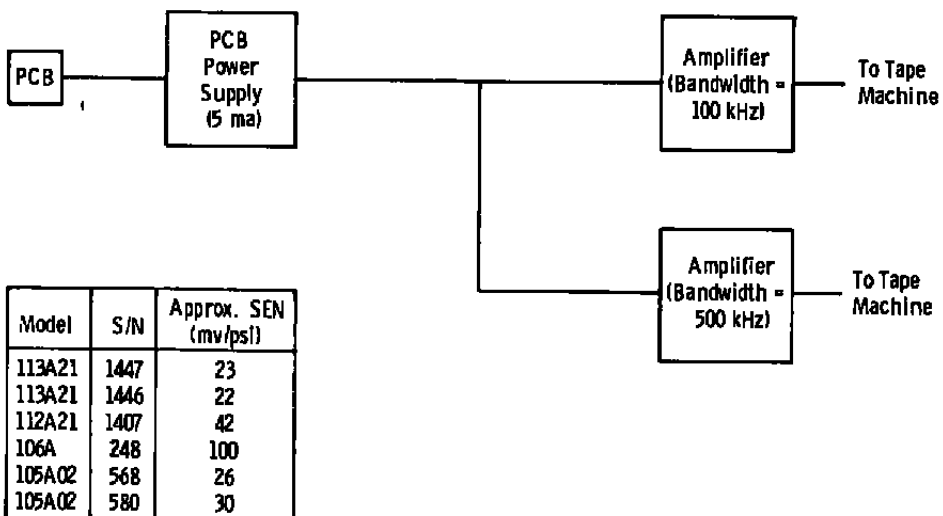
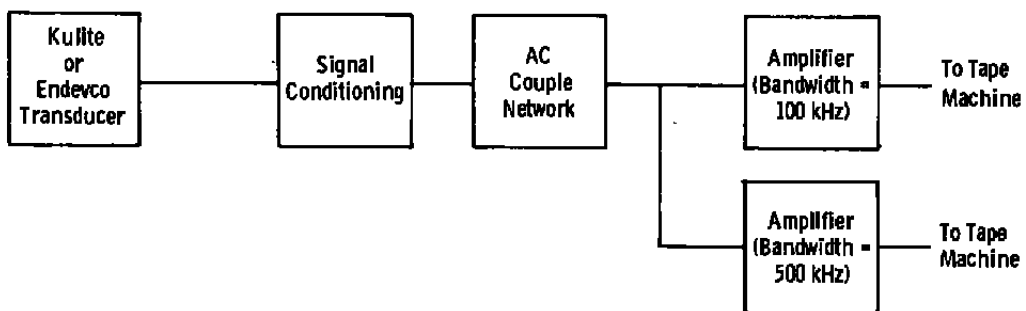


Figure B-1. Shock tube and data system schematic.



**b. PCB® transducer signal conditioning**

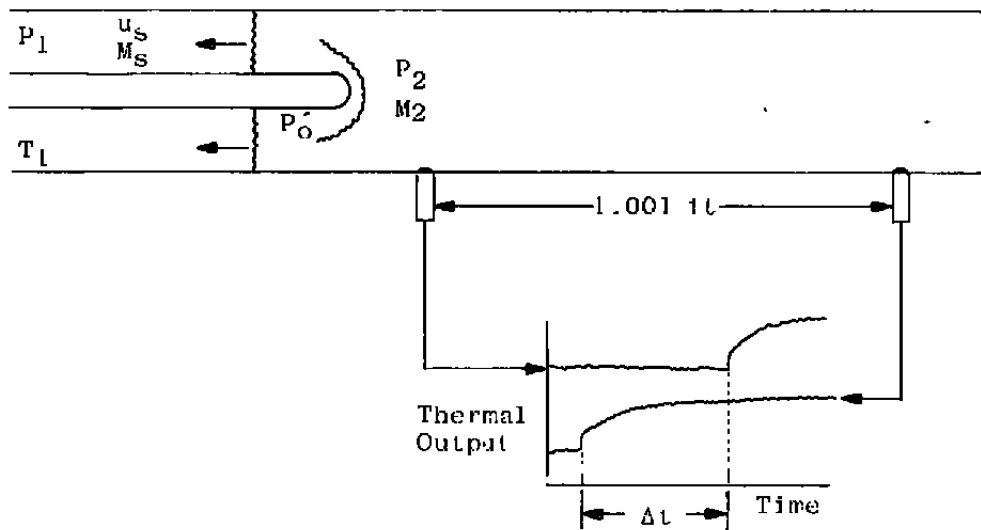
Figure B-1. Continued.



Transducer	Excitation, VDC	Scale Factor, mv/psi	Bridge Resistance, $\Omega$
J1-36 (Kulite)	5	15.7	2,500
J1-37 (Kulite)	5	15.5	2,500
G1-51 (Kulite)	15	12.0	3,500
8510-5 (Endevco)	10	≈ 70.0	1,800

**c. Kulite and Endevco transducer signal conditioning**

Figure B-1. Concluded.



#### Calculation of Step Input

##### I. Tube Shock Wave Velocity and Mach Number:

$$u_s = 1.001/\Delta t$$

$$M_s = u_s / [(49.0223)\sqrt{T_1}]$$

##### II. Mach Number in Supersonic Flow Region Behind Shock:

$$M_2 = 2(M_s^2 - 1) / \left[ \sqrt{[2\gamma M_s^2 - (\gamma - 1)]} \left[ (\gamma - 1)M_s^2 + 2 \right] \right]$$

##### III. Pressure Ratios Based on $M_2$ and $M_s$ :

$$P_2/P_1 = \left[ 2\gamma M_s^2 - (\gamma - 1) \right] / (\gamma + 1)$$

$$P_p/P_2 = \left[ (\gamma + 1)M_2^2 / 2 \right]^{\gamma / (\gamma - 1)}$$

$$\times \left[ (\gamma + 1) / \left( 2\gamma M_2^2 - (\gamma - 1) \right) \right]^{1 / (\gamma - 1)}$$

##### IV. Pressure Step.

$$P_p = (P_p/P_2)(P_2/P_1)(P_1)$$

Figure B-2. Calculation of shock tube pressure step.

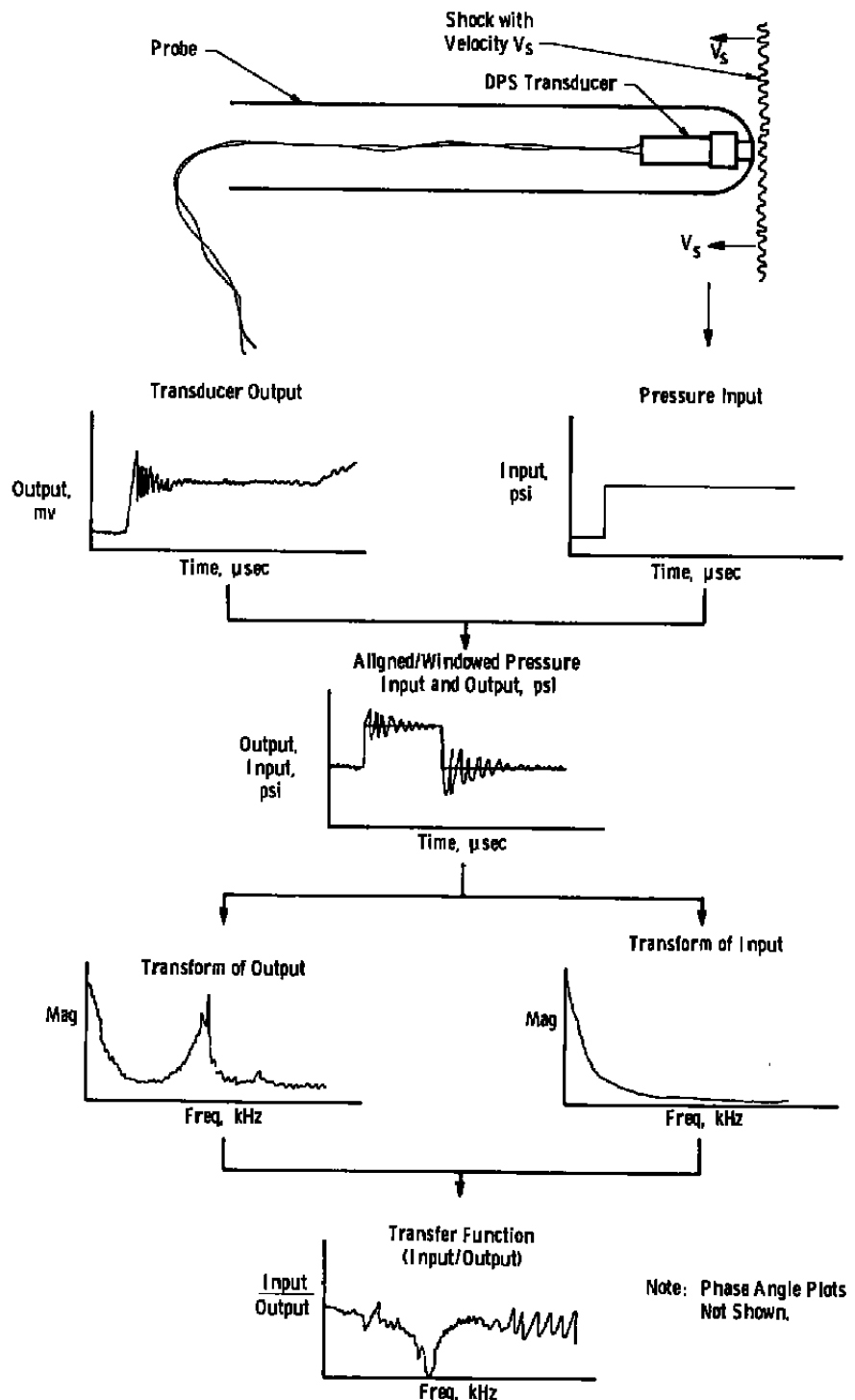


Figure B-3. Dynamic calibration data reduction.

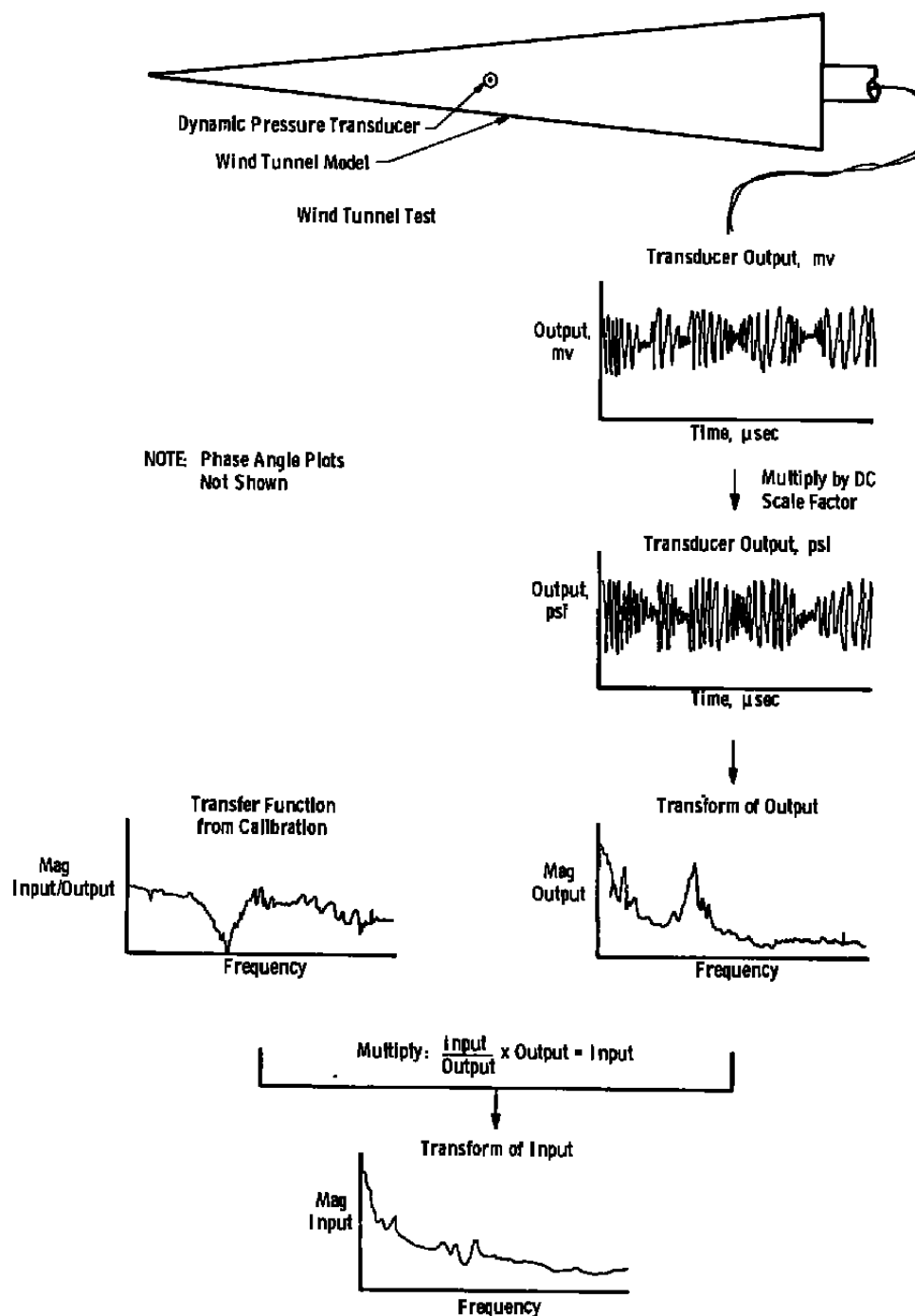


Figure B-4. Wind tunnel test data reduction using dynamic calibration.

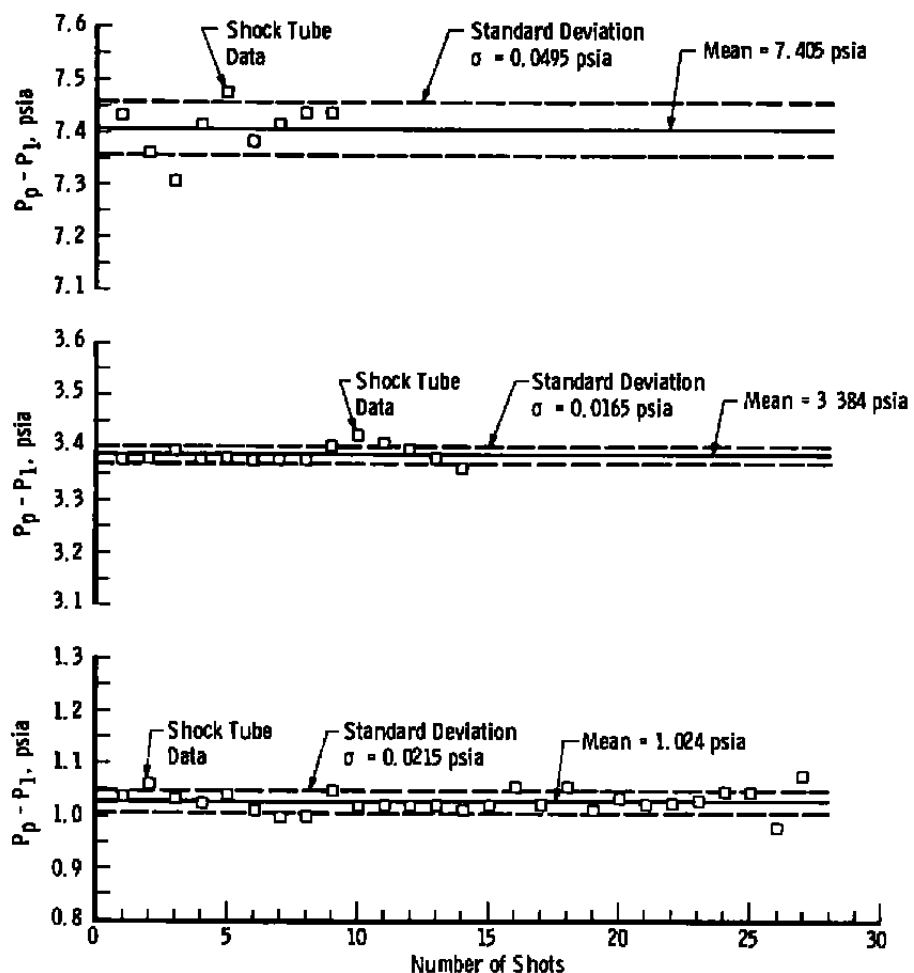
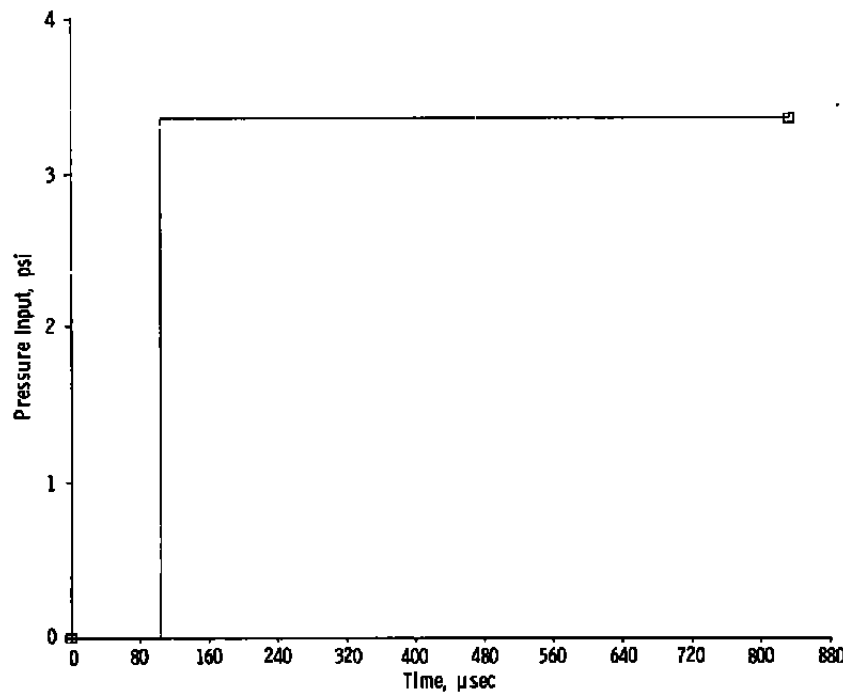
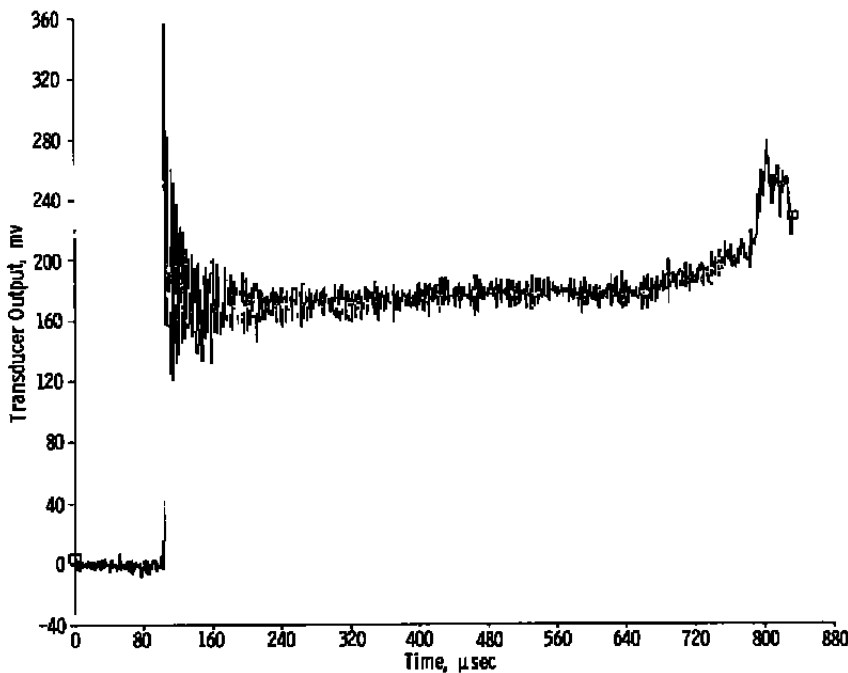


Figure B-5. Shock tube repeatability.

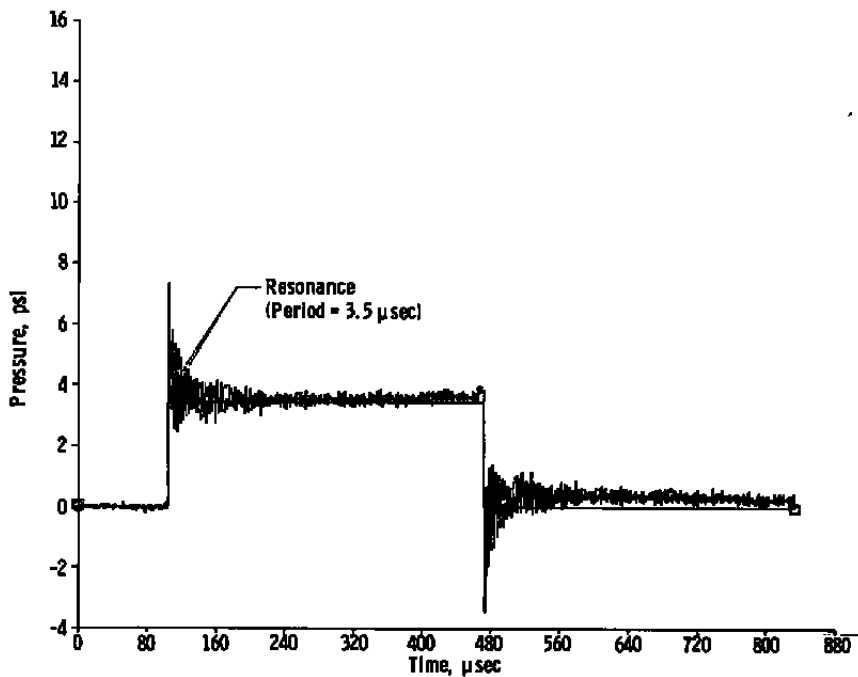


a. Step input

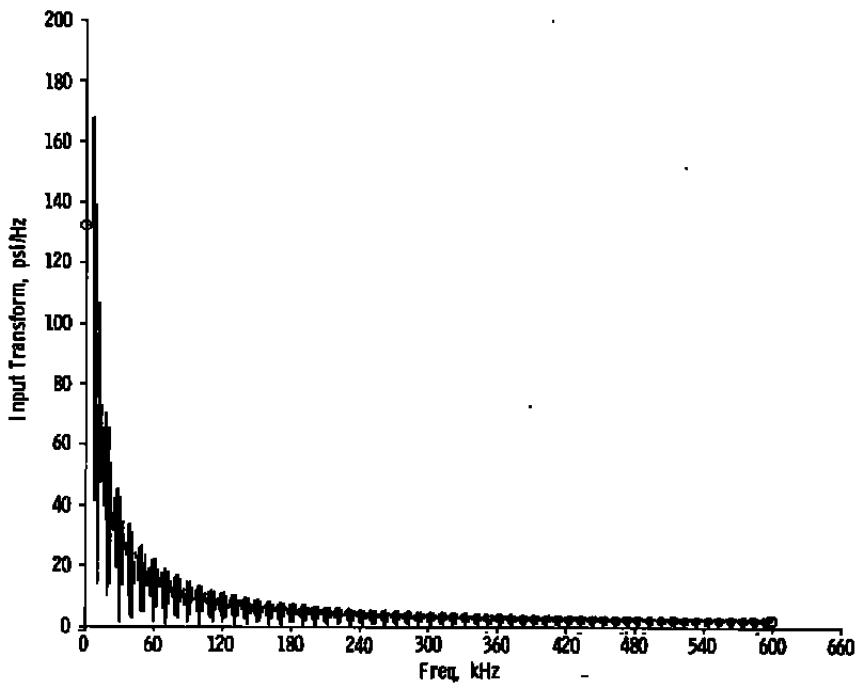


b. Transducer response to step input

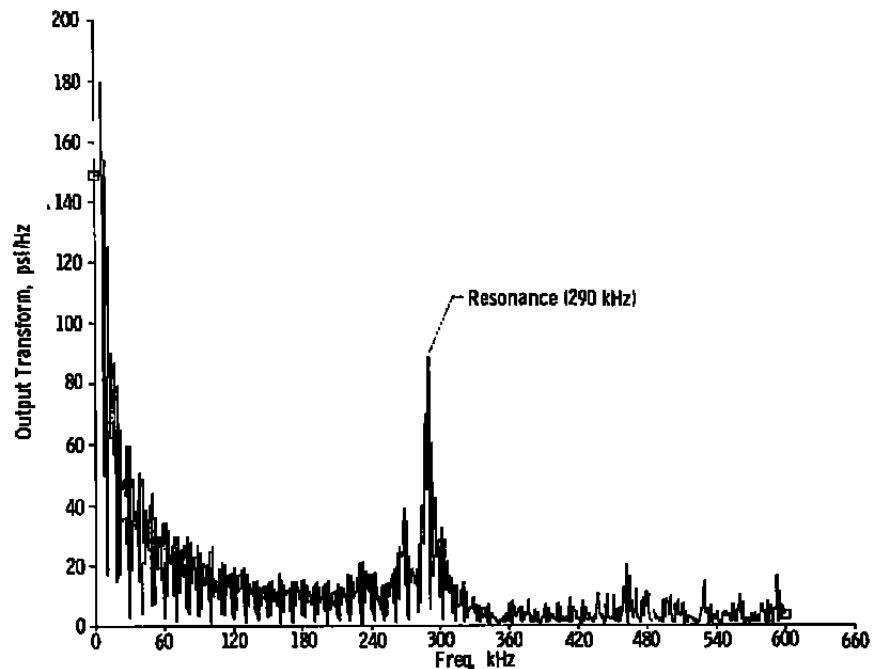
Figure B-6. Dynamic calibration of a PCB-112A21 (1407).



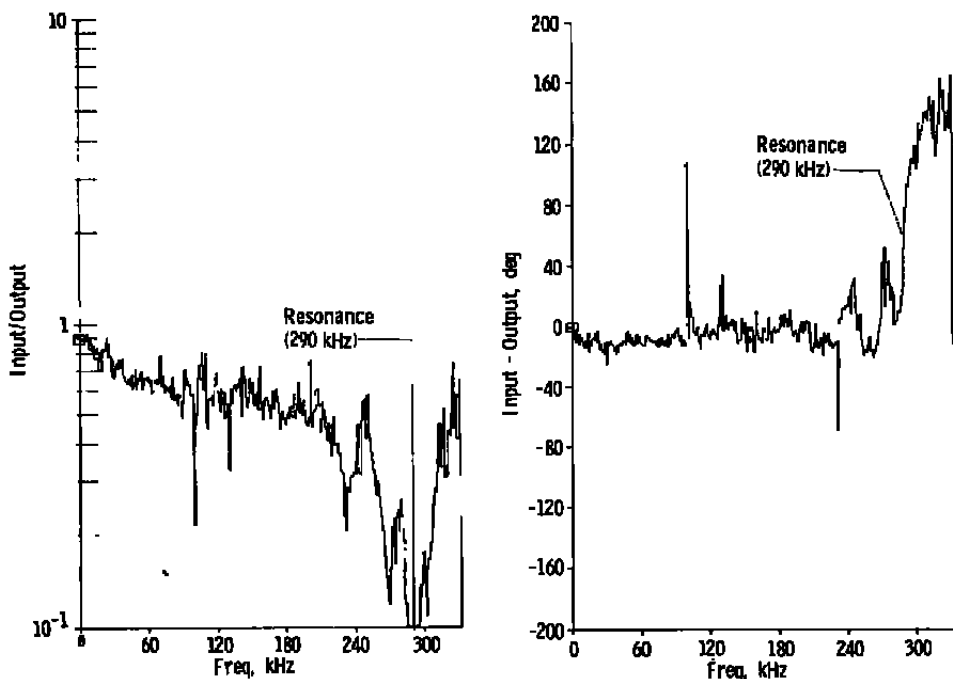
c. Input and output aligned in time and windowed



d. Transform of step input  
Figure B-6. Continued.

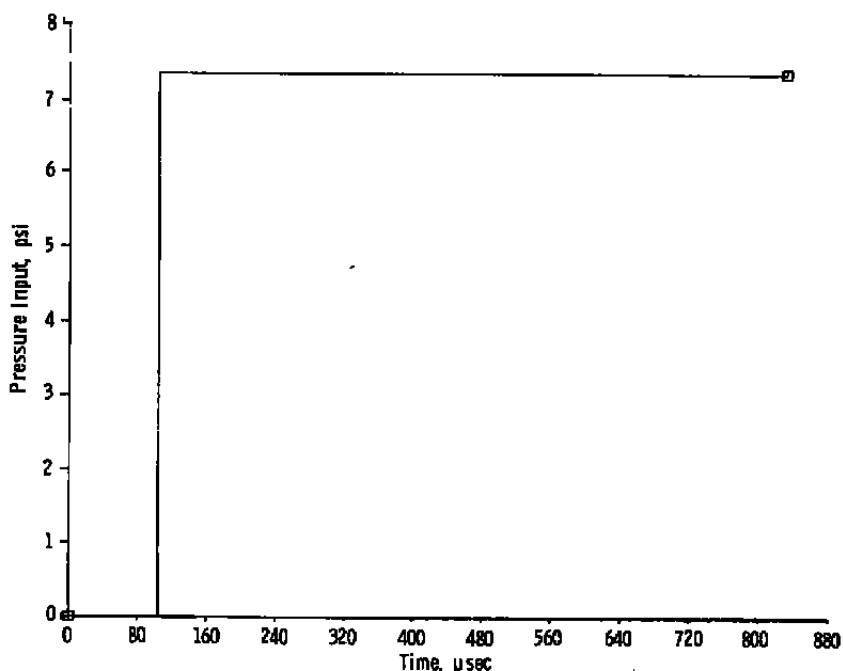


e. Transform of transducer response

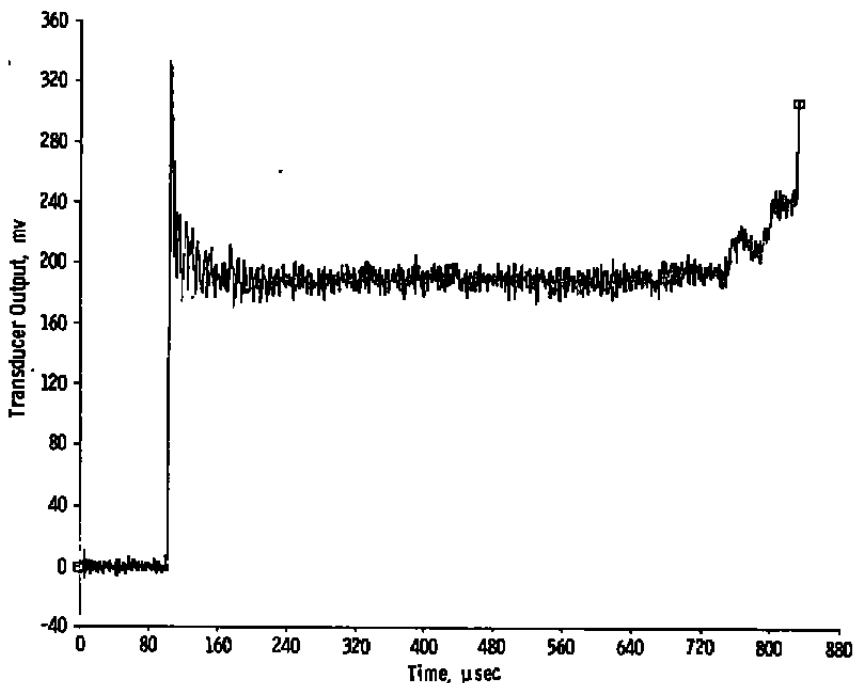


f. Transfer function

Figure B-6. Concluded.

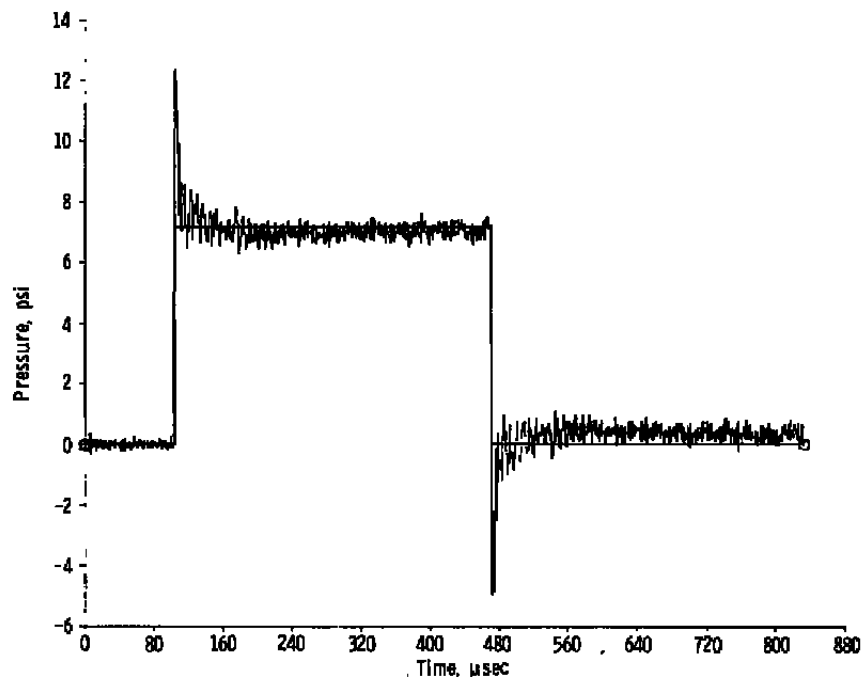


a. Step input

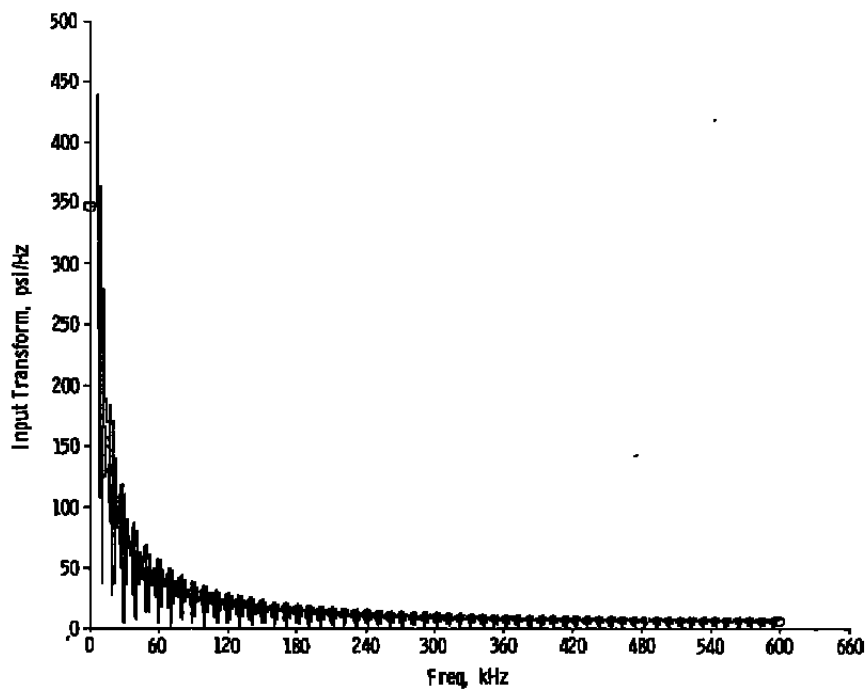


b. Transducer response to step input

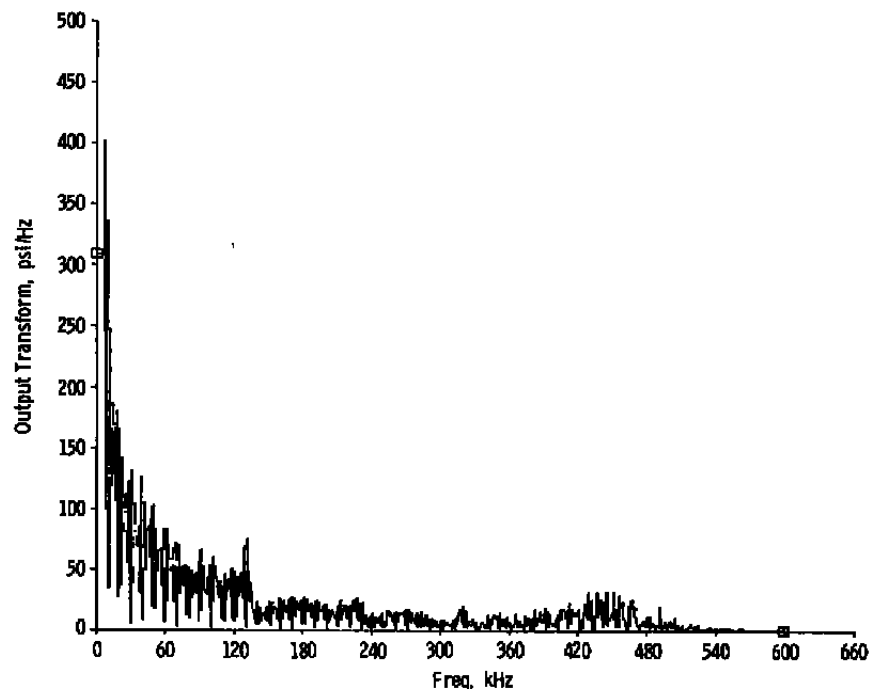
Figure B-7. Dynamic calibration of a PCB-113A21.



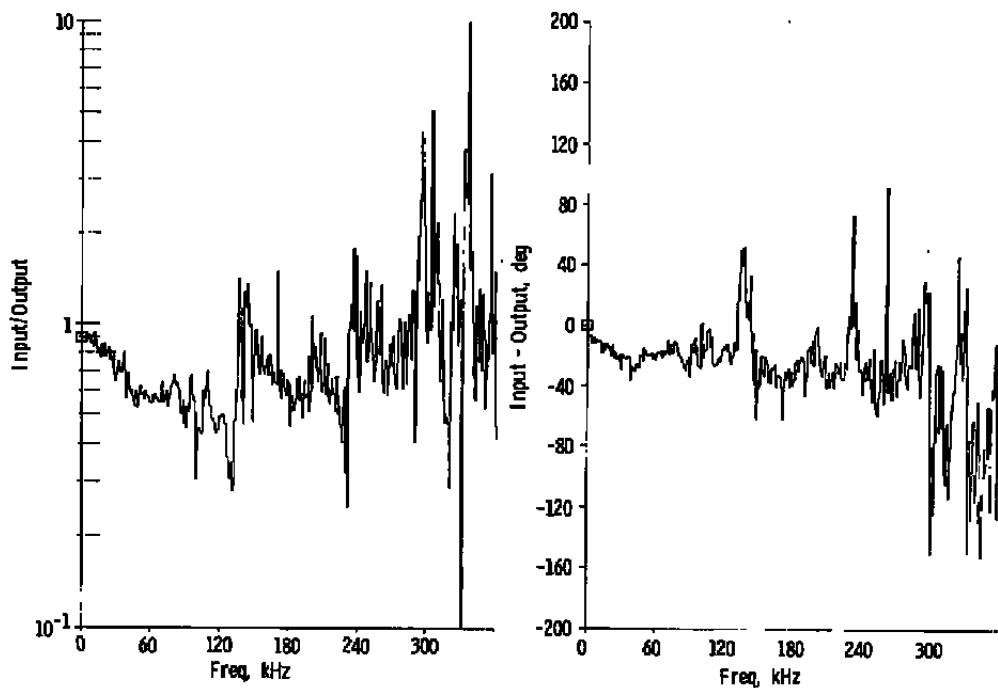
c. Input and output aligned in time and windowed.

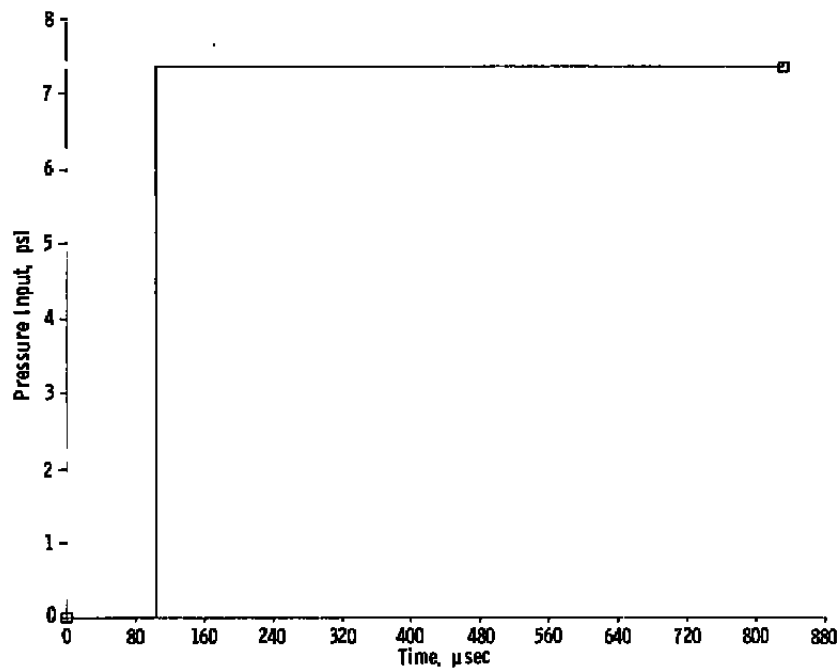


d. Transform of step input  
Figure B-7. Continued.

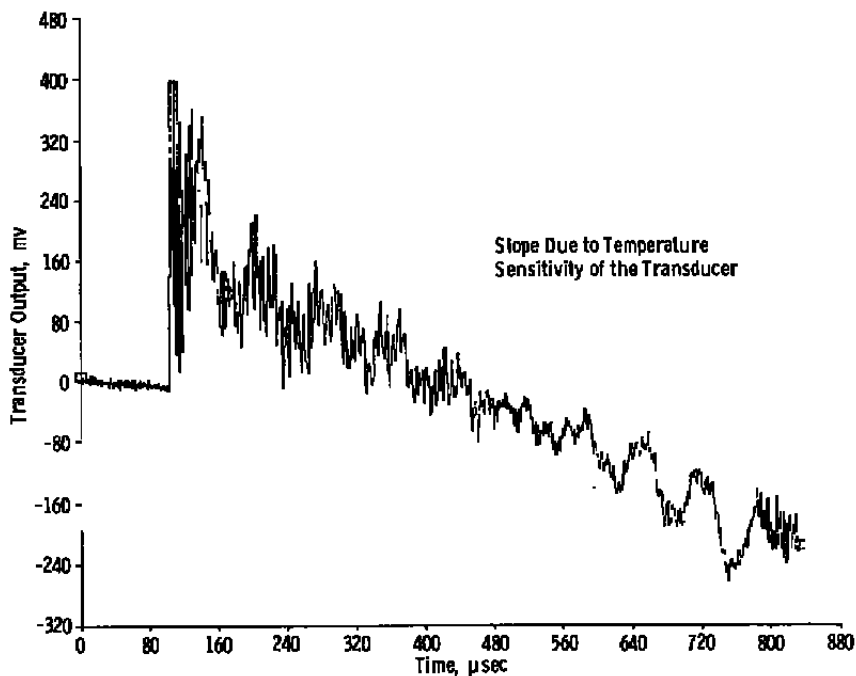


e. Transform of transducer response

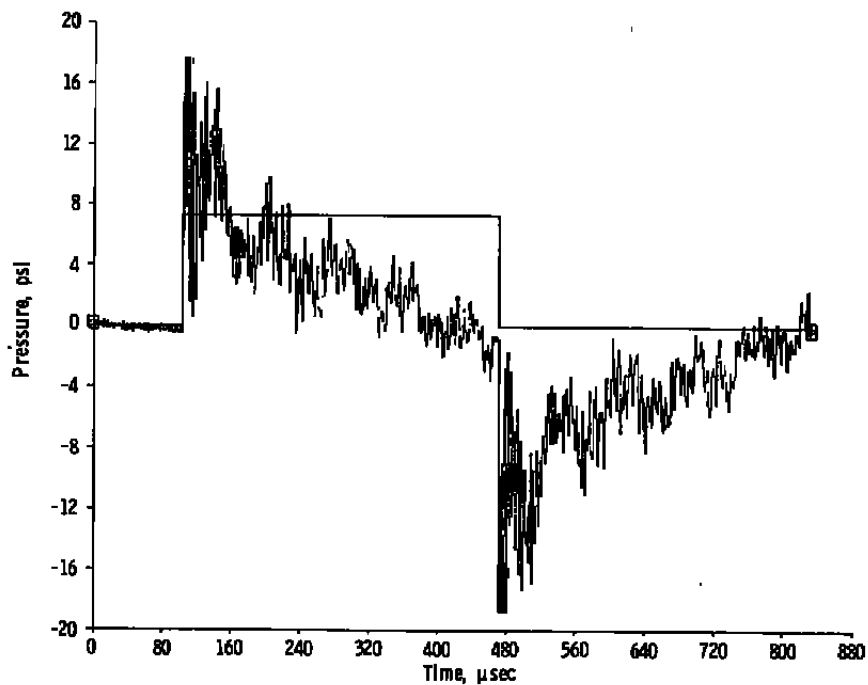
f. Transfer function  
Figure B-7. Concluded.



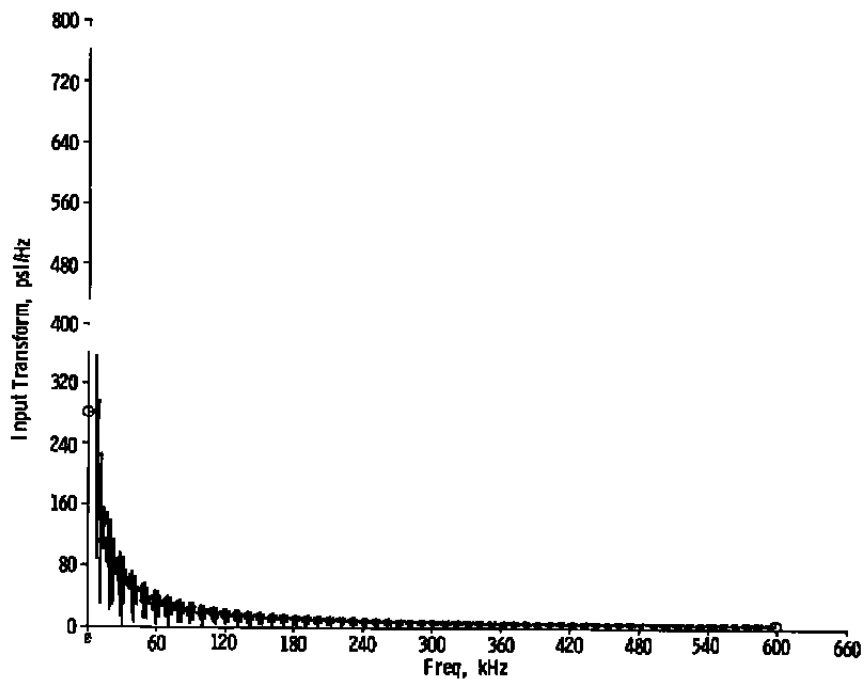
a. Step input



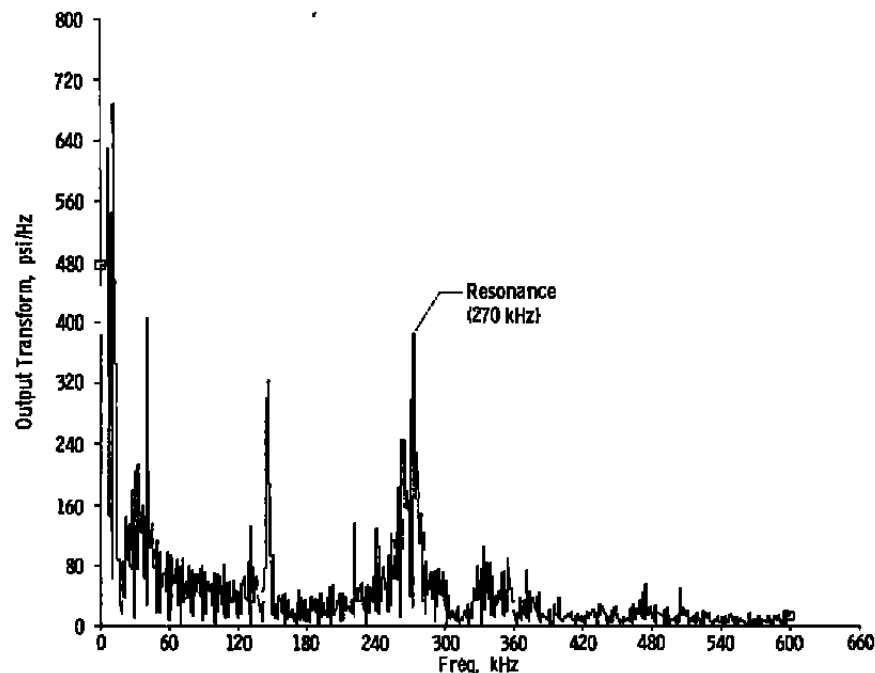
b. Transducer response to step input  
Figure B-8. Dynamic calibration of a PCB-105A.



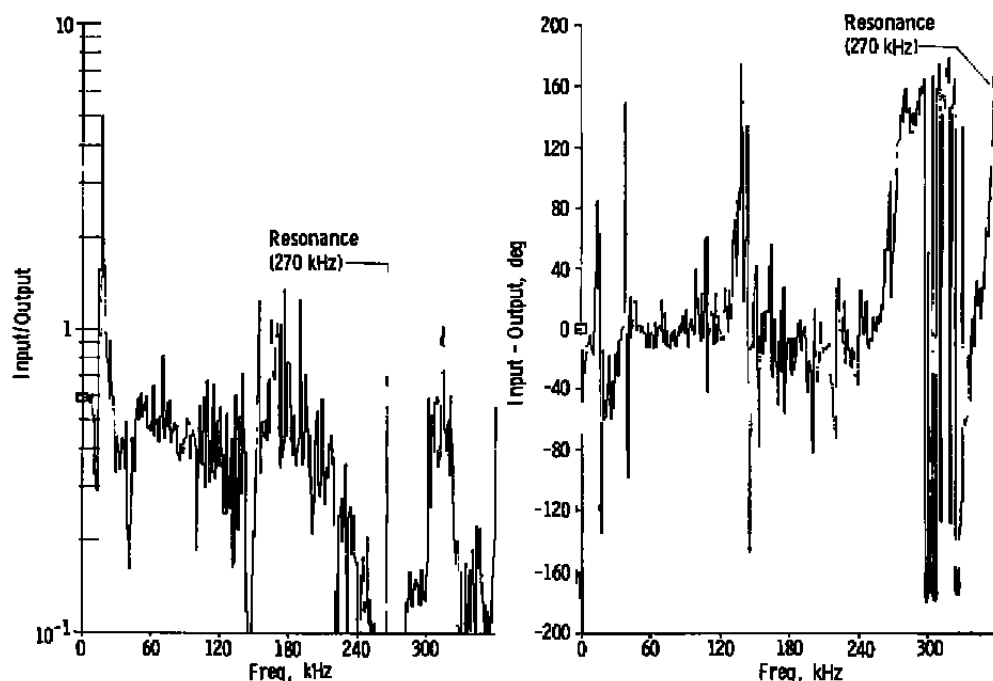
c. Input and output aligned in time and windowed



d. Transform of step input  
Figure B-8. Continued.

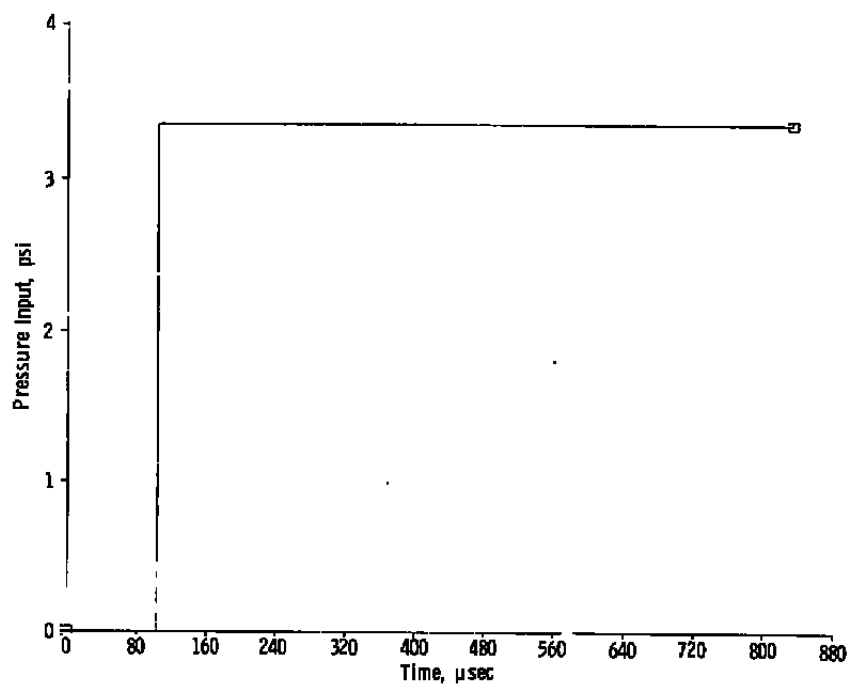


e. Transform of transducer response

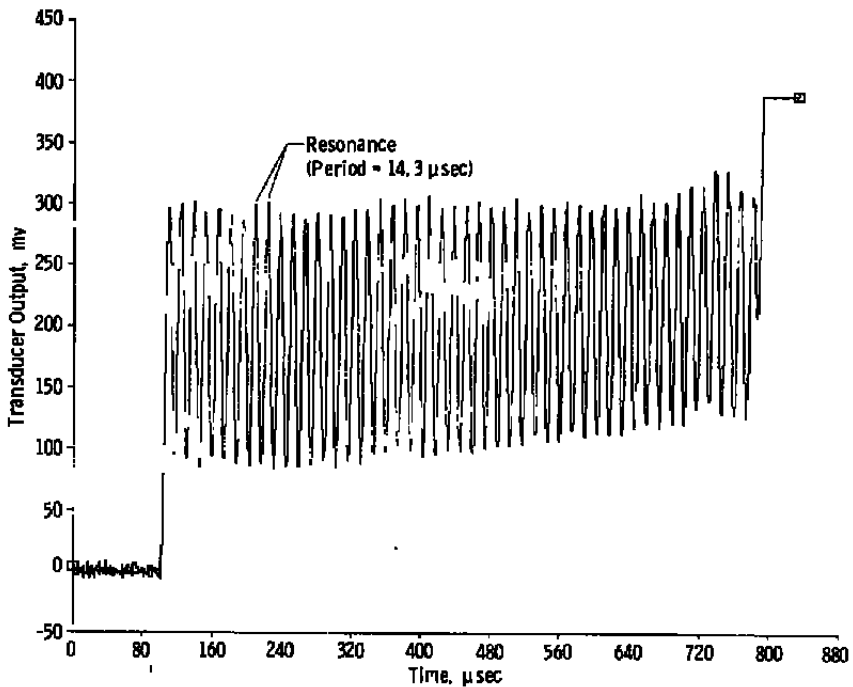


f. Transfer function

Figure B-8. Concluded.

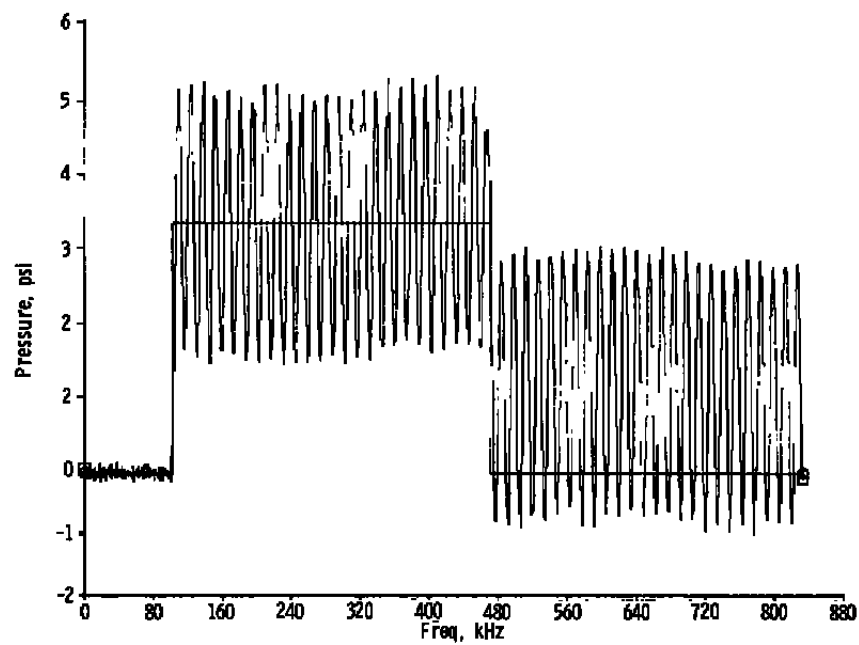


a. Step input

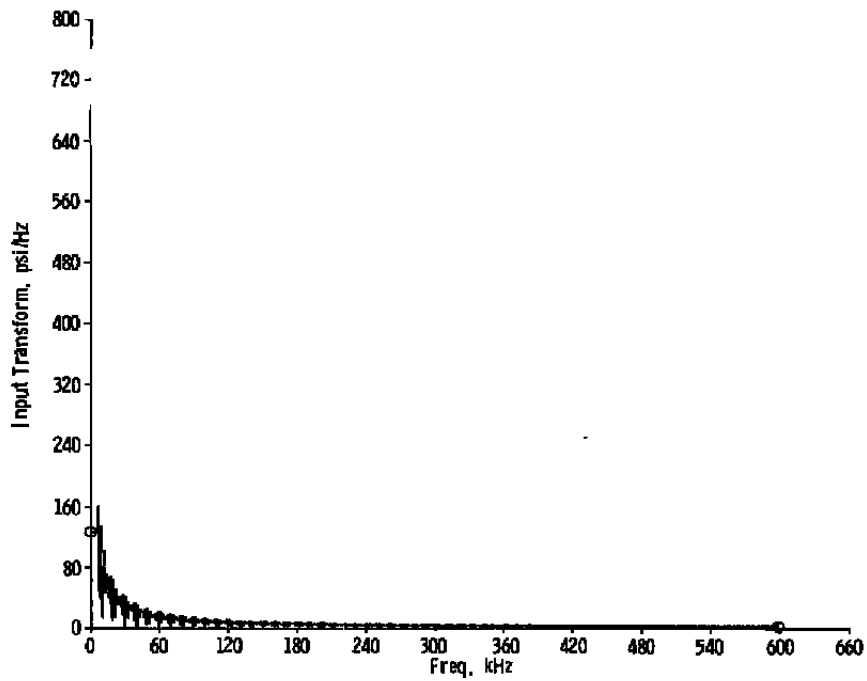


b. Transducer response to step input

Figure B-9. Dynamic calibration of an Endevco 8510-5 transducer.

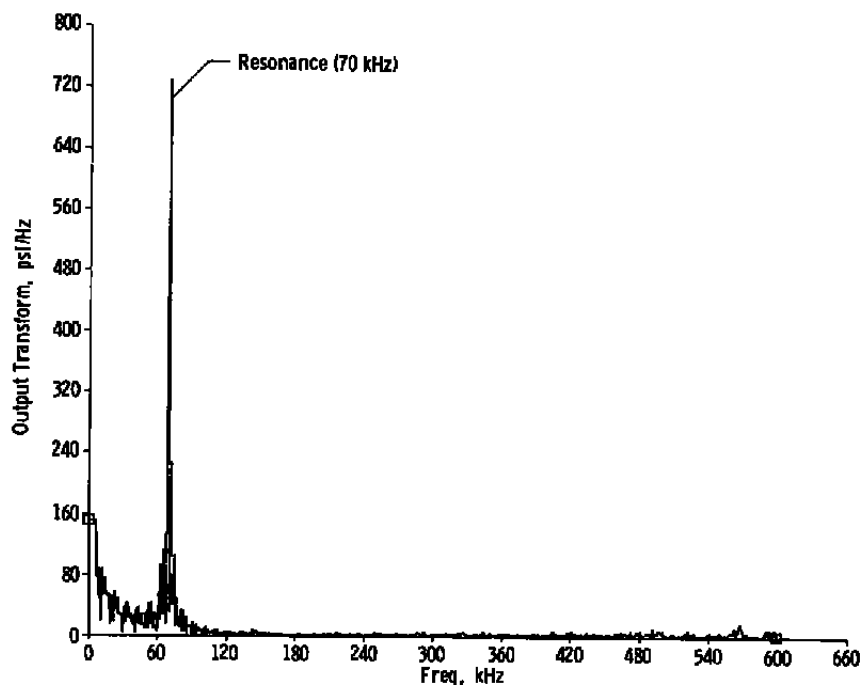


c. Input and output aligned in time and windowed

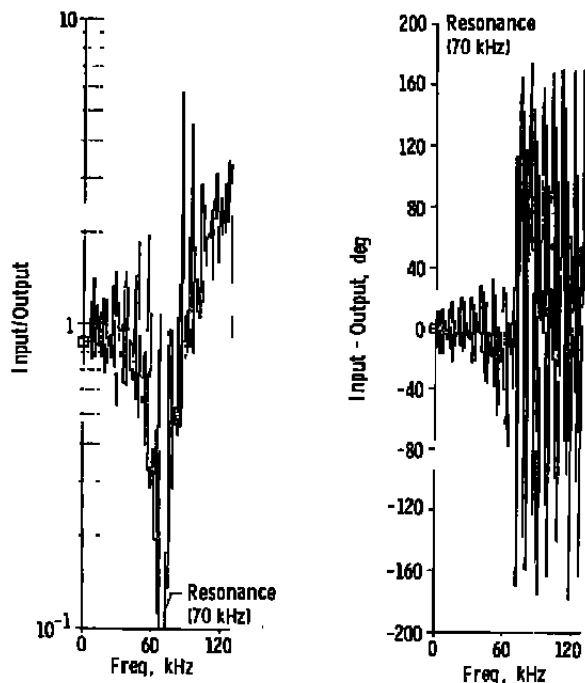


d. Transform of step input

Figure B-9. Continued.



e. Transform of transducer response



f. Transfer function

Figure B-9. Concluded.

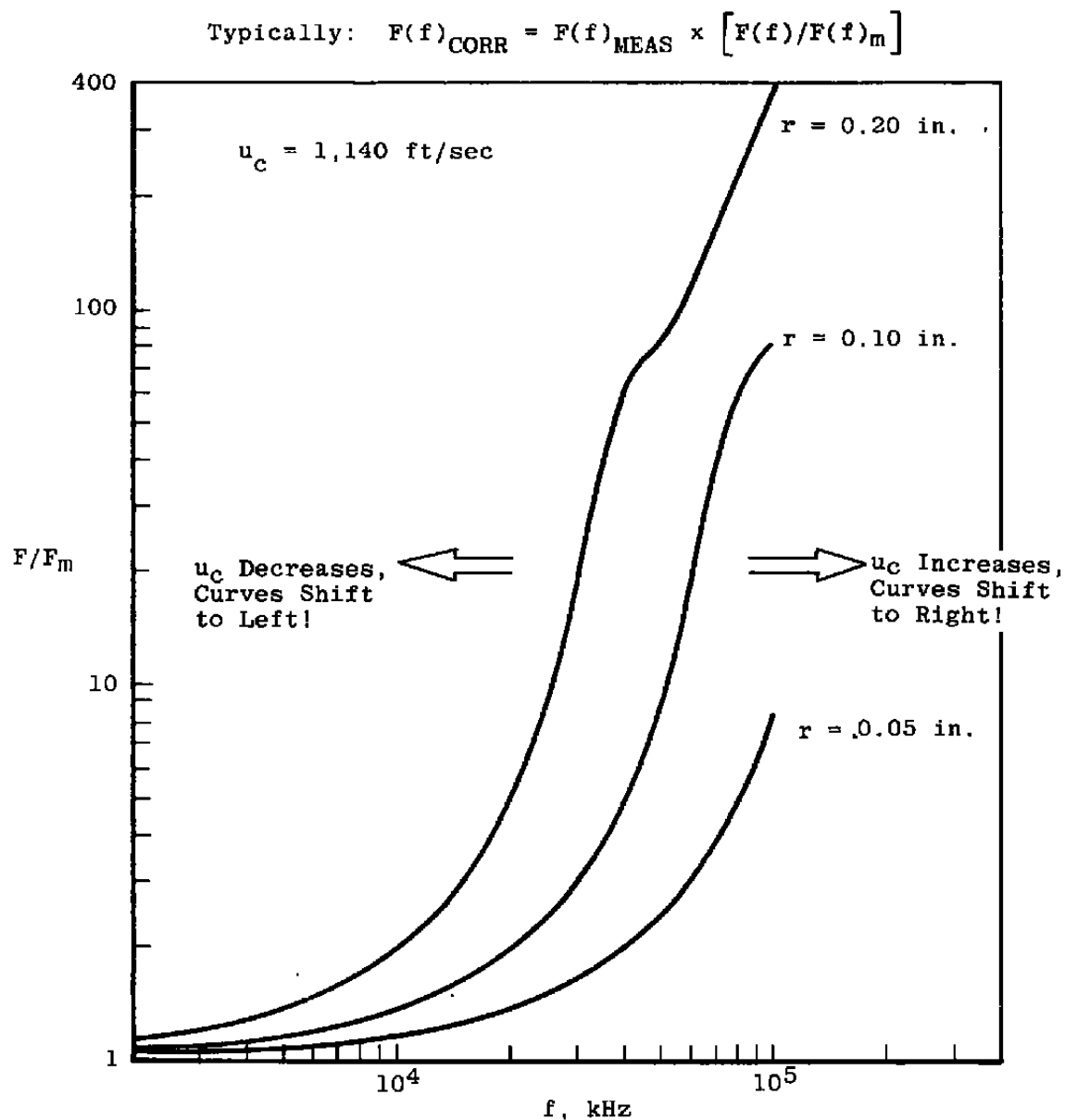


Figure B-10. G. M. Corcos transducer size attenuation factors

Table B-1. FY79 Transducer Calibrations

Gage No.*	Type	Serial No.	Scale Factors, mv/psi		Location
			Subatmospheric Calibration	Factory (Atmospheric) Calibration	
1	Kulite	J1-36	{ 16.80}* {-2.17}	15.7	Stilling Chamber
2		J1-37	{ 16.39}* {-2.06}	15.5	Nonoperating Sidewall
3		G1-51	{ 13.14}* {-0.57}	12.0	Operating Sidewall
4	PCB 113	1446	{ 26.38}* {-0.33}	22.0	Flat Plate, PW1
5	PCB 106	248	84.8 ± 4.4	100.0	Flat Plate, PW2
6	PCB 112	1407	{ 52.72}* {-0.78}	42.0	Window Wall, PWW
7	PCB 105	580	28.0 ± 2.0	30.0	Tank, PMIT
8	PCB 105	568	25.4	26.0	Pitot Probe
9	B&K Mic		803.2	N/A	

\*Scale factor sensitive to local pressure: SF = mP + B;  $\left\{ \frac{B}{m} \right\}$ .  
 Not enough data to fully evaluate Gages 5, 7 through 9 for scale factor-pressure effects.

Table B-2. FY80 Transducer Calibrations

Gage No.*	Type	Serial No.	Scale Factors, mv/psi		Location
			Subatmospheric Calibration	Factory (Atmospheric) Calibration	
1	PCB 105	845		24.5	Sta 11.0
2		828		17.2	Sta 12.0, Blind
3		846		28.5	Sta 11.0
4	PCB 113	1447	{ 28.04 }** { -0.36 }	23.0	Sta 12.5
5	PCB 105	826		20.6	Sta 25.0
6	ENDEVCO	DM-43	{ 68.86 }** { -3.64 }	N/A	Sta 25.0, Blind
7	PCB 113	1446	{ 26.38 }** { -0.33 }	22.0	Sta 25.0
8	ENDEVCO	DN-76	{ 71.94 }** { -2.06 }	N/A	Sta 25.0
9	PCB 112	1407	{ 52.72 }** { -0.78 }	42.0	Sta 40.0
10	PCB 105	829		18.5	Active, Pitot
11	PCB 105	827		18.2	Blind, Pitot

\*Gages 1 through 9 on 6-deg cone: Sta 0 at cone nose.

\*\*Scale factor sensitive to local pressure; SF = mP + B;  $\left\{ \frac{B}{m} \right\}$ .

## APPENDIX C

### WIND TUNNEL TEST PARAMETERS

The basic parameters characterizing the general features of the tunnel wall turbulent boundary, which contributes significantly to the test section turbulence, are  $Re_\theta$ ,  $\delta^*$ , and  $\delta$ . These boundary-layer parameters were extracted from Refs. 40 and 41 and are summarized in Figs. C-1 through C-4. It is interesting to note that the Reynolds number based on the tunnel wall boundary-layer momentum thickness appears to be solely a function of the test section Reynolds number in Tunnel A, which is an uncooled, two-dimensional nozzle. In Tunnel B, which is a water-cooled, axisymmetric nozzle,  $Re_\theta$  is dependent upon the tunnel unit Reynolds number and nozzle Mach number.

The Van Driest II analysis (Ref. 42) for thin, turbulent boundary layers in compressible streams with zero pressure gradients was used to estimate the growth of the boundary layer along the Tunnel A nozzle wall. In this analysis, the local Reynolds number,  $RE_x$ , was evaluated as an integral function of the local nozzle stream properties; that is,

$$RE_x = \int_0^x (\rho u / \mu) dx$$

The local boundary-layer profiles and thickness parameters were evaluated at equal intervals along the nozzle wall from the throat to the test section of Tunnel A. A comparison of the experimental values of  $RE_\theta$  with the theoretical estimates is given in Fig. C-4. The theoretical results show a Mach number effect which is not present in the experimental results. This discrepancy may be due to the fact that in the theoretical analysis the pressure gradient effects on the nozzle wall boundary layer were neglected, the boundary layer was assumed to be fully turbulent from the nozzle throat to the test section, and the boundary layers were quite thick.

The experimentally defined values of  $RE_\theta$  based on results from Ref. 40 and the Winter and Gaudet correlation (Ref. 43) were used to estimate the nominal test section wall skin friction coefficient given in Fig. C-5. In this correlation, which was found to agree with wind tunnel results presented in Ref. 44, the skin friction is defined as follows:

$$c_f = [0.0110(F_\delta RE_\theta)^{-0.1775}] / F_c$$

where

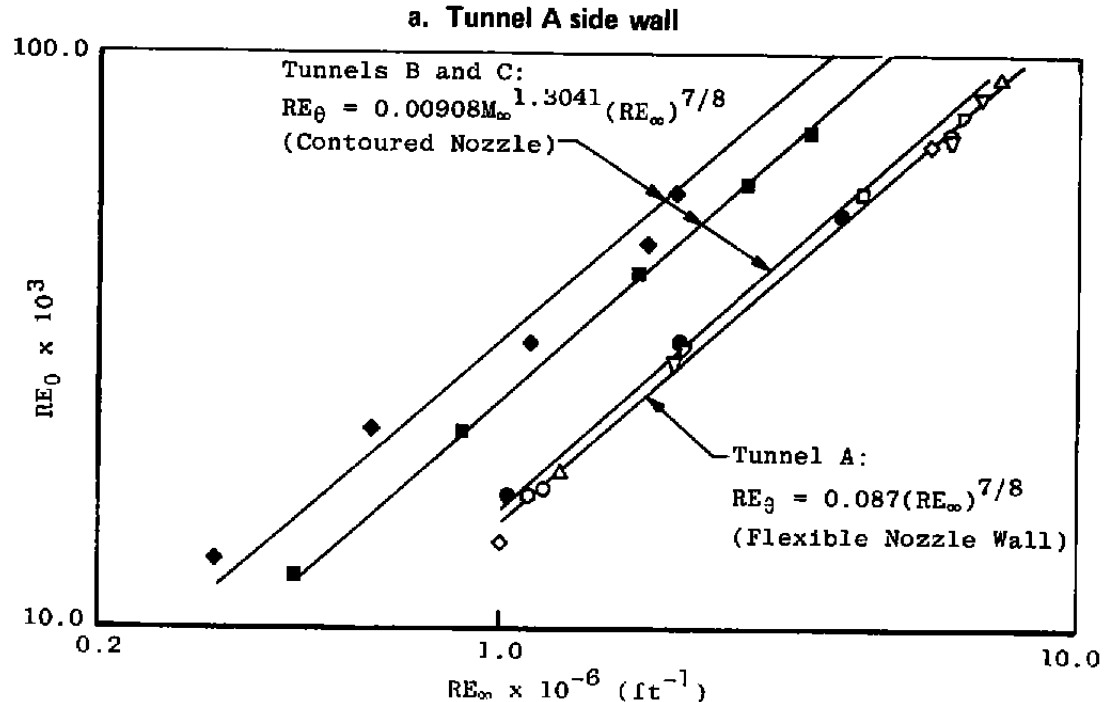
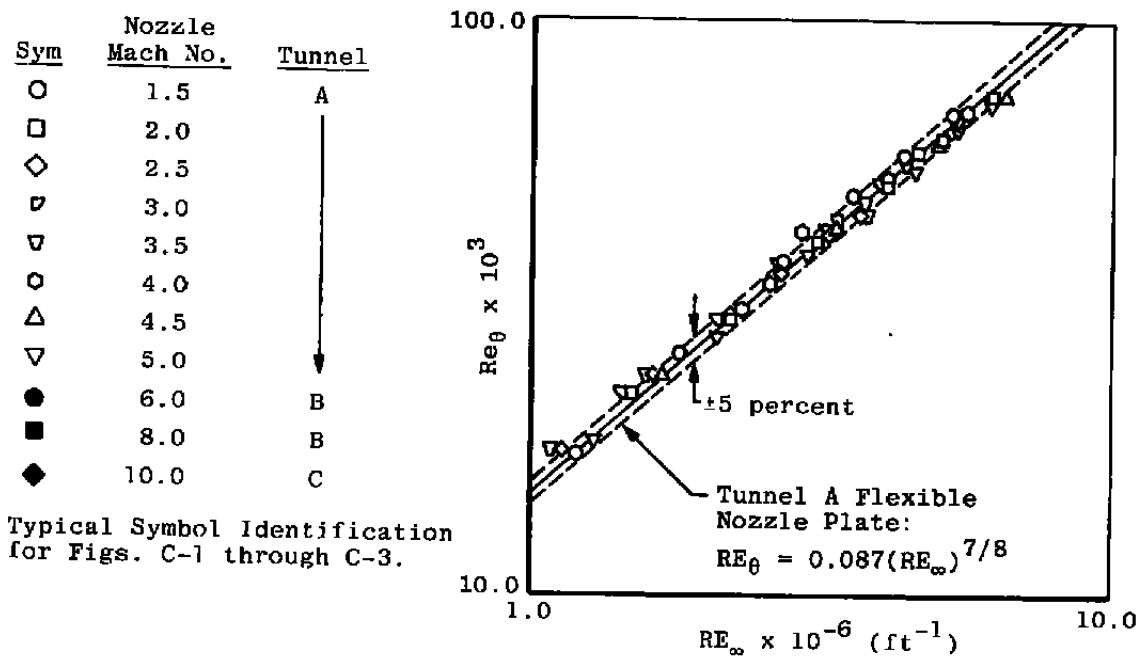
$$F_\delta = 1 + 0.056 M_\infty^2$$

and

$$F_c = (1 + 0.2 M_\infty^2)^{0.5}$$

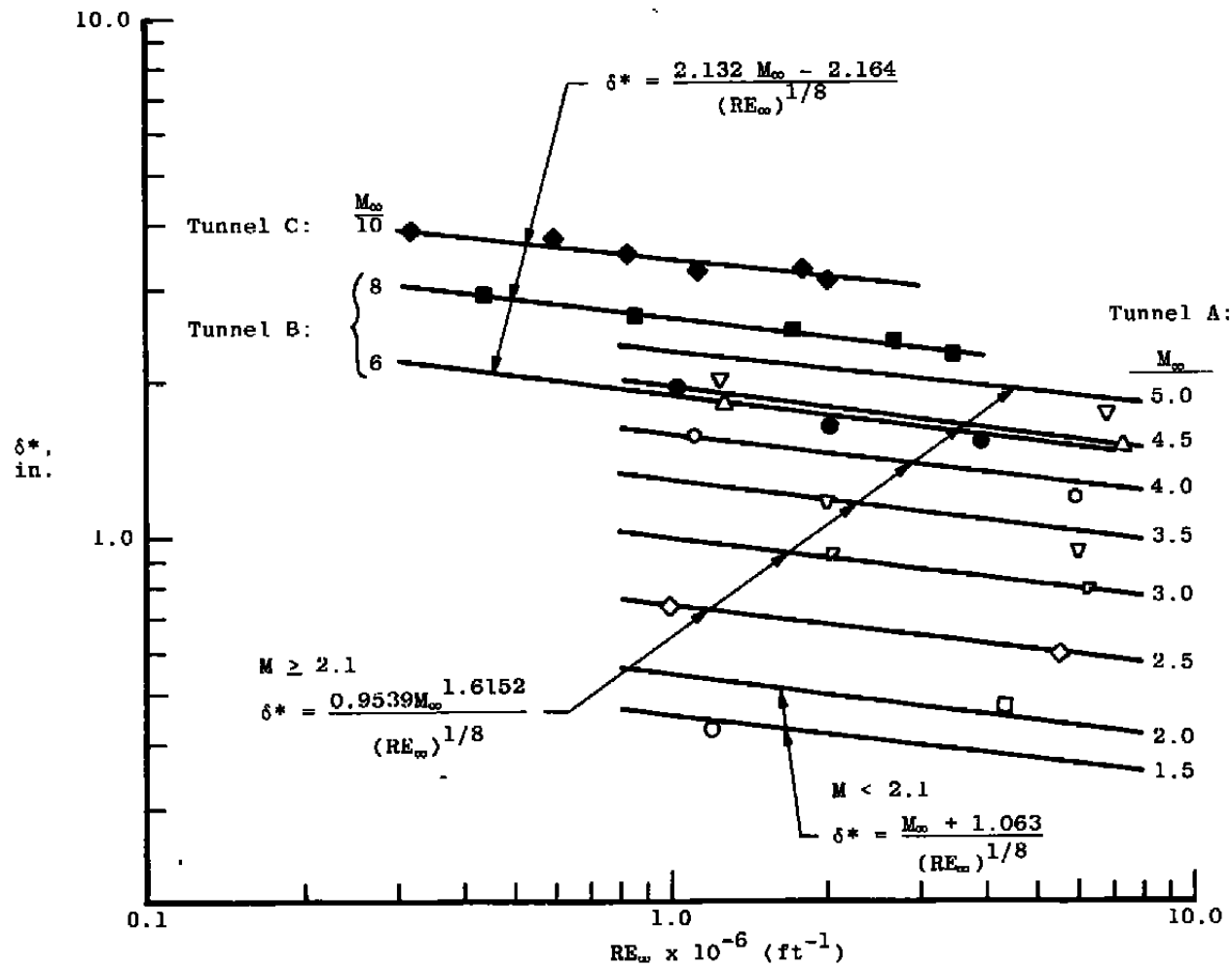
As noted in Section 2.0 the local friction or shear coefficient can be shown to be roughly proportional to the test section free-stream pressure fluctuations. Therefore, the parameter ( $c_f$ ) would be a useful correlating (or normalizing) parameter for free-stream fluctuation measurements.

Figure C-6 defines the shape factors associated with the test section, tunnel wall, and turbulent boundary-layer thickness parameters. There is reasonable agreement between the Tunnel A boundary-layer shape factor ratio based on " $\delta^*/\Theta$ " and the semi-empirical correlation given in Ref. 20 for other wind tunnel shape factors.

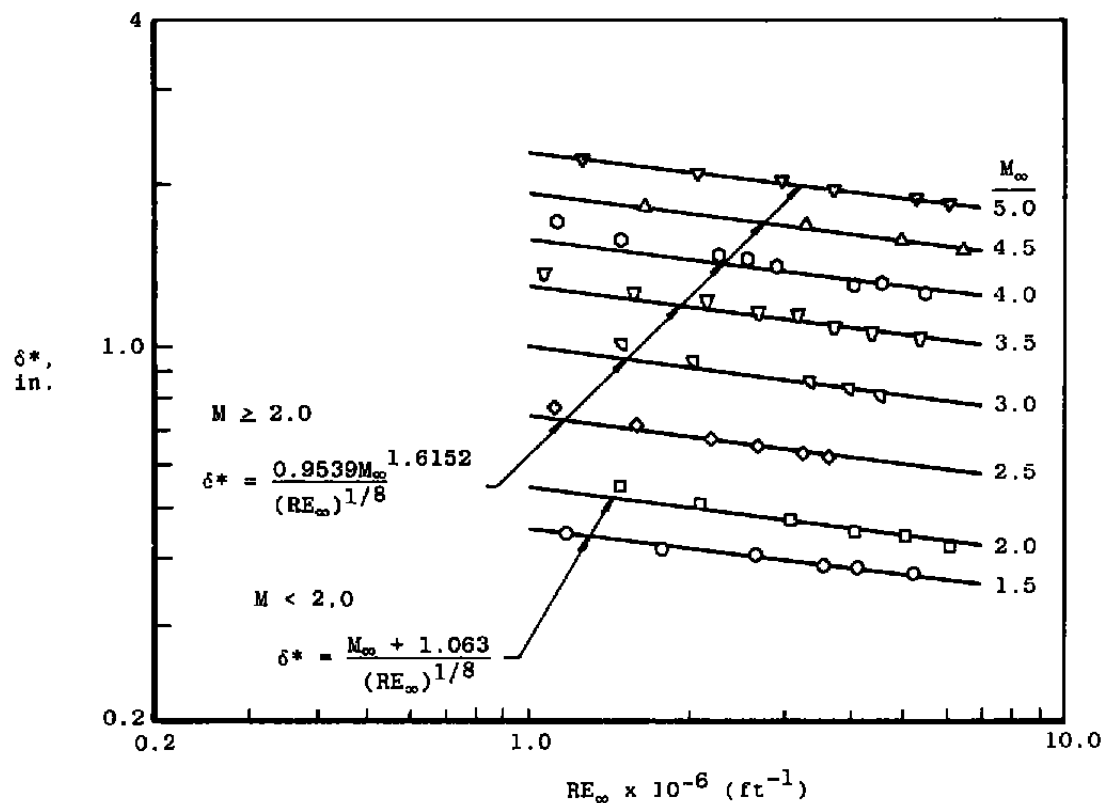


b. Axisymmetric contoured nozzle or flexible plate  
 Figure C-1. Simple relationship for the Reynolds number based on the tunnel wall momentum thickness.

150

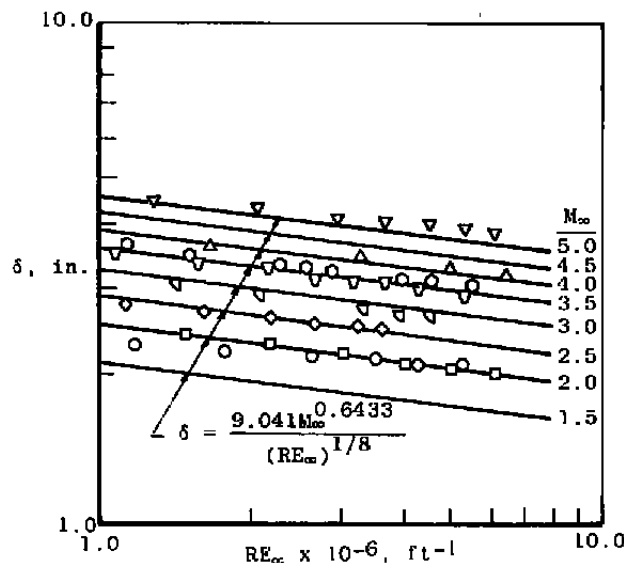


a. Contoured nozzle/flexible plate  
 Figure C-2. Tunnel wall boundary-layer displacement thickness.



b. Tunnel A side wall

Figure C-2. Concluded.



a. Tunnel A side wall

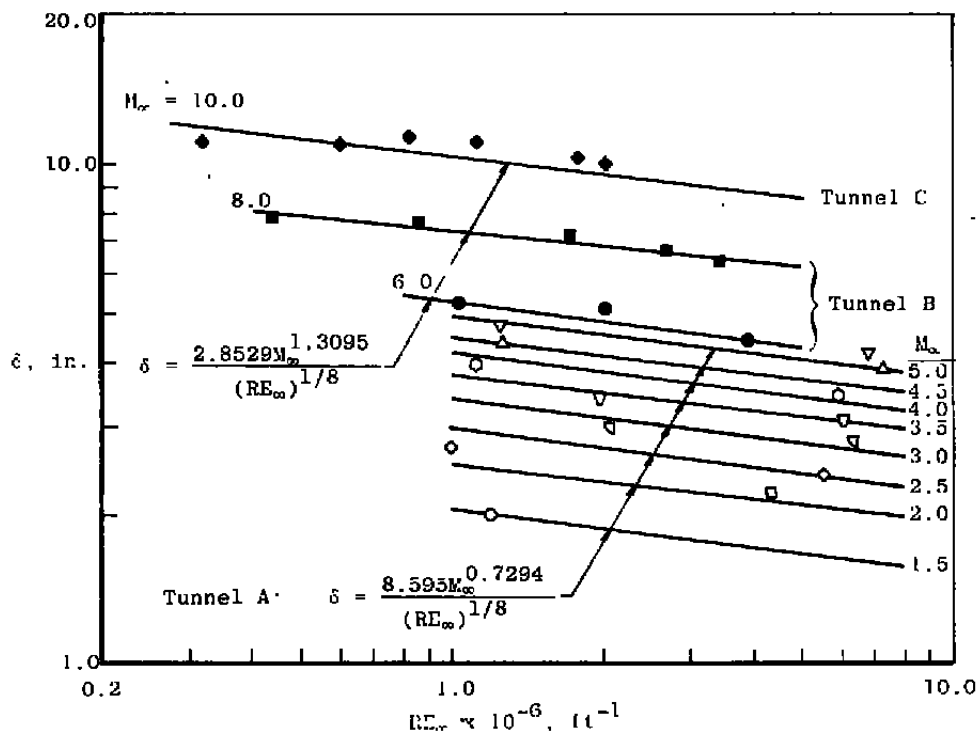


Figure C-3. Simple relationship for defining the tunnel wall boundary-layer thickness ( $u/u_{\infty} \approx 0.99$ ).

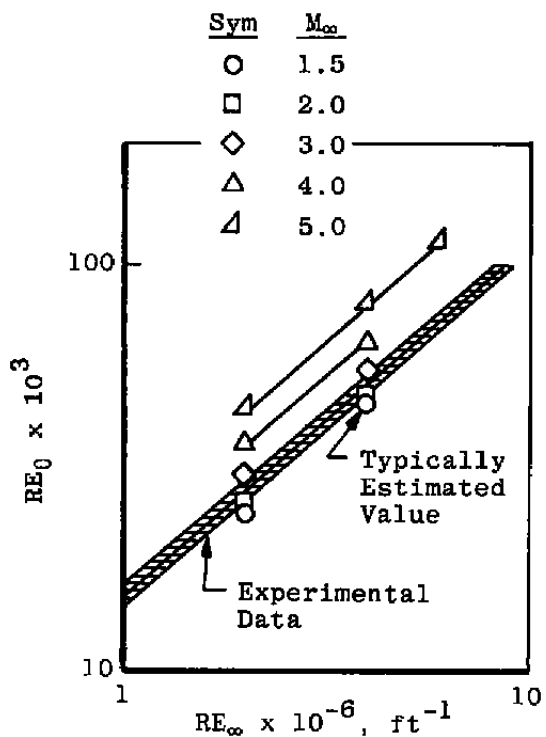


Figure C-4. Comparison of estimated and measured  $RE_0$  parameter in Tunnel A.

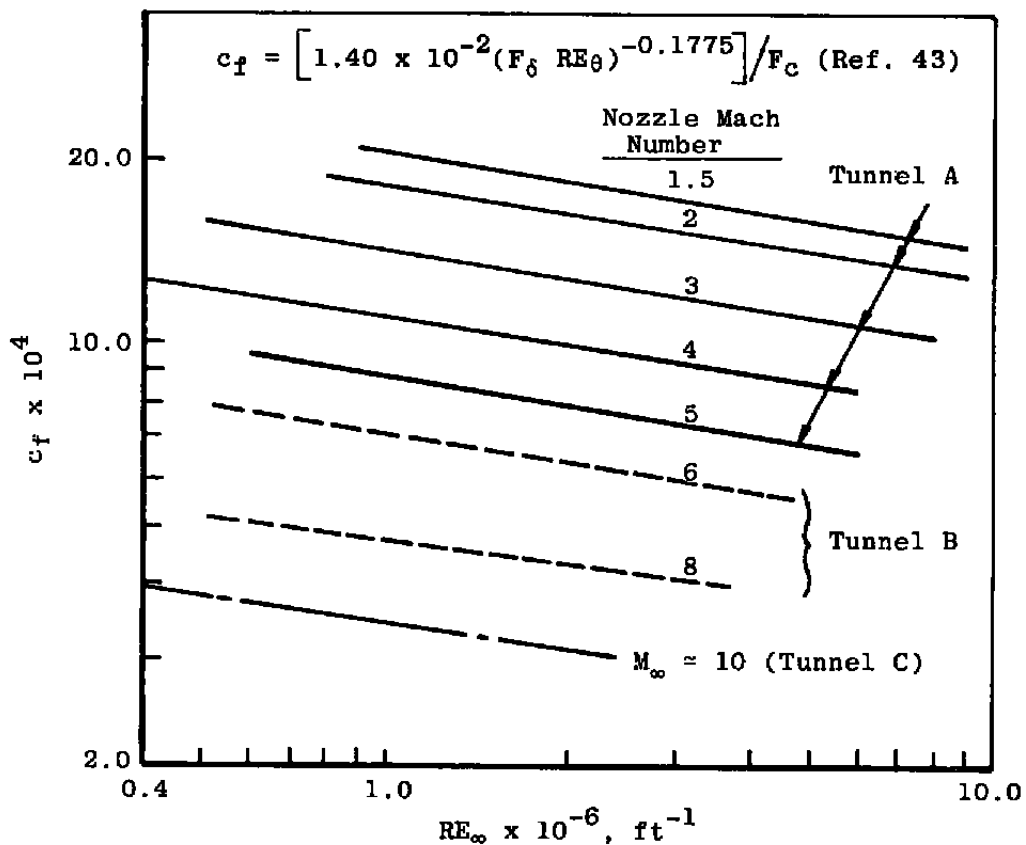


Figure C-5. Estimated local friction coefficient on the nozzle wall in the tunnel test sections over the operational Reynolds number ranges.

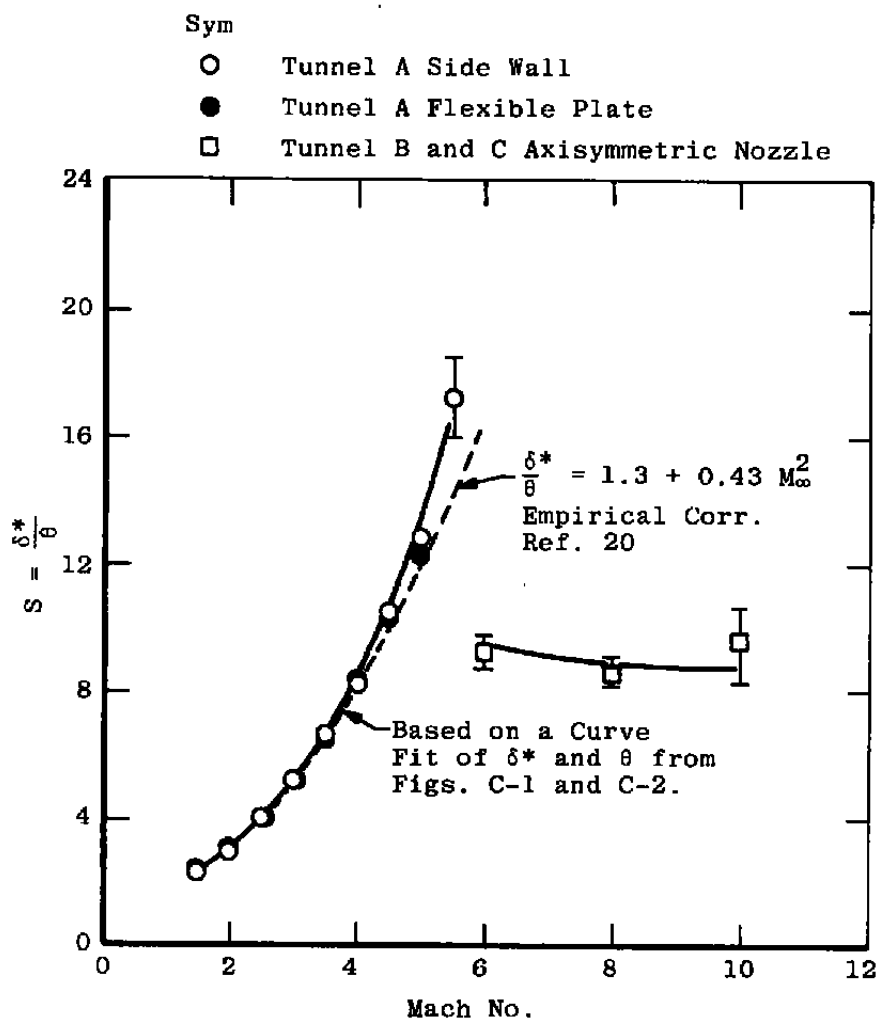
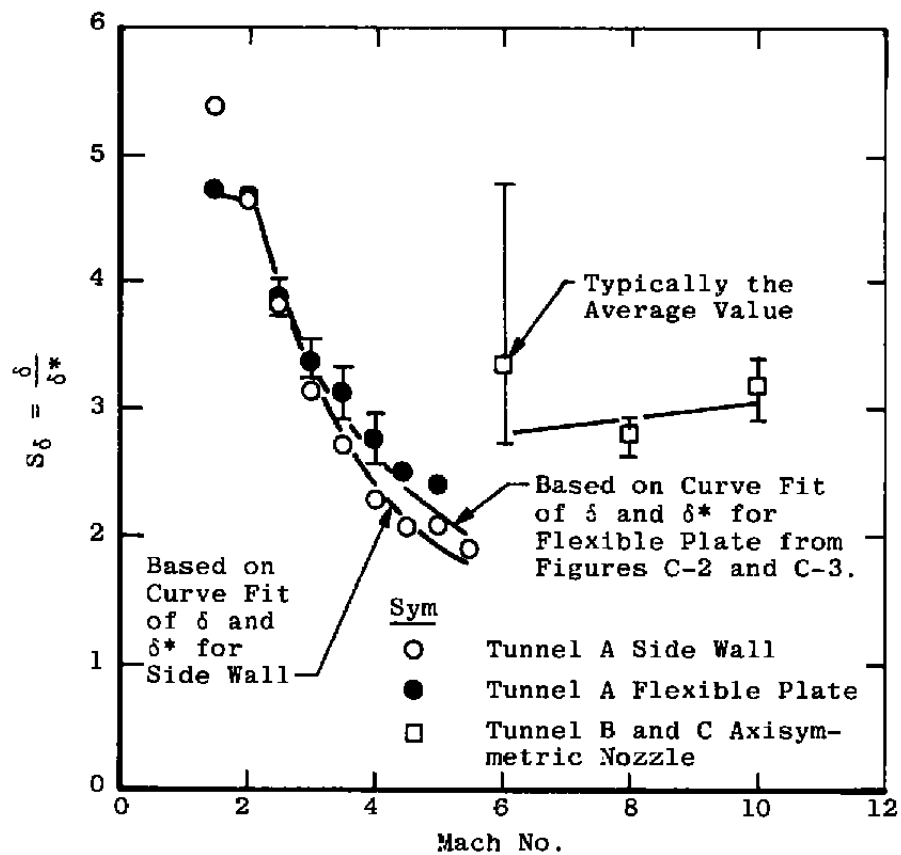
a.  $\delta/\delta^*$ 

Figure C-6. VKF tunnel wall turbulent boundary-layer shape factors.



b.  $\delta/\delta^*$   
Figure C-6. Concluded.

Table C-1 Summary of Tunnel Conditions

## a. Tunnel A

Mach No.	Stilling Chamber			Test Section								Probe Measurements			
	PT, psia	TT, °R	DP, °F	T <sub>∞</sub> , °R	P, psia	Q, psia	RHO, lbm/ft <sup>2</sup> x 10 <sup>2</sup>	U, ft/sec	MU, (1)* x 10 <sup>7</sup>	RE <sub>∞</sub> , ft <sup>-1</sup> x 10 <sup>6</sup>	PT2, psia	P <sub>p</sub> , psia	ML	MUO x 10 <sup>7</sup>	RE <sub>O</sub> , ft <sup>-1</sup> x 10 <sup>-6</sup>
1.51	6.9	560	5	385	1.85	2.96	1.30	1,450	2.93	2.0	6.39	6.27	1.56	3.95	1.50
	10.2				2.74	4.37	1.92			3.0	9.45	N.D.	N.D.	N.D.	N.D.
	13.7	↓	↓	↓	3.68	5.87	2.58	↓	↓	4.0	12.69	N.D.	N.D.	N.D.	N.D.
2.00	4.0	560	10	311	0.51	1.43	0.44	1,730	2.44	1.0	2.88	2.83	2.02	3.96	0.60
	5.0				0.64	1.79	0.55			1.2	3.60	N.D.	N.D.	N.D.	N.D.
	6.1				0.78	2.18	0.68			1.5	4.40	N.D.	N.D.	N.D.	N.D.
	8.0				1.02	2.86	0.89			2.0	5.77	5.59	2.04	3.97	1.20
	12.0				1.53	4.29	1.33			2.9	8.65	8.45	2.04	3.96	1.81
	14.1	↓	↓	↓	1.80	5.05	1.56			3.4	10.16	N.D.	N.D.	N.D.	N.D.
	16.1	↓	-5	↓	2.06	5.76	1.79	↓	↓	3.9	11.61	N.D.	N.D.	N.D.	N.D.
3.01	7.0	560	5	199	0.19	1.19	0.25	2,080	1.60	1.0	2.28	N.D.	N.D.	N.D.	N.D.
	13.8				0.37	2.35	0.50			2.0	4.49	4.32	3.06	3.98	0.80
	20.4				0.55	3.47	0.74			3.0	6.64	6.48	3.04	3.98	1.18
	27.2				0.73	4.63	0.99			4.0	8.85	8.84	3.01	3.99	1.60
	34.1	↓	0	↓	0.91	5.80	1.24	↓	↓	5.0	11.10	11.08	3.01	4.00	1.98

\*(1) Slugs/sec-ft or 1bf-sec/ft<sup>2</sup>

Table C-1. Continued  
a. Concluded.

Mach No.	Stilling Chamber			Test Section								Probe Measurements			
	PT, psia	TT, °R	DP, °F	T <sub>∞</sub> , °R	P, psia	Q, psia	RHO, 1bm/ft <sup>3</sup> x 10 <sup>2</sup>	u, ft/sec	MU, (1) x 10 <sup>7</sup>	RE <sub>∞</sub> , ft-l x 10 <sup>6</sup>	PT2, psia	P <sub>p</sub> , psia	ML	MUO x 10 <sup>7</sup>	RE <sub>0</sub> , ft-l x 10 <sup>-6</sup>
4.01	12.0	575	-15	136	0.078	0.88	0.15	2,300	1.10	1.0	1.65	1.66	4.00	4.08	0.26
	24.1	575		136	0.155	1.75	0.31	2,300	1.09	2.0	3.29	3.52	4.03	4.07	0.45
	36.0	580		137	0.231	2.61	0.45	2,310	1.10	3.0	4.91	4.92	4.02	4.05	0.81
	48.0				0.308	3.48	0.61			3.9	6.55	6.58	4.02	4.05	1.08
	60.0				0.385	4.35	0.76			4.9	8.19	8.16	4.02	4.07	1.33
4.01	6.6	610	25	145	0.043	0.48	0.08	2,360	1.16	0.5	0.908	0.920	4.00	N.D.	0.14
	13.0				0.084	0.95	0.16			1.0	1.79	1.78	4.02		0.28
	18.3				0.119	1.34	0.22			1.4	2.52	2.48	4.03		0.38
	24.4				0.159	1.78	0.30			1.9	3.36	3.24	4.03		0.50
	30.4				0.198	2.22	0.37			2.3	4.18	4.08	4.04		0.64
5.03	23.0	635	18	105	0.042	0.74	0.11	2,520	0.84	1.0	1.39	1.39	5.03	N.D.	0.19
	45.8		-3	105	0.084	1.48	0.22			2.0	2.76	2.72	5.05	4.36	0.39
	68.5		-3	104	0.124	2.20	0.32			3.0	4.10	4.05	5.06	4.38	0.57
	90.5		-17		0.161	2.88	0.42	2,530		3.9	5.37	5.32	5.06	N.D.	0.75
	115.3				0.206	3.67	0.53			5.0	6.85	6.80	5.06		0.95
	137.4				0.245	4.37	0.64			6.0	8.16	8.04	5.07		1.13

Table C-1. Concluded  
b. Tunnel B

Mach No.	Stilling Chamber			Test Section								Probe Measurements			
	PT, psia	TT, °R	DP, °F	T <sub>∞</sub> , °R	P, psia x 10 <sup>-2</sup>	Q, psia	ρ <sub>∞</sub> , lbm/ft <sup>3</sup> x 10 <sup>2</sup>	u, ft/sec	μ, (1) x 10 <sup>7</sup>	RE <sub>∞</sub> , ft <sup>-1</sup> x 10 <sup>-6</sup>	PT2, psia	P <sub>p</sub> , psia	ML	μ <sub>0</sub> x 10 <sup>7</sup>	Re <sub>0</sub> , ft <sup>-1</sup> x 10 <sup>-5</sup>
5.88	26.4	850	-55	107.4	1.89	0.458	0.0476	2,990	0.863	0.51	0.851	0.768	6.03	5.35	0.828
5.89	53.7			107.0	3.81	0.925	0.0960		0.861	1.04	1.72	1.61	5.99	5.35	1.68
5.89	79.5			107.0	5.64	1.07	0.142		0.861	1.53	2.55	2.35	6.00	N.D.	2.88
5.91	107.1		-41	106.4	7.44	1.82	0.189		0.856	2.05	3.38	3.30	5.95	5.37	3.24
5.92	160.0			106.1	11.00	2.70	0.280		0.853	3.05	5.02	4.99	5.93		4.80
5.94	212.0			105.5	14.28	3.53	0.365		0.848	4.00	6.55	6.59	5.93		6.36
5.95	273.3	↓	↓	105.2	18.22	4.52	0.468	↓	0.846	5.14	8.39	8.38	5.95	5.38	8.04
5.92	159.0	1,115	-55	139.0	10.93	2.68	3.420					7-Stage Operation			
7.89	115.5	1,340	-45	99.6	1.29	0.564	0.0351	3,860	0.801	0.525	1.04	0.950	8.06	7.23	0.588
7.94	231.6	1,360		99.9	2.49	1.10	0.0673	3,890	0.803	1.01	2.03	1.92	8.04	7.31	1.08
7.99	462.3	1,350		98.1	4.77	2.13	0.131	3,880	0.788	2.01	3.95	3.84	8.04	7.27	2.16
8.00	693.0			97.8	7.10	3.18	0.196		0.786	3.00	5.88	5.66	8.07	7.28	3.24
8.00	849.4	↓	↓	97.8	8.70	3.90	0.240	↓	0.786	3.68	7.21	6.93	8.07	7.28	3.96

## APPENDIX D

### SIX-DEGREE SHARP NOSE CONE SURFACE AND FLOW-FIELD PROPERTIES

The measurements obtained on the 6-deg sharp nose cone were normalized, when appropriate, by the surface properties given in this Appendix (see Fig. D-1). The local surface velocity measurements at Mach number 4 and 6 are based on the local mean flow-field measurements, namely the local wall static pressure, the pitot pressure just above the boundary layer, and the stream total temperature. The theoretical estimates of the local cone properties were based on the inviscid sharp cone solutions of the Taylor-Maccoll equation (Ref. 45). There is agreement between the theory and experimental values of the local velocity and cone surface pressure ratios at the maximum free-stream Reynolds number.

Assuming a Prandtl number of 0.71, a comparison between the measured cone surface temperature and the estimated value is reasonable in the Mach number range from 1.5 to 5. The lower experimental value at Mach number 6 was obtained in Tunnel B where the model was not allowed to reach a stable (essentially adiabatic) condition.

The estimated laminar boundary-layer thickness for the 6-deg sharp nose cone at the upper and lower free-stream Reynolds number is shown in Fig. D-1d. These theoretical estimates were based on results derived from Refs. 46 and 47. The corresponding experimental results at Mach Nos. 4 and 6 were based on mean flow measurements made at model station 25 (in.) on the cone. Unfortunately, the 14 percent disagreement between the Mach No. 6 results and the theory was probably due to a large bias in the uncertainty in the pitot probe displacement measurement used to define the boundary-layer profile. In this study, the analytically defined parameters were selected for normalizing cone surface pressure fluctuation measurements.

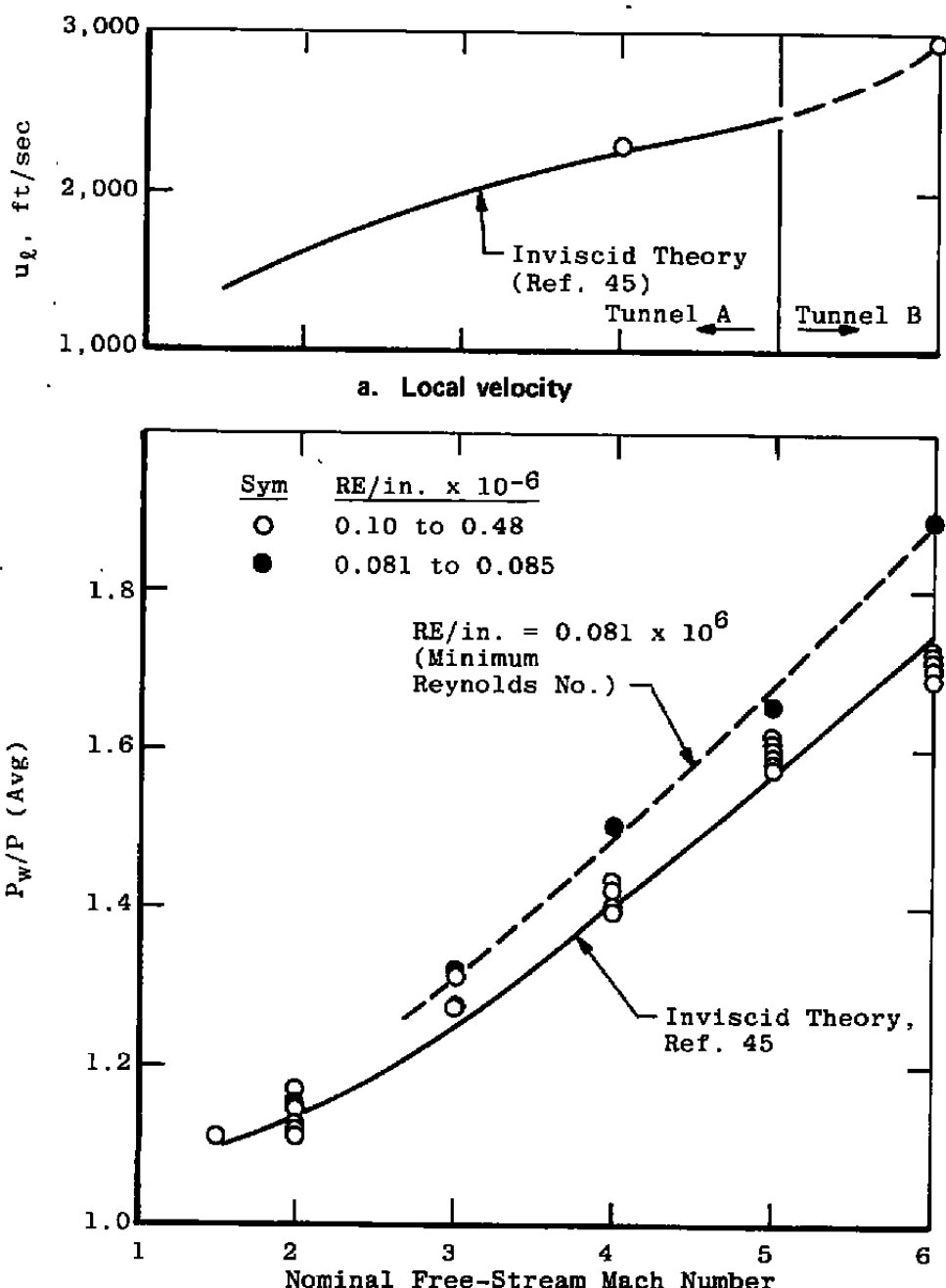
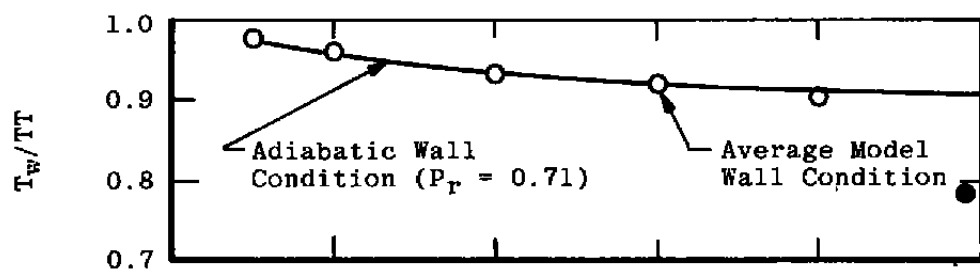
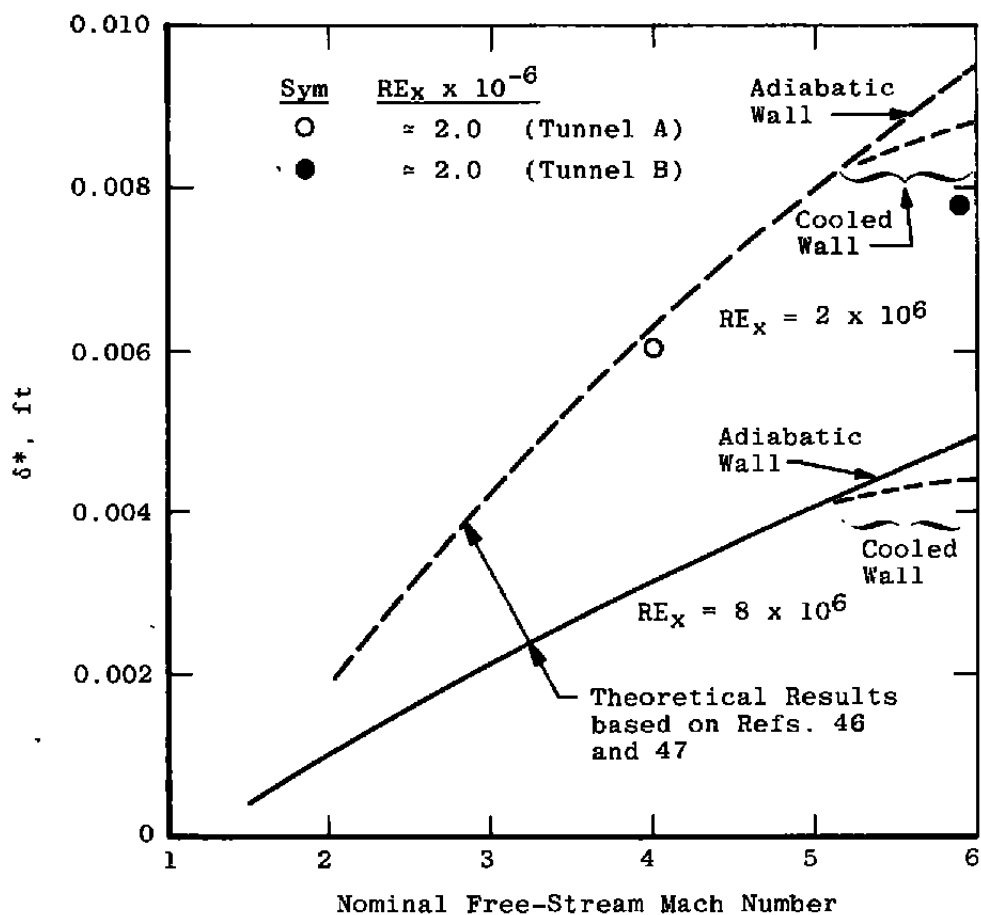


Figure D-1. 6-deg sharp nose cone surface properties.



c. Average model wall temperature

d. Boundary-layer displacement thickness  
Figure D-1. Concluded.

## NOMENCLATURE

<b>A</b>	Constant
<b>A<sub>T</sub></b>	Test section cross-sectional area, in. <sup>2</sup>
<b>a</b>	Speed of sound, ft/sec
<b>B</b>	Intercept of (SF = m P + B)
<b>BW</b>	Total bandwidth of the analysis, Hz
<b>C<sub>( )</sub></b>	Coefficient, ( )/q <sub>∞</sub>
<b>c<sub>f</sub></b>	Local wall shear stress coefficient
<b>D<sub>j</sub></b>	Coefficient, j = 1 to 5
<b>DE</b>	Effective diameter, DE = (4A <sub>T</sub> /π) <sup>1/2</sup> , in.
<b>DP</b>	Dew point, °F
<b>e</b>	Voltage across wire, volts
<b>Δe<sub>( )</sub></b>	Sensitivity coefficient of wire for ( ) component, volts
<b>F</b>	Power spectral density function, units <sup>2</sup> /Hz
<b>F<sub>c</sub>, F<sub>δ</sub></b>	Winter and Gaudet (Ref. 43) correlation parameters
<b>f</b>	Frequency, Hz
<b>g<sub>1</sub>, g<sub>2</sub></b>	Coefficients defined by Eqs. (18) and (19), respectively
<b>H</b>	Transform, units/Hz
<b>h</b>	Real time signal, units
<b>I</b>	Imaginary
<b>k</b>	Number of the discrete point in the real time signal
<b>L<sub>1</sub>, L<sub>2</sub></b>	Pitot-acoustic probe support length, in.

$M_\infty$	Mach number
ML	Local Mach number
MUO	Viscosity based on TT, lbf-sec/ft <sup>2</sup>
MU, $\mu$	Viscosity based on T, lbf-sec/ft <sup>2</sup>
m	Slope of (SF = m P + B)
N	Number of discrete points in a signal sample (N = 1,024 points)
NED	Normalized energy ratio (see Fig. 30)
Nu <sub>o</sub>	Nusselt number based on TT
n	Number of the discrete amplitude point in the frequency domain
n <sub>d</sub>	Number of signal samples
n <sub>x</sub>	Directional cosine of the normal to the sound plane-wave front relative to the mean-flow direction
P	Static pressure, psia
P <sub>1</sub> , P <sub>2</sub>	Pressure upstream and downstream, respectively, of a normal shock, psia
P <sub>p</sub>	Pitot probe pressure, psia
Pr	Prandtl number
PST	Stilling chamber pressure fluctuation, psi
PSW	Side wall static pressure fluctuation, psi
PT	Stilling chamber pressure, psia
PT2	Computed total pressure downstream of a normal shock, psia
P <sub>w</sub> , PW( )	Wall or surface pressure, psia

PWW	Tunnel window wall static pressure fluctuation, psi
Q, q	Dynamic pressure, psia
R	Real number
$R_{( )}$	Resistance of wire at condition ( ), ohm
$R_{( \times )}$	Correlation coefficient for components indicated by subscripts
r	DPS gage radius, in.
RE	Reynolds number based on $T_\infty$
RE <sub>0</sub>	Reynolds number based on TT
RHO, $\rho$	Density, lbm/ft <sup>3</sup>
S	Boundary-layer shape factor
SF	Scale factor of DPS gage, psi/mv
T, t	Time, sec, or sample length
T	Temperature (typically subscripted or superscripted), °R
$T_{( )}$	Temperature of wire at condition ( ), °R
TRMS	True rms
TT	Stilling chamber or free-stream total temperature, °R
TW, $T_w$	Local wall temperature, °R
u	Velocity, ft/sec
X	Overheating parameter, $\Delta e_r/\Delta e_o$
x	Surface length, ft
Y	Nondimensional rms voltage fluctuation, $\tilde{e}/\Delta e_o$
$\alpha$	Temperature linear coefficient of resistivity, ( $^{\circ}\text{C}$ ) <sup>-1</sup>
$\gamma$	Ratio of specific heats ( $\gamma = 1.4$ )

$\Delta f$	Bandwidth between points in a spectrum, Hz
$\Delta(\ )$	Incremental difference of the property ( ) from its mean value
$\delta$	Boundary-layer thickness, ft
$\delta^*$	Boundary-layer displacement thickness, ft
$\epsilon$	Uncertainty parameter
$\eta$	Recovery factor
$\theta$	Boundary-layer momentum thickness, ft
$\Lambda$	Integral scale of parameter ( )
$\pi$	Sound mode "amplitude," normalized
$\sigma$	Entropy mode "amplitude," normalized
$\tau$	Local shear value, psi, or vorticity mode "amplitude," normalized
$\phi$	Phase angle or model roll angle, deg
$\omega$	Angular velocity, $2\pi f$ , radians per second

## SUBSCRIPTS

2	Downstream of a normal shock
C	Convective quantity
CORR	Corrected or input value
D	Discrete or digital value
DE	Effective test section diameter, $2(\text{area}_{\text{test section}}/\pi)^{1/2}$
d	Wire diameter
f	Pertaining to reference temperature of 32°F
l	Local
m	Measured
o	First mode

r	Reference value
ST	Stilling chamber
STA	Model (or tunnel) station
s	Source (or shock) velocity
t	Transition location
w	Pertaining to temperature of heated wire or wall
x	Based on surface length
$\Theta$	Based on boundary-layer momentum thickness
$\pi$	Pertaining to sound mode
$\sigma$	Pertaining to entropy mode
$\tau$	Pertaining to vorticity mode
$\infty$	Free stream

## **SUPERSCRIPTS**

( $\bar{}$ )	Square root of the mean square value
( $'$ )	Fluctuating component
*	Complex conjugate or reference
( $\bar{\bar{}}$ )	Average with respect to time